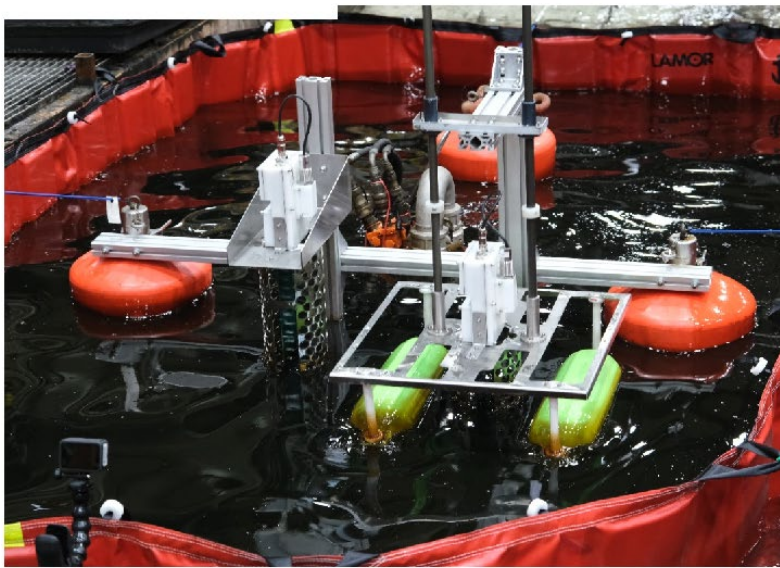# Bureau of Safety and Environmental Enforcement
# Oil Spill Preparedness Division
# Development of an Oil Thickness Sensor Phase II

Final Report

February, 2022



(Photo: CRREL and American University of Beirut, 2022)

**Imad H. Elhajj, Daniel Asmar, Mahdi Saleh, Ali Rida Tabikh, Moustafa Ammouri, Sevag Babikian, Ghassan Oueidat, Mahmoud Alayass, Mohammad Alameh**

**US Department of the Interior**
**Bureau of Safety and Environmental Enforcement**
**Oil Spill Preparedness Division**

# Development of an Oil Thickness Sensor Phase II

Final Report

OSRR # 1103

February 2022

Authors:
Imad H. Elhajj, Daniel Asmar, Mahdi Saleh, Ali Rida Tabikh, Moustafa Ammouri, Sevag Babikian, Ghassan Oueidat, Mahmoud Alayass, Mohammad Alameh

**US Department of the Interior**
**Bureau of Safety and Environmental Enforcement**
**Oil Spill Preparedness Division**

# DISCLAIMER

# REPORT AVAILABILITY

The PDF file for this report is available through the following sources. Click on the URL and enter the appropriate search term to locate the PDF:

| Document Source | Search Term | URL |
| --- | --- | --- |
| Bureau of Safety and Environmental Enforcement (BSEE) | Project Number – 1103 | https://www.bsee.gov/what-we-do/research/oil-spill-preparedness/oil-spill-response-research |
| U.S. Department of the Interior Library | Development of an Oil Thickness Sensor Phase II | https://library.doi.gov/uhtbin/cgisirsi/?ps=8L0mpW5uPV/SIRSI/X/60/495/X |
| National Technical Reports Library | Development of an Oil Thickness Sensor Phase II | https://ntrl.ntis.gov/NTRL/ |

Sources: a) BSEE (2019), b) DOI [2021], c) National Technical Information Service (2021)

# CITATION

Elhajj I., Asmar D., Saleh M., Tabikh A., Ammouri M., Babikian S., Oueidat G., Alayass M., Alameh M. (American University of Beirut, Beirut, Lebanon). 2022. Development of an Oil Thickness Sensor Phase II. Washington D.C. (NW): U.S. Department of the Interior, Bureau of Safety and Environmental Enforcement. Report No.: 1103 Contract No.: 140E0118C0003.

# ABOUT THE COVER

Cover image by CRREL and AUB team shows the different sensors and accessories developed being in use.

# EXECUTIVE SUMMARY

This report summarizes the tasks conducted under the BSEE contract number 140E0118C0003, Development of an Oil Thickness Sensor Phase II. This work built on the BSEE contract E17PC0001 results (OSRR project 1078) for the purpose of enhancing floating oil thickness measurement in the field using handheld and skimmer mounted sensors. The two motivating use cases are: 1) a handheld sensor that will measure slick thickness during tests at facilities such as Ohmsett and CRREL or similar test facilities, or for use from onboard vessels to obtain sample measurements in the field; 2) a sensor that can be mounted on skimmers, buoys, or in an oil spill boom apex to provide thickness data in a field application.

The objective of this project is to improve the sensor accuracy and usability. This requires optimizing the measurement method, packaging, and algorithm. The figure below shows the old sensor (left) and the new sensor (right).
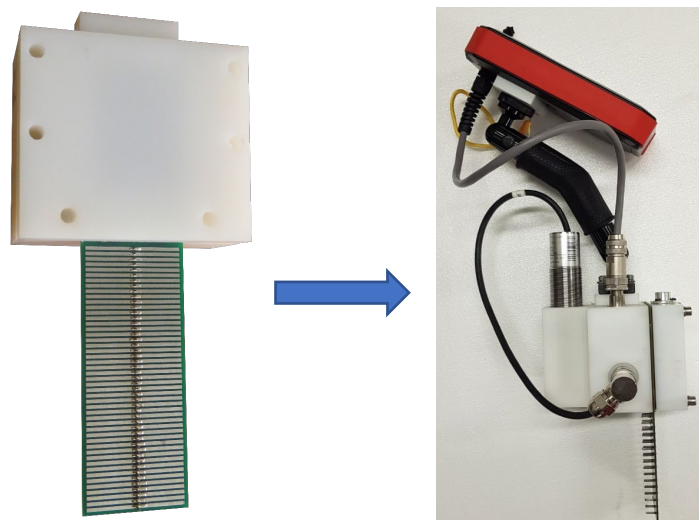


To accomplish the project objectives, the sensor cartridge design was optimized, packaging and attachments were designed to support the use cases, a machine learning (ML) enabled algorithm was developed, and extensive testing was conducted in the lab and at the Cold Regions Research and Engineering Laboratory (CRREL) over 10 days during the period of 18 October to 29 October 2021.

To optimize the sensor cartridge, which is the transducer immersed in the oil/water mixture, several iterations were conducted for the board design. We converged to a knife-like board with pins protruding from the boards to mitigate oil fouling. To further mitigate oil fouling, we tested several hydrophilic/oleophilic and hydrophobic/oleophobic coatings to assess their ability in improving sensor performance. None of the materials tested could further mitigate the oil fouling, without being washed off when dipped into oil/water and without impacting the electric properties of the sensor.

The sensor was also modified to employ a dual measurement principle where on one hand an ultrasonic sensor measures the distance to the oil surface, and on the other the board itself detects the oil/water interface. The board uses capacitance measures to detect if the pins are in oil or are (about to be) short circuited in the water. Several models were fabricated but the main ones we tested include:

Handheld 1:        Resolution +/- 2mm        Sensing Range:  94mm
Handheld 2:        Resolution +/- 3mm        Sensing Range:  141mm
Skimmer sensor 1:    Resolution +/- 12 mm      Sensing Range:  564 mm
Skimmer sensor 2:    Resolution +/- 7mm        Sensing Range:  329 mm

Two different waterproof packages were developed, one for each sensor. The handheld package had two separate parts; one part is the display and processing unit, and another part is the sensor cartridge housing. The skimmer sensor had one package, which includes the cartridge housing and processing unit. Both sensors were equipped with temperature sensors and a GPS unit. The skimmer sensor was also equipped with a wireless transmitter to support report operation. The final sensors are shown below (left: handheld, right: skimmer mount).



We also developed accessories to support each sensor use case. For the handheld sensor, we developed an extendable pole to support remote measures at a distance (*e.g.*, into a tank or off a vessel). We also developed a floating platform, which would allow the handheld sensor to be left free-floating on the water surface while being tethered. For the skimmer sensor, we developed a bridge to allow multiple sensors to be mounted on a skimmer, a fixed and a floating platform to attach to the bridge, and cages that provide support for the sensor cartridges and protection from debris.

A machine learning algorithm composed of multiple filtering stages was also developed. The objective of the algorithm was to support measurements under dynamic conditions (waves) and under fouling conditions (oil sticking to sensor). The advantage of the developed algorithm is that it does not require calibration to neither the type of oil being measured, neither the water, nor to

environmental conditions. Each sensor cartridge only requires a one-time calibration at the time it is manufactured.

Extensive testing was carried out at CRREL using Diesel, Hydrocal 300, Calsol 8240, Weathered HOOPs, and Emulsion. The sensors were tested under different oil thicknesses and using different configurations (handheld, on pole, on float, on skimmer). The tests were divided into static and dynamic, where four different wave configurations were generated. In most tests, the sensor performed as expected and gave expected performance. The following is a summary of the main results:

**Handheld 1** static testing gave an overall average absolute error of **2.72mm and 92.1%** average repeatability.
**Handheld 2** static testing gave an overall average absolute error of **2.25mm and 89.94%** average repeatability. On pole testing gave an overall average absolute error of **3.73mm and 82.96%** average repeatability. On float testing gave an overall average absolute error of **0.72mm for static and 5.56mm in waves and 97.61%** average repeatability for static and **98.81%** in waves.
**Skimmer-mounted Sensor 1** static testing gave an overall average absolute error of **3.73mm and 93.20%** average repeatability and in wave testing gave an overall average absolute error of **5.64mm and 93.30%** average repeatability.
**Skimmer-mounted Sensor 2** static testing gave an overall average absolute error of **9.01mm and 96.97%** average repeatability and in wave testing gave an overall average absolute error of **5.63mm and 94.82%** average repeatability.

Overall, all sensors provided average absolute error within the expected range for each use case. Recommended improvements and enhancements: (1) reducing the weight of the overall packages for both sensors; (2) optimizing the attachment/detachment of different configurations (handheld -- float -- pole), (3) improving skimmer mounting to reduce weight and make it easier to mount; (4) enhancing the algorithm using additional machine learning techniques to possibly eliminate the need for the ultrasound sensor; this is expected to reduce cost, weight, and power consumption.

# Contents

# List of Figures

# List of Tables

# 1  Introduction

This report summarizes the work and findings done under BSEE contract 140E0118C0003, Oil Thickness Sensor Phase II. The purpose of this project is to continue the development of a capacitive oil thickness sensor that was developed by the American University of Beirut under contract E17PC00001 (BSEE project 1078). The improvements made were motivated by the test outcomes from testing at the Ohmsett Facility in November 2017.

The project's objective is to develop sensors capable of measuring floating oil thickness for two different use cases. Use Case I is a handheld sensor that will measure slick thickness during tests at facilities such as Ohmsett and CRREL or similar test facilities, or for use from onboard vessels to obtain sample measurements in the field. Use Case II is a sensor that can be mounted on skimmers, buoys, or in an oil spill boom apex to provide thickness data in a field application.

The report is organized in four main chapters:
- **Chapter 1** Introduction and sensing principle.
- **Chapter 2** details the instrumentation, hardware design, sensor optimization, and packaging.
- **Chapter 3** details the final measurement algorithm implemented and some assessment of its principles.
- **Chapter 4** details the experimental setup and procedures followed at the Cold Regions Research and Engineering Laboratory (CRREL).
- **Chapter 5** presents the test results for the handheld sensor carried out at CRREL
- **Chapter 6** presents the test results for the skimmer sensor carried out at CRREL.
- **Chapter 7** concludes the report with observations, lessons learned, and recommendations for future enhancements.

## 1.1  Sensing Principle and Challenges

Capacitive sensors are widely used in liquid-level sensing applications. Usually, the sensor is composed of a couple of metallic rods (electrodes) inserted into the examined liquid. In the case of conductive liquids, the electrodes are insulated to avoid short-circuiting. Since the relative permittivity (also known as the dielectric constant) of liquids differs from that of air, the measured capacitance could be used to infer the liquid level. This method is known as the continuous sensing technique and requires establishing a relation between the measured capacitance and the liquid level. In the case of single-phase conductive or non-conductive liquids, such as water or oil, this relation could be inferred using the traditional multi-point calibration process, where the measured capacitance is recorded at several liquid levels, and a regression is applied to calculate the coefficients. However, in our application, calibration is much more complicated since we are dealing with a multiphase air/oil/water mixture. For instance, to extract the equation relating each of the possible oil/water combinations, the calibration should be repeated for every possible type of oil and with different thicknesses. Given that during oil spills different kinds of oils could mix forming unpredicted mixtures, and the sensor should work in various environmental conditions (salinity, temperature, dynamic and wavy liquid), calibration is difficult and is unlikely to produce reasonable results.

In contrast to the continuous sensing technique, we developed a discrete sensing method which does not require calibration for different liquids. It works by detecting the number of cells immersed in the oil and calculates the oil thickness by using the geometrical properties of the cells. The proposed method is implemented using a Printed Circuit Board (PCB) holding a set of coplanar sensing cells. After measuring the capacitance at each cell, the sensor uses an algorithm to detect the interfaces separating different phases (air/oil and oil/water). This algorithm allows the sensor to infer which cells are immersed in different materials and accordingly to calculate the oil thickness. We demonstrated the effectiveness of this design in the previous phase of this project. However, based on this sensing principle, several design challenges should be considered, including:

- **Oil contact (fouling):** oil sticks to the sensor body due to its high viscosity, causing erroneous identification of the state of the sensing cells.
- **Limited resolution:** the resolution of the sensor is limited by the geometrical dimensions of the sensing cells.
- **Electrical connections:** since the sensor includes many electrodes, careful consideration should be given for routing, while attaining relatively small dimensions of the sensor cartridge.
- **Signal processing:** the sensor should be able to detect and track the position of more than one interface at the same time (air/oil and oil/water). Given that the acquired capacitance signal is multi-dimensional, the processing needed to extract the oil thickness is much more complicated than the continuous sensing case. A real-time filtering method is also necessary to allow the sensor to work under dynamic liquid conditions without affecting the accuracy of the measurements or delaying the response time of the sensor.
- **Capacitance measurement:** the method for measuring the capacitance should be characterized by high signal-to-noise ratio, fast response rate, low power consumption, be multi-channel, have an immunity to stray capacitance and to external interference.
- **Control unit**: the control unit should be compact in size, be low-cost, consume low power, and feature high processing capabilities. In addition, it should be water- and dust-proof to allow it to work under harsh field conditions.

In this report we document the work done to overcome those challenges by considering several design optimizations both in hardware and algorithms used.

# 2  Sensor Optimization (Instrumentation, Hardware, Packaging)

We have followed an iterative design process with several alternatives evaluated for each component followed by integration. In this chapter, we document the main design stages for:

- Sensing cell design (electrodes)
- Fouling mitigation approaches
- Sensor board design
- Control unit design
- Packaging design

## 2.1  Sensing Cells Design (Electrodes)

### 2.1.1  Design variables and evaluation parameters

In a coplanar design, the measured capacitance depends on a set of geometrical and structural properties of the electrodes, including the Material Under Test (MUT), the substrate (PCB) type and size, and the shielding. To evaluate the performance of the sensor under different design variables, we rely on three metrics: the sensitivity, the dynamic range, and the penetration depth of the electric field. The sensitivity is defined as the ratio between the change in the measured capacitance and the change in the dielectric constant. The dynamic range is the difference between the maximum capacitance measured in the presence of the MUT and the base capacitance. The penetration depth is defined as the distance along the z-axis (perpendicular to the PCB plane) required for measuring a detectable change in the output capacitance.

### 2.1.2  Alternative Designs

#### 2.1.2.1  First Phase: Electrodes Topology

To identify the optimal design of the sensing cells, we considered several alternatives, including the parallel, interleaved, concentric, and pins-based configurations (Figure 2.1). Using the Maxwell package included in the ANSYS 19.0 software, a set of electrostatic finite element simulations were performed to evaluate the models relative to the evaluation parameters introduced above. Thickness sweep simulations aimed to study the sensitivity and the dynamic range of the sensor were performed by increasing the thickness of the MUT while recording the capacitance. Lift-off simulations aimed to study the penetration depth of the electric field and were performed by setting the thickness of the MUT to a constant value and changing its vertical position (lift-off distance) along the z-axis while recording the capacitance.
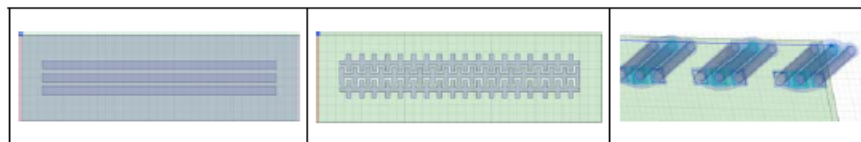


**Figure 2.1: 3D simulation models; (left) coplanar parallel, (middle) interleaved, (right) pins**

We implemented several prototypes (Figure 2.2 - Left) and measured their capacitances, using an LCR meter instrument (BK Precision 875B) to validate the simulations. The measurements favorably agreed with the simulations and demonstrated the following:

1. The interleaved coplanar design was the most sensitive in comparison to other co-planar designs.

2. The concentric and parallel models encountered similar limited capacitance change after being immersed in oil.

3. All coplanar configurations showed a minimal penetration depth which limits their capability of dealing with the oil fouling problem.

4. The pins-based designs showed an intermediate base capacitance with high sensitivity and penetration depth.

5. The sensitivity of the pins-based designs increased linearly with the number of cells included in the sensing row (Figure 2.2 - Right).
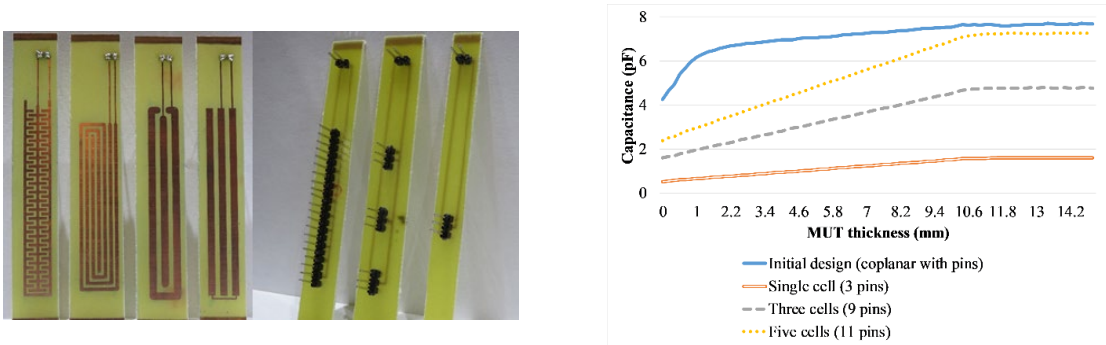


**Figure 2.2: Left: Alternative sensing cells. Right: Capacitance (pF) vs. MUT thickness (mm)**

Based on the results of the simulations and experiments performed during this phase, we concluded that the **pins-based design** is preferred, especially for the handheld device where a very high resolution is desired. By using this design, the output signal of the sensor is expected to be more representative of the material distribution and is a more promising design for accurately measuring oil thickness. For the type and shape of the pins, a set of press-fit and solder-mount PCB pins provided by Mill-Max company was used [1]. The analysis and discussion of the optimizing of the sensor design was published in the proceedings of the IEEE 2019 I2MTC conference [2].

### 2.1.2.2  Second Phase: Pins Configuration and Acquisition

In the first phase, the pins were selected due to their role in reducing the effect of oil fouling; however, the pins could be implemented in different configurations and using different acquisition options. Before deciding on the final distribution of the sensing pins, we implemented and evaluated several different designs. Also, we tested two types of capacitive transducers: 1) capacitive touch/proximity controller MPR121 provided by NXP and 2) capacitance-to-digital converter chip FDC1004 provided by Texas Instruments.

In summary, five sensor boards were implemented: PCB#1 to PCB#3 were equipped with the MPR121 capacitive touch/proximity controller, and PCB#4 and PCB#5 were equipped with the FDC1004 capacitance-to-digital converter. The five boards were evaluated under identical

14

experimental conditions, using a linear actuator mounted vertically on the laboratory experimental setup. The actuator followed a periodical motion while dipping the boards into the liquid sample; a mixture of engine oil and tap water. The voltages measured by each sensing unit were logged at a sampling rate of one sample per 100 msec. The sensors were not cleaned or dismounted during the testing cycles.

The analysis of the experimental results revealed that the boards equipped with the MPR121 transducer showed a similar behavior despite the small differences in their geometrical properties. Due to oil fouling (coating of pins with oil layer) the measured voltages didn't drop to less than 100 $V_{ADC}$ when moving from the oil phase into the water phase within a time frame of two seconds. In contrast, when the pins were immersed in water under steady-state conditions, the measured voltages dropped to around 10 to 20 $V_{ADC}$. Despite this difference between the changes in the amplitudes of the voltage signals measured under steady-state and dynamic liquid conditions, the signal showed an observable and almost immediate drop in amplitude when the sensing unit moved from the oil phase to the water phase. Although the fouling limited the final value of this drop (100 $V_{ADC}$); however, the initial drop from when the pin was in oil was measurable and relatively fast. This result motivated our decision to use temporal features and not only absolute values to detect the sensing units transitioning from oil to water phases as described later in the algorithm.

Similar to the MPR121 boards, the FDC1004 boards (PCB#4 and PCB#5) were mounted on the same linear actuator and evaluated under identical motion parameters. The experimental results showed that the measured capacitance decreases until reaching a value of 2-3 pico-farads in the oil phase. On the other hand, capacitance increases to a saturation value of 100 pF when immersed in water under steady-state conditions. We noted that the capacitance didn't saturate immediately when moving from oil to water under dynamic liquid conditions.

Based on these results, we concluded that the needle-like pins with the diagonal distribution provides the fastest response of signal change when moving from oil to water. Also, the results showed that the number of pins included in the sensing cells (2 or 3) and the separation gap between pins of the same cell (2 or 5 mm) doesn't cause a significant change in the measured voltages. This is due to oil fouling which is preventing the direct contact between the pin and water. However, this doesn't imply that these geometrical parameters don't affect the amplitude of the voltage signal in air or oil phases. Increasing the separation gap would decrease the sensitivity; thus, the signal-to-noise ratio would be affected. Also, increasing the number of pins in the same sensing unit would increase the sensitivity.

Another conclusion made from these experiments is that the performance of the sensors equipped with the FDC1004 chips was affected by oil fouling similar to the boards equipped with the MPR121 controllers. It is important to note that there is a significant difference between the two transducers in terms of signal excitation; FDC1004 uses a square wave voltage signal and the MPR121 device uses a DC current excitation signal. Another limitation of the FDC1004 module is that it supports only four channels.

This result showed that the problem of oil fouling is highly related to the viscosity of the oil and affects different types of capacitance measurement methodologies (AC and DC) while working

at low frequencies. The time needed for any sensor pin to get rid of the oil coating and become in direct contact with water is a major factor in preventing immediate changes in the amplitudes of the voltage signals. Based on this result, we decided to keep using the MPR121 devices as the capacitance transducers in our device.

### 2.1.2.3 Final Phase: Assessment of the Capacitive Measurement

Another set of tests were performed to assess the stability of the capacitance measurements under static and dynamic liquid conditions. In these tests, the MPR121 controllers were configured with a charging current of 32 micro-Amperes and a charging time of one microsecond. The reading rate was set to 100 milliseconds. In all experiments, we used the lab experimental setup containing tap water and SAE 140 GEAR oil. For consistency, a set of voltage measurements were recorded for each sensor board for a specific amount of time. The specifications of the tested boards are listed in Table 2-1.

**Table 2-1: The four boards characteristic**

| Board ID | 1 | 2 | 3 | 4 |
|---|---|---|---|---|
| Number of pins in each cell | 2 | 3 | 2 | 25 |
| Separation gap between pins (mm) | 2.4 | 2.4 | 4.8 | 2.4 |
| Number of rows | 12 | 12 | 12 | 12 |
| Vertical distance between rows (mm) | 4 | 4 | 4 | 4 |

We summarize the major conclusions obtained from this set of experiments by the following:

- Under steady-state conditions, all voltages measured by different sensing cells are stable and differ by their amplitude based on the type of material that surrounds the pins. The base voltages (measured in air) differ from one sensing cell to another based on the length of the connection tracks and other manufacturing differences. Thus, normalization should be done before applying the classification algorithm.
- To facilitate the detection of the air/oil interface based on the capacitive sensing principle, we should maximize the signal-to-noise ratio in the case where the sensor changes from the air phase to the oil phase. To increase the signal change relative to the calibration values, the capacitance measured by the sensing cells when immersed in oil should be maximized. To maximize this capacitance variable, we can increase the length of the pins, decrease the distance between them, and increase the number of pins included in each row. One example of this design was implemented in Board, which is shown in Figure 2.3. Even though the signal-to-noise ratio highly increased when using Board 4, one major limitation of this design is that it is prone to thick oil fouling (Figure 2.4).
- In contrast to Board 4, where dense rows of pins were used, the diagonally distributed sensing cells were less prone to oil fouling. This design was implemented with slight differences in Boards 1, 2 and 3. For demonstration, photos taken while moving the sensor boards in a thick oil mixture are shown in Figure 2.5.

16
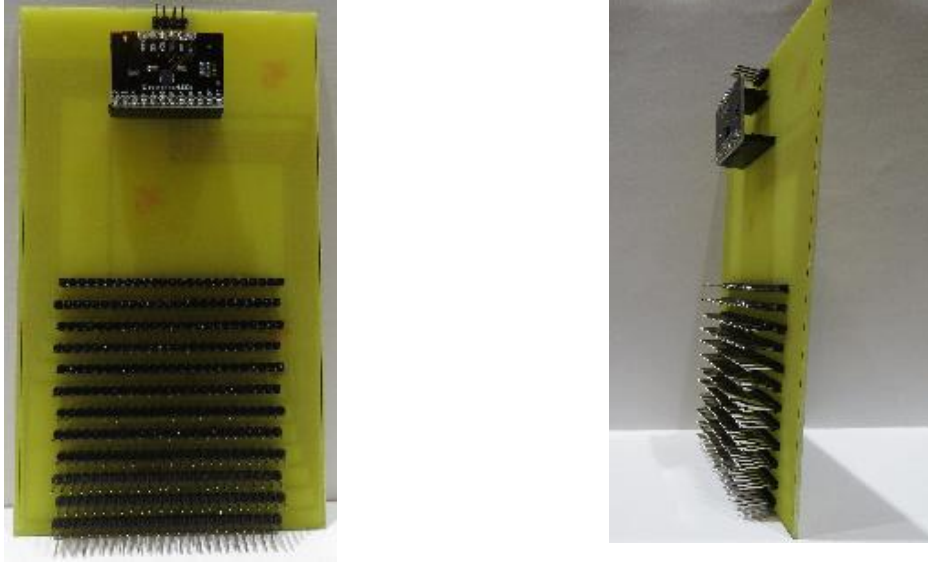
**Figure 2.3 Board 4- 25 pins in each row**
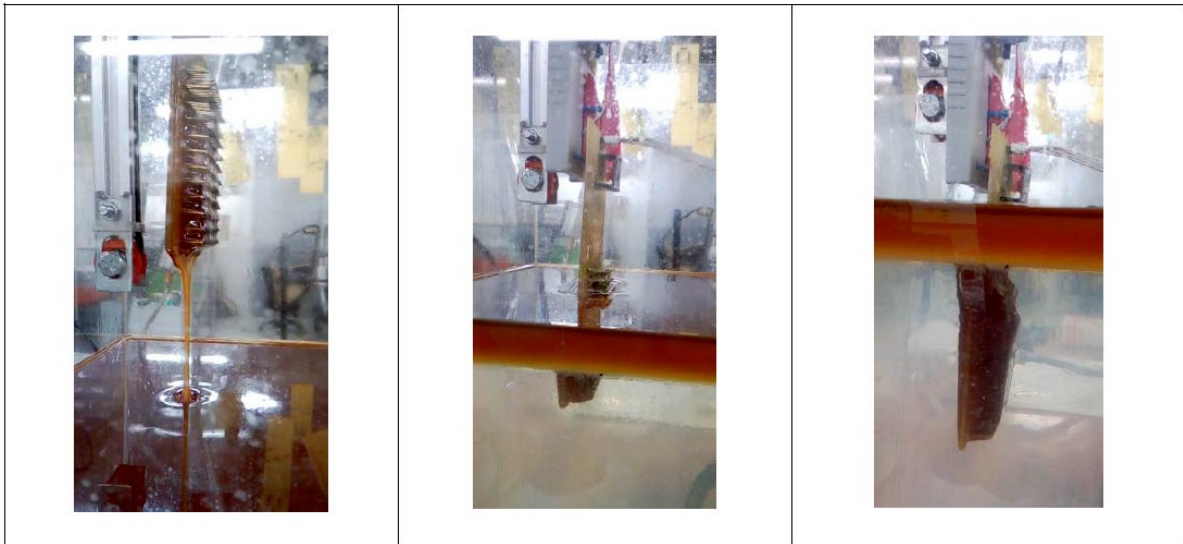


**Figure 2.4: Effect of fouling on Board 4**
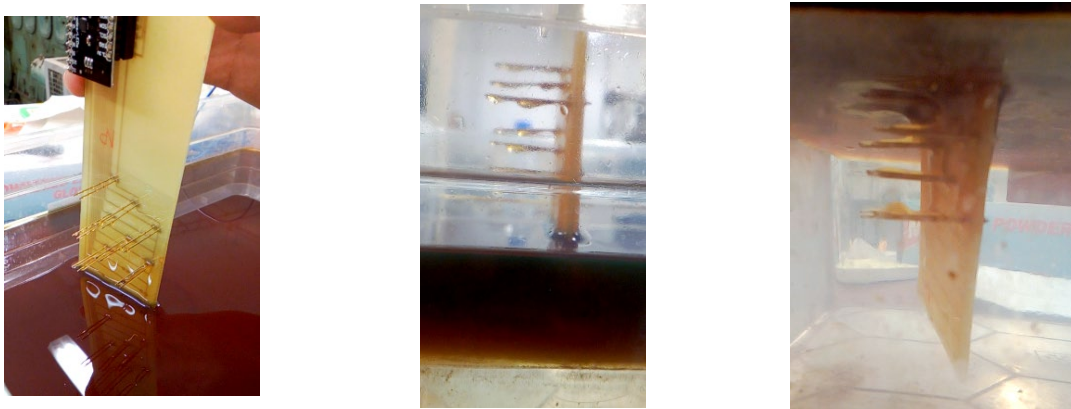


**Figure 2.5: Photos for the diagonally distributed sensor design in dynamic experiment**

As a general conclusion we can say that using dense rows of pins similar to what was implemented in Board 4 is preferred for detecting the air/oil interface. In contrast, to detect the oil/water interface, single distanced sensing cells, with maximized gaps should be used to avoid the effect of fouling. Therefore, one solution may be to merge the two sensing designs on a double-sided board. Another solution is to use another sensing technique to detect one of the interfaces and to adopt one of the capacitive sensing modalities to identify the other interface. This idea motivated our choice of a dual sensing modality where an ultrasonic sensing technique is used to detect one of the interfaces (air/oil interface) while adopting the distributed capacitive cells to detect the other interface (oil/water interface).

### 2.1.3  Principle of Dual-Modality Sensing (ultrasonic/capacitive)

Sensor fusion is a term used to describe the process of combining data from different sensors in order to measure a physical quantity. The process of sensor fusion includes the use of multiple sensors of the same or different types, and can be applied in three ways: competitive, cooperative, and complementary. Competitive or redundant sensor fusion represents the case where every sensor independently measures the same property. In cooperative fusion, data from a set of independent sensors is combined to achieve information that is not possible to achieve using the data obtained from a single sensor. In complementary fusion, sensors do not depend on each other directly, but their measurements could be combined to give a complete view of the measured physical quantity.

In our sensing methodology, we combined two types of sensor fusion. First, in the capacitive sensor array, we used a cooperative sensor fusion process to estimate the water-level or the position of the oil/water interface. We can classify it as a "cooperative" fusion because this information could not be obtained from a single capacitive sensor. For instance, if a single capacitive sensor is immersed in the multiphase mixture, the measured capacitance value will not depend only on the water level. Instead, it will depend on the water level and the amount of oil accumulated above the water surface. Therefore, since oil may or may not exist on the water surface, relying on the measured values (example: voltage/capacitance) obtained from a single capacitive sensor is not sufficient to detect and track the water-level in such a situation. As explained before, our proposed capacitive sensor array is composed of several independent point sensors distributed vertically on a planar platform. After obtaining the set of capacitances corresponding to each sensor in the array, a classification algorithm is applied to detect the water-level or the position of the oil/water interface.

In addition to the cooperative method described above, we adopted a complementary sensor fusion method by introducing a different type of sensing (ultrasonic) to provide additional information about the oil level or the position of the air/oil interface. As the oil/water interface is detected by the capacitive sensor array, the distance measured by the ultrasonic sensor provides the missing information about the air/oil interface required for estimating the oil thickness. In this way, the additional information obtained by the ultrasonic sensor is combined with the information obtained from the capacitive sensor array to form a complete view of the measurand (oil thickness).

### 2.1.3.1 Dual-modality Sensing: Proof of Concept

In this section, we describe the first prototype we implemented to prove the concept of the dual modality sensing technique. This prototype used the *HRXL-MaxSonar-WR* sensor provided by *MaxBotix* [5]. This sensor was selected due to its high precision, low-voltage operation, and low-cost. After developing the software for measuring the distance using the ultrasonic sensor, we tested the capability of the sensor in detecting the surface of the liquid. For this purpose, we implemented a platform to mount the ultrasonic and the capacitive sensors together (Figure 2.6). The ultrasonic sensor has a 30 cm dead zone where anything below this distance cannot be detected; therefore, the extension was needed to hold both the ultrasonic sensor and capacitive sensors at variable distances above 30 cm. The extension was designed to be mounted on the lab tanks and to provide the option of changing the distance between the ultrasonic sensor's sensing surface and the capacitive sensor's first sensing strip.
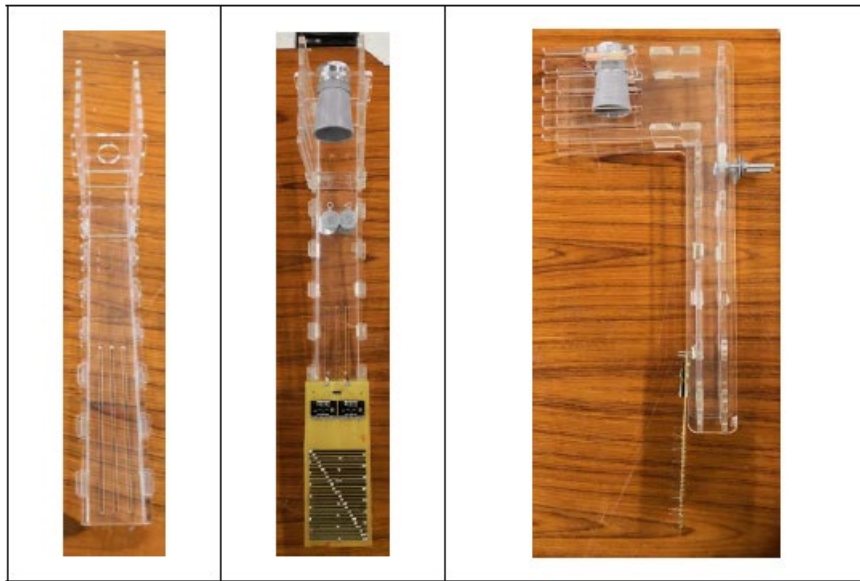


**Figure 2.6: Dual-modality sensing platform – Prototype 1**

To measure the oil thickness based on the dual-modality approach, a new algorithm was implemented. The algorithm uses distance measurements acquired by the ultrasonic sensor to detect the air/oil interface and calculates the water depth based on the voltages acquired from the capacitive sensor. Then, the two distances are subtracted to obtain the oil thickness. After connecting the two sensors to the microcontroller and implementing the algorithm in software, the sensing platform was evaluated against a set of different oil thicknesses. The oil sample used was a mixture of fuel oil and SAE 140 gear oil. Different thicknesses were set by using the oil pump in the experimental lab setup. A photo of the experimental setup is shown in Figure 2.7. After immersing the sensor into the oil/water mixture, a set of thickness measurements were recorded. The actual thickness was estimated visually using a measuring tape. A sample of the oil thickness measurements categorized by test IDs (1 – 6) is plotted in Figure 2.8. The statistical summary of the results is shown in Table 2-2.
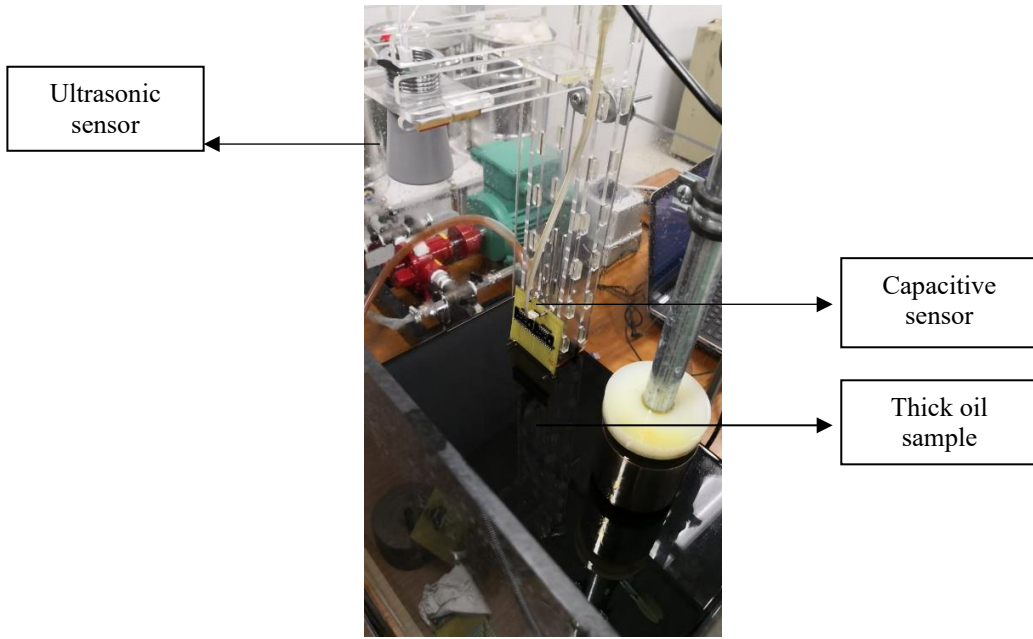
**Figure 2.7: Experimental setup - Dual-modality sensing**
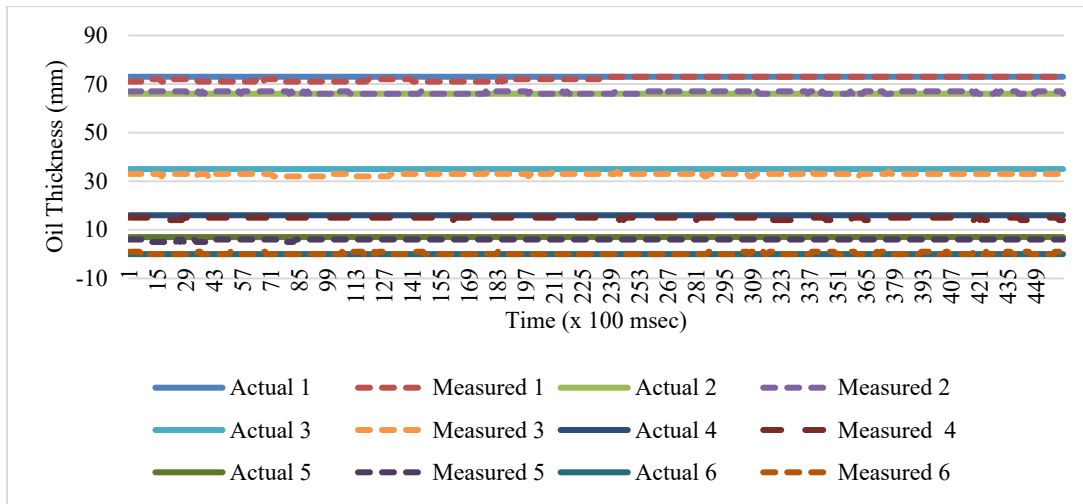


**Figure 2.8: Oil thickness results – Dual-modality sensing platform**

**Table 2-2: Dual-modality sensing technique - Summary of experimental results**

| Test ID | 1 | 2 | 3 | 4 | 5 | 6 |
|---|---|---|---|---|---|---|
| **Actual thickness (mm)** | 73 | 66 | 35 | 16 | 7 | 0 |
| **Average measured (mm)** | 72.01 | 66.78 | 32.86 | 14.78 | 5.94 | 0.23 |
| **Standard deviation** | 0.62 | 0.41 | 0.38 | 0.41 | 0.23 | 0.42 |
| **Average absolute error (mm)** | 0.98 | 0.78 | 2.13 | 1.21 | 1.05 | 0.23 |

Based on the results shown above, we concluded that the dual-modality sensing technique was very successful in measuring the oil thickness under static conditions. The measurements were

very stable, and the absolute error ranged between 1 and 2 millimeters. Also, the maximum average absolute error of many measurements was around two millimeters.

## 2.2 Fouling Mitigation

To mitigate the effect of fouling, we evaluated mechanical and chemical techniques.

### 2.2.1 Mechanical Fouling Mitigation

Several mechanical solutions for the sensor fouling were considered and analyzed. The different techniques were evaluated and compared based on cost, complexity, and effectiveness. These techniques included Vibration, Direct air, and Vacuum. The vibration method was the only one considered feasible and tested. Direct air and Vacuum ideas are based on delivering a jet stream or suction at the board from the top so that oil is removed from pins (mainly in the air). Unfortunately, those two methods would result in complicating the sensor cartridge design and packaging at an insignificant advantage. In addition, they would require significantly more power to operate and would not address fouling in water, which is the main cause of errors.

The vibration method was tested using a 12V vibrating motor with an offset weight on its rotor shaft, when the rotor rotates around its major axis, the rotating offset weight causes a periodic force inducing vibrations on the stator part of the motor. The periodic vibrations are transferred to the sensor board by mechanical contact which in turn causes the board to vibrate in all directions, with the highest percentage of vibrations being transmitted orthogonally to the sensor's major axis and along the normal vector of the sensing area.
Two vibration configurations were tested:

1. rotor axis normal to the sensor's sensing plane and major axis
2. rotor axis parallel to the sensor's sensing plane and major axis

The results of the first vibration configuration were in the form of three-dimensional swaying caused by Euler rotations due to torque-induced precession relative to the sensor's sensing plane normal vector, induced by the periodic moment of the offset mass on the rotor axis. The combination of the periodic moment, precession, and the conditional nutation, cause the sensor board to vibrate by rotating about the normal axis of the non-disturbed sensor board in the same fashion as the described Euler rotations with a phase shift and linearly increasing amplitude with the distance from the center of rotation. The three described phenomena are deflections in roll, pitch, and yaw along the major sensor board axis.

The results of the second vibration configuration were in the form of periodic two-dimensional swaying with the energy being transferred on the perpendicular plane to the major axis of the sensor board, which can be measured as roll and pitch deflections along the board's major axis with amplitudes linearly increasing with the distance from the center of rotation. Therefore, comparing both configurations, and according to the conservation of energy, the second vibration configuration transmits a bigger portion of energy along desired directions, since the yaw direction has little to no effect on the pin deflections and thus the compression and elongation of oil stuck in fouling between said pins.

The sensor was held by hand during the experiments, this causes the holder to absorb a good portion of the vibrations. In the experiments performed using the first configuration, no apparent cleaning benefits were observed. As for the second configuration, improvements were minimal.

### 2.2.2 Coating Fouling Mitigation

In this phase of our study, and to mitigate the oil-fouling problem on the sensor cartridge, we tested the idea of using chemical coatings to the sensor board surface in hope of reducing the adhesion of the oil to the cartridge. To that end, we started by learning about the different mechanisms of adhesion. Then, we studied the material that makes up the sensor board and its electrodes and investigated the different types of oils and their chemical components. With this knowledge, we were able to further understand how the different mechanisms of adhesion play a role in causing the oil to 'stick' to the sensor board surface.

#### 2.2.2.1 Sensor Board Material and Crude Oil Chemical Components

The sensor board material is made up of fiberglass-reinforced epoxy resins with copper foil bonded onto one or both sides. Epoxy resins tend to be highly reactive due to their structure, which contains an unstable three-membered ring made up of two carbon atoms and an oxygen atom. This makes the structure very susceptible to nucleophilic and electrophilic interactions. The copper part of the sensor board has high electrical and thermal conductivity owing to the presence of many delocalized electrons in the metallic structure. These delocalized electrons give the metal its high-energy properties that can readily cause chemical and electrical interactions.

The components of crude oil typically found in marine spills can be divided into three main types: light, medium and heavy. Normally, crude oil is composed of (15%-60%) paraffins, (30%-60%) naphthenes, (3%-30%) aromatics and (around 6%) asphaltics. The key constituents of light oils such as diesel are short paraffinic hydrocarbons, which have branched or straight-chained structures. While the heavy oils mostly constitute heavy naphthenic hydrocarbons with depleted hydrogen atoms, which have saturated ring structures. The light oils are the more desirable, lighter, and cleaner components of crude oil, while the heavy oils are less desirable and tend to contain much more contaminants, such as sulfur. These elements, amongst others, bring forward the differences in properties between light and heavy oils in which light oils are much lower in density, have a lower viscosity index, lower specific gravity, and higher API gravity, than heavy oils.

#### 2.2.2.2 Adhesion Mechanisms and their Impact on Oil-Fouling

With knowledge of the relevant characteristics of both the surface substrate (sensor board) and the adhering material (oils), and to explain how the oil adheres to the senor board surface we considered four main types of adhesion theories: (1) electrostatic, (2) chemical, (3) thermodynamic, and (4) mechanical. The interplay between these four mechanisms causes the oil to readily foul the sensor board surface. Therefore, we initiated our investigation by speculating on how these mechanisms directly cause the oil to interact with the sensor board, and how to reduce that effect. The chemical coating that would best suit our application must be able to reduce the effect of all the effective adhesion mechanisms.

In our experiments, it is evident that the issue of oil-fouling is much more significant when testing heavy oils than light oils. This is attributed to their greater density, which makes them

easily miscible with water. Heavier oils, owing to their large molecule size, have stronger intermolecular forces between them, thus making their molecules hold on to each other more strongly, making it harder for them to slide off the sensor surface. Another chemical aspect we considered, while studying the 'stickiness' of oils, is hydrogen bonding, which is the strongest intermolecular force responsible for the attraction and adhesion of all molecules that contain H-atoms bonded to F, O, N-atoms. Electrostatically, adhesion occurs between charged molecules, meaning polar molecules. These molecules commonly exist in heavy oils due to the presence of many contaminants such as S, O, N-atoms. These atoms are highly electronegative, therefore can readily make molecules polar, thus making them highly attracted to the charged sensor board surface. The most important adhesion theory that was thoroughly studied was the thermodynamic theory, where we consider crucial properties of surfaces in wet environments, such as hydrophilicity/oleophilicity (water/oil loving) and hydrophobicity/oleophobicity (water/oil fearing). When a surface is wetted by water or oil it is considered hydrophilic or oleophilic, respectively. Our aim was to create a surface that cannot be readily wetted by oils (oleophobic), and to achieve that we needed to lower the surface energy of the sensor board below the surface tension of the oils. Therefore, we researched several chemical coatings that would lower the surface energy to levels that would create a surface that does not get readily wetted by oils.

### 2.2.2.3  Chemical Coatings Studied and Tested

#### 2.2.2.3.1 Fluoropolymers

The most prominent surface modifying coatings that improved durability and reduced wetting of surfaces are fluoropolymers. They can create a surface functioning at low surface energy, thus making it superhydrophobic and oleophobic. This is due to the self-segregation and self-organization of the fluorinated segments. Polytetrafluoroethylene (PTFE) is the simplest linear fluoropolymer. The PTFE polymer is produced by the polymerization of tetrafluoroethylene ($-CF_2-CF_2-$) thousands of times. The main chain of the structure is made of C–C bonds and the functional groups are made of C–F bonds, which are both very strong bonds. The small size of fluorine atoms permits a complete and continuous wrapping around the carbon atoms, which shields them from any chemical interaction, hence giving the molecule its stability and chemical resistance. It also does not dissolve in any known solvent. The fluorine cover is also responsible for the low surface energy (18 mN/m). All these properties make PTFE the perfect coating candidate since it is chemically and electrostatically inert and can produce a very low energy surface.

Researchers have added small amounts of other monomers to the PTFE polymerization to produce different modifications of PTFE designed for specific applications. One of the PTFE modifications that we were able to purchase was made by a fluoroacrylic copolymer. The product named Fluoropel 800 was purchased from a company called Cytonix in the US. This coating showed great hydrophobic and oleophobic properties. It also showed low friction properties when the oil slid off its surface. It needs approximately one minute or more for the surface to completely dry from the oil.

Tests performed with Fluoropel 800 included tests for boards with pins and board with co-planar electrodes.

After observing some promising results from the Fluoropel 800 oleophobic coating, we performed a series of experiments to test the effectiveness of this coating in our application. In our first experiment, we aimed to compare between a set of uncoated pins and a set of coated pins. We manufactured a PCB having an MPR121 device with two channels (Figure 2.9): the first channel is connected to 25 uncoated pins and the second channel is connected to another 25 pins coated with Fluoropel 800. The pins were placed on the same horizontal line for all of them to be dipped into the oil/water container at the same time.
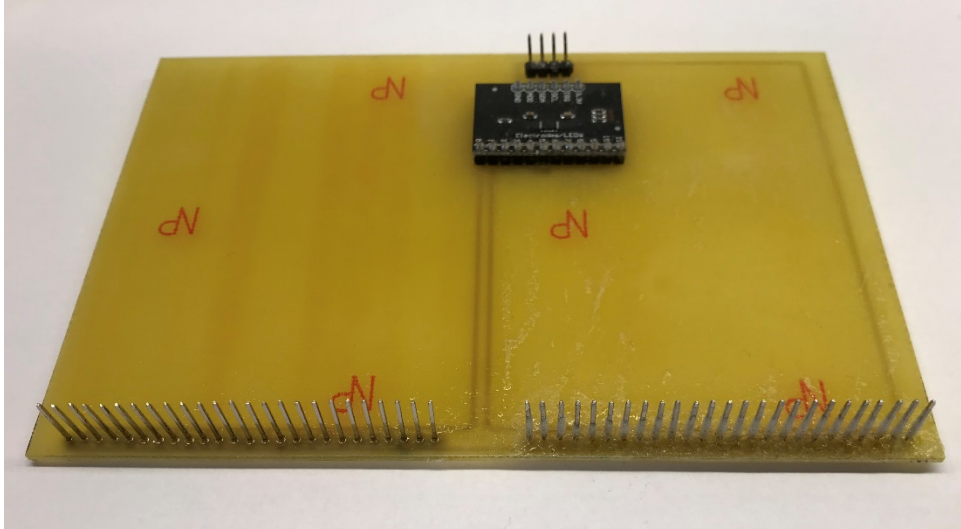


**Figure 2.9: PCB equipped with MPR121. Left channel uncoated pins, right channel coated pins**

In our first test, we studied the effect of partly coating the pins. We completely covered with paper tape the set of pins that were not coated, and we also covered with paper tape the heads of the pins to be coated. Then, we applied the coating using an aerosol spray, which ensured its uniform distribution and perfect adhesion. This produced pins that had coating covering 0.8cm of their 1.3cm total exposed length. The coating on the pins was left to dry for 10 minutes.

In a large rectangular container, we filled with water to two-thirds, and then poured oil (Power Gear 140W gear oil) on top of it to form a layer of approximately 2 cm in thickness. The PCB was then connected to the interface running the data acquisition software. Voltage readings were taken at a rate of 50 ms.

First, we measured the voltage for the pins while they were still above the oil surface to provide a comparative reference. The experiment was initiated while the pins were inside the oil layer. As the software started reading voltage, we let the pins reside in the oil layer for 5 seconds and then raised them up into the air for another 5 seconds and then back into the oil. This maneuver was repeated several times to achieve an averaged reading of the voltages. The data was calibrated against the reference voltages taken in air only; therefore, we were able to produce for each set of pins plots of change of voltage over time (Figure 2.10). As a result, we were able to observe the behavior of the pins at the air/oil interface. As it is clear from the plots, there is no

24

significant difference between the uncoated and partly coated pins. The response time of both sets coincide very closely to each other.
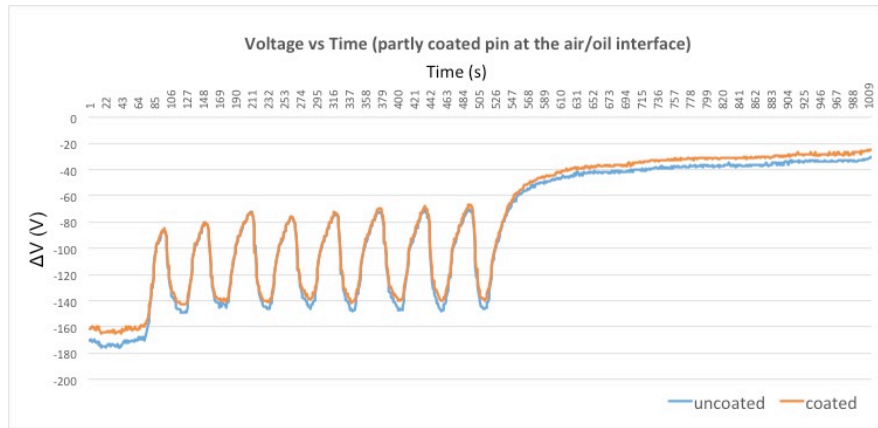


**Figure 2.10: Variation in voltage with time at the air/oil interface for the uncoated and partially coated pins**

We next repeated the same experiment, but instead of raising the pins from oil to air, we dipped them from oil to water, thereby allowing us to observe the behavior of the pins at the oil/water interface. A similar maneuver was also performed, in which the voltage reading was initiated while the pins resided inside the oil for 5 seconds then dipped into the water for 5 seconds, and finally raised up into the oil again. These voltage readings were also calibrated across the reference voltages of air only, and a second plot of change of voltage with time was plotted (Figure 2.11). Similarly, the two sets of pins showed slight difference in response times, which was attributed to the increase of thickness of the pins caused by the deposition of a thick layer of the coating. The thicknesses of the coated and uncoated pins were measured, and the coated pins were thicker by 0.5mm. This caused the spacing between the coated pins to decrease by that same amount in comparison to the uncoated pins. This decrease in pin spacing was enough to cause the oil to adhere more tightly to the pins leading to such discrepancy in the results. The response in timing would be somewhat identical if the coating thickness was lower, thus keeping the thickness of both sets of pins the same.
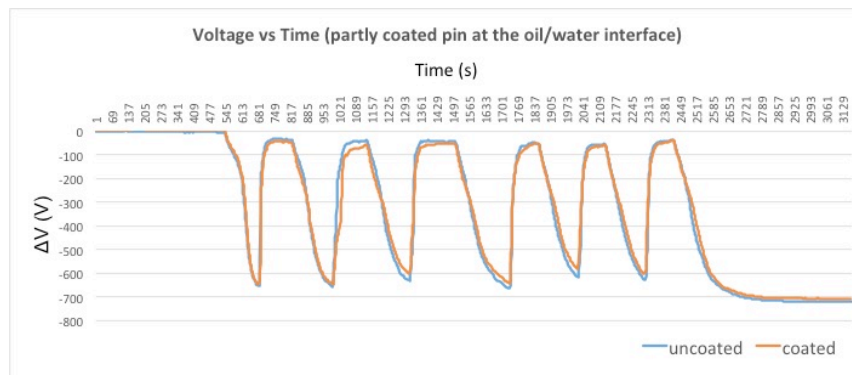


**Figure 2.11: Plot of change of voltage with time at the oil/water interface for the uncoated and partially coated pins**

25

In our second test, we studied the effect of completely coating the pins. The set of pins not to be coated were entirely covered using paper tape and the other set of pins were fully sprayed with the coating material. The same two tests were carried out, where we monitored the behavior of the pins at both the air/oil and the oil/water interfaces. Two plots were produced to show the change of voltage over the time interval of the experiments (Figure 2.12 & Figure 2.13).
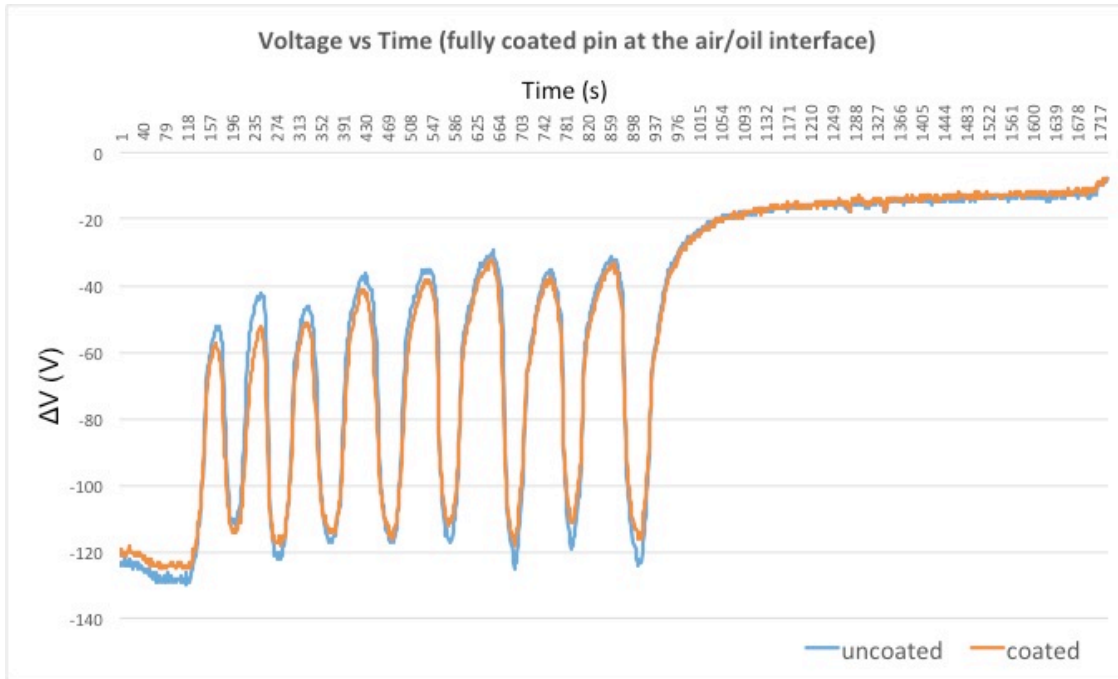


**Figure 2.12: Variation in voltage with time at the air/oil interface for the uncoated and fully coated pins**
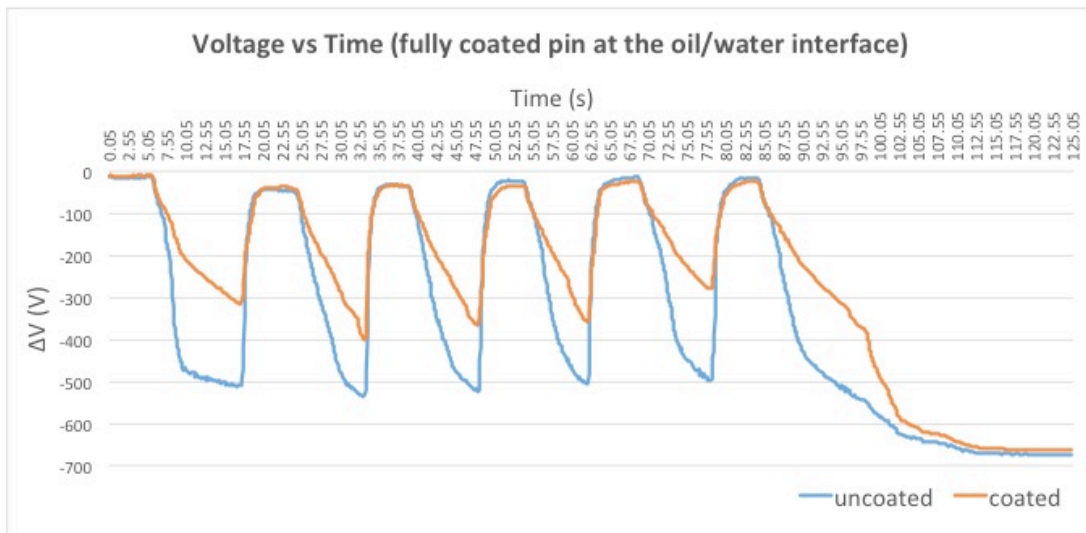


**Figure 2.13: Variation in voltage with time at the oil/water interface for the uncoated and fully coated pins**

26

In this experiment we observed a significant alteration in the behavior of the pins especially at the oil/water interface. The response time of the coated pins was much slower than the uncoated ones; it took nearly double the time. This result was due to the extremely low conductivity of the coating which increased the time needed for the water to short circuit the current passing through the pins. Another reason is that below the oil/water interface, where the oil is dragged down into the water with the dragging of the sensor board, the oil much more readily covers the pins thus blocking the water from nearing the pins, and causing the short circuiting required to detect that the pins have reached the water. Since under the oil/water interface the competition is between oil and water only, it is much easier for the oil to surround the coated pins because their surface tension is much closer to that of the coating than the surface tension of the water. The combination of these effects lead to the observed difference in response time for both sets of pins.

### COATED AND UNCOATED SENSOR BOARD WITH COPLANAR ELECTRODES

These results showed that the coating did not have any significant advantage for our application. Therefore, to further test the coating, we carried out a comparison using sensor boards with no pins, but instead, with coplanar electrodes. We cut three pieces of PCB (8cm x 1cm), we left the first piece uncoated to serve as a control reference, to the second we applied one layer of coating using a smooth brush, and to the third we applied multiple layers of coating (4-5 layers). The three boards were held together using paper tape. Then, they were dipped at the same time into an oil/water filled beaker. After the boards were raised into the air, the coated boards started drying from oil at the sides within 10 seconds; at about 20 seconds, the boards were about 50% dry. After less than a minute of removal from the oil/water beaker, only two to three drops of oil remained on the boards (Figure 2.14). The single-layer and multiple-layer coated boards showed no noteworthy difference between them; their behavior was very similar. The uncoated board remained completely wetted with oil throughout the entire time of the experiment. When the coated boards became completely dry (1.5-2 minutes), the uncoated board was still fouled with oil.
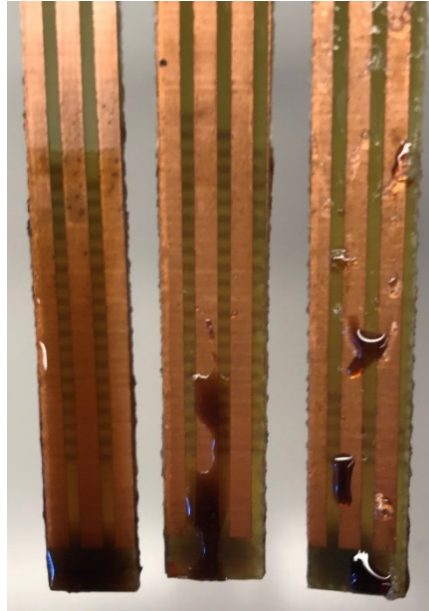
**Figure 2.14: Three PCB pieces with coplanar electrodes showing the remaining oil fouling the surface after one minute in the air. Uncoated (left); single layer coating (center); multiple layer coating (right).**

This experiment concluded that the coating was in fact oleophobic and can readily allow the oil to slide of coated substrates. Yet, the sliding of the oil off surfaces would happen at a rate that would be too slow for our application. Also, the coating demonstrated its proper function on flat surfaces but did not show any effect while applied on thin surfaces like the pins. The oil fluid dynamics around the pins is different than that on a flat surface. With the pins, the oil has two axes to move on (the length of the pin and the perpendicular surface of the board), while on the flat surface it slides off only one axis, which is the face of the board. The proximity of the pins with respect to each other contributes significantly to hindering the sliding of the oil. The closer the pins are to each other, the easier it is for the intermolecular forces in the oil to keep holding it together and slowing it from sliding off the pins. Tests were also carried out on single pins, one uncoated and one coated, both connected to the same board. They were dipped into a layer of oil and monitored. They also showed no notable difference in sliding of the oil. This further demonstrated that this coating is not effective on a thin surface like the pins.

This type of fluoropolymer coat is in fact oleophobic and can prevent surfaces from being wetted by oils. It also has high chemical and electrical resistance, which causes it to withstand the conditions of the experiments without disintegrating and prevents oils from adhering to coated surfaces for a long time. When being applied to flat surfaces, it has low friction properties, allowing oils to readily slide off. Yet, for our application the oil is required to slide off at a much faster rate to compensate for the movement of waves in the ocean. Another limitation is that when applied to thin surfaces like pins, its effect is diminished to an extent that no significant difference is observed between coated and uncoated pins.

### 2.2.2.3.2  Oil Repellent Paints

We also studied some industrial coatings such as oil repellent paints. These paints are mainly produced to coat industrial floorings and walls of factories, where they are exposed to frequent spillage of oils and other solvents. These paints are also used in boat coatings to protect them from fouling and marine oil spills. They are nano-enhanced to improve the efficiency and to provide new functionalities to paints. Nanoparticles are added to enhance these functionalities (*i.e.*, water/dirt repellent, self-cleaning), protection from UV radiation, resistance to microbial fouling, scratch resistance, or extending the lifespan of the paints.

Two different types of oil repellent paints were purchased from a Lebanese manufacturer called Tinol. The two paints were: Tinopoxy coating, gloss, series 8000 and Tinopoxy floor coating, series 13000. Both paints share a common compatible primer coat named Tinopoxy primer sealer and lacquer, Nr. 15500. These coatings showed no oleophobic behavior. All the types of oil that we tested readily wetted them. The coatings were very stable and chemically resistant, but the oils did not slide off their surface. The special feature of these coatings was that they made it very easy for the sensor board to be cleaned from the fouling oils, a simple wash or wipe with paper towels would return the sensor to its original state. These coatings were not further investigated because even though they had high chemical resistance and made it simple to clean the sensor board, the oil continued to foul the surface and did not immediately slide off.

### 2.2.2.3.3  Other Chemical Coatings

Other chemical coatings were also tested for their oleophobicity, including nanoprotech and plastik (conformal coating), both used for insulation of electronics from water, and Ultra-Ever-Dry (UED), bottom and top coat, used to reduce the oil-fouling of heavy fuels on the sensor board strips. We tested the hydrophobicity and oleophobicity of the chemical coatings by measuring the contact angle of droplets of water and oil with the sensor board. We also tested their chemical stability by monitoring their behavior in our experimental conditions.

A large PCB was cut into small pieces, approximately 2cm x 8cm each. Nanoprotech and plastik were sprayed on to two board pieces each. UED bottom and topcoat were tested separately. Unto two board pieces, only the bottom coat is sprayed using the provided aerosol sprays and to another two board pieces, both the bottom and topcoats were sprayed. All the board pieces were roughened with sandpaper before applying the coats to enhance the adhesion of the coating liquid to the surface. All coated boards were then left to dry overnight, for approximately 24 hours, to ensure complete dryness.

The next day, one of each coated boards was tested for the wetting behavior of seawater and of two chosen oils, Power 10W engine oil and Power Gear 140W gear oil. Using a micropipette, a 50µL volume of seawater is dropped on to the three boards coated with Nanoprotech, Plastik and UED bottom coat. Using a Canon DSLR camera equipped with 18-55mm lens, a macro side image was taken of the drops on the boards (Figure 2.18). To the other end of the boards, we performed a similar test by dropping a 50µL volume of Power 10W engine oil, and a second side image was taken of the droplets (Figure 2.18 (b)). The images were analyzed using Photoshop software and the contact angle between the liquids and the board surface was measured. Figure 2.18 (a) shows that seawater has a contact angle of less than 90° with both Nanoprotech (49°) and Plastik (62°). This proves that these coatings are not suitable in the application of insulating

electronics from water, since their repellency of large amounts of liquid is weak. They could more properly be applied to prevent moisture or humidity from electronics, but not to completely repel volumes of water, like in our case where the entire board is required to be dipped in water. On the other hand, the bottom coat of UED showed a more promising result. The contact angle of the seawater with the board was more than 90° which indicates that the coating is hydrophobic and cannot be wetted by water. In Figure 16 (b), we show the wetting of Power 10W engine oil on the coated boards. Observing that the oil completely wets (contact angle = 0°) the boards coated with Nanoprotech and Plastik, it is clear that they are not manufactured to repel any oils. The contact angle between the Power 10W oil with the UED bottom coat, being less than 90°, also shows that this coat is not designed for oil repellency.
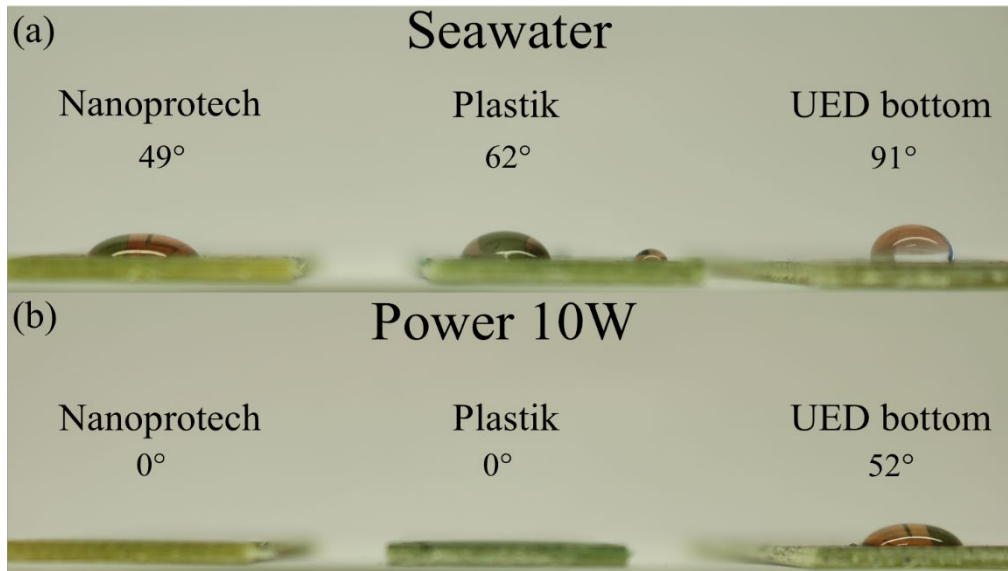


**Figure 2.15: Side view images showing the wetting behavior and contact angles of (a) seawater and (b) Power 10W engine oil on PCBs coated with Nanoprotech, Plastik and UED bottom coat.**

Next, on one of the boards coated with both bottom and to coat of UED, we dropped three 50µL volumes of seawater, Power 10W, and Power Gear 140W. Figure 2.16 shows a side view image of the three drops on the board. The two coats of UED combined displayed great liquid repellency. Both oils and seawater had contact angles with the board above 90°. The water had contact angle of 133° and both oils had contact angle of 126°. This means that together, these two coatings are both hydrophobic and oleophobic.
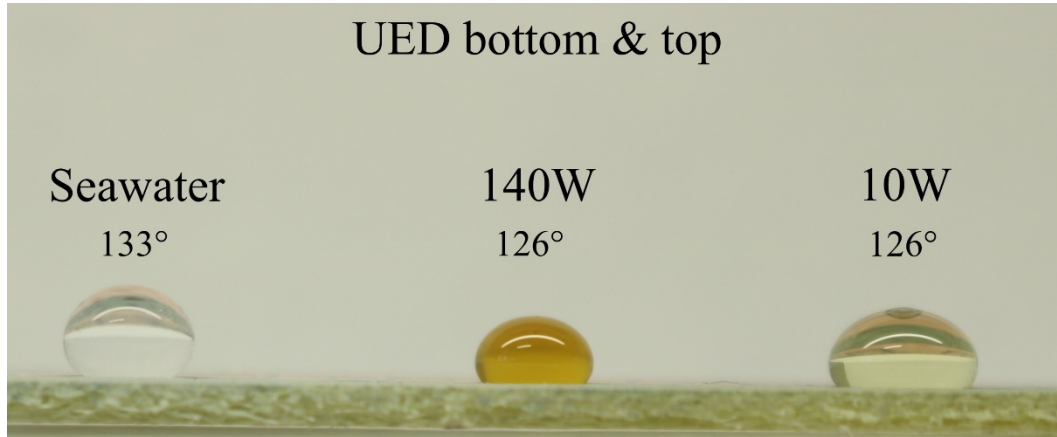
**Figure 2.16: Side view images showing wetting behavior and contact angles of seawater, 140W gear oil and 10W engine oil on PCBs coated with UED bottom and topcoats.**

This result seems to be promising for our application, yet the UED coating did not accomplish its functions once exposed to our experimental conditions. To test for that, we replicated the conditions the sensor board would experience by creating the air/oil/water interface in a beaker. The beaker was filled with seawater and topped with a layer of Power 10W oil. We dipped and raised the coated board steadily into the beaker to imitate the wave-like motion. We observed that the oil fouling issue was still present, and the coating layer was dissolved off the board. The board was then removed and tested again for its hydrophobic/oleophobic behavior, but it was completely wetted by both the seawater and the oil. This meant that the coat was surely deformed, and the surface lost its repellent character. To further settle this conclusion, another board was coated with both bottom and topcoats of UED and left to dry for 24 hours. On this board we dropped a 50μL volume of seawater and Power 10W and monitored the behavior of these two drops for a period of one hour. A side view image of the drops was taken every 10 minutes for one hour (Figure 2.17). The contact angles of both droplets were measured in all the images, and it was found that the angles gradually decreased with time, dropping from 135° to 120° for seawater and from 126° to 106° for Power 10W. This also showed that UED loses its liquid repellency properties over time. This was attributed to the fact that the coating could not endure liquids with surface tensions below 30 mN/m, while all the oils we were testing have surface tensions ranging between 20 and 30 mN/m.
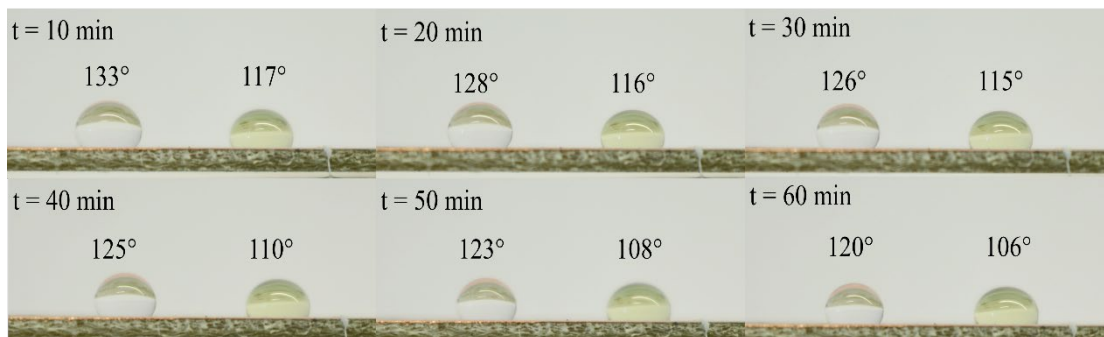


**Figure 2.17: Side view images, with 10 minutes intervals, showing the wetting behavior and the decrease of the contact angles, over a period of 1 hour, of both seawater (left) and Power 10W engine oil (right) on a PCB coated with UED bottom and topcoats.**

31

We tested sprays from the German company, Würth. The two items were Dry Lubricant Spray PTFE and Slide Wax. This product contained some PTFE molecules and is manufactured to increase lubrication and reduce friction between gears and metal parts of cars and motorbikes. These sprays were not chemically resistant to exposure to the oil. They contained the required chemical components for reduction of friction but instantly dissolved when dipped in the oil, which deemed them not suitable for our application.

The two sprays were applied to two pieces of PCB and left to dry for an hour. After drying, each board piece was dipped in oil and removed. The oil readily fouled the board and did not slide off. The pieces were then wiped with tissue to remove the oil, which then exposed that the coating has completely been disintegrated. Figure 2.18 shows images of the test done on Dry Lubricant PTFE. This result concluded that these sprays could not be used in our application, and they are more suitable to be used in cases where friction needs to be reduced between metal parts or gears.
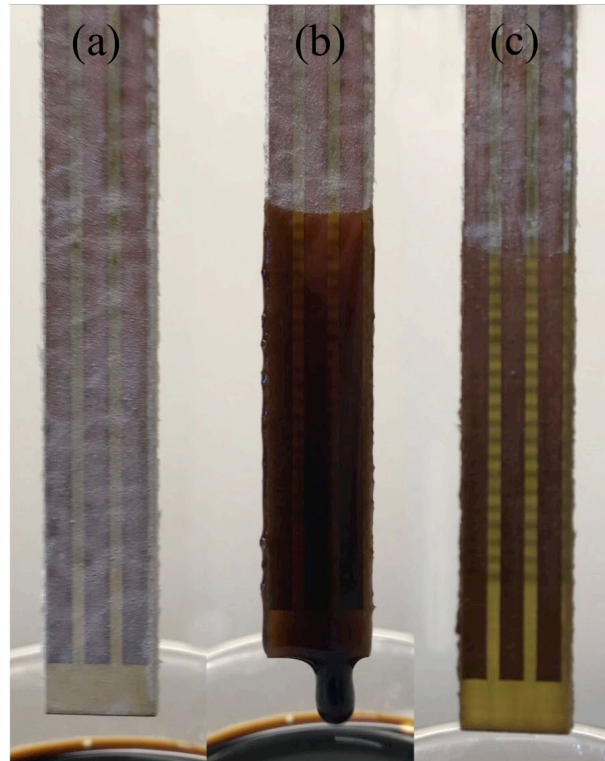


**Figure 2.18: (a) Piece of PCB coated with Dry Lubricant Spray PTFE. (b) Piece of PCB completely fouled after dipping in the oil. (c) After wiping with tissue, piece of PCB shows that the oil has removed the coating.**

### 2.2.2.3.4 Hydrophilic Coatings

Hydrophilic coatings produce surfaces that exhibit high affinity for water molecules, in which they lower the water contact angle, $\theta$, with the surface to less than 5°. Chemically, this means they participate in dynamic hydrogen bonding with surrounding water molecules. In most cases, hydrophilic coatings are also ionic and usually negatively charged, which further facilitates aqueous interactions. Physically, these chemical interactions with water give rise to hydrogel

materials that may exhibit extremely low coefficients of friction. Taken together, such chemical and physical characteristics describe a class of materials that are wettable, lubricious, and suitable for tailored interactions.

Understanding the application of the substrate device to be coated is a crucial factor in determining whether it will benefit from a hydrophilic coating or not. First, it is important to be familiar with all the components making up the substrate material, particularly those on which the coating will be applied. Next, it is beneficial to know the extent to which the substrate will be exposed to chemical interactions from the surrounding experimental conditions and what effects the environment of use maybe be expected to have on the hydrophilic coating. Finally, how much of the surface of the substrate needs to be coated to provide the required device function while providing the benefits of a hydrophilic coating.

The material of the substrate can profoundly affect the adhesion and durability of the hydrophilic coat. This will determine whether the coating will adhere tightly or not at all. The manufacturer's proprietary additive package, processing conditions, and post processing treatment will also vary the extent of adhesion.

Hydrophilic coatings have become of high interest to researchers in many fields. In the field of medicine, they are used to reduce bacterial adhesion on polyurethanes and reduce friction of intravascular medical devices. In the oil industry, hydrophilic coatings are being used to separate oil and water in oceans, resulting from oil spill accidents. Therefore, owing to their extensive use and application, specifically in the oil field, we were interested in investigating the effect of hydrophilic coatings on the sensor board.

We tested AcuWet ON-470, a hydrophilic coat from the US based company, Aculon. This coat was tested to show its hydrophilic properties and whether it can aid in mitigating the oil fouling on the sensor board. The company we purchased the product from kept the proprietary ingredient in the coating a secret, which meant that we did not know what active ingredients are playing the major role in giving the coating its adhesive and hydrophilic properties.

Two pieces of sensor board cut into 2cm x 7cm, were coated using the dipping method. The boards were dipped into the coat solution for 30 seconds then pull out and dried. They were then put in the oven at 60°C for 10 minutes (to ensure surface adhesion). After that, the boards were left for 2 hours before any testing was initiated.

First board was used to test for hydrophilicity of the coat. A drop of water was placed on the surface of the board, and it readily wetted the surface, showing contact angles <20°. This proved that this coating has in fact converted the board into a hydrophilic surface owing to its high affinity to the water molecules, which usually possess high surface tension and would normally exhibit contact angles >70°. The active ingredient of the coating was highly interactive with water and resulted with it spreading readily on the surface. Figure 2.19 shows the water droplet completely wetting the coated board surface.

**Figure 2.19: Water droplet completely wetting the surface of the sensor board piece coated with AcuWet ON-470**

The second board was used to test for oil repellency of the coat. We prepared a beaker filled with water and a layer of oil on top of it. The coated board was dipped into the oil and raised. The oil readily fouled the board surface and was not repelled by the coating. The coating was damaged by the heavy oil used and was no longer covering the board surface. Figure 2.20 (A) shows complete oil fouling of the coated board surface at the moment it was removed from the oil. Figure 2.20 (B) shows board surface still fouled by the oil after 3 minutes of removal from the oil.
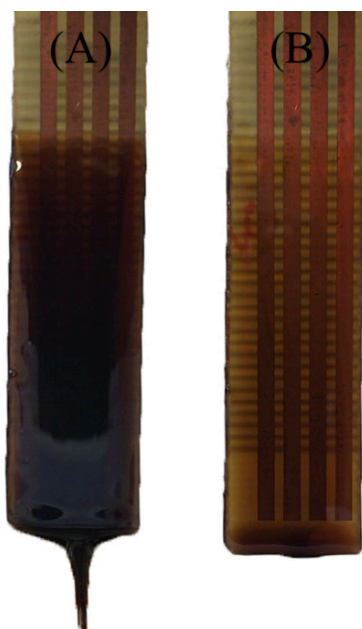


**Figure 2.20: Oil fouling coated board (A) at the moment the board was removed from the oil; (B) 3 minutes after the board was removed from the oil**

The coat was not strong enough to prevent being removed by the heavy oils used in our experiments. These coatings are designed to reduce friction of surfaces using the aid of water. They were bought and tested to determine whether their hydrophilic properties would cause the water to help in not allowing the oil to foul the board surface. Yet, the results show that the volume of oil is much larger than what the water can remove. Also, they showed weak chemical resistance and weak adhesive properties when exposed to the heavy oils.

In conclusion, coatings containing fluoropolymers are the only materials that have shown some promising results. The combination of high chemical resistance, strong adhesion and non-stick properties of fluoropolymers makes them the best contenders for oil repellency on any kind of surface. However, for our use case the oil is required to slide off at a much faster rate to compensate for the movement of waves in the ocean. Another limitation is that when applied to thin surfaces like pins, its effect is significantly diminished.

### 2.2.3 Structural Approach to Oil-Fouling Mitigation

We also attempted to mitigate the oil-fouling issue from a structural approach. We proposed engraving the boards in a manner that would attract the oil into the newly formed channels, thus reducing their volume near the sensing area. We prepared six boards, four were engraved horizontally and two were engraved vertically. The oil was in fact attracted into the engravings and was slightly reduced from the sensing area. Yet, when we compare the volume reduced off the board to the volume available all around the sensor, we realize that the volume is much smaller and is somewhat negligible. Therefore, this method was discarded since it did not add any significant solution to our problem, while it would be adding complexity to the production of our sensor board.

As a summary for the fouling mitigation techniques tested, none provided the performance needed to be incorporated in the final design.

## 2.3 Sensor Board Design

The sensing board is one of the three main parts of the sensor, it is responsible for obtaining the capacitance measurements and sending them to the microcontroller. It is composed of the sensing units and the transducing modules. In this section, we describe the implementation of the sensor board for both the handheld and the skimmer devices.

### 2.3.1 Handheld Sensor Board

#### 2.3.1.1 Sensor Board Version I

Based on our previous assessment of several designs of the sensing cells, we selected the distributed pins-based design to be used in the handheld capacitive sensing unit. The main reason behind this decision is that the role of the capacitive cartridge is limited to measure the level of the oil/water interface instead of detecting the two interfaces. In this case, the optimum design for the sensing unit is the one that minimizes the effect of oil fouling and maximizes the signal change with respect to water contact. This design uses a set of distributed sensing cells, where each cell is composed of three needle-like pins (diameter of 0.5 mm), separated from each other horizontally by 2.54 mm. The vertical distance separating the base pads of the pins is 1 mm, and the total width of the base pad is 2 mm.

To decrease the water-fall fouling effect on the pins when the sensor is immersed in the oil/water mixture, we used a diagonal-based distribution of the sensing cells. This method ensures the existence of a considerable vertical distance between the sensing cells vertically without affecting the vertical spatial resolution. The schematic of the capacitive sensing unit is shown in

Figure 2.21, 3D model of the PCB is shown in Figure 2.22, and implemented prototype is shown in Figure 2.23.
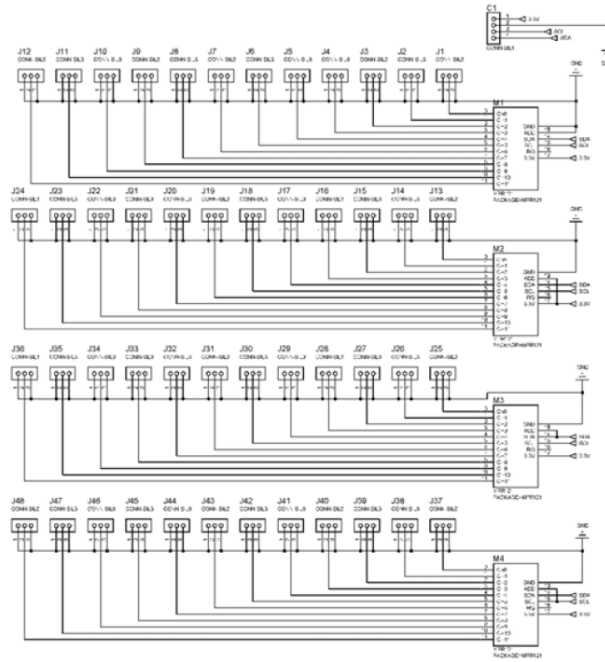


**Figure 2.21: Left: Capacitive sensing unit – schematic**



| PCB Layout | Bottom layer | Top layer |
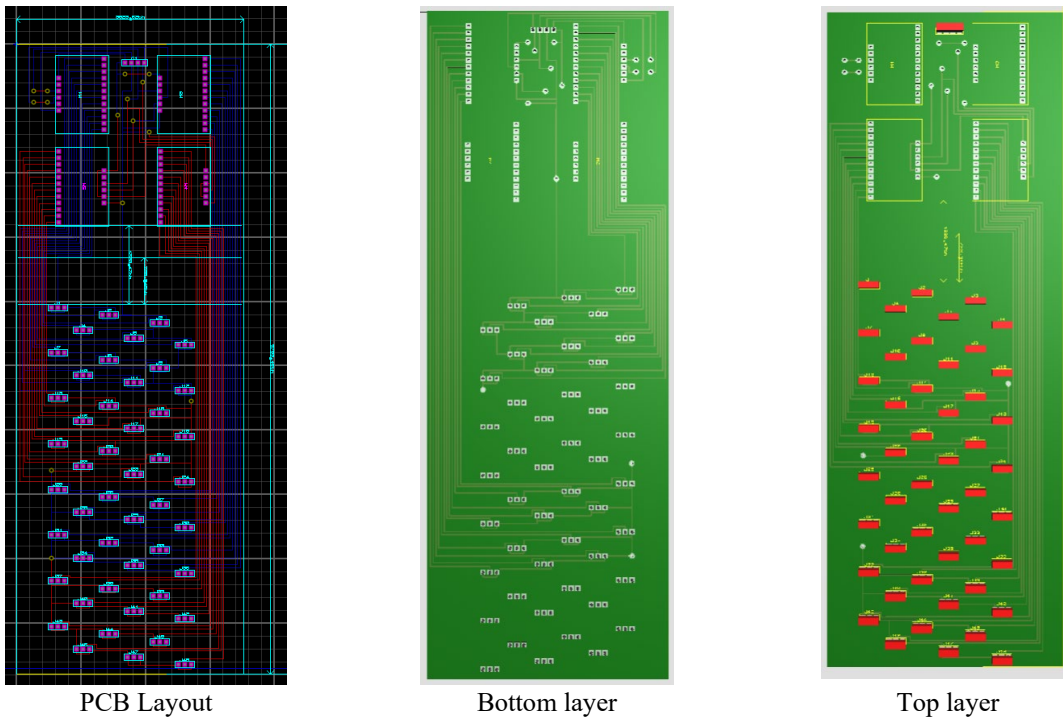
**Figure 2.22: 3D model of the capacitive sensing unit**

| Top view | Bottom view | Side view |
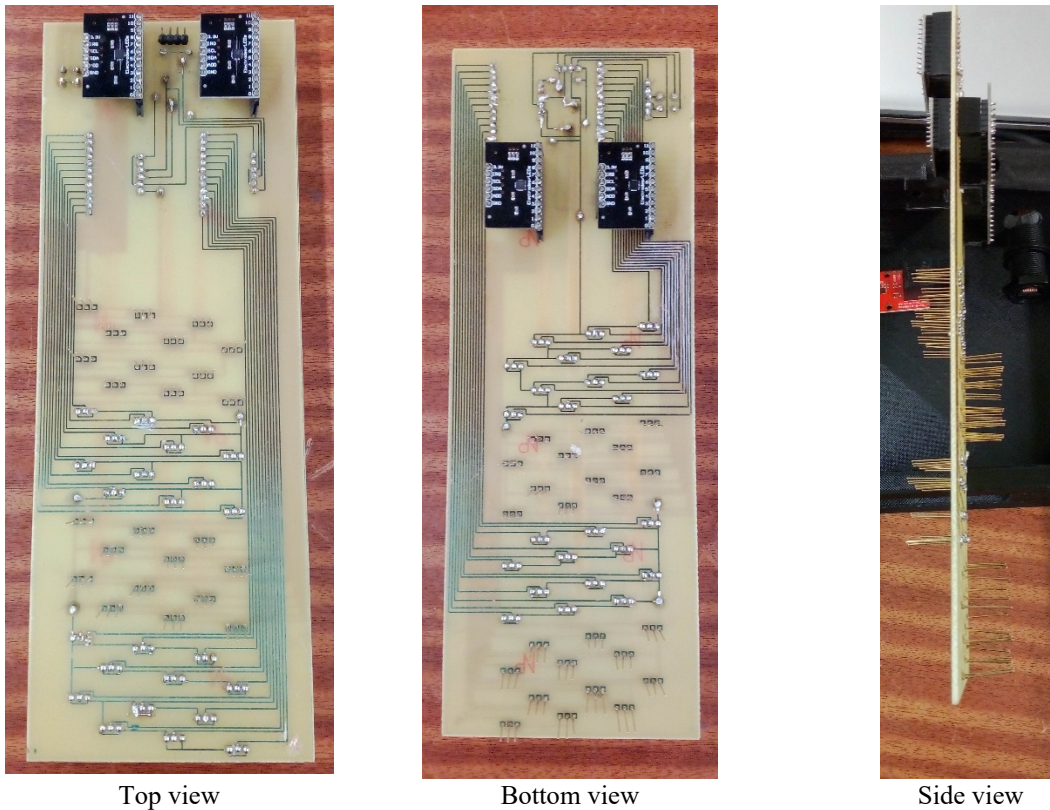
**Figure 2.23: Capacitive sensing unit - Implemented PCB**

### 2.3.1.2   Sensor Board Version II

In this section, we describe the design and implementation of the second version of the sensing unit which will be used in the final design. The new sensor board is a 6-layer PCB manufactured at PCBWAY (https://www.pcbway.com/). The main modifications applied to the new board (Figure 2.24) can be summarized as follows:

- The addition of two copper sheets connected to power ground (GND) above and under the layers that contain the connection tracks for the sensing units (Inner 1 & Inner 4). This modification is essential because it isolates the connection tracks from any possible external interference.

- The tracks connecting the four MPR121 devices to the 48 sensing units were made very thin (10 thou) to minimize the base capacitance. As shown in Figure 2.24, these tracks are embedded in the inner layers of the PCB (Inner 2 and Inner 3).

- The power (3.3V and GND) and I2C signal lines (SCL, SDA) were mounted at the two outer layers (Top Copper and Bottom Copper). This ensures that the power and the I2C signals are completely isolated from the sensing tracks.

- For labeling and naming of the components, a silk-screen layer (white) was added to the top and bottom copper of the PCB.

As shown in Figure 2.25, the base-pads for the sensing pins are squares with equal lengths and widths of 2 mm. The horizontal gap between the centers of the pins is 2.4 mm. The vertical gap

37

between two consecutive sensing cells is 1 mm. The holes used to mount the pins are plated through holes with a diameter of 1 mm. The plated-through holes allow for several mounting mechanisms of the pins such as soldering and press-fit technology. This configuration results in a sensing resolution (inter pin distance) of three millimeters for the capacitive sensor and sensing range (first to last pin distance) of 141mm. Note that since the ultrasonic sensor provides continuous distance measures with high resolution (less than 1 mm), the handheld device would be able to measure oil thicknesses that are less than 3 mm.

Top (Power)   Inner 1 (GND)   Inner 2 (Connections)   Inner 3 (Connections)

Inner 4 (GND)   Bottom (Power)   Top Silk (2 MPR121)   Bottom Silk (2 MPR121)
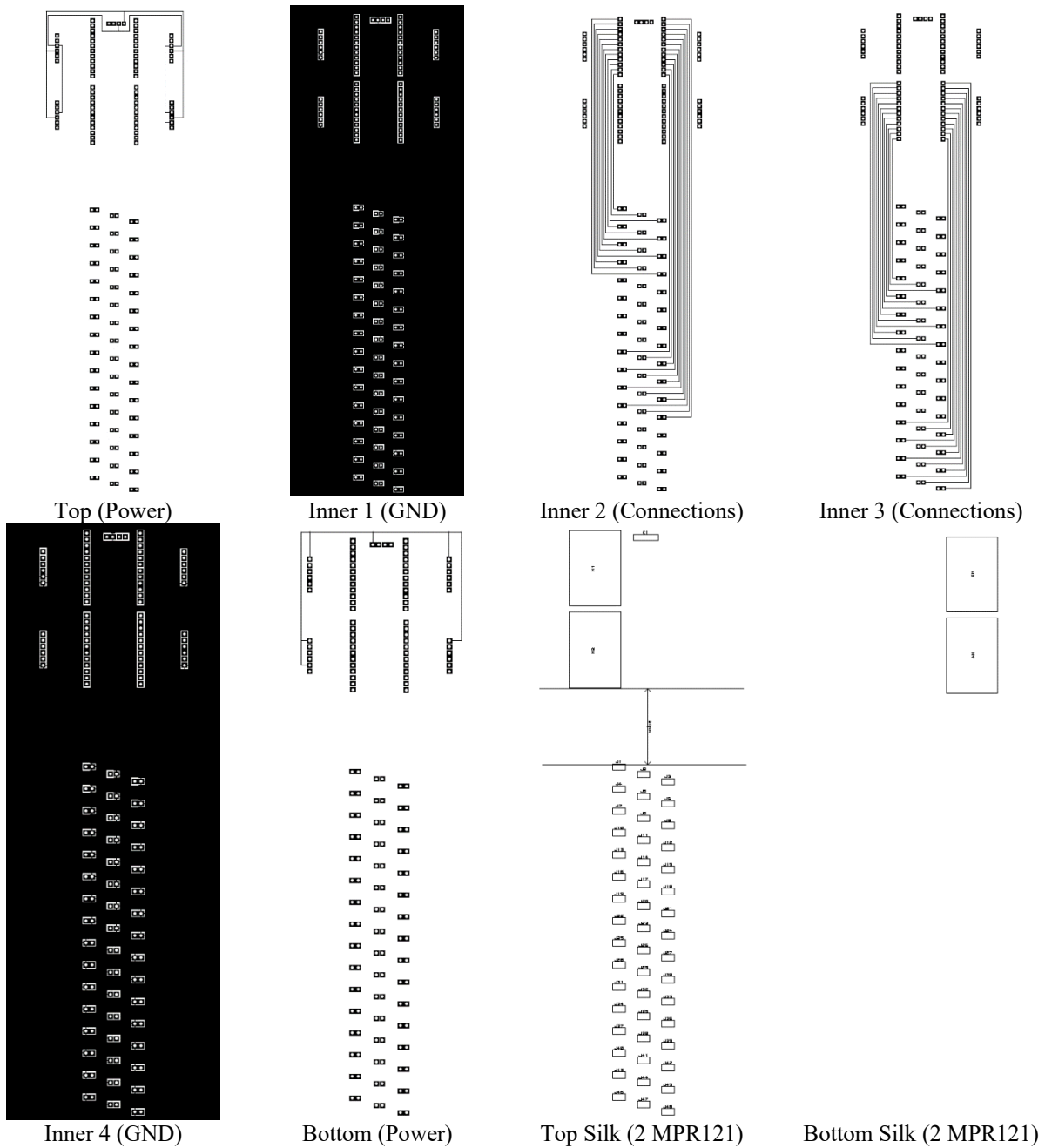
**Figure 2.24: Layers of the multi-layer handheld sensor board**
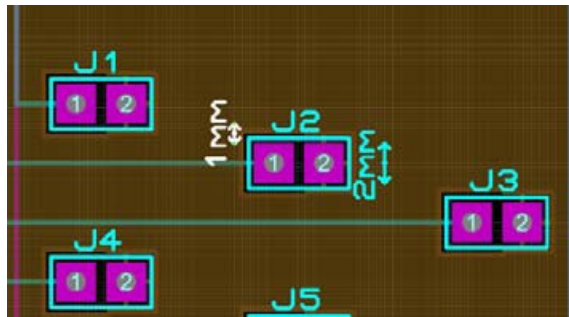
**Figure 2.25: Dimensions of the sensing units – multi-layer sensing unit**

The PCB was given a T-shape and equipped with 6 mm mounting holes at its edges to facilitate the mounting into the sealed package. Images showing the designed 3D model and the implemented PCB are shown in Figure 2.26.

Four base sockets and a set of 96 pins were soldered to the new sensor board as shown in Figure 2.27. The base sockets were used instead of direct soldering to mount the MPR121 devices to the PCB, and would facilitate the replacement of any of the four breakout boards in case of failure. Similar to the previously developed sensor, two MPRs were mounted at each layer (top and bottom) of the PCB. This configuration facilitates the routing of the connection tracks. A four-point male PCB header with 2.4 mm pitch was soldered to the PCB to connect it to the control unit through power and communication lines. The pins used in this board have a diameter of around 1 mm and a length of around 10 mm.
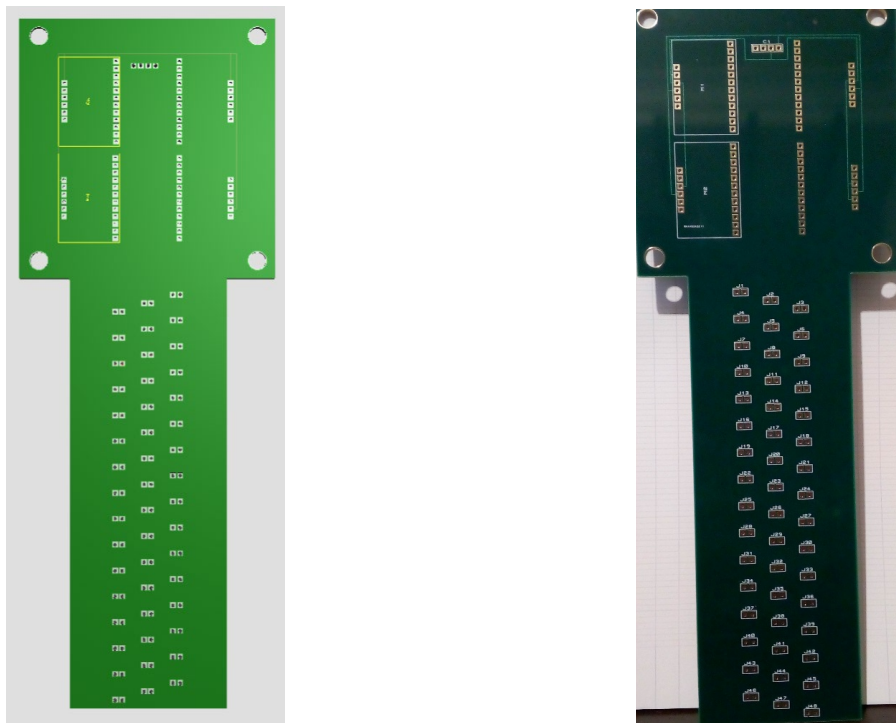


**Figure 2.26: Multi-layer sensing unit: 3D model (left) - Implemented PCB (right)**
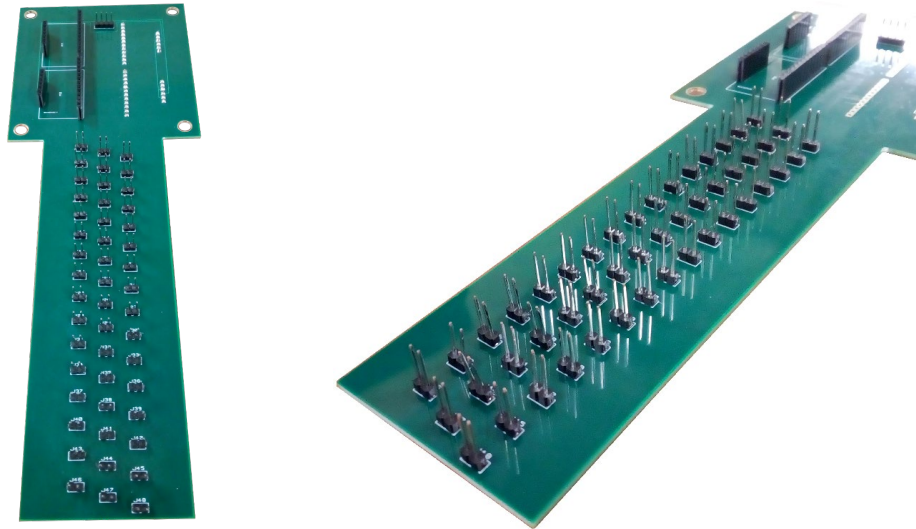
**Figure 2.27: multi-layer sensor board with pins soldered**

Two additional designs were implemented to enhance the resolution of the measurement. In the first design, the vertical gap between the pins was reduced from 1 mm to 0.5 mm, which increased the measurement resolution by 0.5 mm and decreased the total sensing range from 141 mm to 117.5 mm. In the second design, the vertical gap is removed, making the inter pin resolution 2 mm and decreasing the sensing range to 94 mm. Note that the size of the single sensing cell (base + gap) in the previous design was 3 mm. The three designs are shown side by side in Figure 2.28.
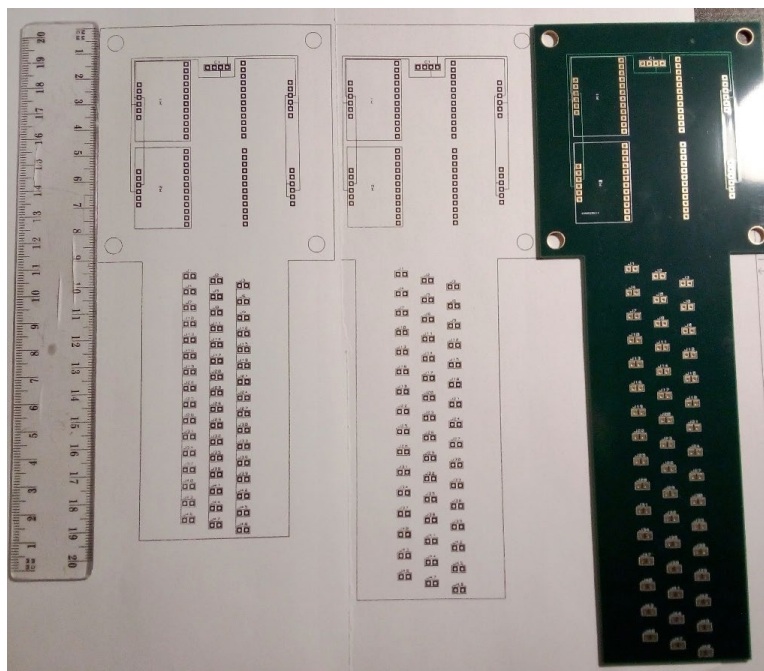


**Figure 2.28: Handheld capacitive sensor (left: no gap, middle: gap = 0.5 mm, right: gap = 1 mm)**

### 2.3.2 Skimmer Sensor Boards

Similar to the handheld sensor device, the skimmer-mount sensor cartridge used the distributed needle-like pins with the diagonal distribution to minimize the effect of oil fouling. The main difference between the two boards is in the sensing resolution and range. The skimmer-mount sensor has a measurement resolution (pin to pin distance) of 12 mm whereas the handheld sensor has a higher resolution of 3 mm. Based on the project requirements, the range of the skimmer mount sensor is 50 cm whereas the handheld sensor covers a range of 10 cm.
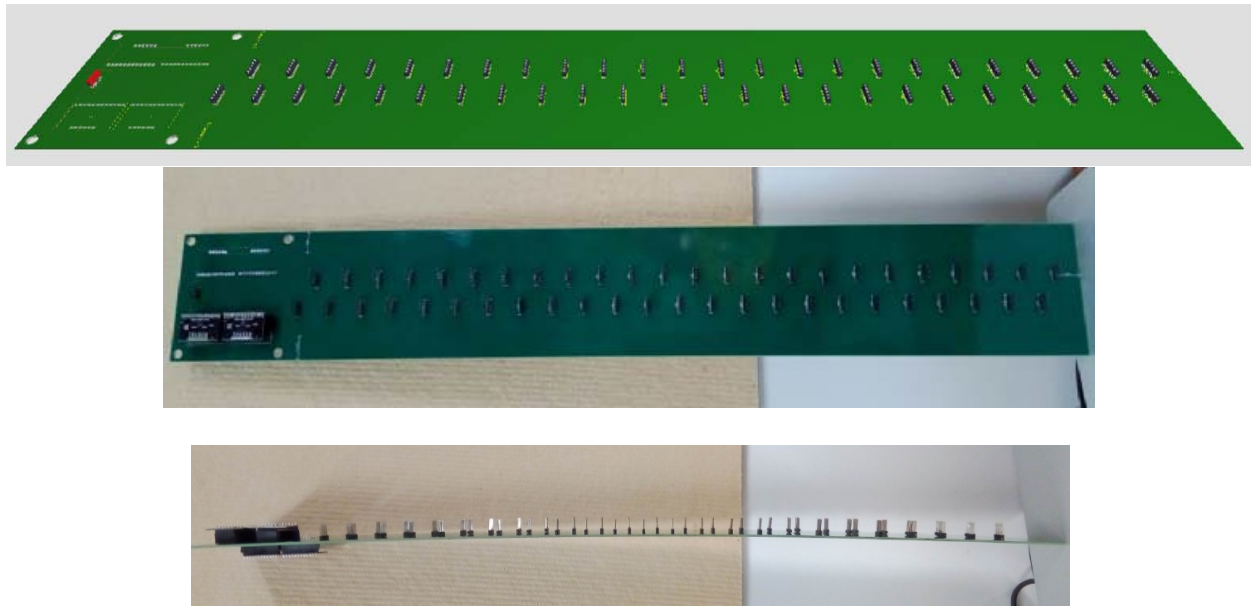


**Figure 2.29: Skimmer-mount sensor (3D model and fabricated board)**

The second prototype of the skimmer-mount capacitive sensor was designed to match the full sensing range of 50 cm. An image showing the second prototype (3D model and fabricated board) is shown in Figure 2.29. The sensor board is composed of 6 layers and four MPRs. The vertical gap between the sensing units is 10 mm (12 mm inter pin distance). Each sensing unit contains 5 pins where 2 pins are connected to the sensor pad and 3 pins connected to GND. The internal layers were configured in a similar way to the handheld board. The total board width is 100 mm and total length is 680 mm. The length of the sensing zone (first to last pin distance) is 564 mm. The board was given a rectangular shape with empty areas between its edges and the connection tracks to allow for possible mounting on a fixed metallic platform (Figure 2.30).
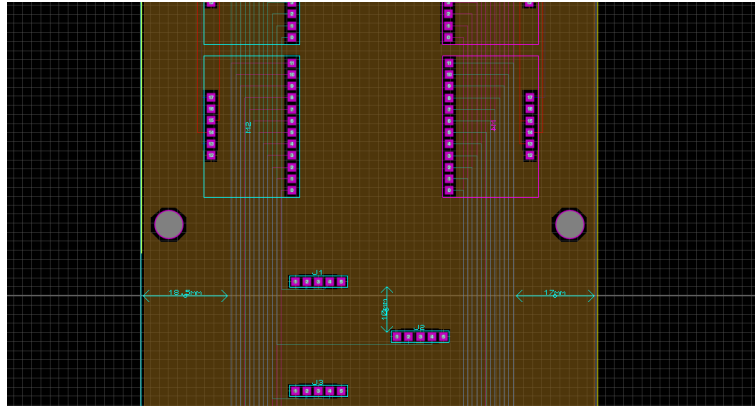
**Figure 2.30: Dimensions and sensing cells of the second prototype - Skimmer-mount**

The pins selected for the skimmer-mount sensor were assembled using the press-fit technology to avoid using soldering on the sensor body. The pins have a diameter of 1 mm and a length of 10 mm. Also, the thickness of the board was increased from 1.6 mm to 2 mm. Photos showing the press-fit pins mounted on the second sensor prototype are shown in Figure 2.31.
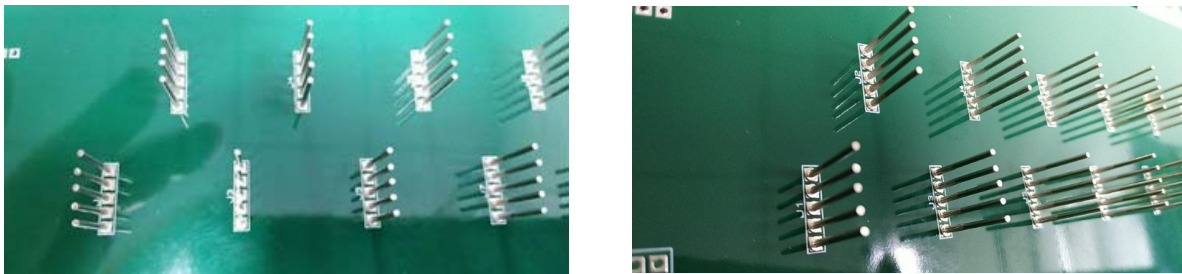


**Figure 2.31: Second prototype of skimmer-mount capacitive sensor with press-fit pins**

Two other sensor designs were implemented to enhance the sensing resolution of the skimmer-mount cartridge. The new designs are shown in comparison to the handheld sensor in Figure 2.32. In the first design, the vertical gap between the pins was reduced to 3 mm (5 mm inter pin distance) and in the second design to 5 mm (7 mm inter pin distance). This makes the sensing range (first to last pin distance) for the two new sensors 235 mm and 329 mm respectively. If the sensor is used without a floater, the longer design is recommended to cover the full sensing range (more than 50 cm). In this case, structural support is needed due to the length of the sensor. The new designs are shorter with enhanced measurement resolution and increased stiffness. In the case of using a floater, the new designs could be used without the need for structural support. We also fabricated skimmer boards with soldered pins, in addition to the press fit.
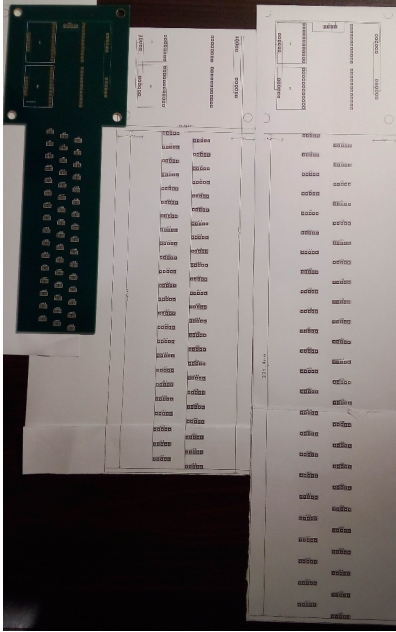
**Figure 2.32: Skimmer-mount sensor (left: handheld sensor, middle: gap = 3 mm, right: gap= 5 mm)**

### 2.3.3 Sensor Model

The theoretical modeling of the sensor at the circuit level is important to provide an accurate description of the sensor behavior. This section focuses on the model and its validation via simulations.

#### 2.3.3.1 The relation between voltage and current in capacitors

The relation between the voltage and current in a capacitor is not defined using a constant value as in resistors (Ohm's law). Instead, the changes relative to time are taken into consideration:

$$i = C\frac{dv}{dt} \quad (1)$$

where $C$ is the capacitance measured in Farads, $i$ is the instantaneous current flowing through the capacitor, and $\frac{dv}{dt}$ is the rate of change of the voltage of the capacitor (Volts per second).

Equation (1) describes that the current passing through a capacitor is the derivative of the voltage with respect to time. For example, if the voltage is constant $\left(\frac{dv}{dt} = 0\right)$, no current will pass through the capacitor $(i = 0)$; capacitors act as an open-circuit at steady-state. In physical terms, when the potential difference between the plates does not change, charges are note urged to move from one plate to another. Thus, a change in the voltage over time is essential to cause electrical current to flow through the circuit. When the voltage is increasing or decreasing, current flows through the circuit. For instance, if the voltage is increasing at a fixed rate of change; $\frac{dv}{dt} = 1\ V/sec$, the current is a positive constant since it is the product of two positive constants $(C\frac{dv}{dt})$. Under this condition, the capacitor is considered charging because as current flows through the circuit, more charges are accumulated on the capacitor's plates. As more

charges are accumulated on the plates, the intensity of the electric field between the plates also increases since the electric field is directly related to the charge amount; electric charge is the source of the electric field. On the other hand, if we flip the sign of the voltage rate of change, for example, $\frac{dv}{dt} = -1 \, V/sec$, the current will also be a constant but takes a negative sign. In physical terms, this means that charges are leaving the capacitor plates. The charge accumulated on each of the capacitor's plates and consequently, the electric field intensity decreases. As a result, the voltage of the capacitor decreases until reaching zero. This process is known as discharging.

### 2.3.3.2  The capacitance measurement method used by the MPR121 transducer

The capacitance measurement method adopted by the capacitive transducer (MPR121) is based on Direct Current (DC) excitation applied in the form of short-duration pulses. To measure the channel capacitance, it provides a specific amount of electric current ($I$) for a defined duration of time (T). Before discharging the channel, it measures the voltage between the channel and the system ground. The voltage measured at the end of the charging phase ($V_T$) could be represented by integrating equation (1) with respect to time:

$$\int_0^T i \, dt = C \int_0^T \frac{dv}{dt} \, dt$$
$$iT - iT_0 = CV_T - CV_0$$
$$\frac{IT}{C} = V_T \qquad (2)$$

where $I$ is the charging current in Amperes (Coulomb/second), $T$ is the charge duration in seconds, C is the capacitance in Farads, and V is the voltage in Volts. Note that before the charging is started ($t = T_0 = 0$), the channel is grounded to ensure that the voltage starts from zero ($V_0 = 0$). Since the electric current $I$ is the rate of flow of charges ($dq/dt$), then, the current multiplied by the duration of time $T$ gives the amount of charge transferred to the sensing channel; $Q = I \, x \, T$ (Coulombs). Therefore, the capacitance of the sensing channel $C_{Ch}$ could be represented as:

$$C_{Ch} = \frac{Q}{V} \left( \frac{Coumb}{Volt} \right)$$

where $C_{Ch}$ is the total channel capacitance in Farads, $Q$ is the amount of charge accumulated on the sensing channel in Coulombs, and $V$ is the electric potential between the channel and the system ground. Note that SI unit Farad is defined as one Coulombs per Volt. Based on Equation (2), the voltage of the channel will increase linearly as the current is a positive constant. Note that the slope of the voltage is directly related to the value of the current. As the current increases, the slope of the voltage will be steeper and vice versa. The voltage measured at time instant T is represented in equation (2). The complete measurement cycle is illustrated in Figure 2.33.
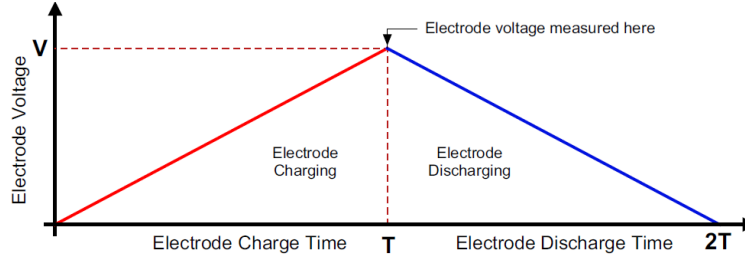
**Figure 2.33: Excitation and measurement cycle - MPR121**

After measuring the voltage, the MPR121 chip converts the analog voltage value to a digital value using an embedded 10-bit Analog-to-Digital Converter (ADC). 10-bit ADCs can represent a certain analog range in 1024 steps. Thus, the converter works based on the supply voltage $V_{DD}$. In our circuits, we used a 3.3V supply for the power supply; $V_{DD} = 3.3\ V$. The digital value could be calculated based on the analog value as shown below:

$$V_{ADC} = \frac{V_{Analog} x\ 1023}{3.3} \qquad (3)$$

As mentioned in the datasheet of the MPR121 device, there are some limits for the ADC to work correctly. Valid analog voltages (visible for the ADC) should be between: $V_{Analog\ (low)} = 0.7\ V$ and $V_{Analog\ (high)} = V_{DD} - 0.7\ V$. In our case, since $V_{DD} = 3.3\ V$, then the limits are:

$$V_{Analog\ (low)} = 0.7\ V, V_{Analog\ (high)} = 2.6\ V$$

Based on these limits, we can get the digital limits using equation (3).

$$V_{Digital\ (low)} = 217, V_{Digital\ (high)} = 806$$

Digital voltage values in this interval are considered valid and could be used to infer the capacitance as described in the previous section. To convert digital voltage values to capacitances:

$$C = \frac{Q\ x\ 1023}{3.3\ x\ V_{Digital}}$$

### 2.3.3.3 Simulation of the measurement method used by MPR121 device

To demonstrate how this method could be applied to measure the capacitance, we designed a simulation project using the Proteus Design Suite software (Labcenter Electronics). To simulate the controlled current source used by the MPR121 for excitation, we used two current sources as shown in Figure 2.34.
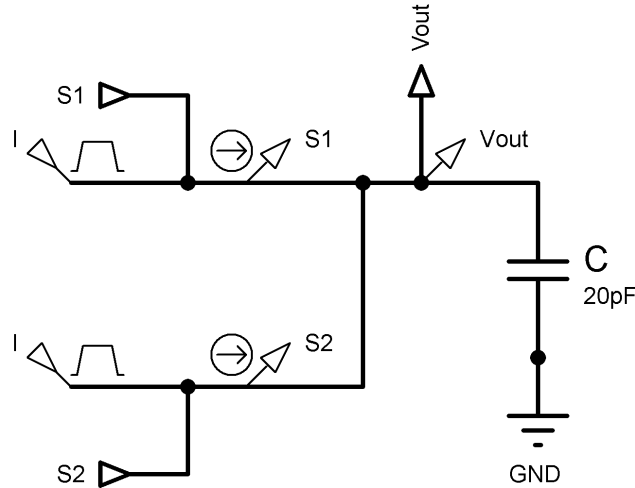
**Figure 2.34: Simulation circuit for MPR121 capacitance measurement method**

We aimed to use actual values that could be applied in real MPR121 devices, thus, we selected I = 63 μA and T = 0.5 μsec. Based on our previous analysis, the limits for a valid capacitance measurement using these configuration values could be calculated as:

$$C_{low} = \frac{I \times T}{V_{DD} - 0.7} = \frac{(63 \times 10^{-6})(0.5 \times 10^{-6})}{(3.3 - 0.7)} = 12.11 \, pF$$

$$C_{high} = \frac{I \times T}{0.7} = \frac{(63 \times 10^{-6})(0.5 \times 10^{-6})}{(3.3 - 0.7)} = 45 \, pF$$

As shown in the circuit, we selected a capacitor of 20 pF which lies in the valid range to measure in this simulation. To generate the desired current signal, we configured the current sources as shown in the table below.

| | Analog type | Initial (low) current | Pulsed (high) current | Pulse width | Frequency | Start (Sec) |
|---|---|---|---|---|---|---|
| **Current Source 1** | Pulse | 0 | 63 μA | 500 nsec | 1 MHz | 0 |
| **Current Source 2** | Pulse | 0 | -63 μA | 500 nsec | 1 MHz | 500 nsec |

To observe the current signal generated by this configuration, we created an Analog Analysis Graph (AAG) and provided it with the current probes S1 and S2. The time interval of the analysis is set to [0 10 μsec], allowing us to observe 10 consecutive measurement cycles as performed by the MPR121 device in a real scenario. A second AAG with a similar time interval was created to plot the voltage measured by the voltage probe $V_{out}$. Samples of the current and voltage signals are shown in Figure 2.35.

46
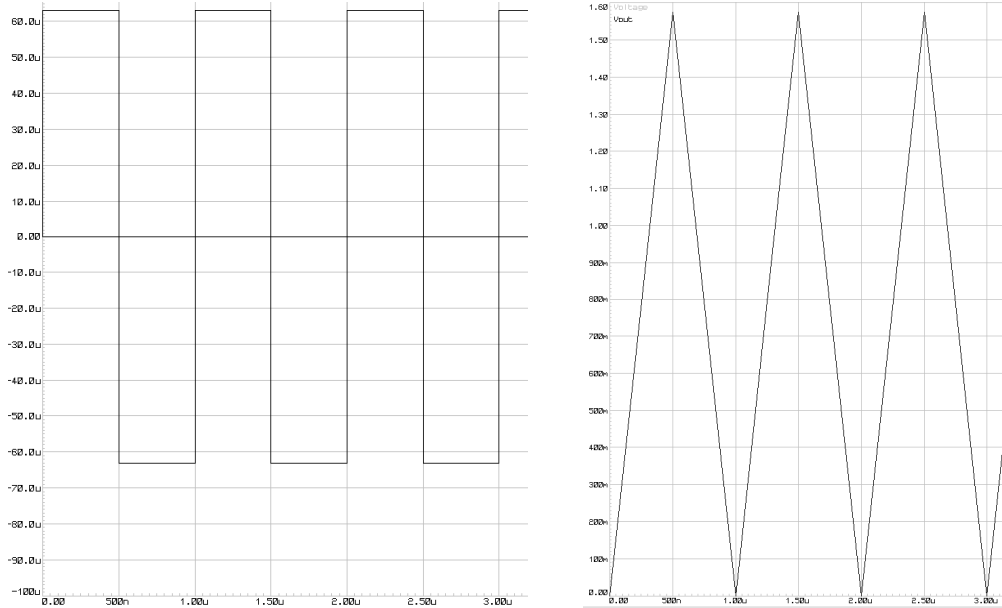
**Figure 2.35: Left: Current source signal. Right: Voltage at the capacitor**

As discussed, to calculate the capacitance, we should get the voltage value at the peak of the voltage signal; the voltage recorded at the end of the charging phase. This value is obtained from the simulation results as V = 1.57 V. Given I = 63 uA and T = 0.5 uSec, we can calculate the capacitance as C = Q / V = (I x T) /V = [(63 x $10^{-6}$) (0.5 x $10^{\wedge-6}$)] / 1.57 = 20.0636 pF which is almost identical to the value of the capacitor used in the circuit (*i.e.,* 20 pF). This result demonstrates how the MPR121 method could be used to measure the capacitance and validates the triangular behavior of the capacitor's voltage when supplied by a pulsed DC excitation.

### 2.3.3.4  Sensor model and the application of the MPR121 measurement method

In our sensor, the sensing cells (electrodes) are connected to the twelve sensing pins of the capacitive transducers (MPR121) via thin conductive tracks surrounded by grounded conductive sheets acting as passive shields. When we apply the capacitance measurement method to our sensor model, we should note the following. The measured capacitance introduced above $C_{Ch}$ represents the capacitance of the whole sensing channel. This means that $C_{Ch}$ is composed of several component capacitances, which include: 1) capacitance between the channel pin and the pins of the other channels (grounded) on the breakout board holding the MPR121 chip, 2) capacitance between the connection track and the surrounding copper shielding (grounded) covering the sensor body, and 3) the capacitance between the pins in the sensing cell. Based on this configuration, one sensing channel could be modeled as shown in Figure 2.36.

47
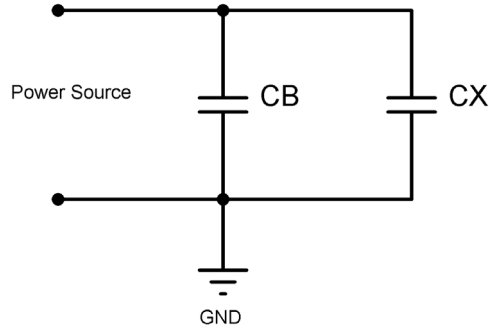
**Figure 2.36: Single channel circuit model**

Noting $C_B$ as the base capacitance and $C_X$ is the capacitance between the sensor pins (sensor capacitance), $C_B$ is constant and the only capacitance that changes due to material contact is the capacitance $C_X$, which is connected in parallel with the base capacitance. Since the two capacitances are connected in parallel, they could be added to obtain the total channel capacitance $C_{Ch}$:

$$C_{Ch} = C_B + C_X$$

By substituting in the Equation (2), we obtain:

$$C_{Ch} = C_B + C_X = \frac{Q}{V} = \frac{IT}{V}$$

The value measured by the MPR121 device is the voltage and not the capacitance, thus, to make things easier, we represent the output voltage in terms of the base and sensor capacitances as:

$$V = \frac{Q}{C_B + C_X}$$

The MPR121 transducer allows us to set the charging current $I$ and the charging time $T$. For instance, in our previous experiments, we used the following values: I = 63 uA and T = 0.5 uSec. The charge amount Q is constant. Also, $C_B$ is constant due to passive shielding. The sensor capacitance $C_X$ is variable and depends on the dielectric constant of the material filling the gap between the pins. Based on this, we can conclude that the output voltage measured by the MPR121 is inversely related to the sensor capacitance $C_X$. However, this relation is not linear and the base capacitance $C_B$ plays a major role in affecting the sensitivity of the output to the sensor capacitance $C_X$.

### 2.3.3.5 Simulation of the sensor model

To validate the theoretical model we used to describe our sensing channel, we performed another simulation after adding the base capacitance ($C_B = 10 \, pF$) to the circuit as shown in Figure 2.37.
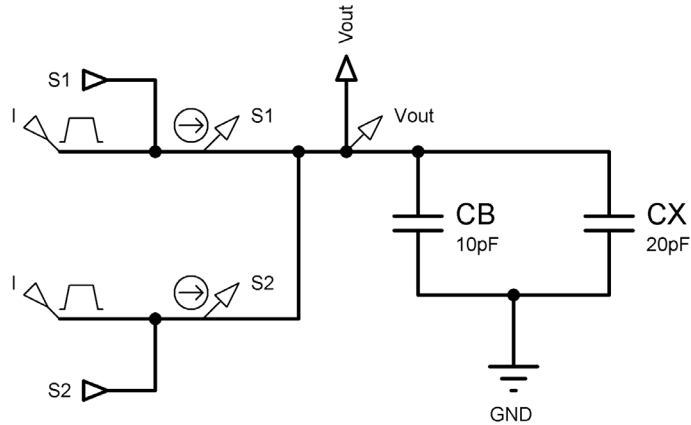
**Figure 2.37: Sensing channel model - base capacitance included**

Assuming that $C_B$ is constant, we changed the capacitance of the sensor from 1 pF to 20 pF. The output voltage relative to the sensor capacitance $C_x$ is plotted based on our calculations and compared to the results obtained from the simulation as shown in Figure 2.38.
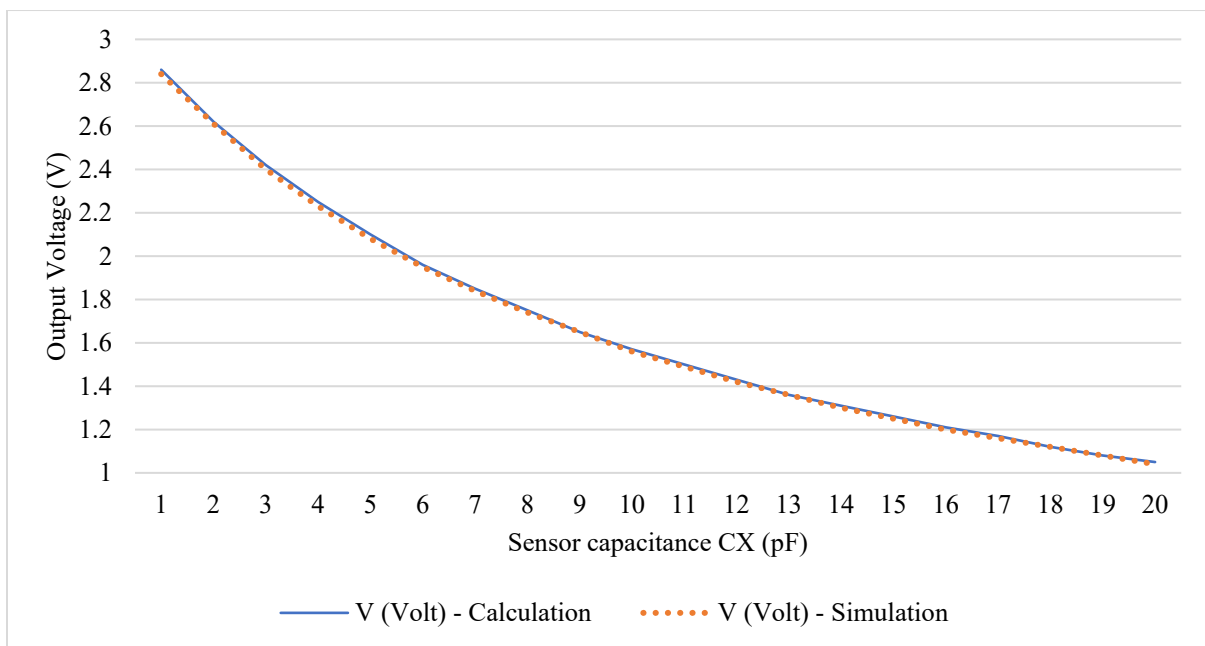


**Figure 2.38: Output voltage vs. sensor capacitance Cx (Calculations vs. Simulation)**

As shown in the figure, the output voltage is inversely and non-linearly related to the sensor capacitance $C_x$. This result was expected by the theoretical model. Also, the voltages obtained from the simulations are almost identical to the calculations. This allows us to use our calculations while exploring the effect of the other parameters.

Based on this result, another question arises related to the effect of the size of the base capacitance on the sensitivity of the sensor. In other words, how is the sensitivity affected when the base capacitance increases. By the sensitivity we mean the change in the output voltage with

respect to a change in the sensor capacitance $C_x$. To answer this question, we increased the value of the base capacitance gradually from 10 pF to 20 pF with increments of 2 pF. After each change in the base capacitance, the output voltage is calculated while changing the sensor capacitance $C_x$ from 1 pF to 20 pF. The voltage curves relative to different base capacitances are plotted in Figure 2.39.

This result shows that the increase in the base capacitance decreases the sensor's sensitivity. Note that the steepness of the slope decreases as the base capacitance increases. In other words, since the base capacitance is in the denominator of the voltage equation, as it increases, it reduces the effect of changing $C_x$ on the sensor output. The results matched the conclusions previously obtained through our experimental work. Base capacitance is a major problem in this type of sensors and should be minimized to maximize the sensor's sensitivity.
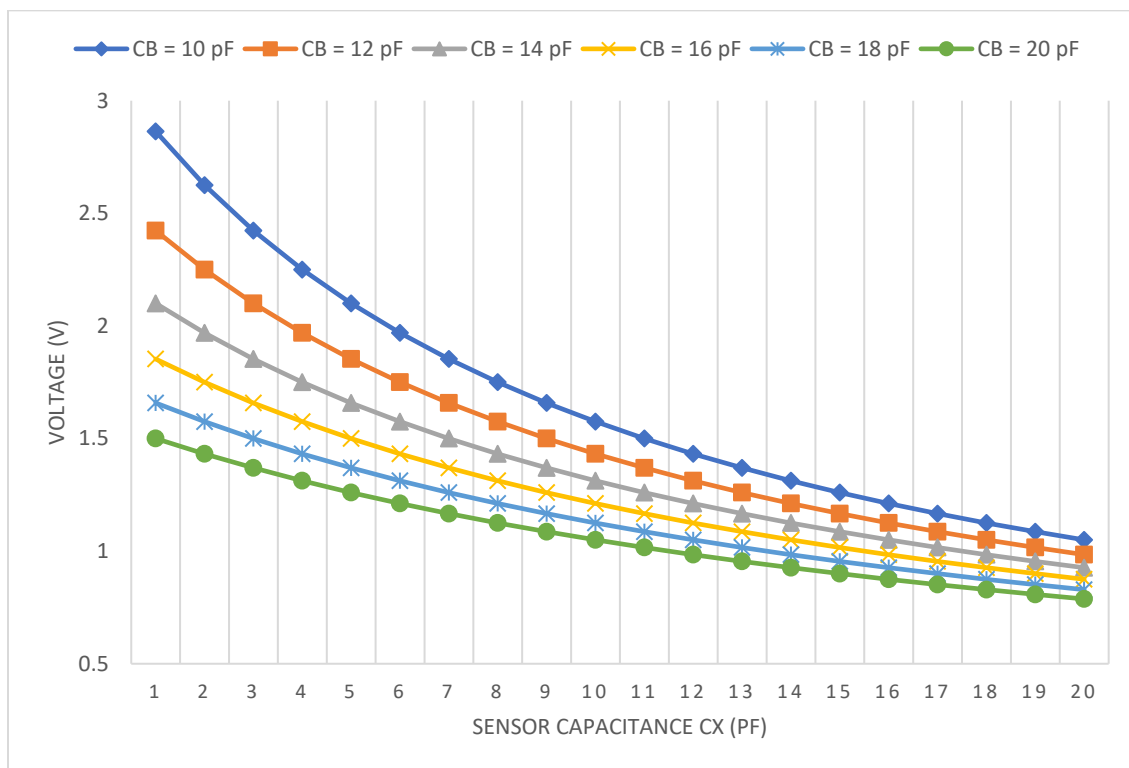


Figure 2.39: Output voltage w.r.t to changes in CX (1 – 20 pF) - Several base capacitances

## 2.4 Control Unit Design

The second main part of the sensor is the control unit. It is responsible for data acquisition, processing, display, and logging. The handheld and skimmer sensors share a common main control unit, however the data display and user interfaces in both sensors differ based on the use case requirements. In this section, a detailed overview for both sensors' control boards will be presented.

### 2.4.1 Handheld Sensor Control Unit

Several sensors and electrical components were selected to satisfy the requirements of the handheld device including sensors for measuring the environmental conditions (temperature), GPS module for acquiring the location coordinates (longitude and latitude), memory module (SD Card) for data logging, and OLED display for real-time output display. In this section, we describe the circuit design and list important notes regarding the power and control requirements of the circuit components.

#### 2.4.1.1 Control Unit Version I

The overall control circuit schematic is shown in Figure 2.40. We added several optional data and power ports to allow for minor changes without requiring hardware modifications to the circuit. We added the necessary power and serial ports required to operate the ultrasound sensor. Also, as shown in the schematic, four push buttons were included to read the user commands. The circuit was designed using Proteus Professional 8 software provided by Lab Center Electronics.
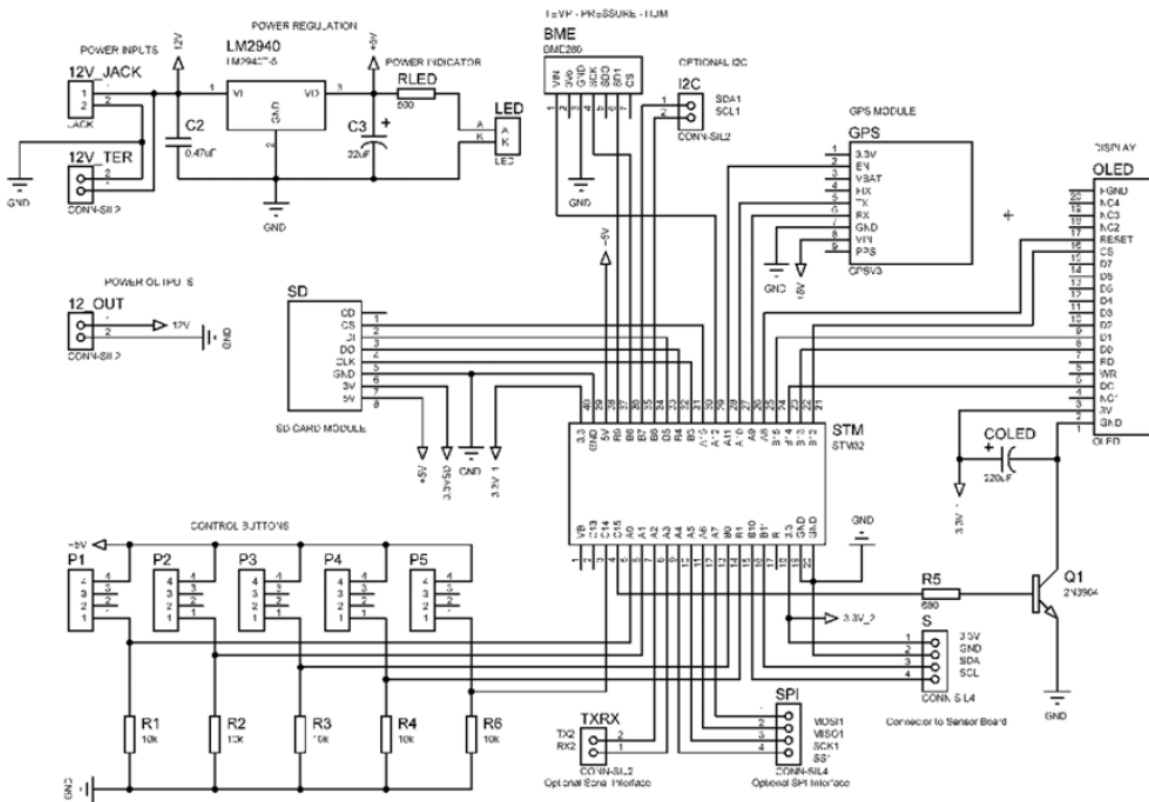


**Figure 2.40: Electrical schematic Handheld sensor- Version I**

As shown in the schematics, the modules we used include:
- LM2940-5 linear voltage regulator with a low dropout voltage of 500 mV, designed to provide an output current up to 1 A. This regulator takes an input voltage up to 26 V and outputs a stable voltage signal of 5 V.

- The BME280 sensor (breakout board provided by Adafruit) measures temperature, barometric pressure, and humidity. In addition to the surface-mount sensor, the board is equipped with a 3.3 V voltage regulator which allows it to be powered directly through the 5 V signal.
- The GPS module (Ultimate GPS breakout provided by Adafruit) is powered directly by the 5 V regulated signal and controlled via a digital pin of the microcontroller (digital pin 2).
- The OLED display is powered by the 3.3 V signal and connected through the microcontroller via SPI connection. An NPN bipolar transistor was used to allow controlling the OLED via software commands.
- The micro-SD breakout board is also provided with a 3.3 – 6 V voltage regulator and a level shifter that allows it to work with different types of microcontrollers.

### 2.4.1.2  Control Unit Version II

After performing several tests and scenarios on the first version of the control unit, we concluded that the STM32 board can work correctly in simple scenarios, but it may not represent a complete and reliable solution for our application. Therefore, and to avoid possible technical problems under real operational conditions, we worked on solving this problem using two strategies. First, we replaced the currently used processor by a more advanced system that is equipped with additional processing and memory capabilities. Second, we worked on optimizing the software design by using an object-oriented methodology to decrease the size and the complexity of the code. In the following sections, we summarize these modifications and describe the second version of the control circuit.

The Teensy microprocessor-based development board provided by PJRC, is a breadboard-friendly development system with advanced processing features. These boards include a 32-bit microprocessor and are pre-flashed with a bootloader. Thus, no additional devices are required for re-programming the modules other than the USB cable. The software for the Teensy modules may be developed using traditional C editors or using the *TEENSYDUINO* add-on, which integrates with the well-known Arduino IDE. We updated the electrical schematic of the control unit to fit the configuration of the Teensy modules. Before implementing the PCB, we tested the connections using breadboards and wires. In addition to the modifications listed above, another electronic module was added to the system to handle the problem of I2C signal attenuation. This module is provided by *Sparkfun* and named the *Differential I2C Converter*. It extends the range of the I2C communication bus by using the NXP's PCA9615 IC. The module works by converting the default I2C signals into four differential signals, two for SCL and two for SDA. The converted signals carrying the digital values corresponding to the voltages measured at each sensing unit are sent over an Ethernet cable with RJ-45 connectors. This allows the I2C signals to reach around 30 m. These modules allowed us to use Ethernet cables between the control unit and the sensing unit with a length of 4.5 meters. Testing of the modules showed that the values were not affected and no delays between the sensing and receiving of the values was recorded.

After performing the necessary initial tests using breadboards and wires, we developed the main control PCB. The schematic of the new circuit is shown in Figure 2.41.
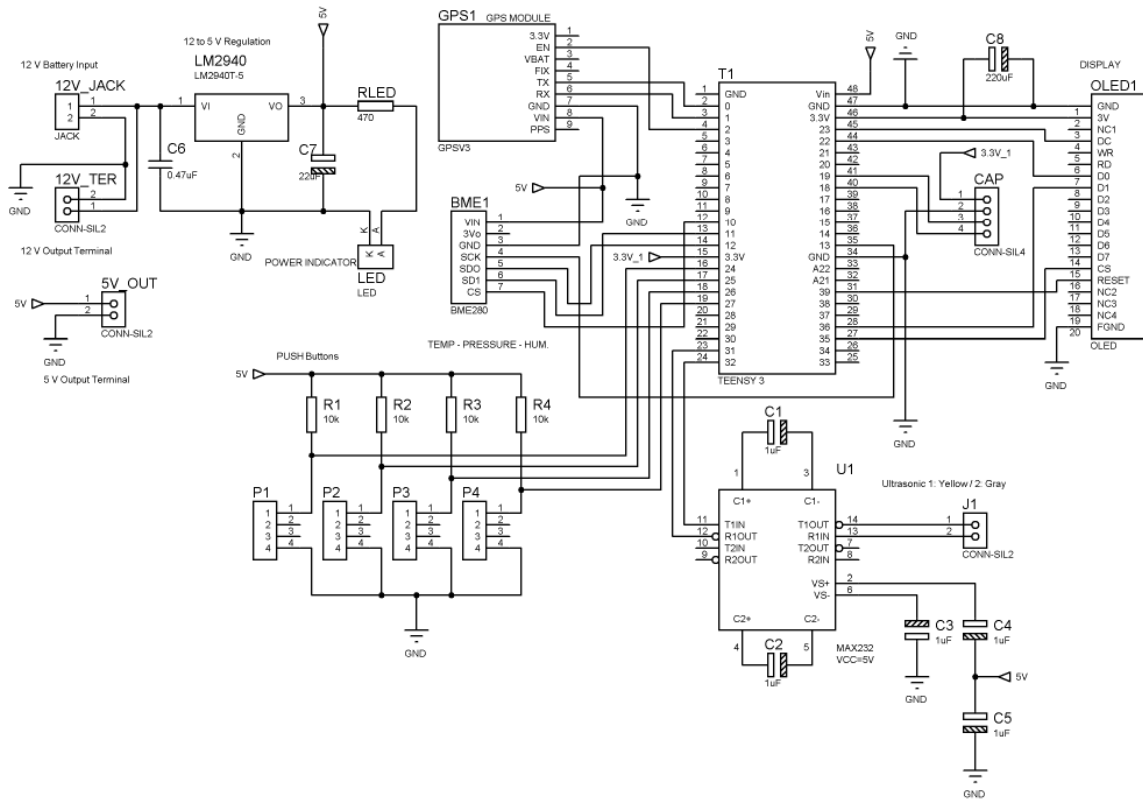
**Figure 2.41: Electrical schematic Handheld sensor- Version II**

After designing the circuit schematic, the corresponding PCB layout was designed using the ARES software package and the board fabricated and assembled. For compactness of the device, we used a double-sided PCB with vias. The 3D model and the implemented board are shown in Figure 2.42.



3D model with components      PCB with components
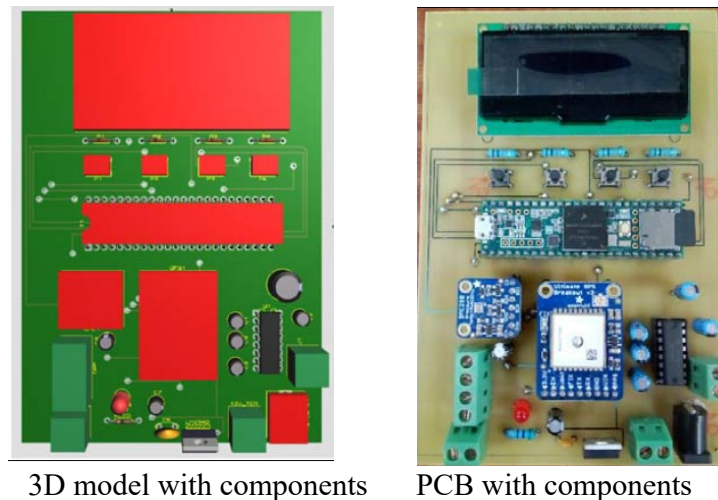
**Figure 2.42: 3D and implemented handheld control unit V2**

### 2.4.1.3 Control Unit Version III

Version III of the control board focuses on optimization of size to have the control board fit inside the new handheld device enclosure. While the length and width of the Version 2 control board were acceptable (about 70x100mm), the thickness was the main issue since a few modules were used (mostly for power) instead of having the circuitry re-designed and fitted on the control board. Another main improvement needed was the reduction of the different peripherals, since wires and cables connecting the board to function buttons, power button and any other peripheral was a problem.

The PCB design is shown in Figure 2.43. The main components that will be installed on the front surface are the screen, buttons, and GPS (which will be kept as a module). The Teensy and the peripheral connectors are the main components installed on the back side of the PCB.
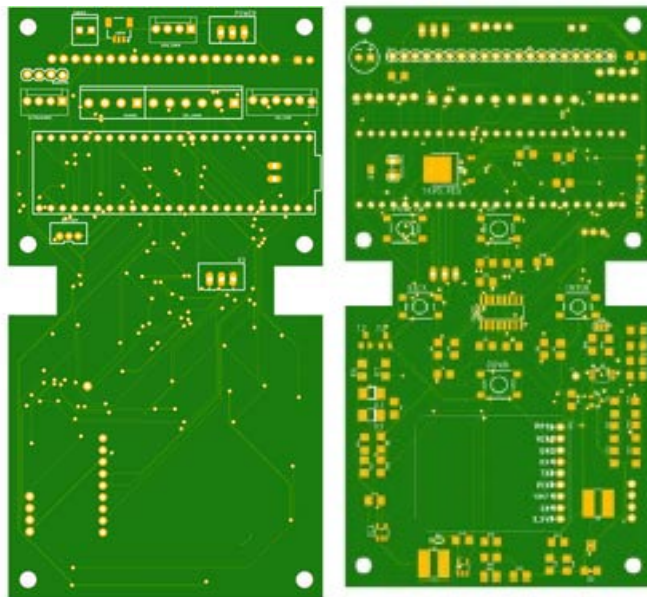


**Figure 2.43: PCB V3 design: Right: Front, Left: Back**

The biggest challenge for the V3 design is the introduction of 3 new circuits: step-down, step-up and I2C differential conversion. The circuits are based on AP3012 step-up boost regulator, TPS62172 step down regulator and the PCA9615 differential I2C converter. The circuits are shown in Figure 2.44 and Figure 2.45.
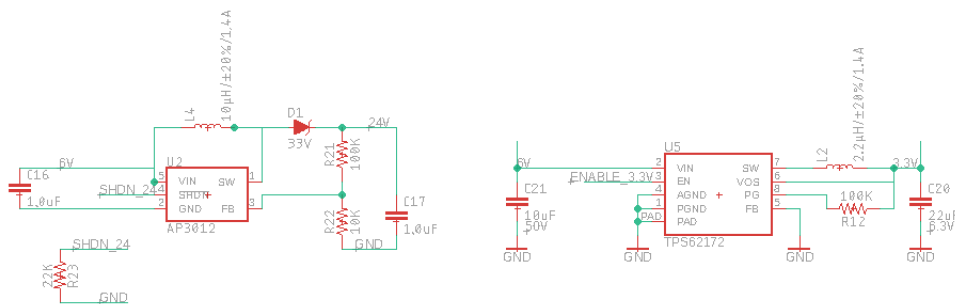


**Figure 2.44: TPS62172 and AP3012 circuits**
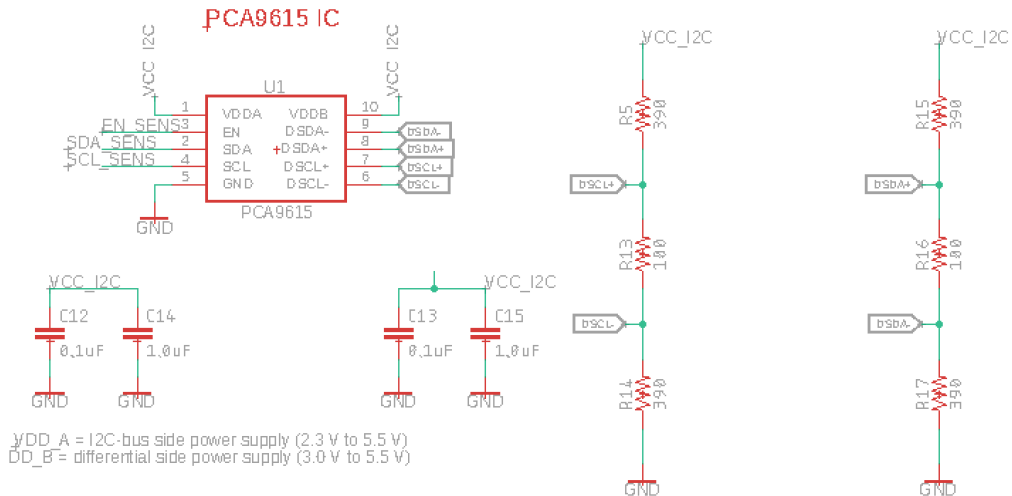
**Figure 2.45: PCA9615 differential I2C converter circuit**

One final change was the elimination of the BME module and introduction of an NTC sensor for temperature. The NTC sensor consumes less power and gives more accurate measurements. In addition, it requires less connection (only two terminals connected in series with another resistor).

The Printed Circuit Board (PCB) for the final handheld package was acquired and assembled, the different parts of the circuit were tested and are fully functional. The different parts of the circuit include a booster circuit, a step-down voltage regulator, I2C to differential I2C converter, RS232 converter, GPS sensor, screen, and temperature sensor circuit. The assembled circuit is shown in Figure 2.46. The peripheral devices connect to the board from the rear side, as shown in Figure 2.47.
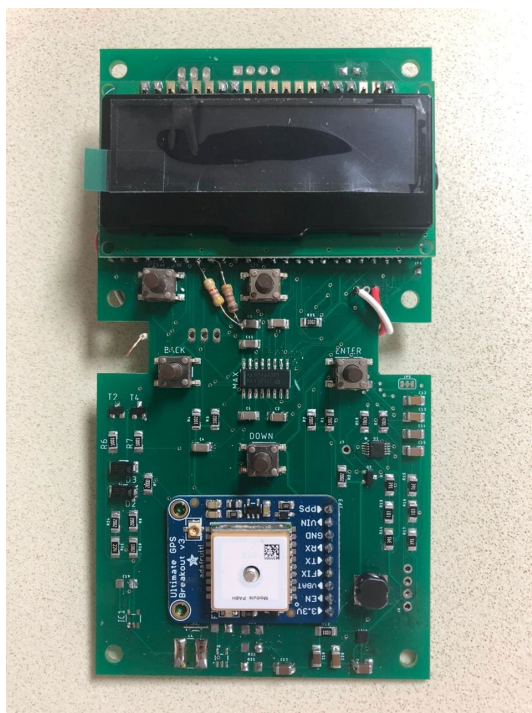
**Figure 2.46: Assembled circuit for handheld device**
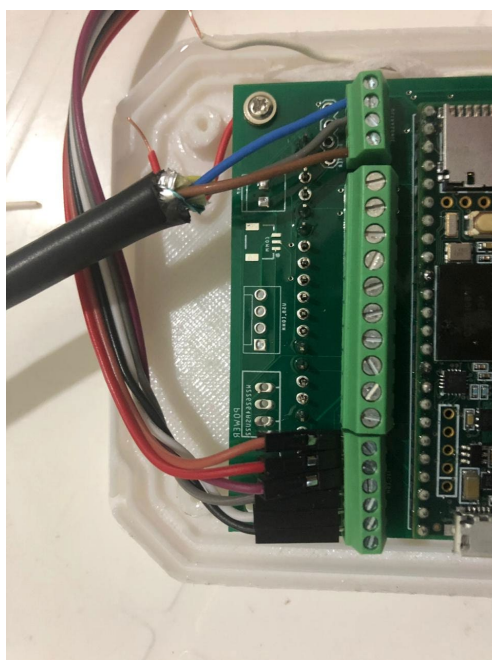


**Figure 2.47: Peripherals connection to handheld device PCB**

### 2.4.2 Skimmer Sensor Control Unit

Several iterations were conducted for the skimmer sensor control unit. We document here the main versions.

### 2.4.2.1 Control Unit Version I

The electrical schematic describing the components and connections of the control unit designed for the skimmer-mount sensor is shown in Figure 2.48. As shown in the schematic, most of the components are like the ones used in the handheld device (described in previous sections). For example, BME280 sensor for ambient conditions, GPS ultimate (Adafruit) for coordinates, MAX232 chip to interface the ultrasonic sensor, and Teensy 3.5 for processing. Note that the OLED screen was removed and the XBEE module was added to allow for wireless communication. The XBEE module was connected to the processor using hardware serial communication Port 1. In addition to the linear voltage regulator used before (LM2940), another regulator was added (LF33ABV) to power the XBEE module by 3.3 VDC signal.
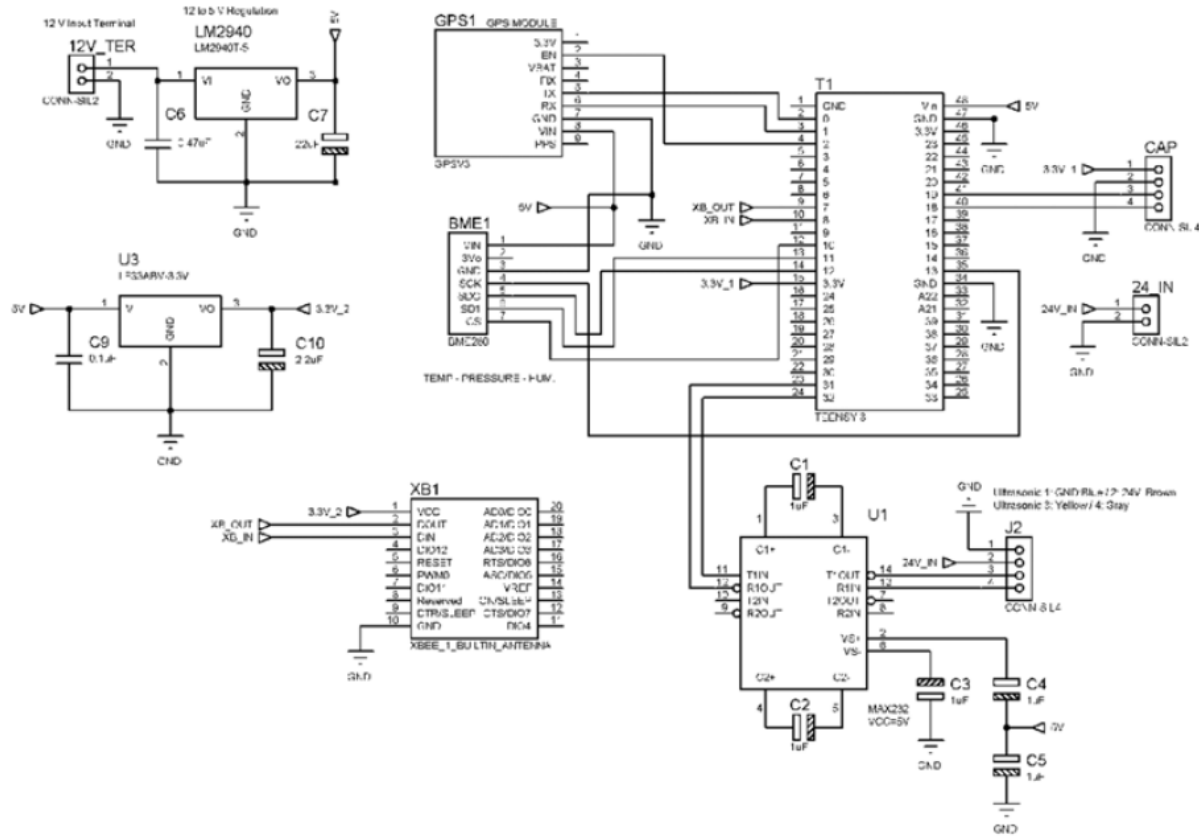


**Figure 2.48: Electrical schematic - Skimmer-mount sensor**

The control circuit was designed using the *Proteus* software and implemented using a double-sided PCB. The 3D model showing the control circuit with the components is shown in Figure 2.49. The implemented PCB with components soldered is shown in Figure 2.50 (control unit left and base station receiver right).
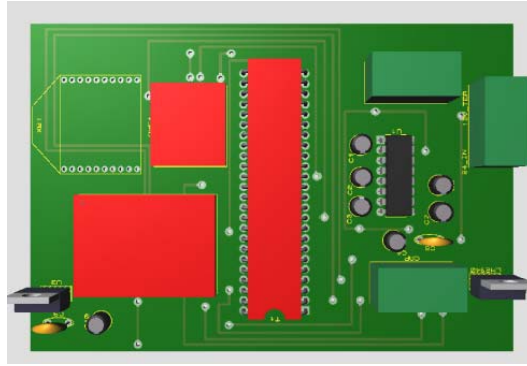
**Figure 2.49: 3D model of the control circuit - Skimmer-mount sensor**

Two XBEE modules were used in the skimmer-mount device. The first module is added to the control circuit that will be embedded inside the package mounted on the skimmer. The second module is integrated with an Arduino microcontroller forming the base station receiver module. In the base station module, the microcontroller reads the values received by the XBEE module and sends them to the PC via serial communication channel.
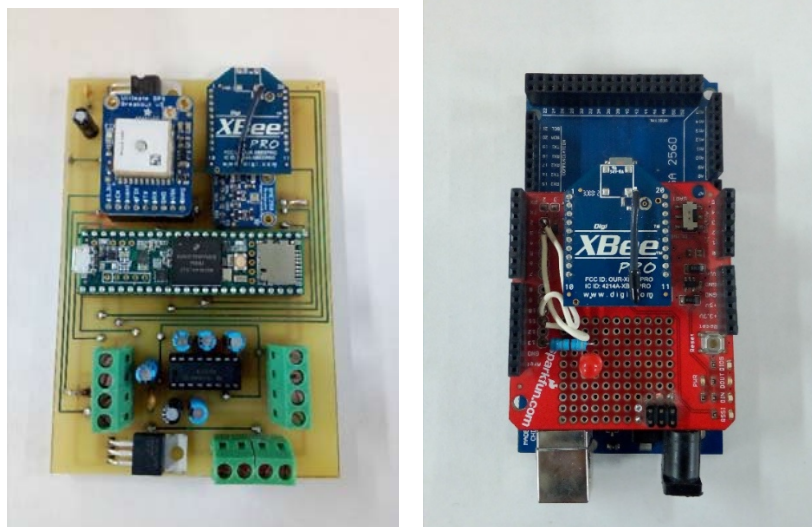


**Figure 2.50: Left: Control circuit for skimmer-mount sensor. Right: Base station receiver module**

### 2.4.2.2   Control Unit Version II

For a first phase of optimization of the PCB, it was important to keep the functionality intact and just improve on the few key factors mentioned in the previous section. It was thus decided to keep the modules and not go into a component level optimization. This enforced an upper limit on the minimum size of the board achievable as modules have their fixed sizes. PCB V2 main components are listed in Table 2-3.

The circuit layout (Figure 2.51) remains mostly unchanged from the previous design. The major addition is the XBee module that would take care of RF communication for the skimmer module. The optimization process led to a smaller footprint for the board, with the dimensions getting to 100x70mm (Figure 2.52 Left PCB, Right 3D model).
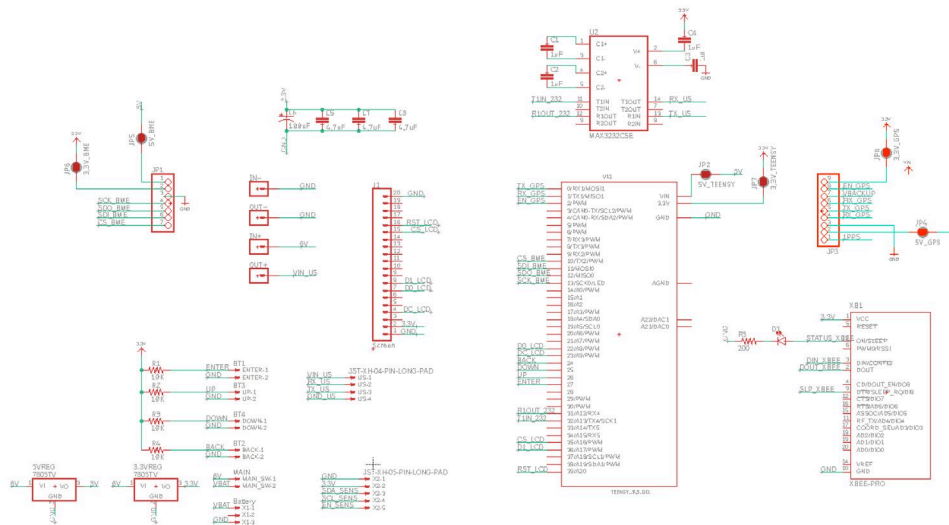
**Figure 2.51: Circuit layout control unit V2**

**Table 2.3 Bill of Materials for the used modules**

| Component name | Description | Picture |
|---|---|---|
| Adafruit ultimate GPS | GPS Breakout Module |  |
| Screen (handheld only) | OLED 2.3inch screen module |  |
| XBee Pro (Skimmer only) | 900mhz XBee RF module |  |
| 3.3V regulator | 3.3V switching regulator module |  |
| 24V voltage booster | DC-DC LM257724 V switching boosting module |  |
| MAX3232 serial converter | TTL to RS232 converter |  |

| | module | |
|---|---|---|
| Connectors | JST connectors for various peripherals |  |
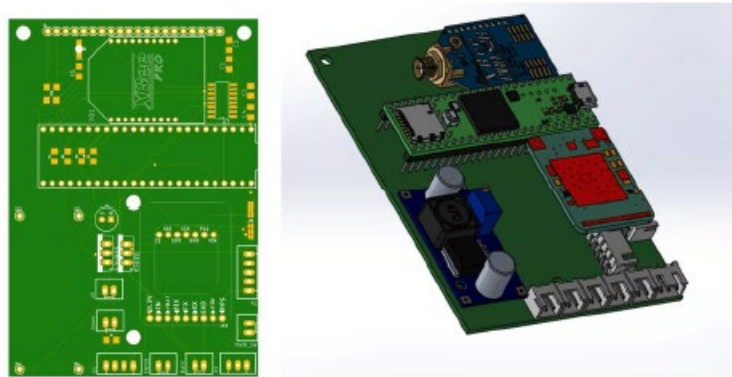


**Figure 2.52: Left: Top side of PCB. Right: PCB with XBee installed (Skimmer)**

The designed PCB was fabricated (Figure 2.53). It is a two-layer board with 1.6mm thickness with clear markings for the components and their sizes. For the first assembly and testing, headers (shown in black in Figure 2.54) for the main components (Teensy, GPS, Screen, XBee) were soldered so the components are not soldered directly to the board just in case they have to be replaced. On the other hand, any peripherals (buttons, connectors, indicators, switches) will be connected through JST XH2.54 low profile connectors.
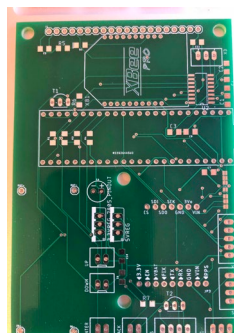


**Figure 2.53: Manufactured PCB (Top)**
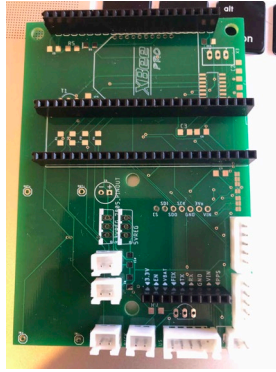
**Figure 2.54: Connectors and headers on PCB**

The final assembled board for the skimmer is shown in Figure 2.55 (Left). Since this board is similar to an earlier handheld design, the same PCB could be assembled with a screen instead of the XBee module as shown in Figure 2.55 (Right).
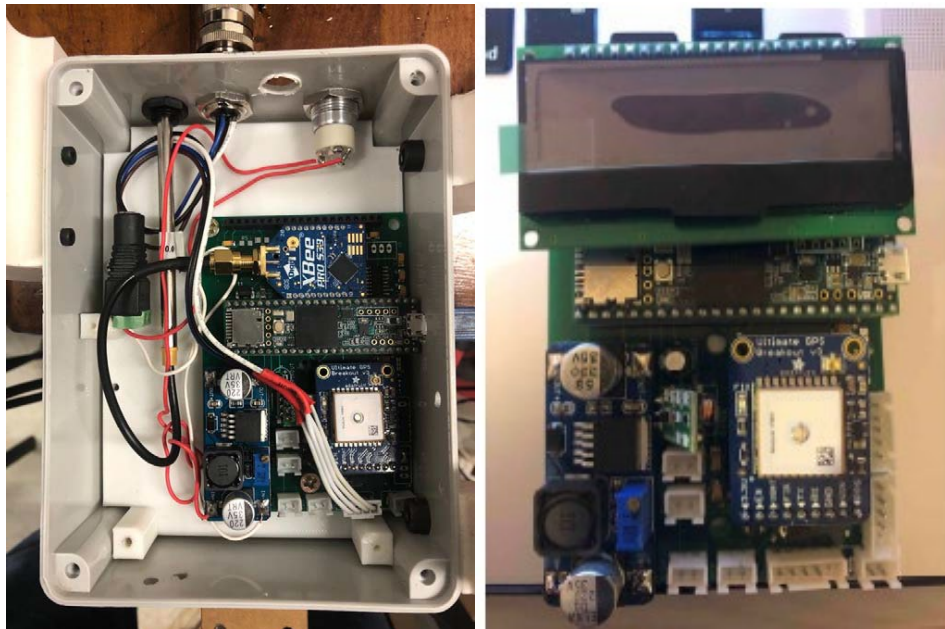


**Figure 2.55: Left: Assembled board for skimmer package, right: Assembled PCB with screen**

## 2.5 Ultrasonic Sensors

In the previous section, we introduced the principle of dual modality sensor and the concept of cooperative sensing between capacitive and ultrasonic sensors. Therefore, after finishing the design of the capacitive sensor and the control unit, the objective was to choose a proper ultrasonic sensor that satisfies both sensors' requirement (power consumption, measurement range, interfacing with microcontroller …).

### 2.5.1 Handheld Ultrasonic

Even though the initially selected ultrasonic sensor (HRXL-MaxSonar-WR) showed good results while evaluated under static and dynamic conditions, one major limitation of this sensor is its large dead-zone distance (approx. 30 cm), which is much larger than the 10 cm target sensing range of the handheld device. Unfortunately, to accommodate this range constraint, a major modification to the handheld device packaging would be required, such that the ultrasonic sensor would be mounted with an offset distance larger than 30 cm from the capacitive sensor. To avoid this issue, we searched for other ultrasonic sensors with smaller dead-zones and could fit our application. As a result, we selected the ultrasonic range/level sensor named ToughSonic 3 Level & Distance Sensor (TSPC-30S2 Series) provided by Senix Corporation (Figure 2.56).



**Figure 2.56: ToughSonic 3 - Close-range ultrasonic range/level sensor**

The main technical specifications that guided the search were:
- Short sensing range (less than 1 meter),
- No or very limited dead-zone distance (less than 5 cm),
- Narrow ultrasonic beam (to avoid interference with surrounding objects),
- High measurement resolution (less than or about 1 mm),
- Digital interface (to communicate reliably with the microcontroller),
- Low power consumption (suitable for battery-operated devices),
- Industrial-rated packaging (IP67/68).

In order to allow the microcontroller to read the measurements from the ultrasonic sensor, an RS232-TTL converter is required. For this purpose, we tested two modules based on the MAX232 chips: a commercially available board and a custom-made conversion circuit equipped with a MAX232 chip and a set of 1 uF capacitors. As a result of these tests, the two configurations were successful in allowing the sending and receiving of the distance measurements at a low period of 50 msec (high frequency). We decided to integrate the MAX232 conversion circuit with the circuit of the control unit to avoid adding external components to the system.


### 2.5.2 Skimmer Ultrasonic

Since the skimmer-mount sensor has an extended sensing range and is expected to work under harsh and splashing conditions, we selected another ultrasonic sensor provided by Senix named ToughSonic 12 (Figure 2.57). This sensor is protected with chemical resistant PVDF material and has the same dimensions of the handheld ultrasonic sensor ToughSonic 3. The maximum range is around 3.7 meters, and the optimum range is 2.1 m. This was considered suitable for the

skimmer-mount application since our maximum sensing range is 50 cm and the measured ultrasonic distance is not expected to exceed 1.5 m. The sensor has a high resolution of 0.086 mm and provides a digital output using an RS232 interface. In addition to the sensing range, this sensor differs from the handheld sensor by having an increased dead-zone of 76mm. However, in our experiments we found that the measurements became unstable below a distance of around 10 mm. This was considered in the mechanical package design where an empty distance of 11mm is provided inside the package to handle the dead-zone issue. The sensor was tested against water and oil surfaces and showed reliable and repeatable measurements beyond the dead-zone range.
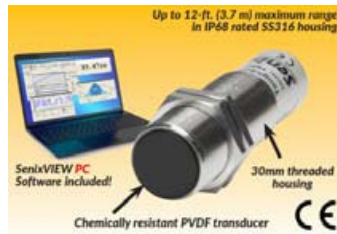


**Figure 2.57: ToughSonic 12 ultrasonic sensor for skimmer-mount device**

### 2.5.3 Calibration of Ultrasonic Sensor

The distance between the ultrasonic sensor and first pad of the capacitive sensor should be obtained through calibration, which is scheduled once after manufacturing, and saved in the software to be used by the measurement algorithm. For this purpose, we recorded a set of measurements while the skimmer-mount sensor was mounted on the experimental setup and oil was added to the water container to reach the top edge of the first sensing unit in the capacitive sensor. Based on this criterion, the average of the measured distances represents the offset distance used in the algorithm of oil thickness estimation described before. The results of this experiment are summarized in Table 2-4.

**Table 2-4: Skimmer-mount Testing – Ultrasonic calibration results**

| | |
|---|---|
| **Average Measured Distance (mm)** | 115.32 |
| **Standard Deviation** | 0.053 |
| **Count of measures** | 3185 |
| **Maximum measured distance (mm)** | 115.44 |
| **Minimum measured distance (mm)** | 115.18 |

In addition to the importance of measuring the offset distance using the ultrasonic calibration experiment, these results showed the stability and accuracy of the measurements obtained by the new ultrasonic sensor (ToughSonic 12). Note that the actual distance as measured visually by a measuring stick was approximately 115 mm. This experimental result was very important because it showed that the measurements of the ultrasonic sensor were not affected by the body of the new package as the sensor is buried inside the package at a distance of 11 cm.

## 2.6  Power Calculations and Battery Units

From the requirements' sheet for the handheld device, the full battery set provides at least 5000 measures and will be equipped with a low power indicator. The device's batteries will be standard off-the-shelf batteries. From the requirements' sheet for the skimmer device, the full battery set is estimated to provide 3 days of continuous measures.

### 2.6.1  Power Budget

To calculate the power budget for the current prototypes, a current meter was used to estimate the current values in milliamps. The different modules (GPS, screen...) were removed from the circuit to calculate their current consumption. The results are tabulated in Table 2-5.

It is worth noting that the figures for power consumption in the table are for continuous readings of around 10Hz, thus no sleep functions are used on any of the elements in the system. This will not be the case with the final device, where these values will be lower once the power consumption is optimized. Nevertheless, to meet the battery life requirements, these values where useful to set a benchmark for the battery usage calculations and choice of battery.

**Table 2-5: Power consumption of different modules in the system**

| Element | Voltage (Volts) | Approx. Current (Sleep or idle) (Amps) | Approx. Current (when functional) (Amps) | Skimmer Power (Watts) assuming all circuits are functional | Handheld Power (Watts) assuming all circuits are functional |
|---|---|---|---|---|---|
| Ultrasonic | 20 | 0.005 | 0.025 | 0.5 | 0.5 |
| Circuit with sensing board (Without Screen and GPS) | 5 | 0.04 | 0.11 | 0.55 | 0.55 |
| Screen | 5 | 0.005 | 0.01 | 0 | 0.05 |
| GPS | 5 | 0.02 | 0.04 | 0.2 | 0.2 |
| Wireless Communication (While sending data) | 3.3 | 0.025 | 0.32 | 1.056 | 0 |
| | | | **Total Power (Watts)** | **2.306** | **1.3** |

### 2.6.2  Battery Life – Low Power Modes and Sleep Functions

Since the current system has a relatively high-power consumption, it is worth analyzing the sleep functionality of the different elements and calculate the expected battery life based on the scenario of having the system sleep between readings and wake up to read from the sensors and transmit or show the data on a screen.

Based on values found in a datasheet for the different components in the device, Table 2-6 was developed. It is clear that when a lower frequency of readings is needed (especially in the case of the skimmer and the handheld device single reading mode), it is possible to have most of the elements sleep between the readings. This will reduce the power consumption by 35% for the

handheld device and 60% for the skimmer device. It is worth noting that the scenario in Table 2-6 is a conservative one and most components are ON 50% of the time for the handheld device and 20% of the time for the skimmer device.

The analysis above shows that the reduction in the frequency of readings will result in an improved battery life especially with the skimmer (>50% improvement) and the handheld device in single reading mode (>30% improvement).

**Table 2-6: Simulated scenario for average power consumption**

| Element | Voltage (V) | Approx. Current (Sleep or idle) (A) | Approx. Current (when functional) (A) | Skimmer % of time ON | Handheld % of time ON | Skimmer Average Power consumption (W) | Handheld Average Power consumption (W) |
|---|---|---|---|---|---|---|---|
| Ultrasonic | 20 | 0.005A | 0.025A | 50 | 50 | 0.3 | 0.3 |
| Circuit (W/out Screen & GPS) | 5 | 0.04A | 0.11A | 20 | 50 | 0.27 | 0.375 |
| Screen | 5 | 0.005A | 0.01A | 0 | 50 | 0.0 | 0.025 |
| GPS | 5 | 0.02A | 0.04A | 5 | 5 | 0.105 | 0.105 |
| Wireless Comm. | 3.3 | 0.025A | 0.32A | 5 | 0 | 0.131175 | 0.0825 |
| | | | | **Total Average Power (Watts):** | | **0.831175** | **0.9** |

### 2.6.3  Testing of Skimmer Power

The main controller board was tested with 4xAA batteries; the different power related parameters were measured along with the time since the start of the experiment. A LabVIEW data logging software was developed that reads every 5 seconds and exports the data to a spreadsheet.

The measurements were as follows:
- Time since the start of the experiment (seconds)
- Current at battery pack (mA)
- Battery voltage (Volts)
- Boost circuit output Voltage (Volts)

The experiment stops when the boost voltage (that provides power to the ultrasonic sensor and the rest of the circuit) drops below the minimum voltage (12V) of the ultrasonic sensor. Instantaneous power consumption calculation is done by multiplying the current out of the batteries and the voltage of the batteries.

$$Power(Watts) = Battery\ Voltage(Volts) \times Battery\ Current(mA)/1000$$

The cumulative energy consumption (in Wh) is calculated as:

$$Energy\ (Wh) = \int_0^{time} Power(Watts)$$

Given that data is being read every 5 seconds, the energy consumption can be calculated as:

$$Energy_t(Watts) = Energy_{t-1} + 5/3600 \times Power(Wh)$$

The battery voltage (Volts) vs time (seconds) is shown in Figure 2.58. It is known for AA alkaline batteries that they start dropping their voltage very quickly but the decrease in voltage gets gradually smaller for the same load. The batteries started at around 5.7 volts and dropped to around 3.1(~0.8V per battery) at the end of the experiment.
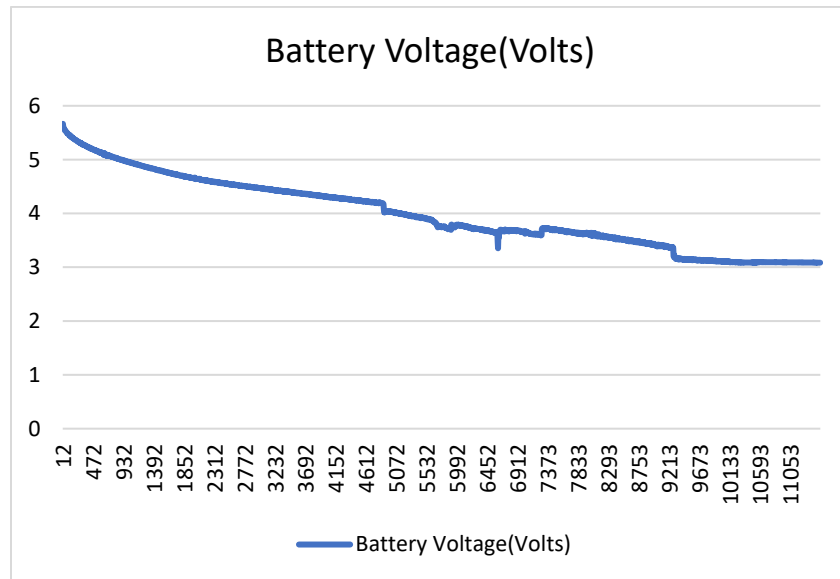


**Figure 2.58: Battery Voltage(volts) vs Time(s)**

The battery current consumption (mA) is plotted versus time and shown in Figure 2.59. Given the presence of the switching boost regulator, the current consumption increases as the battery voltage decreases with time.

66
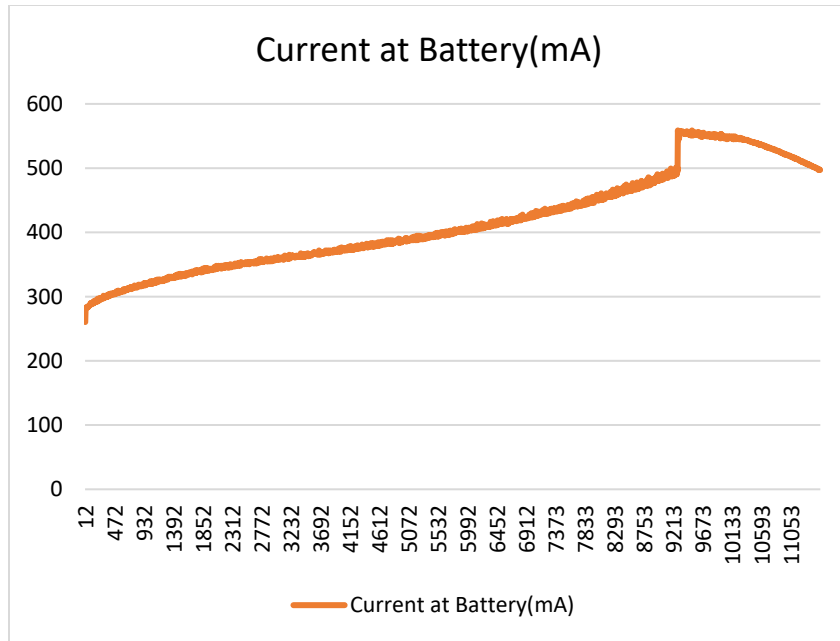
**Figure 2.59: Battery Current(mA) vs Time(s)**

The power consumption of the circuit with all components in an ON state is approximately 1.6W. The switching boost regulator consumes more current for a dropping voltage in an attempt to deliver the required power consumption. Thus, we can see very little change in the power consumption as time passes and battery voltage drops. The graph is shown in Figure 2.60.
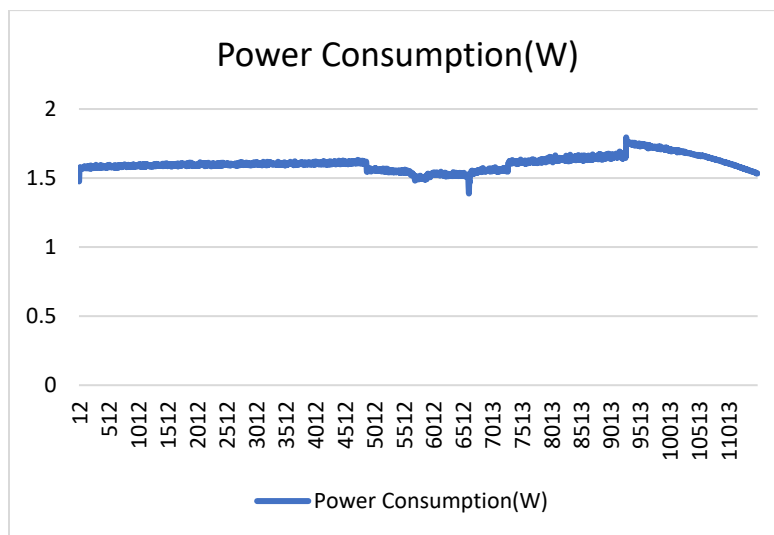


**Figure 2.60: Power consumption (Watts) vs Time(s)**

The batteries used in the experiment were 4 x alkaline Energizer industrial batteries. These batteries have a different capacity value depending on the current consumption, datasheet provides a bench line capacity value for different current consumption scenarios.

In the experiment, the current consumption is variable along with a reduced voltage with time. The batteries died after about 5.1Wh of energy dissipation. It took approximately 3 hours 15min before the experiment stopped. The batteries were not fully depleted then, but the threshold voltage of the boost regulator was reached. Theoretically, with an average current consumption of about 400mA the capacity of the battery is around 1600mAh. This results in approximately 4 hours of battery time, which is not very far from the experimental value.

During the 3h 15min, data was being read at around 10Hz, which results in about 117,000 readings. Thus, turning the different power consuming components off while not in use can be a key for an improved battery life. The main battery drainage sources are the GPS (about 0.3W) and the ultrasonic sensor (about 0.8W).

After performing these tests and power calculations for the whole circuit, we reached a conclusion that the battery unit for the handheld sensor should be composed of at least 4 AA batteries connected in series, while the skimmer device should include at least 6 AA batteries (package shown in Figure 2.61).
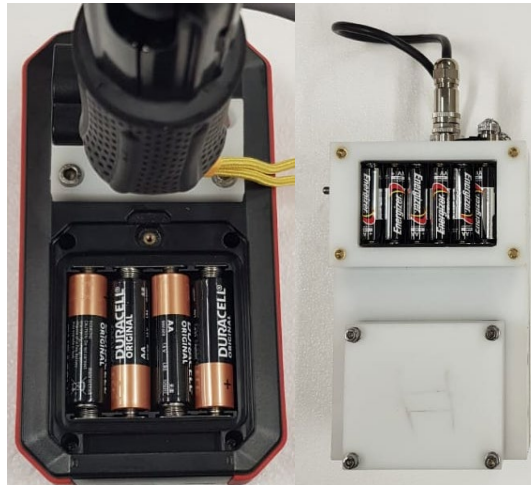


**Figure 2.61: Battery Units (Left: Handheld, Right : Skimmer).**

## 2.7  Wireless Communication

One of the requirements of the skimmer is to be able to send the readings from the oil thickness and from the other sensors to the base station. To achieve this reliably, Xbee Pro modules were tested. The biggest advantage of these modules is their capability to work in different modes (Mesh or Star configuration), on different channels and different frequency ranges, thereby avoiding interference.

As shown in Figure 2.62, a major advantage of Xbee modules is the common footprint of the different modules. While power ratings, antenna specifications, and even sizes are different, the electronic footprint is the same (modules are Pin-for-Pin compatible). This presents a considerable advantage as different transceiver modules could be switched in a very short time without any soldering and/or programming. Most Xbee modules operate at 2.4GHz but some

models operate at 900MHz, this is an advantage, as 2.4GHz devices have a chance of facing interference. 900MHz devices can be a quick replacement in these circumstances.
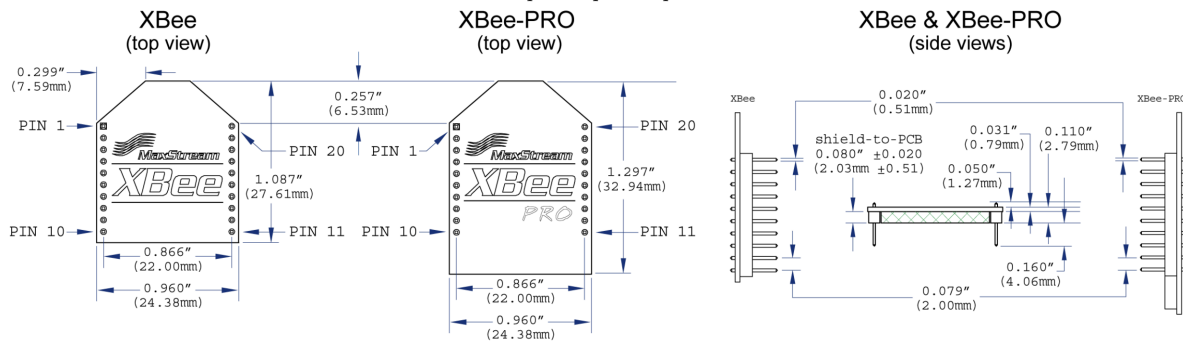


**Figure 2.62: Xbee and Xbee Pro sizes and footprint**

Table 2-7 shows the major differences between the different Xbee modules (Xbee pro vs Xbee vs Xbee 900).

**Table 2-7: Comparison of different Xbee models**

| Xbee Model | Outdoor Range | Max current consumption at 3.3V | Frequency | Networking Topologies | Power | Data rate |
|---|---|---|---|---|---|---|
| Series 1 1mW | 300 ft | 50mA | 2.4GHz(Software configurable channels) | Point-Point | 1mW | 250kbps |
| Series 1 (Pro) 60mW | 1 Mile | 215mA | 2.4GHz Software configurable channels) | Point-Point | 60mW | 250kbps |
| Series 2 (Pro) 50mW | 1 Mile | 295mA | 2.4GHz Software configurable channels) | Zigbee Mesh | 50mW | 250kbps |
| Series 3 250mW 900Mhz | 4 Miles | 229mA | 902-928MHz (Software configurable) | DigiMesh, Point-Point | 250mW | 200kbps |

.

Xbee Pro Series 1, configured as Point-Point, was tested. Xbee USB explorer is a serial base unit for Xbee modules and was used as receiver.

The test results are shown in Figure 2.63. The test comprised three phases:
**Phase A (Start - 11:56):** User moved with a car from approximately 20 meters to 220 meters from base. A few trees were obstructing the line of sight between the antennae.
**Phase B (11:56-11:57:15):** User moved with a car from approximately 220 meters distance to base to 20 meters. A few trees were obstructing the line of sight between the antennae.
**Phase C (11:57:15-End):** User moved from approximately 20 meters to 250 meters and back to 50 meters. A few cement walls were obstructing the line of sight.

In Phase A and Phase B, the RSSI drops with distance (From -60dBm to -95dBm) but the reliability of the connection is 100% throughout the test. In Phase C, the RSSI dropped due to the multiple obstacles, which caused a drop in the reliability of the connection. The connection is reliable for the range needed and with the few obstacles expected.

**Figure 2.63: Xbee Pro S1 range test results**

## 2.8 Temperature Testing

To assess the impact of low temperature on the device, an experiment was conducted where the handheld sensor was placed inside a fridge (Figure 2.64) at approximately -20 degrees Celsius as ambient temperature. To make conditions even tougher for the system, the HMI and the sensor package were not fully assembled so the low temperatures reach all components of the system. The temperature was recorded using the onboard temperature sensor and the capacitive touch sensor's readings were recorded.

The system was left to "freeze" until the temperature sensor read approximately -20 degrees Celsius and then the system was left to "defrost" outside the freezer until the recorded temperature was close to the room temperature of about 26 degrees Celsius. All elements of the circuit were fully functional throughout the experiment.

Figure 2.65 shows the raw readings from the capacitive touch sensors versus the temperature readings. It was noticed that most of the sensors had minimal change in the reading (most had less than 10% difference) and that is due to the mist inside the freezing compartment. It was also noticed that probe 7 had a drop from about 500 to zero (and back to 500 when the system was defrosted) This is due to a droplet of water freezing on the probe. It was also observed that the ultrasound sensor measurement did differ a few millimeters between the two extreme temperatures. To resolve this issue, we enabled the temperature compensation feature on the ultrasound sensor.

70
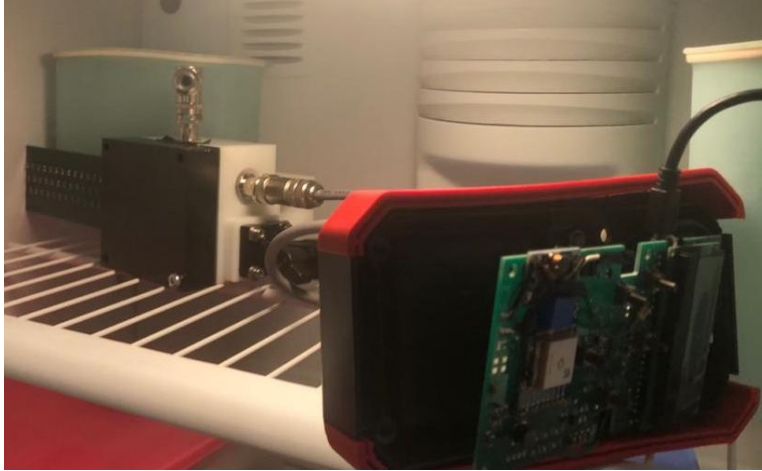
**Figure 2.64: Handheld system in freezing conditions.**



**Figure 2.65: Capacitive touch values vs temperature.**

## 2.9   Packaging Design

This section summarizes the work done on the packaging design and implementation of the handheld package and the skimmer package. The handheld device consists of a sensor package, control unit enclosure (HMI), and attachments (gooseneck or telescopic pole), while the skimmer package only has a sensor package.

### 2.9.1 Handheld Control Unit Enclosure (HMI)

Several designs and prototypes were developed for the handheld control unit enclosure. The first enclosure, shown in Figure 2.66, had a transparent plexi plate glued to the package cover to protect the screen and waterproof it. Four plastic cylinders were manufactured to give access to the board buttons, which were not waterproof. The second iteration is shown in Figure 2.67.



**Figure 2.66: First iteration handheld enclosure**
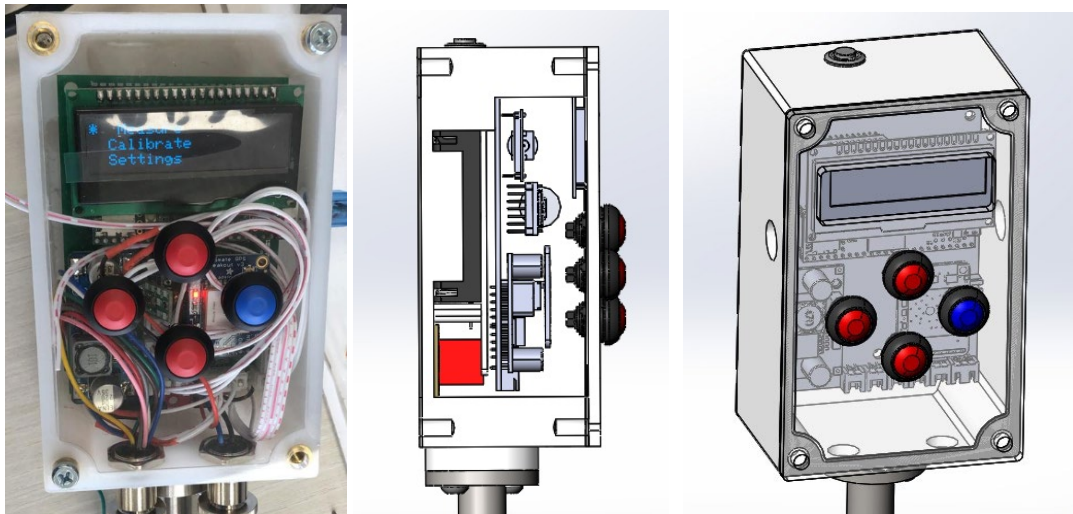


**Figure 2.67: Second iteration handheld enclosure**

The final enclosure that was chosen was a customizable off-the-shelf IP67 enclosure. The front cover has 6 holes where the custom designed version 3 of the control unit board will be fixed (Figure 2.68).
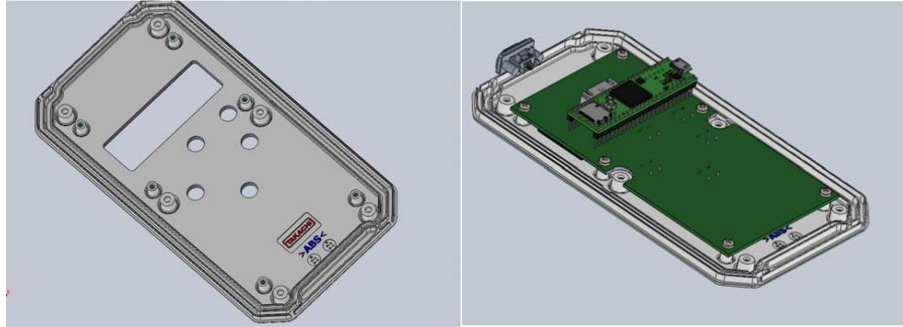
**Figure 2.68: Left: IP67 enclosure cover, right: PCB Version 3 fixture to enclosure**

The 3D model of the handheld device's enclosure was 3D printed as a draft to test the PCB, screen and buttons positioning and assembly. As seen in Figure 2.69, the board fits well in the casing along with the screen and buttons.



**Figure 2.69: Handheld enclosure with assembled PCB**

The biggest advantage of using this enclosure is the fact that the buttons can now be surface mounted on the board, and the user can press those buttons through the cover. In the same manner, the power button can now become a long push button that will turn the system on and the processor itself can turn itself off preventing battery drain when system is left turned on and on standby for a long while.  The USB connection (programming and communication) of the system will be through a special IP67 Micro USB connector, provided by Amphemol (Figure 2.70). The enclosure also contains a 4xAA battery pack.

**Figure 2.70: Top view of the handheld enclosure showing USB socket and temperature sensor**

We equipped the front side of the enclosure with screen protection to avoid scratches and guarantee readable measurements. The screen protection was chosen after testing different types of material. The final enclosure is shown in Figure 2.71.



**Figure 2.71: 3D and manufactured handheld enclosure**

### 2.9.2 Handheld Sensor Packaging and Configurations

The sensor package has all the sensing components inside it. Main components are the capacitive sensor and the ultrasonic sensor. The objective was to develop a package that has the following features:

- waterproof (Ingress Protection targeted at IP67): the main challenge of the package is to be waterproof, thus the inlets and outlets from the package need to be minimized,
- lightweight: since the sensor package could be attached to a pole extended up to 3 meters, the weight of the package must be minimal for easier operation,
- compact size: the device has several modes of operation; it can be either mounted on the telescopic pole or held in hand for lab testing. So, optimizing the package size will make it easier to operate.

Several design iterations were done, where we highlight here only the main ones. Package R01 (Figure 2.72) consisted of two chambers (separated from the inside) and two covers. The left chamber had the capacitive sensor and some electrical components, while the right chamber had the ultrasonic sensor. The process of preplacing the sensors in this iteration is not easy (8 screws

74

for the capacitive sensor, and 4 screws for the ultrasonic), also it had many inlets and outlets, which made waterproofing more difficult. This design was not prototyped.
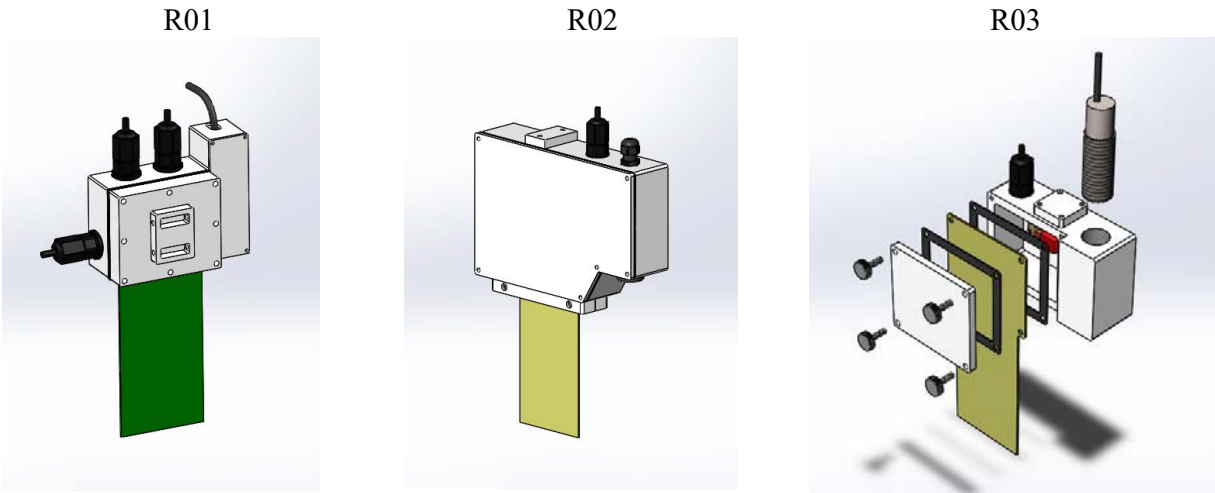


**Figure 2.72: Handheld sensor package design iterations**

Based on the reviews on the first iteration, R02 sensor package was designed and implemented. The main modifications were:
1. combining the two compartments into one,
2. reducing the four cable outlets to two,
3. raising the ultrasonic sensor distance from the bottom of the package to prevent it from measuring inside its dead zone (less than 5cm),
4. changing the package mounting to the top side to simplify assembly,
5. modifying the sensor installation, such that it is installed without the need to open the main side of the package. This new design will make it faster to install and will protect electrical components inside the package,
6. adding an adaptor for the ultrasonic sensor. With this new design, both connections are plug-and-play, and changing cables of different lengths does not require disassembling.

The package was 3D printed and tested. Waterproofing was an issues since it had a lot of screws and seals which made the handling hard. Screw threads in the package were damaged after several tests. Package was lightweight but the size was large and not easily handled.

Package R03 had outside dimensions much smaller than the previous iteration. Replacing both the capacitive sensor and the ultrasonic sensor was easier and faster. The need for initial calibration was eliminated due to the accurate installation of the sensors. The ultrasonic sensor had a fixed distance of 5 cm from the bottom of the package. This protected the sensor from any possible damage due to a physical collision and ensured all sensor measurements are valid (not in the sensor's dead zone).

2mm rubber seals were initially used for waterproofing but proved not to be properly sealed. The softness of the seals required high forces to seal properly, and 4 screws were not sufficient to compress the seals. A new type of seals was selected (Fel-Pro 3025) that is used as a gasket for

car pumps (Figure 2.73). The seal has a thickness of 1mm and requires much less force to tighten. After installing the new seals, a 30-minute underwater test was performed, and no leakage was detected.
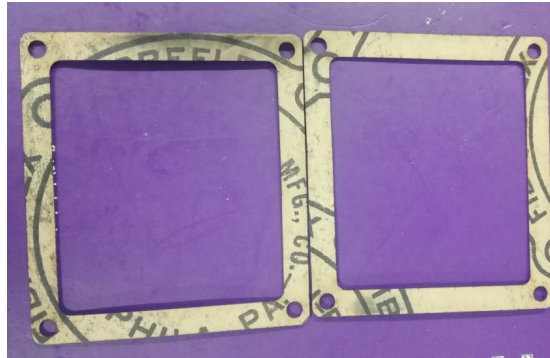


**Figure 2.73: Fel-Pro 3025 seals**

After several times tightening the knobs, the thread in the package was damaged. So, a different method was implemented to solve this problem. The threaded knobs were replaced with female knobs, and 4 stainless steel M6x70 bolts were installed from the backside of the package as shown in Figure 2.74. This solution would simplify the replacement of the sensor since the bolts would also be used as guidance for the installation of the seals.
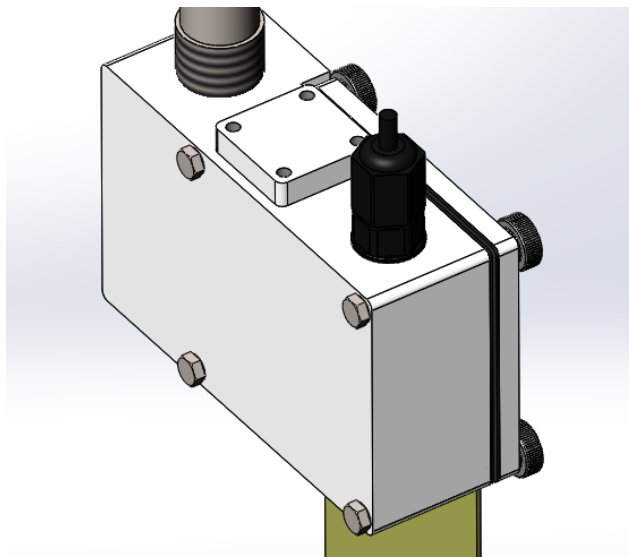


**Figure 2.74: Seals tightening upgrade**

After several adjustments, we reached the final package design shown in Figure 2.75. This configuration is the direct handheld mode where the control unit enclosure is connected to the sensor package via an adjustable gooseneck support. This provides several degrees of freedom for adjusting the positions of the sensor and control unit.

**Figure 2.75 Images for the final handheld sensor package**

In addition, a circular surface-mount level (Figure 2.76) was added on the handheld package cover to help the operator align the ultrasonic sensor. This improved the results taken since the error from the ultrasonic inclination would be minimized.
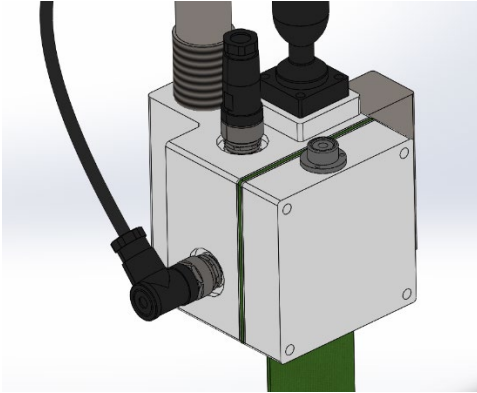
**Figure 2.76: Circular level mounted on the handheld sensor pacakge.**

Two additional configurations for operation were also designed and fabricated: pole and floating configuration. To switch from lab to pole configuration (Figure 2.77), the operator will do the following**:**

1. unplug the sensors connector,
2. disconnect the gooseneck support,
3. attach the gooseneck support to the pole,
4. plug the sensors connector to the cable extension,
5. attach the sensor package at the end of the pole.

This will allow the operator to alternate between the two configurations. It is worth mentioning that for short/mid-range applications, the operator can use the pole in retracted position.

After several tests done in the lab, it was concluded that the angle of sensor inclination will affect thickness measurement. This will impact the results especially when the pole is extended since the operator cannot precisely see the level. So a floating accessory shown in Figure 2.78, was designed to minimize the effect of misalignment.

The weight of the accessory alone is approximately 1.2 kg, and the total weight of the package including the floater attached is 2.1 kg. 3x130 mm diameter PVC floaters were used to give a total buoyant force of 33 N (equivalent to ~3.4 kg). Approximately 60% of the floaters will be submerged, thereby making the point of contact between the sensor and the water surface at the middle of the sensor length.
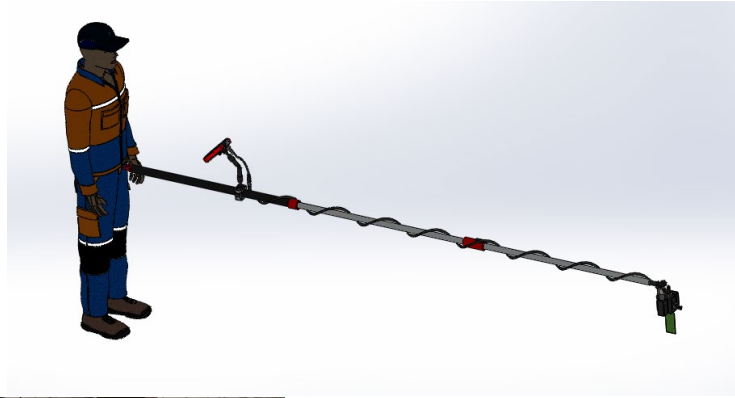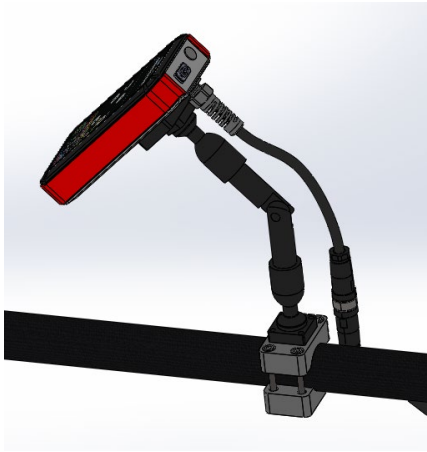
**Figure 2.77: Handheld control unit and sensor mounted on the pole**



**Figure 2.78: Floating configuration for the handheld sensor**

### 2.9.3　Skimmer Sensor Packaging and Configurations

The skimmer sensor packaging also went through several phases. Two of the main phases are shown in Figure 2.79. The final skimmer sensor package is shown in Figure 2.80. The disassembled package shown has four openings at the top and one on the side. The top openings are (from left to right) the external power connector, the ultrasonic sensor connector, the USB connector, and the ON/OFF button. The opening on the right is the waterproof temperature sensor.
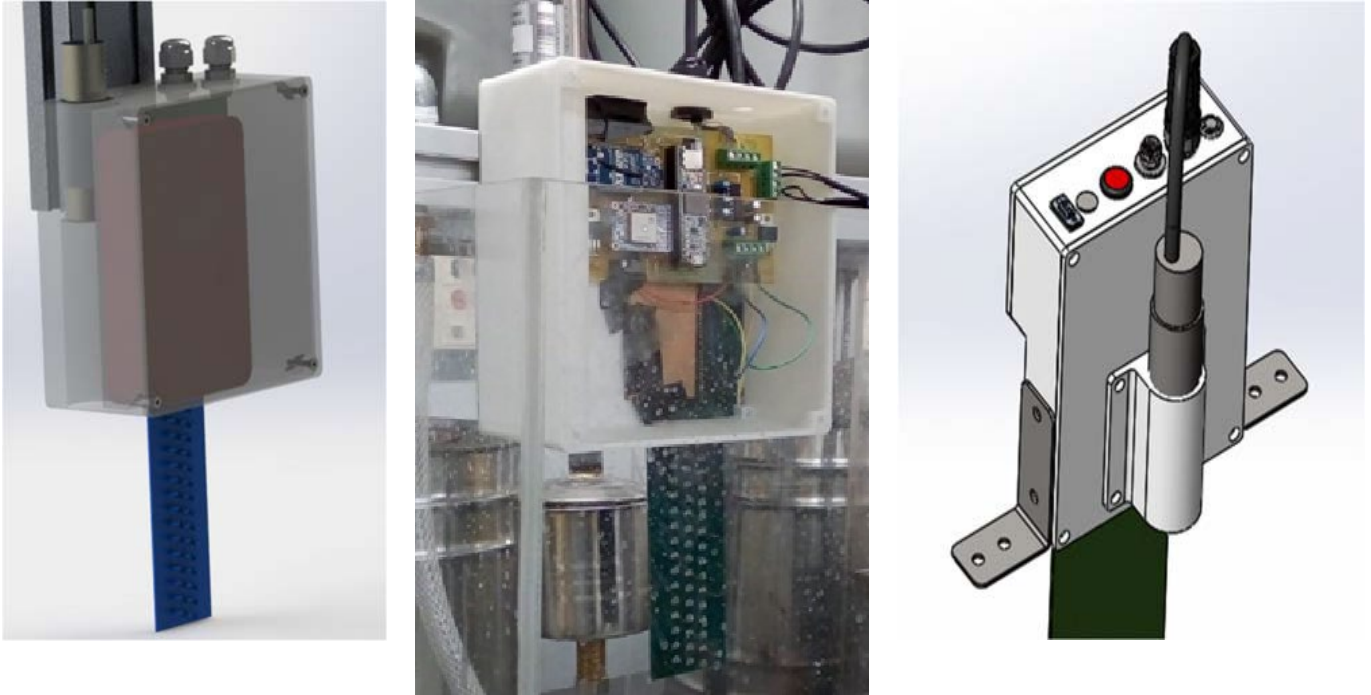


**Figure 2.79: 3D representation and real skimmer sensor**

The skimmer package manufacturing had to be divided into several steps to prevent any damage to the body. Given that the surfaces where the seals are located should be flat and smooth, after installing the heat inserts, the surface had to be machined again to remove any additional material. The process of smoothening the surface was previously done after all the machining was complete. This time, the heat inserts were inserted at the beginning (Figure 2.81) and all the milling was done afterwards. This ensured that no damage is done to the final package. Different views of the final assembled skimmer sensor, with and without the cartridge, are shown in Figure 2.82.
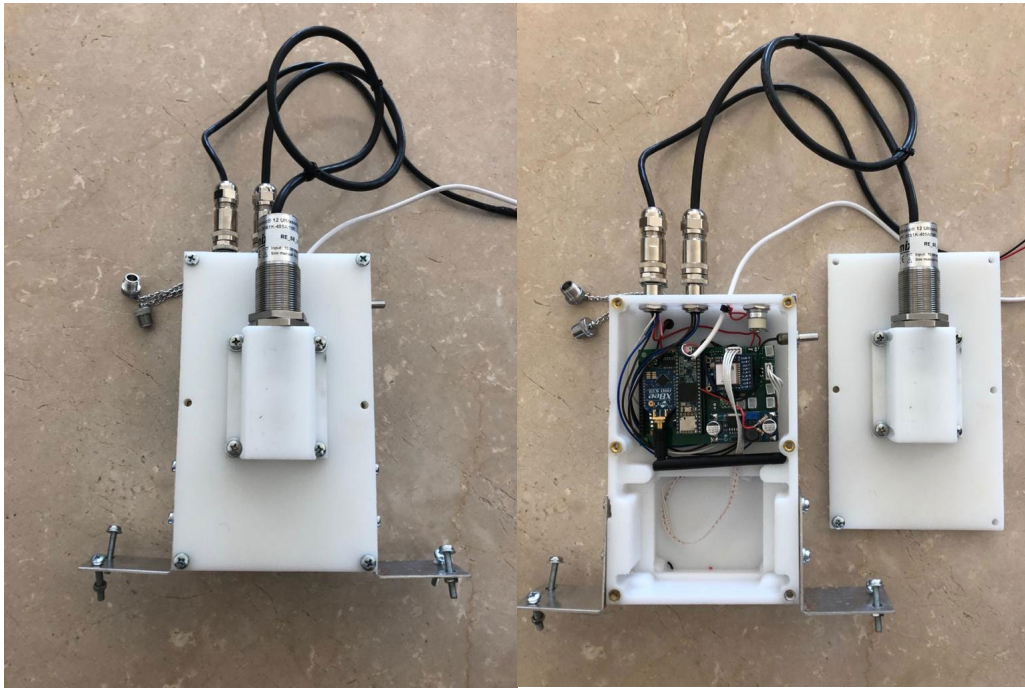
**Figure 2.80: Assembled skimmer prototype**



**Figure 2.81: Skimmer package before milling**
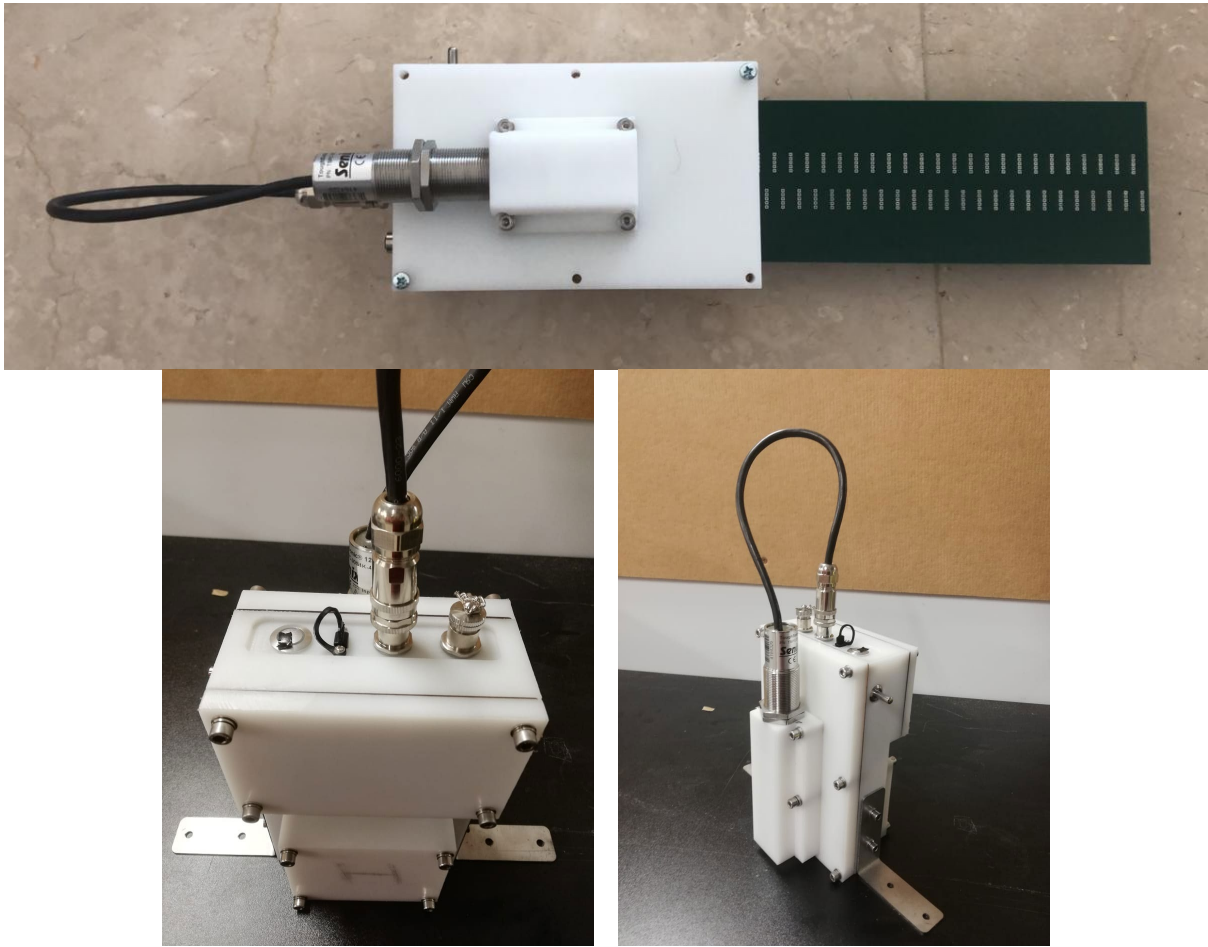
**Figure 2.82: Skimmer sensor final package**

Since the use case of this sensor requires it to be mounted on a skimmer, we developed two options for mounting. In addition, we developed cages which can protect the sensor from debris and can also function as a support for the long sensor.

To decide if the shorter sensor requires mechanical support, finite element analysis was performed. Figure 2.83, shows the stress distribution among the sensor length along with the parameters assumed to calculate the wave drag force (drag force, drag coefficient, density, cross-sectional area of the plate, and finally water speed).

The speed selected was 4 knots, which is equivalent to 2 m/s, and the drag force is calculate as $F = \frac{1}{2}C\rho v^2 A = 20\ N$. The calculated drag force was then used as an input to SolidWorks to estimate the corresponding stress, and the ensuing safety factor was found to be approximately 3, which is considered safe for usage. As a result, we assessed that no support within the cage would be necessary for the short sensor plates.
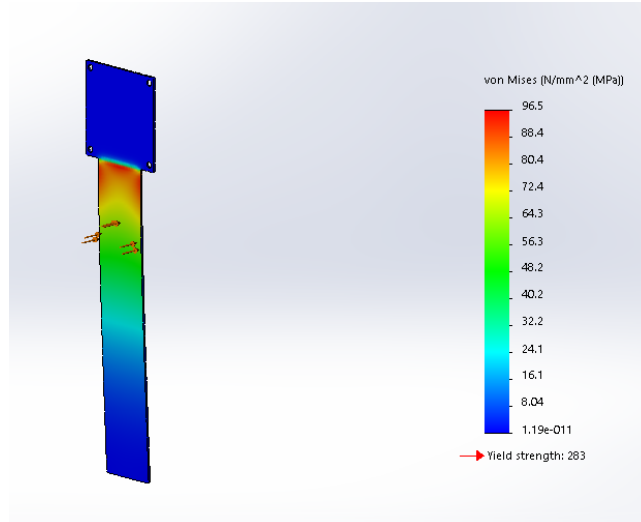
| F | Drag force | N | 20 |
|---|---|---|---|
| C | Drag coefficient | Ratio | 1 |
| ρ | Density | kg/m3 | 1000 |
| A | Cross-sectional area | m2 | 0.01 |
| v | Speed | m/s | 2 |

**Figure 2.83: 300mm sensor stress result.**

Several iterations were carried out for the cage design and attachments. One of the early designs is shown in Figure 2.84. Both the long and the short sensors can be attached to the floating device. For the long sensor the cage must be always installed because it also acts as a support to prevent the sensor from bending. The cage has a slot at the bottom, which the sensor board is inserted into; this is expected to reinforce the board. The short sensor can be installed without the cage and the floaters as shown and would allow for a wider range of testing setups. The initial plan was to use either sheet metal or a plexiglass tube to manufacture the cages. The floating platform prototype was fabricated using wood.
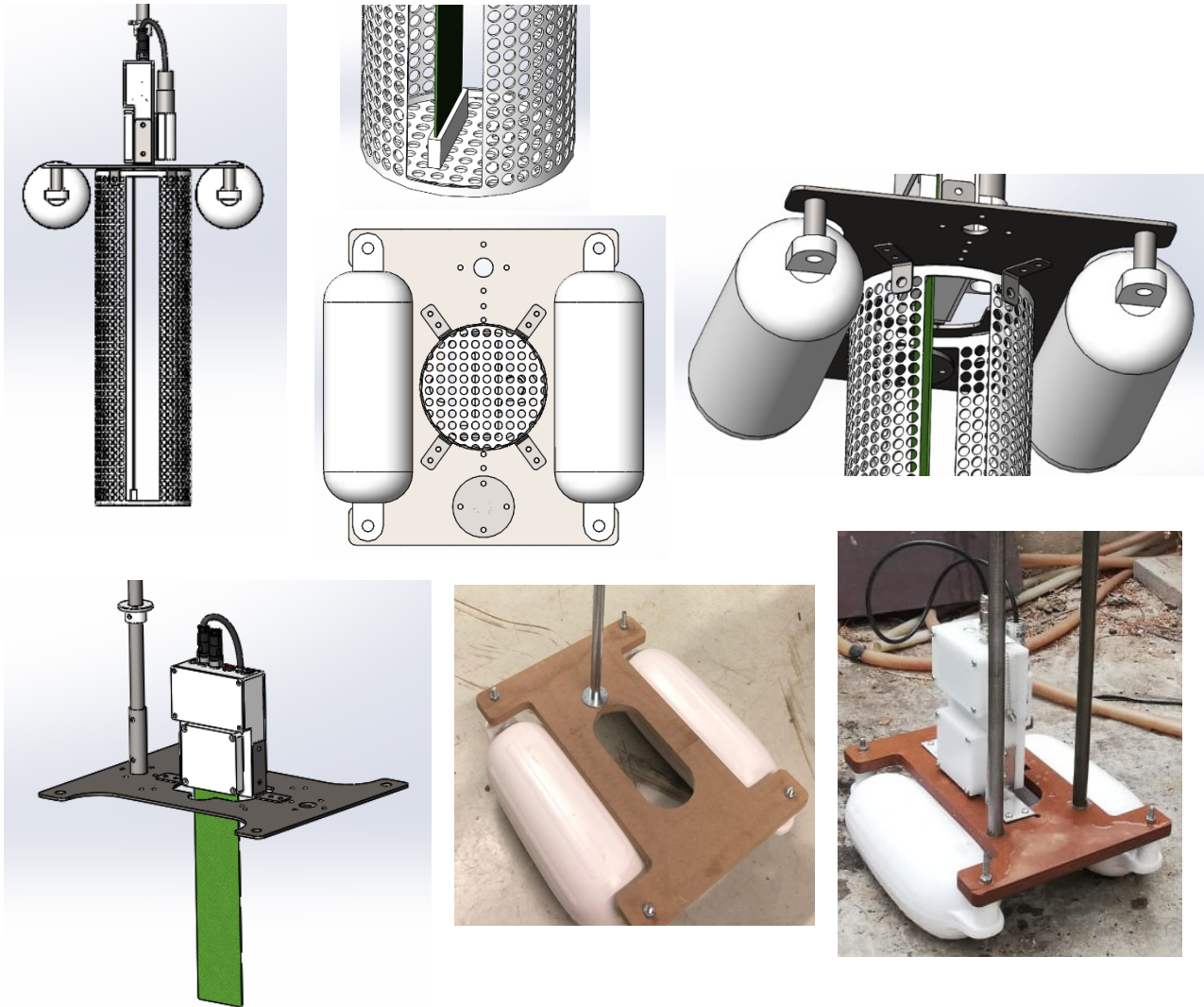
**Figure 2.84: Cage and floating platform early design.**

Another design iteration for the cage is shown in Figure 2.85. The holes of the long sensor's cage were changed to slots of 50 mm width. The intent of these openings is to allow water and oil to flow to the sensor, while reducing risk of damage to the sensor from external debris.
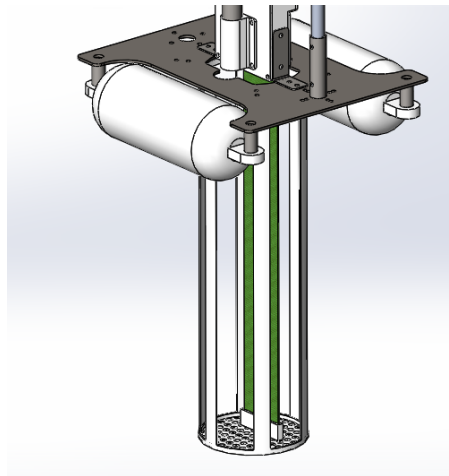
**Figure 2.85: Cage and floating platform second iteration design.**

The cage design was changed from a 4mm plexiglass tube to a 0.8mm SS316 sheet metal. This change was due to manufacturing limitations and the lack of a CNC laser cutting machine with a rotation axis. The stainless-steel cage has the same weight as the plexiglass cage (~ 1kg). The cage consisted of main cage frame, sensor guides, and bottom plate as shown in Figure 2.86. The guides and the plate were welded to the cage. When the sensor is installed in the cage, the guides will keep it protected from bending due to waves.
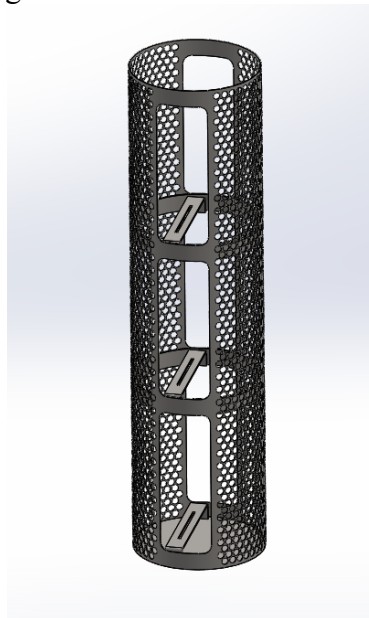


**Figure 2.86: Cage third iteration design.**

The final cage design and floater mechanism are shown in Figure 2.87. The final cage design and fixed setup are shown in Figure 2.88. Both sets can be easily mounted to the bridge attachment (discussed next) using 4xM8 bolts. The fixed skimmer set has a long cage to fit the long sensor, while the floating set has the short cage to fit the shorter sensor. The cages can be switched for testing different sensors on different setups.
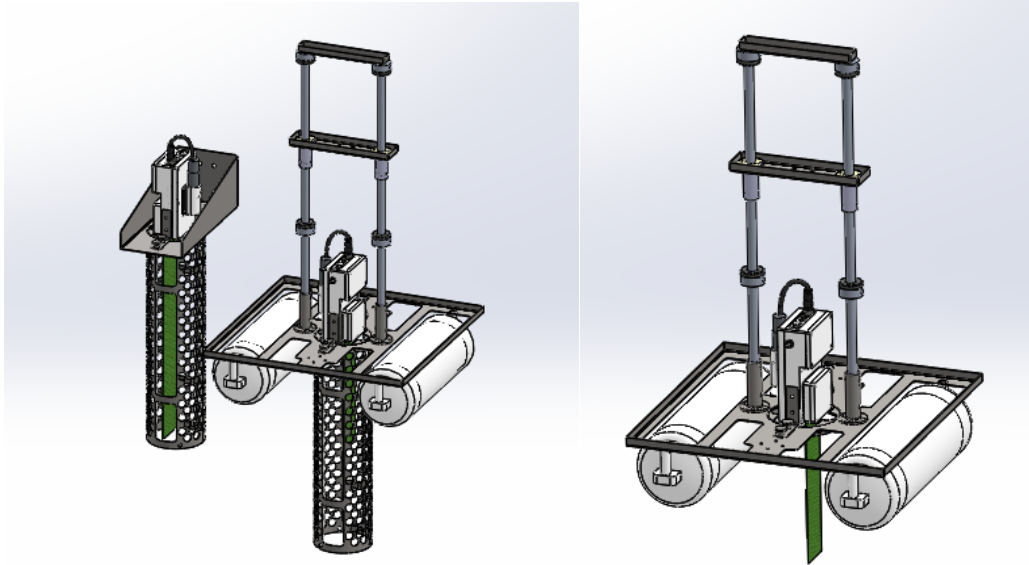
**Figure 2.87: Final floating mechanism and cage.**



**Figure 2.88: Final fixed mount and cage.**

The floating mechanism provides the sensor with a single sliding degree of freedom (up and down). The sensor is fixed on the buoyant system that would allow it to follow the motion of the waves. The sliding mechanism features two aluminum shafts fixed to the buoyancy plate by custom made fixtures, shown in red in Figure 2.89 (Left). This guarantees that the shafts will never dive in the water, they will instead be following the motion of the buoyancy plate and the buoys. On the upper extremity of the shafts, they are fixed together using a laser cut plate and screws as shown in Figure 2.89 (Right).
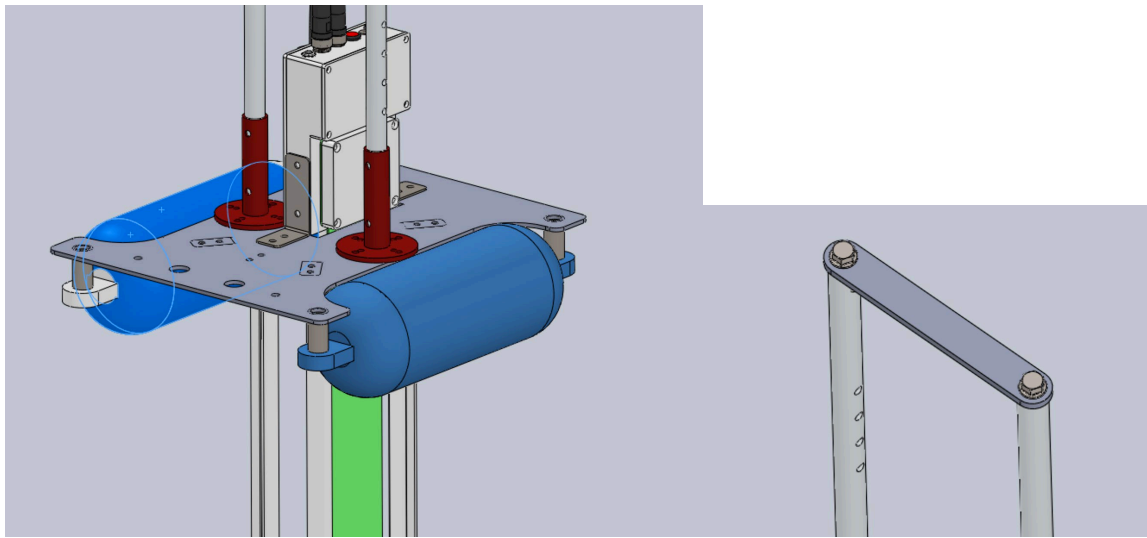


**Figure 2.89: Left: Buoyant system and sliding shafts fixture. Right: Sliding Shafts upper fixture**

The sliding occurs at the fixed side (on the skimmer bridge) of the mechanism, special dry bearings are used (shown in red in Figure 2.90), which are in their turn bolted to a laser cut stainless steel plate (in grey in Figure 2.90) that is fixed to the extruded aluminum (shown in yellow in Figure 2.90).
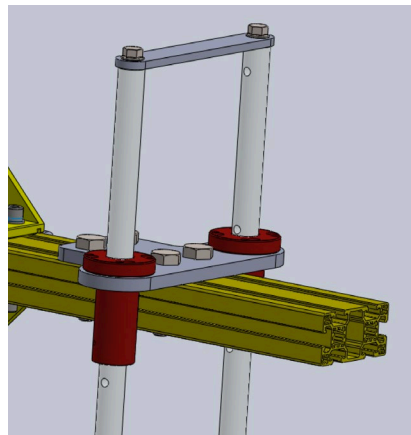


**Figure 2.90: Sliding mechanism bearings and fixture**

The sensors (floating and fixed) are designed to attach to the Termite skimmer using a bridge as shown in Figure 2.91. It is worth nothing that the attachment can be modified to mount to other

types of skimmers. As shown in Figure 2.91, the bridge will allow for 2 skimmer sensors to be attached beside each other. A sheet metal attachment was designed to secure the fixed sensor in a similar position as the floating sensor. Both sensors will have a minimum distance of 380mm from the nearest side of the bridge. Pushing the sensor away from the bridge will reduce the splashing effect caused by the skimmer. This effect was noticed in the last field test.
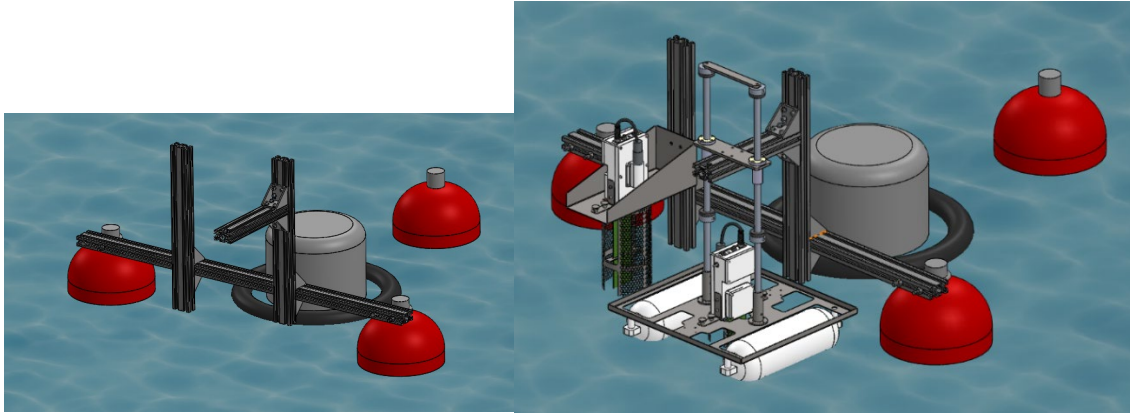


**Figure 2.91: Left: Skimmer bridge. Rright: Skimmer mount fully assembled.**

The bridge is attached to the skimmer using U-bolts M12 length 140mm. The bridge was fabricated from aluminum profile 40x80 light Type I. Using the aluminum 40x80mm profiles would greatly increase flexibility of the installation of the skimmer sensors. In both cases (the fixed and the floating systems) it is possible to adjust the position in X, Y and Z, as seen in Figure 2.92 (Left). This is achieved by loosening and tightening the screws on the L-shaped reinforcement corners as shown in Figure 2.92 (Right).
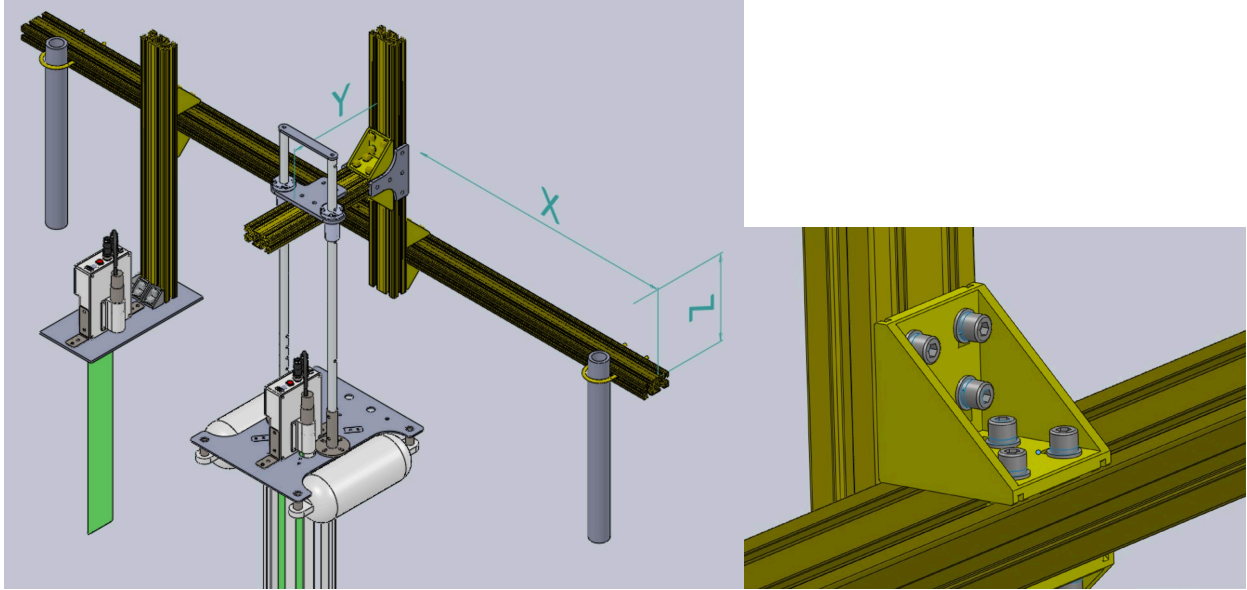
**Figure 2.92: Left: Adjustment of the skimmer sensor package. Right: Adjustable reinforcement corners.**

### 2.9.4 Enclosure and Packages Waterproof test

The handheld enclosure was tested in a water tank. The test procedure was done to check the water IP rating of the package. The enclosure was submerged 1m under the water surface for 30 minutes. The enclosure passed the test without any leakage. The same test was done for the handheld and skimmer sensor packages. After the test was complete, the package was opened and examined. No water drops were found inside the package. However, the seals did slightly absorb water.

### 2.9.5 Storage Bags

Two hardcover specialized bags were acquired and customized for the sensor's storage and shipping as shown in Figure 2.93.
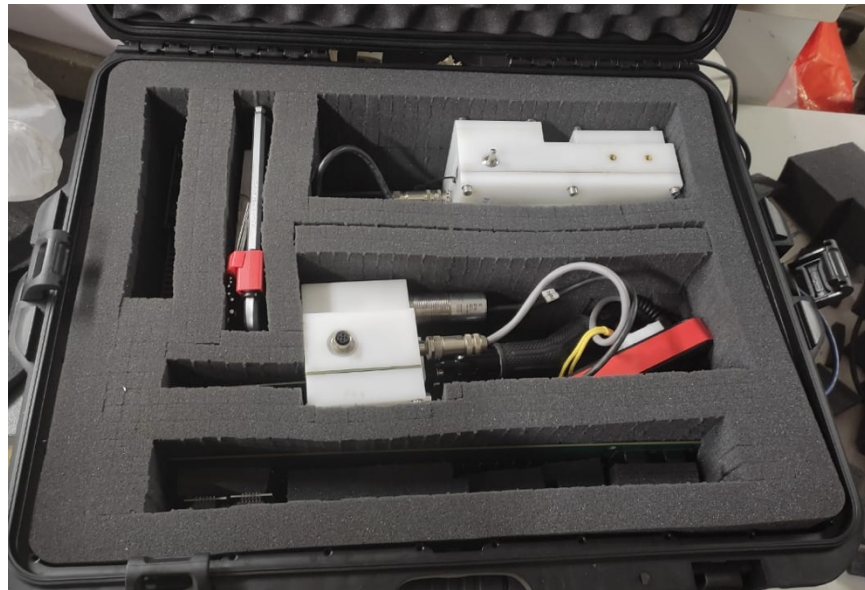
Figure 2.93: Sensor packaging for storage and shipping

# 3 Measurement Algorithms and Principles

In this chapter we present the details of the measurement algorithm and some of the main iterations it went through. Since the algorithm is based on comparing the measures of the sensing cells relative to dry in air conditions, we start by discussing the calibration done for each sensor cartridge once at manufacturing.

## 3.1 Calibration Voltages

To calibrate the capacitive sensor, a set of voltages must be recorded while the sensor is dry and in air, such that those voltages can later be used as references in the oil-thickness estimation algorithm. As shown in Figure 2.92, the calibration voltages decreased as the distance between the unit and the transducer increased. To interpret this result, we refer to the theoretical definition of capacitance which makes it directly proportional to the area of the conductive plates. In the case of a parallel-plate capacitor, the relation between the capacitance and the area of the plates is linear since a uniform electric field is assumed. In our case, since the connection tracks are coplanar, the electric field is not uniform and the fringing part of it is dominant. Based on this fact, the capacitance of the tracks increases with their area in a non-linear manner.

The MPR121 transducer measures the voltage, which is inversely related to the capacitance: *Capacitance = Charge / Voltage*. Thus, as the capacitance increases, the measured voltage decreases. The relation between the measured voltage and the position of the sensing unit can be modeled as follows:

$$y = -146 \ln(x) + 777.94 \qquad (1)$$

where y is the measured voltage and x is the index of the sensing unit.
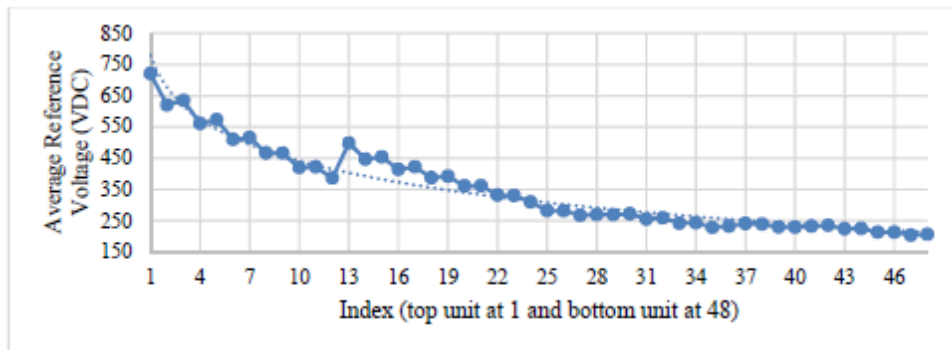


**Figure 3.1: Voltage vs. unit index – Skimmer-mount capacitive sensor (soldered).**

## 3.2 Thickness Measurement Algorithm

In this section, a detailed explanation of the general measuring algorithm used in the sensor is provided. The interface detection and oil thickness estimation algorithm can be summarized by following steps:

1. detection of the position of the oil/water interface based on the voltages measured by the capacitive sensor array,

2. detection of the position of the air/oil interface using the distance measured by the ultrasonic sensor,

3. calculation of the oil thickness based on the difference between the positions of the two interfaces: air/oil and oil/water. Since we know the geometrical dimensions of the capacitive sensor array, we can calculate the oil thickness in millimeters given the number of electrodes immersed in oil.
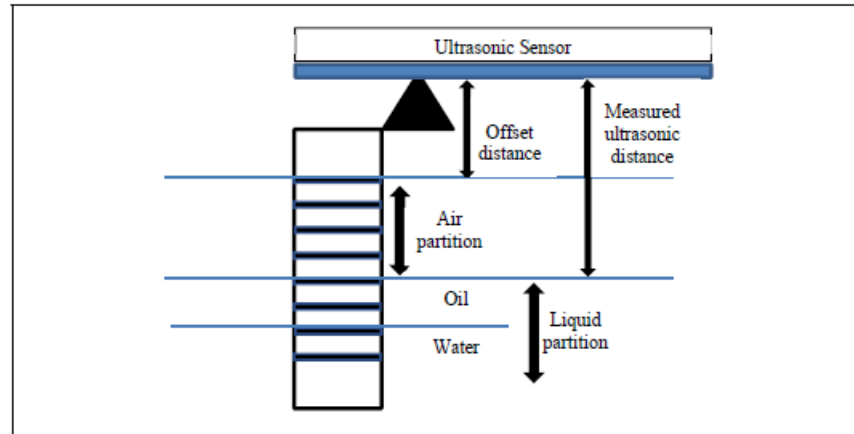


**Figure 3.2: Sensing principle and measurement parameters.**

Given that the dielectric constant of water is much larger than that of oil and air, we initially used a global threshold to classify the water electrodes. The process can be summarized as follows (see Figure 3.2 for illustration):

1- save a set of voltages measured by each electrode while the sensor is immersed in air. These values are called the calibration voltages (mentioned in the previous section),

2- after immersing the sensor in the multiphase mixture, get the relative changes for each electrode; relative Change [i] = (|Measured [i] – Calibration [i]| / Calibration [i]), where Measured [i] is the voltage measured at real-time, and Calibration [i] is the voltage stored during calibration for the electrode with index i,

3- compare the relative changes with a threshold (example: water-threshold= 50%) and classify the electrodes with values greater than the threshold as water electrodes,

4- count the electrodes classified as water and multiply their number by the dimensions to obtain the distance of water covering the sensor in millimeters.

5- get the height of the sensor body immersed in air by subtracting the ultrasonic measured distance from the offset distance (obtained via calibration).

6- calculate the oil thickness based on the following:

**Oil thickness (mm) = (total sensor height – water partition) – air partition**

Experiments showed that this simple method could be applied to measure the oil thickness accurately under steady-state conditions, which refer to the cases where the sensor is immersed in a static manner for a sufficient duration of time. For example, Figure 3.3 shows an intensity-based image representing the relative changes calculated as explained above. The x-axis in the

figure represents the time where each sample is taken at 200 millisecond of sampling rate. The y-axis represents the index of the electrodes starting from the top electrode with index 1 to the bottom electrode at the index 48. Each column in this image represents the measurements taken a time instant *t*. Yellow color represents high intensity values referring to electrodes immersed in water. Blue color represents low intensity values referring to electrodes immersed in air or oil.
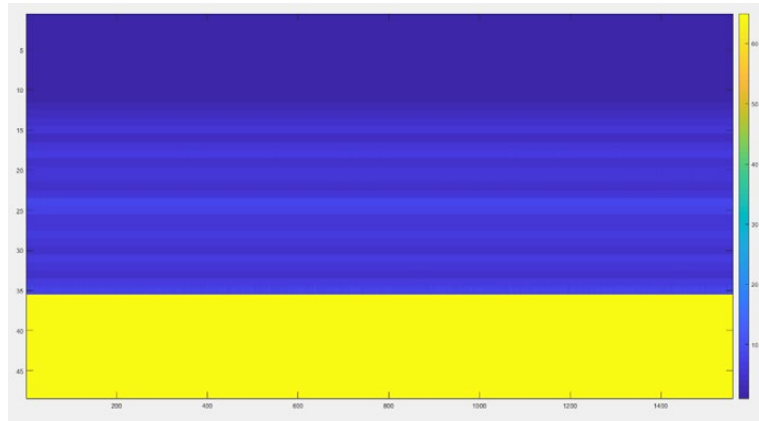


**Figure 3.3: Relative changes (%) - Steady-state conditions.**

The procedure described above was initially based on applying the algorithm to every single row of voltages acquired by the capacitive sensor. However, to deal with dynamic conditions, we saved several rows of voltages in a temporary matrix before applying the thickness estimation procedure. This was done to benefit from the temporal features in addition to the instantaneous relative changes in the classification process. As described before, the main task of the algorithm is to infer the water electrodes from the oil electrodes. Under dynamic or continuously changing liquid state, relying on the threshold only may cause errors depending on the type of the waves. Thus, we introduced another factor that relies on the temporal history of the measurements. This factor is based on calculating the difference between the last and first measures recorded by each sensing unit during a window of two seconds. The fouled sensor units that were initially classified as oil based on the threshold are then investigated using this feature (temporal change) to confirm or change their label. If the temporal change shows that the voltages measured by the sensing unit is decreasing (less than 10 VADC), the unit is classified as immersed in water. If not, the algorithm keeps the initial classification label (oil). After completing the classification process using the two features (Global and Temporal thresholds), the algorithm counts the oil sensing units and calculate the oil thickness.

### 3.2.1  Initial Algorithm Testing

Several tests were performed to demonstrate the performance of the initial thickness measurement algorithm. Photos showing the experimental setup and the handheld control unit during these experiments are shown in Figure 3.4.
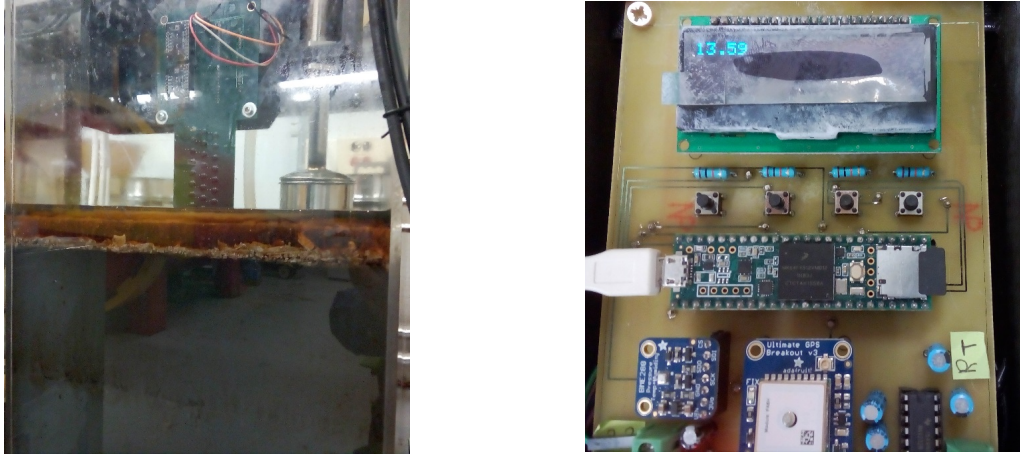
**Figure 3.4: Thickness measurement testing using the handheld sensing device.**

A statistical summary of the results obtained from one experiment is shown Table 3-1. These measurements were recorded continuously by the handheld device. Light engine oil (10 W) was used in this experiment. The oil was added to the top surface of a container filled with tap water. The actual thickness of the oil layer (13 mm) was measured visually using a meter stick placed at one transparent side of the container.

**Table 3-1: Statistical summary of thickness measurements 1 – handheld device**

| | |
|---|---|
| **Average Measured Thickness (mm)** | 13.53 |
| **Average Absolute Error (mm)** | 0.53 |
| **Standard Deviation** | 0.071 |
| **Count of measures** | 732 |
| **Maximum measured thickness (mm)** | 13.68 |
| **Minimum measured thickness (mm)** | 13.33 |

Another sample of oil thickness measurements recorded by the handheld device while working in the continuous measurement mode are shown in Table 3-2. This test used a mixture of light and thick oils forming a layer of 33 mm.

**Table 3-2: Statistical summary of thickness measurements 2 – handheld device**

| | |
|---|---|
| **Average Measured Thickness (mm)** | 33.37 |
| **Average Absolute Error (mm)** | 0.37 |
| **Standard Deviation** | 0.06 |
| **Count of measures** | 577 |
| **Maximum measured thickness (mm)** | 33.53 |
| **Minimum measured thickness (mm)** | 33.19 |

As shown in the statistical summaries, the oil thickness measurements were very stable. This could be concluded clearly from the low standard deviation value. Also, the measurements were accurate since the absolute error did not exceed 0.5 mm. Note that based on the requirements, the resolution of the handheld device is about 3 mm.

To test the performance of the handheld sensor under dynamic liquid conditions, a linear actuator was configured to follow a periodical vertical motion dipping the sensor in the oil/water mixture continuously. In these test, fuel oil (thick) with a thickness of 62 mm was used. A statistical summary of the obtained measurements is shown in Table 3-3.

**Table 3-3: Statistical summary of thickness measurements 3 – handheld device**

| | |
|---|---|
| **Average Measured Thickness (mm)** | 60.99 |
| **Average Absolute Error (mm)** | 1.01 |
| **Standard Deviation** | 1.71 |
| **Count of measures** | 499 |
| **Maximum measured thickness (mm)** | 65.31 |
| **Minimum measured thickness (mm)** | 53.25 |

The result of the dynamic conditions showed an increased range of error. For instance, the measurements ranged from 53 mm to 65 mm when the actual thickness was around 62 mm. However, we should note that these high changes in the measured value were recorded during the sudden immediate change in the position of the linear actuator. In other words, when the actuator starts a fast motion upwards or downwards. These results were not filtered or altered based on the motion of the sensor. One suggestion to handle this problem was to use an adaptive filtering method to neglect the fast changes in the measured thickness. At other states, when the sensor is relatively in static mode at the upper or lower positions, the measurements become more accurate and stable. This can be concluded from the small average absolute error recorded (=1 mm) and low standard deviation vale (= 1.7). These types of filtering techniques were introduced in subsequent iterations to improve the sensors performance under dynamic conditions.

### 3.2.2 Second Iteration Algorithm

In this section, a more refined and detailed algorithm is detailed.

#### 3.2.2.1 Phase 1: Data Acquisition

Data acquisition and normalization are demonstrated in a flowchart shown in Figure 3.5.
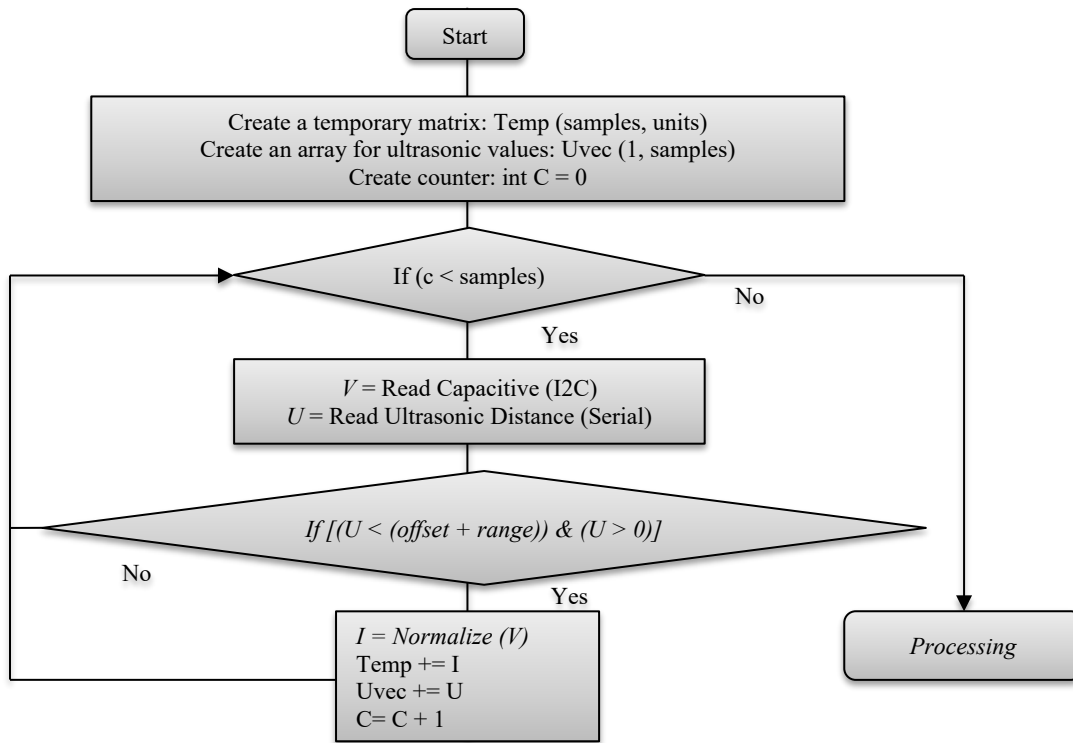
**Figure 3.5: Data acquisition flowchart.**

The process starts by storing a fixed number of measurements using a set of cycles. At each measurement cycle, the algorithm records an array of voltages from the capacitive sensor and a single distance from the ultrasonic sensor. A validity check is applied to the measurements before adding them to the buffer (temporary matrix). After passing the validity check, the voltages are normalized by converting them into a set of values ranging between 0 (air) and 100 (water). The term *intensity* is used to denote the normalized values. As shown in Figure 3.5, the intensities are stored in a two-dimensional array named *Temp*. The columns of this matrix represent the sensing units (total of 48) and the rows represent the intensities taken at consecutive instances of time. The number of rows is equal to the size of the temporal window. The matrix structure is shown in (4).

$$Temp = \begin{Bmatrix} I_{t0,1} & I_{t0,2} & \cdots & I_{t0,N} \\ I_{t1,1} & I_{t1,2} & \cdots & I_{t1,N} \\ \cdots & \cdots & \cdots & \cdots \\ I_{tM,1} & I_{tM,2} & \cdots & I_{tM,N} \end{Bmatrix} \quad (4)$$

where $N$ is the number of sensing units and $M$ is the size of the temporal window.

### 3.2.2.2 Phase 2: Processing

The data acquisition phase ends by calling the *Processing* function. The workflow of the processing function is demonstrated in the flowchart shown in Figure 3.6.
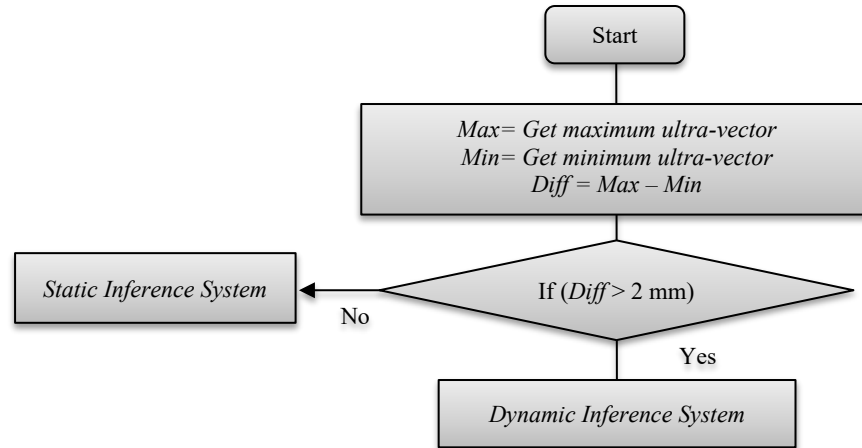
**Figure 3.6: Processing flowchart.**

Given the values stored in the temporary matrix and the ultrasonic array, the processing function is responsible for estimating the oil thickness. First, it checks whether the system is in a static or a dynamic state. The decision about the state of the sensor is based on the difference between the largest and smallest distances measured by the ultrasonic sensor within the temporal window. The test condition is as follows:

$$If\ ([\ Max(Ultra_{vector}) - Min\ (Ultra_{vector})] > threshold)\ \{State = Dynamic\}$$
$$Else\ \{State = Static\}$$

The value of the $threshold$ depends on the resolution of the sensor. For instance, in the handheld sensor, the threshold is 3 mm, whereas in the skimmer-mount sensor the threshold is 1 cm. In other words, the test condition checks if the position of the ultrasound sensor changed considerably in relative to the liquid or vice versa. In each of the two states, a different inference system is used. We should note that one of the two states will be dominant over the other in each of the implemented devices. In the skimmer-mount device, the sensing platform is equipped with a floating buoy which allows the sensor to follow the waves. In this case, the *Dynamic* state is less probable to appear since the floating buoy will raise and lower the sensing platform according to the dynamics of the waves. In other words, despite the amplitude of the waves, waves having relatively low frequencies (large wavelength) will cause the sensing platform to rise and fall smoothly with water. As long as the distance between the ultrasonic sensor and the liquid does not change too much – for example, the span of distance change is less than the sensor resolution – the *Static* case will be selected. The *Static* state will also be selected when the water is steady. However, this will all depend on the motion of the sensor and the liquid.

### 3.2.2.3  Phase 3: Inference

The general structure of the inference process, shown in Figure 3.7, is composed of four main units:

1- Identifier: detects the indexes of the liquid-immersed units and selects the measurements needed for analysis.

2- Feature Generator: takes the signals as inputs and outputs their feature-based representations. The Feature Matrix (5) contains a finite set of statistical measures representing the behavior of the signal.

$$Feature\ Matrix\ = \begin{cases} F_{1,1} & F_{1,2} & ... & F_{1,N} \\ F_{2,1} & F_{2,2} & ... & F_{2,N} \\ ... & ... & ... & ... \\ F_{k,1} & F_{k,2} & ... & F_{k,N} \end{cases} \tag{5}$$

where $N$ is the number of sensing units and $k$ is the number of features.

3- Classifier: takes the feature-based representations and outputs a class label (water/oil). Once the water-immersed units are detected and counted; we can simply estimate the oil thickness.

4- Oil thickness estimator: calculates the oil thickness and filters the thickness measurement based on the dynamic situation of the sensor.
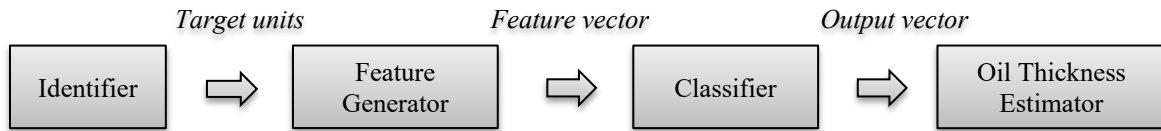


**Figure 3.7: General inference structure (block diagram).**

### 3.2.2.4  Static Inference System

The static inference system starts by calculating the average of the ultrasonic measured distances. For the result, it estimates the index of the air/oil interface. The signals of units located beneath the interface are considered liquid-immersed and sent to the feature generator. After extracting the features, a classifier is called to detect the water-immersed units and calculate the oil thickness. Different methods of classification and their testing is discussed in later sections.

#### 3.2.2.4.1  Rule-Based Classifier

This method is based on checking the features against a set of rules. The first rule is applied to the intensity of the signal (last value). If the intensity is greater than a threshold (20%), the sensing unit is classified as water. Otherwise, the sensing unit is classified as oil. If the unit is classified as oil, a second rule is applied to its slope. If the slope is greater than a certain threshold (2%), we re-classify the unit as water. In this way, we correct the classification error that may exist in the first step. The testing and results of this method are discussed in a later section.

#### 3.2.2.4.2  Machine Learning Classification using Support Vector Machines

Since uncertainty characterizes the measurements under different environmental conditions, we planned to find a more robust classification method. Instead of using a simple rule-based classifier, we implemented a machine-learning-based classifier that can learn from experience. In machine learning, supervised learning methods aim to infer a function that relates the output class label to the input feature-based vector by observing a set of labeled samples known as the training set. The training set contains <input, output> pairs, where the input is the feature-based representation of the sample denoted by $X = [x_1, x_2, ..., x_K]$ and $K$ is the number of features, and

the output is the desired class label denoted by $Y \in [C_1, C_2, ..., C_M]$ where $M$ is the number of classes. In the literature, there is a wide variety of supervised classification algorithms. However, for binary classification problems, where the output label is either 1 or 0 (true or false), Support Vector Machines (SVM) are widely used.

Support Vector Machines (SVM) define a hyperplane, which best separates a given set of training samples: $(xi, yi) \mid i = 1, ..., m; \ yi \in \{-1, +1\}$ where the samples are represented by the feature vectors $xi$, the corresponding labels are represented by $yi$, and the number of samples included in the training set is denoted by $m$. In the training phase, the hyperplane is defined by maximizing its distance to the closest instances from each class (support vectors). After learning the coefficients, the model is used to classify new samples. The model is defined by a function $f(x) = G (WX + B)$, where $G$ returns 0 for negative inputs and 1 otherwise. The inputs to this function are a feature vector $X$, a normalized vector $W$ (learned weights), and the learned bias $B$.

The implementation of the SVM model in the microcontroller's code is simple and involves the execution of one function: Sign [(w1) (relative change) + (w2) (slope) – b]; w1 and w2 are the model coefficients and b is the bias. If the Sign function returns a positive value, the electrode is classified as water immersed; otherwise, the electrode is classified as oil immersed.

### 3.2.2.5 Dynamic inference system

Under dynamic conditions, the exact prediction of sensor behavior is not possible. Based on this fact, we selected a classification technique that does not depend on any previous assumptions. The method is known as the *Jenks Natural Breaks* and performs unsupervised classification. It is based on an optimization process designed to detect the natural boundary between groups of elements having similar statistical properties. In our application, the method is applied to the one-dimensional array containing the normalized values measured by the capacitive sensor array. The output of this method is the index of the oil/water interface.

Before applying the boundary detection method, one of the capacitive measurements should be selected. Based on our experience, the measurement should be selected when the insulating and conducting phases are separated without any ambiguous phase in between. This moment is when the sensor reaches the highest position and could be detected based on the largest measurement of the ultrasonic sensor.

#### 3.2.2.5.1 Implementation of Jenks Natural Breaks

The method is implemented via three major computational steps explained below:

**1- Sum of Squared Deviations for Array Mean (SDAM):** first, we calculate the arithmetic mean of the values included in the array. Then, the deviation of each element relative to the mean and square the result. Finally, the sum of all squared deviations is obtained. The equation of the SDAM could be expressed as:

$$SDAM = \sum_{i=1}^{N} (xi - M)^2$$

where the index of elements is $i$, the size of the array is $N$, and the mean is $M$.

**2- Sum of Squared Deviations for Class Means (SDCM) for each class combination:** for each possible class combination, we should calculate an SDCM value. This is done by summing the SDAMs of each class in each possible class combination. For example, for a four-element array, we have three possible class combinations. In each combination, we have one SDAM value for each class. The SDCM of each combination is equal to SDAM (class 1) + SDAM (class 2). As a result, we will have three SDCM values for a four-element array.

**3- The Goodness of Variance Fit (GVF):** The final step is to calculate the Goodness of Variance Fit (GVF) value for each possible class combination. This is done by calculating the difference between the SDAM value calculated in the first step and the SDCM value of each possible class combination. The result is divided by the SDAM for normalization. The equation of the GVF is expressed as:

$$GVF\ (ci) = \frac{SDAM - SDCM\ (ci)}{SDAM}$$

where $ci$ represents the index of the combination.

Finally, the class combination that has the largest GVF value is selected to split the original array into two distinct classes.

## 3.3   Testing and Assessment of Initial Algorithms

The initial set of algorithms were tested, and datasets collected for the SVM training are discussed in the next subsections.

### 3.3.1   Testing of Rule-Based Methods (Handheld Sensor)

The threshold-based classification method was tested while the handheld sensor was mounted on the linear actuator. The measurements obtained using the first condition only are plotted in Figure 3.8 and the results obtained after adding the second condition are shown in Figure 3.9.
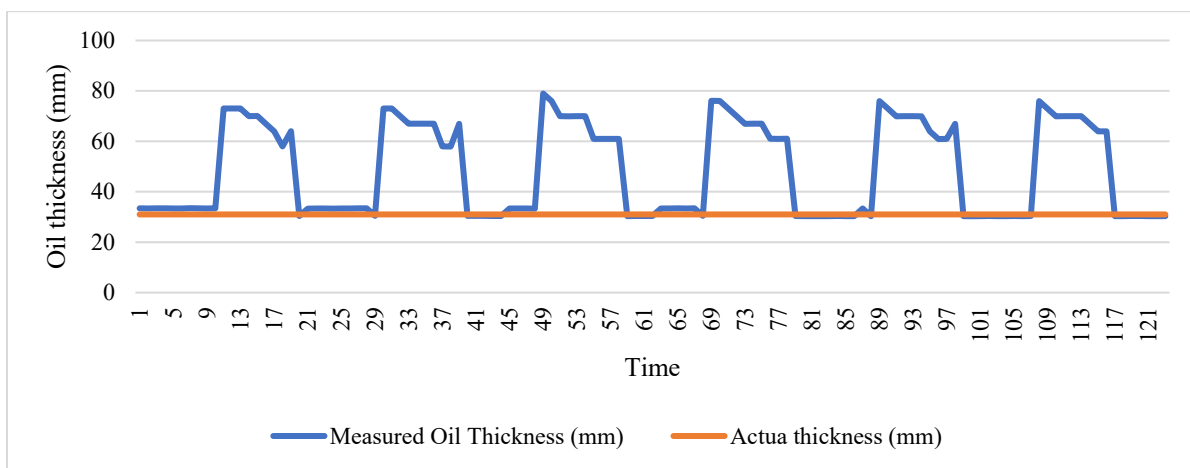


**Figure 3.8: Result of using a single condition for classification – Handheld sensor.**
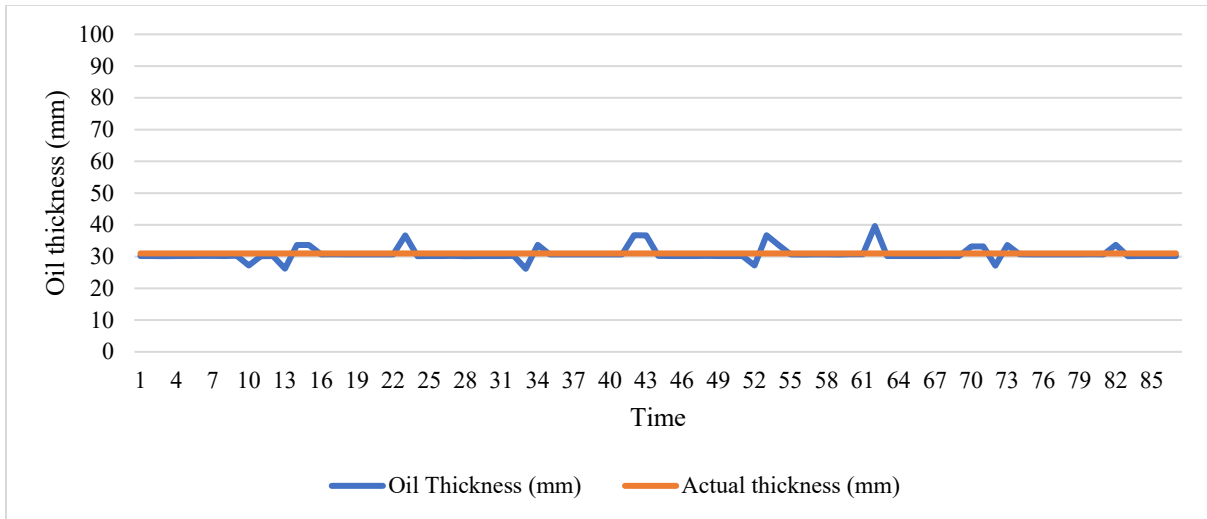
**Figure 3.9: Result after adding the second condition to the rule-based classification system.**

The results showed that the classification via a single condition had a large measurement error correlated with the motion of the linear actuator. The error was highly reduced after adding the second rule. Although the rule-based system showed a good result, the major limitation of this method is that the thresholds should be set manually. This led us to consider the machine-learning classification evaluated in the next sections.

### 3.3.2 Experimental Procedure for Creating the Training Dataset for SVM Models

The SVM model should be trained using many samples. Thus, we designed an experimental procedure to create a dataset. First, we mounted the sensor on the linear actuator which dips it continuously in the oil/water mixture. Voltage measurements were recorded for a single unit (unit of Index 24). By plotting the distances measured by the ultrasonic sensor, we inferred the moments when the unit is in oil and water. Thus, we programmed the microcontroller to calculate the feature vector of the signal related to this unit and send it with a suitable class label to the PC through the serial interface. After testing several features and studying their correlation with the class labels, the dataset was reduced to two features (columns), the *last value* which is now named the *relative change* and the *slope*. A snapshot showing a part of the training set is shown in Figure 3.10.

**Data set**

**Workspace Variable**

| static_training_dataset | 427x5 table | ∨ |

**Response**

| label | double | 0 .. 1 | ∨ |

**Predictors**
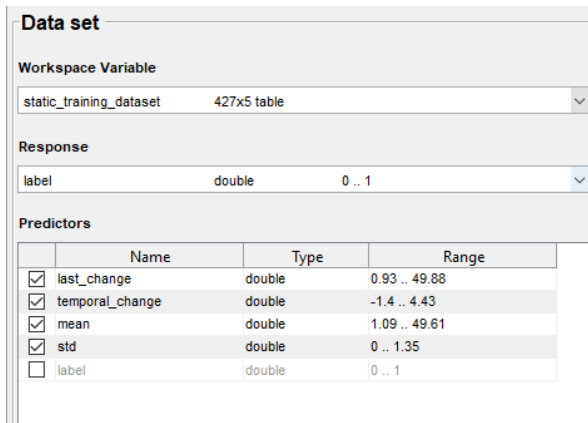
| | Name | Type | Range |
|---|---|---|---|
| ☑ | last_change | double | 0.93 .. 49.88 |
| ☑ | temporal_change | double | -1.4 .. 4.43 |
| ☑ | mean | double | 1.09 .. 49.61 |
| ☑ | std | double | 0 .. 1.35 |
| ☐ | label | double | 0 .. 1 |

| | A last_change | B temporal_change | C mean | D std | E label |
|---|---|---|---|---|---|
| 1 | last_change | temporal_change | mean | std | label |
| 2 | 25.64 | 1.63 | 24.68 | 0.57 | 1 |
| 3 | 27.51 | 1.86 | 26.75 | 0.5 | 1 |
| 4 | 29.84 | 2.1 | 28.82 | 0.6 | 1 |
| 5 | 31.93 | 1.86 | 30.89 | 0.51 | 1 |
| 6 | 33.57 | 1.63 | 32.79 | 0.54 | 1 |
| 7 | 34.97 | 1.17 | 34.3 | 0.44 | 1 |
| 8 | 36.13 | 0.93 | 35.76 | 0.39 | 1 |
| 9 | 37.53 | 1.4 | 36.88 | 0.36 | 1 |
| 10 | 38.23 | 0.7 | 37.98 | 0.23 | 1 |
| 11 | 39.39 | 0.93 | 38.9 | 0.27 | 1 |
| 12 | 40.09 | 0.7 | 39.63 | 0.17 | 1 |
| 13 | 40.79 | 0.7 | 40.45 | 0.24 | 1 |
| 14 | 41.26 | 0.47 | 40.99 | 0.24 | 1 |
| 15 | 41.96 | 0.7 | 41.64 | 0.23 | 1 |
| 16 | 42.19 | 0.47 | 42.03 | 0.21 | 1 |
| 17 | 42.66 | 0.47 | 42.51 | 0.17 | 1 |
| 18 | 43.12 | 0.47 | 42.84 | 0.12 | 1 |
| 19 | 43.59 | 0.47 | 43.32 | 0.11 | 1 |
| 20 | 43.82 | 0.47 | 43.66 | 0.11 | 1 |
| 21 | 2.1 | -1.4 | 2.29 | 0.26 | 0 |
| 22 | 2.1 | 0 | 2.01 | 0.11 | 0 |
| 23 | 2.1 | 0.23 | 2.06 | 0.08 | 0 |

Sheet1  Parameters  ⊕

Ready

**Figure 3.10: Part of the training set showing the features and the class labels.**

The dataset was updated several times. A sample of the first dataset showing the features of the samples with their class labels is shown in Figure 3.11. The oil samples are plotted in blue, and the water samples are plotted in red. Note that most of the samples belonging to oil showed a zero to a negative slope, whereas the water samples showed a zero to a positive slope. Also, the water samples showed a high relative change, and the oil samples showed a low change. Python programming language was used to develop necessary scripts to learn and apply the classification model.
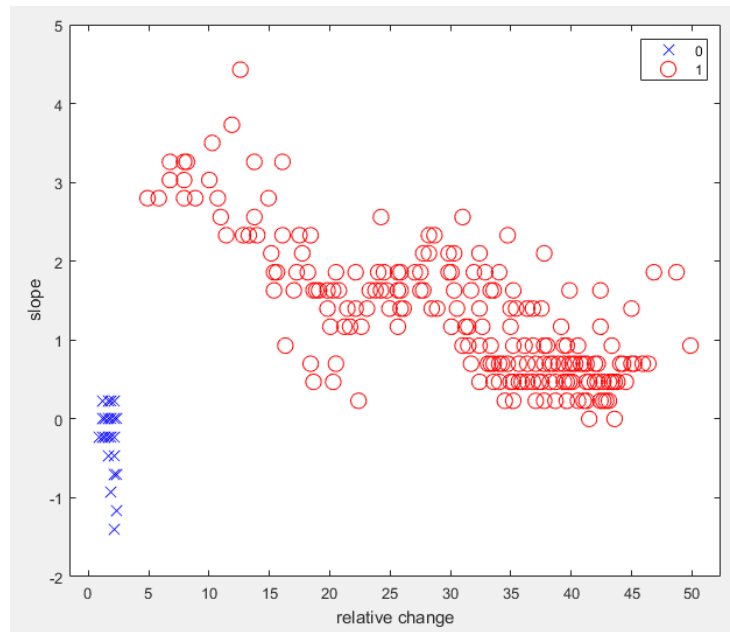
**Figure 3.11: Training samples with corresponding labels – Red for water samples and blue for oil samples.**

### 3.3.3 Testing of the First SVM model (Handheld Sensor)

The first dataset was composed of samples obtained from one sensing unit and under transient conditions. It was used to train the first SVM model with a linear kernel. The following coefficients were obtained:

- weights vector: [0.71428568 0.71428568]
- bias: -2.66428566

To test the performance of the trained model, experiments were performed in real-time. A statistical summary of the results showing the average and confidence interval of more than 150 measures of oil thickness taken using the handheld sensor are summarized in Table 3-4. Note that the actual thickness as measured visually is around 31 mm.

| Average | 30.43 |
|---|---|
| Standard Deviation | 1.78 |
| Count | 158 |
| Maximum | 31.57 |
| Minimum | 25.41 |
| Range | 6.16 |
| Confidence coefficient | 1.96 |
| Margin of error | 0.27 |
| Upper bound | 30.71 |
| Lower bound | 30.15 |

**Table 3-4: Oil thickness measurements using the first SVM model – Handheld sensor.**

### 3.3.4 Dataset Enhancement and Testing the Final SVM Model

The training dataset was enhanced by adding additional samples from different units while the sensor was under steady-state conditions. The new dataset was appended to the original set. Figure 3.12 shows a sample of the new dataset obtained after including the steady-state conditions. The new data showed water samples with a large relative change (> 70 %).
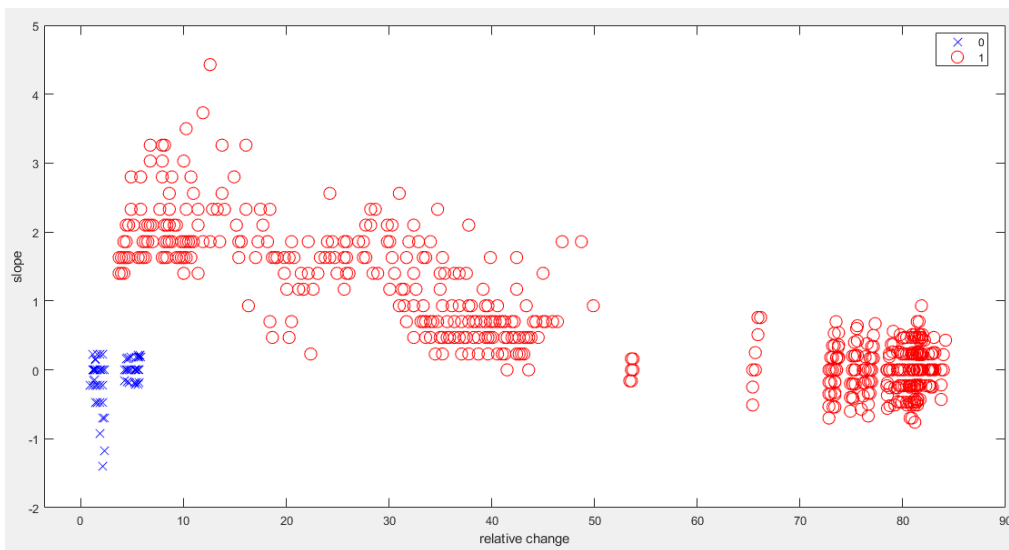


**Figure 3.12: Training set 2 – Red circles for water samples and blue x's for oil samples.**

Another set of experiments was performed to enhance the dataset. We repeated the tests performed before while varying the delay times (from 5 seconds to 60 seconds). As a result, the dataset was expanded to contain around 10,200 samples. The final dataset is obtained after combining the results of the two sets of experiments (Figure 3.13).
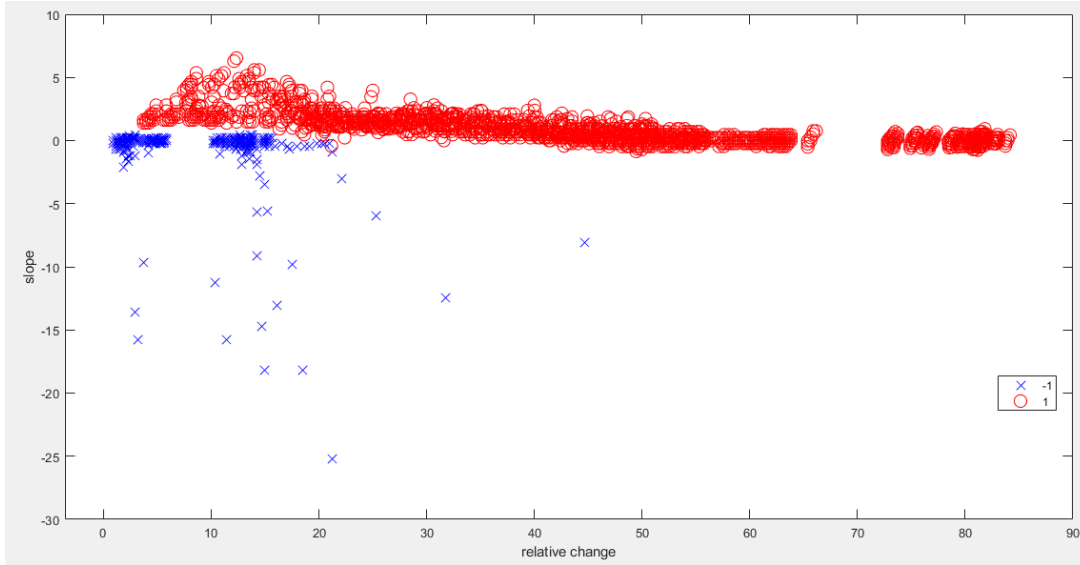


**Figure 3.13: Complete dataset with different sensors and stop time durations.**

Despite the diversity of the feature values obtained in the final dataset, the two classes (oil and water) are still linearly separable. After training the SVM classifier using a linear kernel, the final weights and bias values were obtained as the following:

- weights vector: [0.16396748 3.28375252]
- bias: -4.28615692

The final model was tested under real-time conditions after updating its parameters. In the results shown in Table 3-5, the linear actuator was programmed with the following parameters: minimum position: 120 mm, speed 40 mm/sec, and waiting time: 60 sec. Based on the actual thickness which is around 32 mm, the average measured thickness of 32.7 mm with a low margin of error of about 0.3 mm which is considered much better than the result obtained via the previous model.

| Average | 32.72 |
|---|---|
| Standard deviation | 2.28 |
| Count | 152 |
| Confidence Coeff | 1.96 |
| Margin of error | 0.36 |
| Upper bound | 33.08 |
| Lower bound | 32.35 |

**Table 3-5: Results of testing the final SVM model at experimental setup – Handheld sensor.**

### 3.3.5 Testing of the Handheld Sensor Against a Different Type of Oil

Another small-scale experimental setup was installed to perform outdoors testing. The oil type was changed from the 10W engine oil used in previous experiments to SAE 140 gear oil. The set of tests included the gathering of additional data samples to update the training set and using the sensor to measure the oil slick thickness. The new dataset obtained is composed of 2500 samples added to the previous 10200 samples. The handheld sensor was installed above the container and the oil thickness algorithm was applied continuously with a measurement rate of one measure per two seconds. The actual thickness of the oil as measured visually from the external of the container was around 29 mm. The results are plotted in Figure 3.14
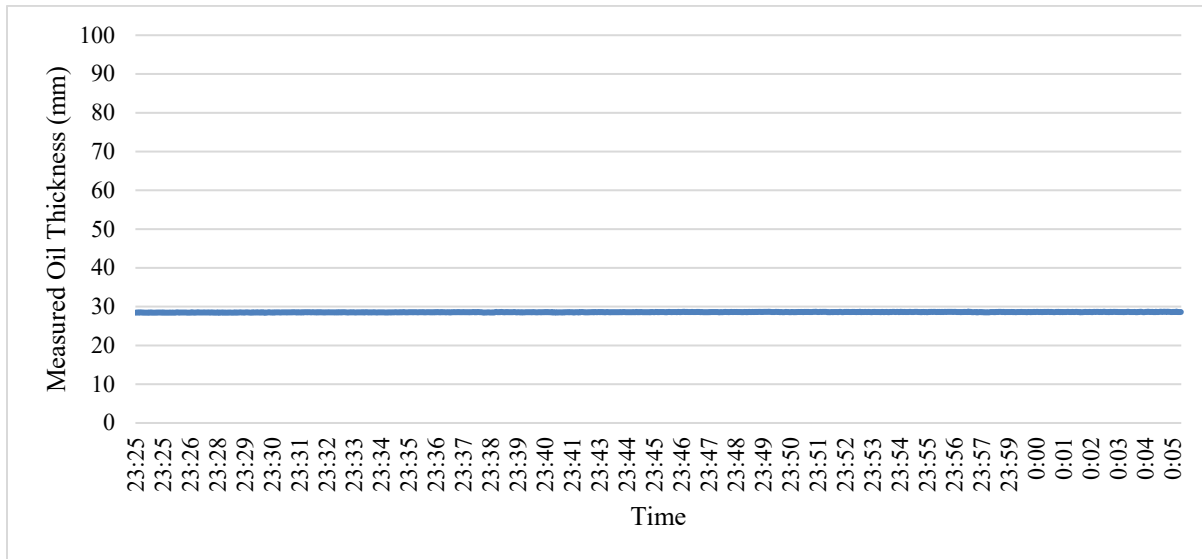


**Figure 3.14: Results of oil thickness estimation experiment.**

The oil thickness measurements were stable with a very low standard deviation value of 0.059 mm. The difference between the maximum and the minimum measured thicknesses (dynamic range) is 0.33 mm. Note that the duration of the experiment is around 40 minutes and the count of measurements taken is 1226. The average measured thickness is 28.57 mm. This result leads to an absolute error of around 0.43 mm if the ground truth is exactly 29 mm as measured visually. In conclusion, we can say that the results of this experiment are very good especially that it was performed against a new type of oil and water and under different experimental conditions. This supports the robustness of the developed model and algorithm.

### 3.3.6 Extended Testing – Handheld (static)

In addition to the previous tests, the handheld sensor was tested outdoors while measuring the oil thickness for more than 3 hours continuously. The measured thickness was reported every two seconds and the results were recorded automatically by the desktop application. During the experiment, the ambient temperature was recorded continuously using the BME 280 temperature sensor connected to the microcontroller. The results are shown in Figure 3.15, Figure 3.16, and Table 3-6.
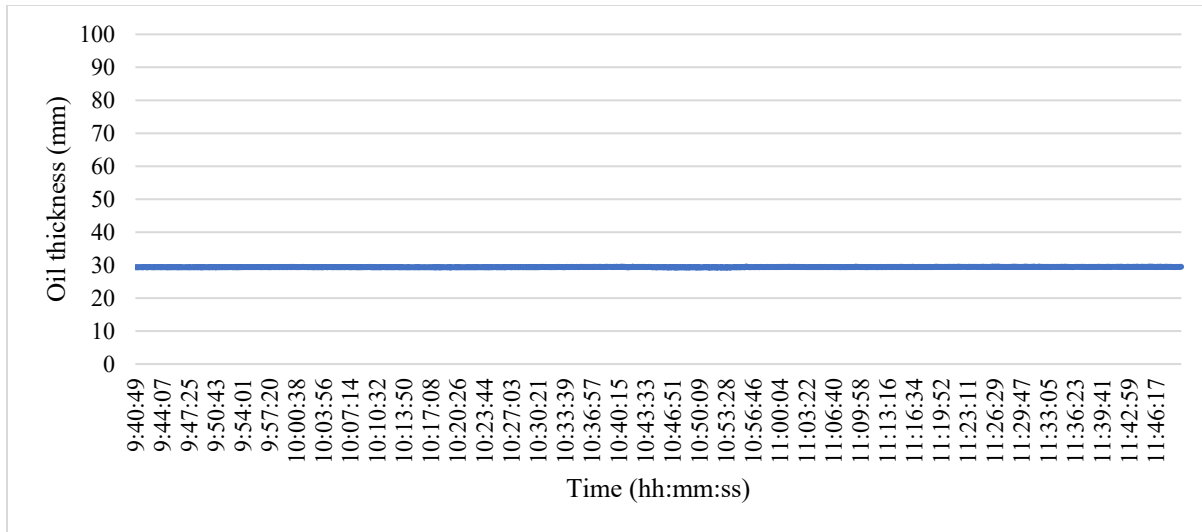
**Figure 3.15: 3-hours experimental results - Oil thickness (mm)**
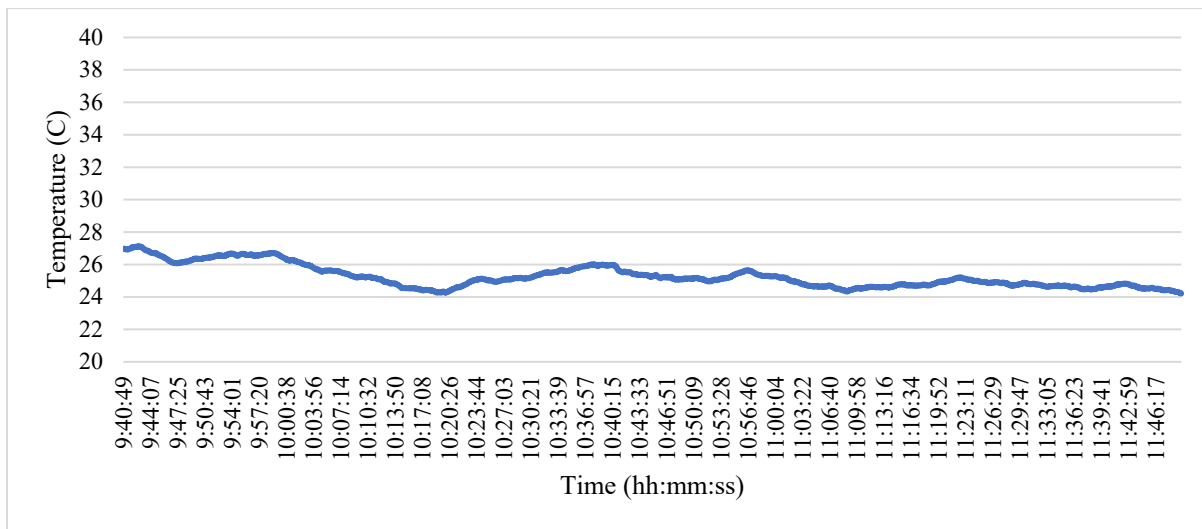


**Figure 3.16: 3-hours experimental results – Temperature**

**Table 3-6: Results of extended testing – Handheld sensor (static)**

|  | Oil thickness (mm) | Temperature (C) |
|---|---|---|
| **Average** | 29.41 | 25.25 |
| **Standard Deviation** | 0.040 | 0.703 |
| **Max** | 29.59 | 27.13 |
| **Min** | 29.28 | 24.21 |
| **Range** | 0.31 | 2.92 |
| **Count** | 3855 | 3855 |

### 3.3.7  Dynamic Testing - Handheld

In addition to the static testing performed, the handheld device was tested under realistic conditions where the platform was held by hand and immersed in a sinusoidal way in and out of a liquid containing a mixture of SAE 140 gear oil and water. Random waves were created in the container by exerting some movement to it. The actual thickness of oil was measured visually to be approximately 30 mm. The final (combined static/dynamic) inference system was used in measuring the oil thickness and the thickness was reported continuously. A sample of the results obtained under dynamic conditions is shown in Figure 3.17.
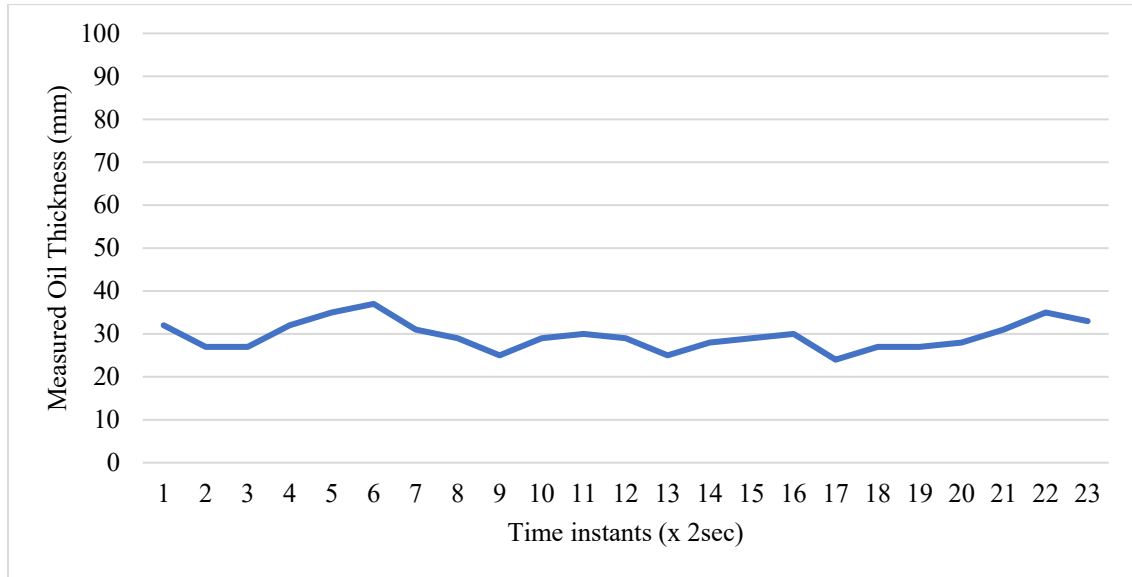


**Figure 3.17: Dynamic testing results - Handheld**

As shown, due to the motion of the sensing platform and the liquid inside the container, the thicknesses measured varied about the actual thickness which is around 30 mm. The average of the measurements is 29.56 mm showing an average absolute error of around 0.5 mm. The standard deviation of the measurements is 3.35 mm which refers to one electrode of error. The results showed that the developed algorithm was successful in handling the problem of oil fouling and keeping the measurements within an acceptable range of variation despite the movement of the sensing platform and waves created in the liquid container.

### 3.3.8  Skimmer Sensor (Static)

The skimmer mounted sensor has a lower resolution than the handheld sensor. First, we assessed the response of the sensor while mounting it to the same experimental setup used before for static testing. The actual oil thickness was around 29 mm. The sensor was immersed in the oil/water solution and measurements were recorded automatically using the same SVM model trained before using the handheld sensor. A sample of the results is plotted in Figure 3.18.

The importance of this test is that it showed that the model trained using the handheld sensor is valid for the skimmer-mount sensor. Note that the average of the measurements is 27.42 mm with an absolute error of around 1.57 mm. This is much lower than the accepted error range of

10 mm. Also, the standard deviation is around 0.056 mm which represents the stability of the measurements.
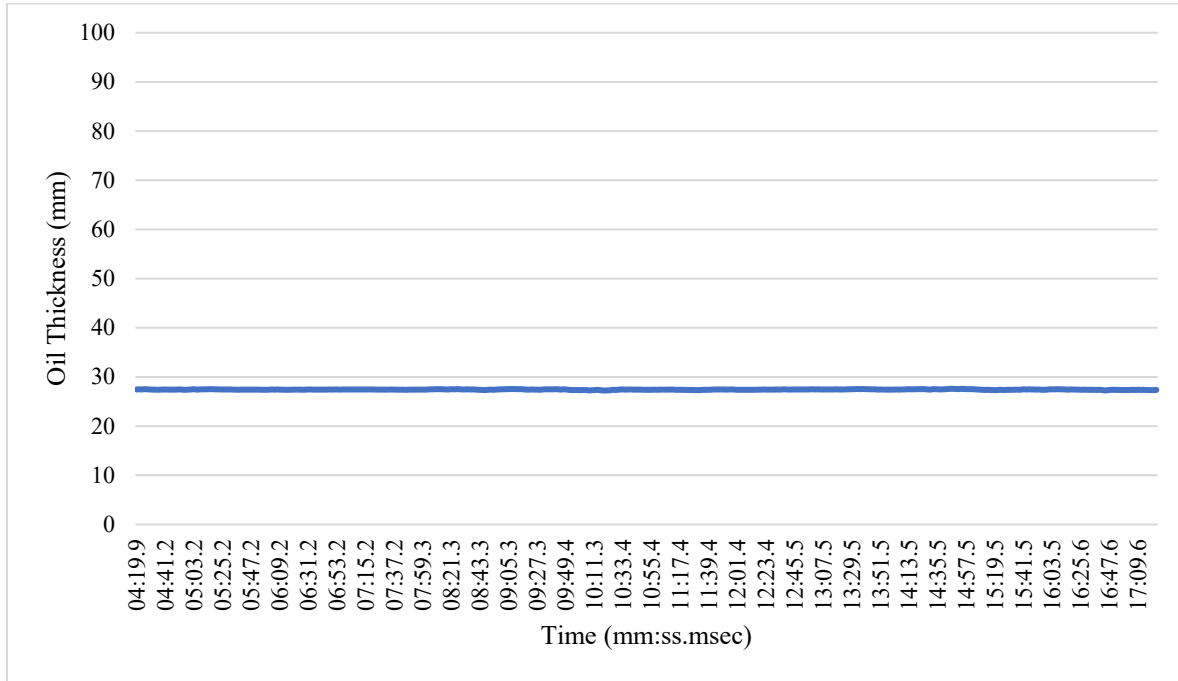


**Figure 3.18: Skimmer mounted oil thickness testing results – static**

### 3.3.9 Skimmer Sensor (Dynamic)

In addition to the static testing, the skimmer mounted sensor was tested under dynamic conditions. The device was held by hand and immersed in a sinusoidal motion in and out of the oil/water mixture. The combined inference system was used. The sample of the results is plotted in Figure 3.19.
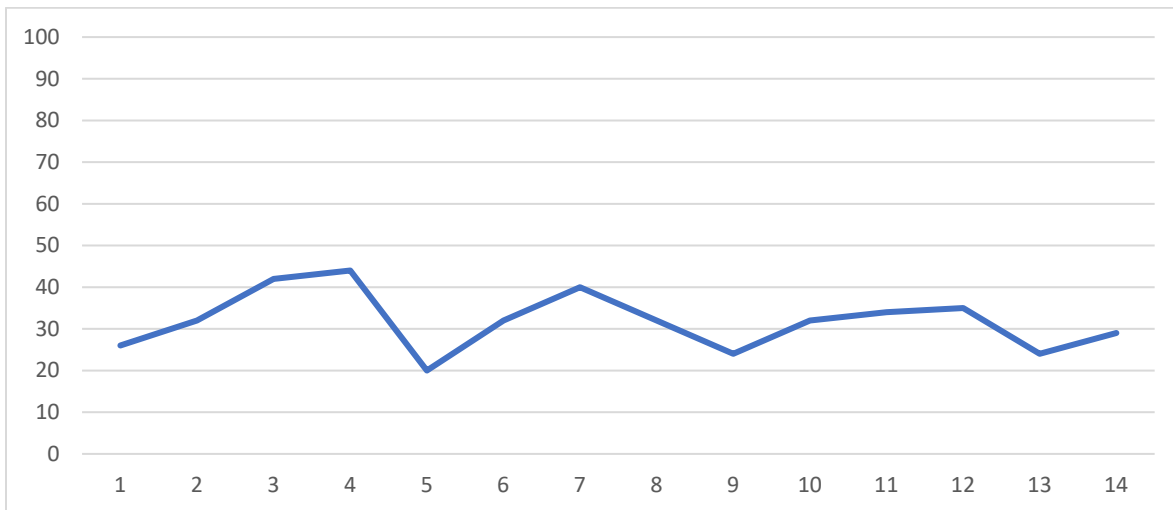


**Figure 3.19: Dynamic testing results – skimmer mounted sensor**

The average of the measurements was 31.85 mm with a standard deviation of 7 mm. This makes the average of absolute error less than 3 mm, and the standard deviation is smaller than the resolution of the sensor which is 10 mm. Note that the results were not filtered or smoothed by moving averages. Despite the movements of the sensor and the liquid, the result of the algorithm was good. This was enhanced in future iterations through filtering and by introducing a measure of standard deviation.

## 3.4 Third Iteration Enhancements of the Measurement Algorithm

In this iteration, significant analysis was done, and changes were made to the algorithm.

### 3.4.1 Signal Analysis

We started this phase by analyzing sensor signal behavior in order to drive the development of the filtering technique that can handle the fluctuations in the sensor measurements under dynamic conditions. The filtering should be designed to be simple and adaptive to the motion characteristics. For this purpose, we performed a detailed analysis of the sensor signals against different types of oil. In summary, the behavior of the sensor under continuous dynamic conditions could be summarized by three major states. Each of these states is demonstrated in Figure 3.20.
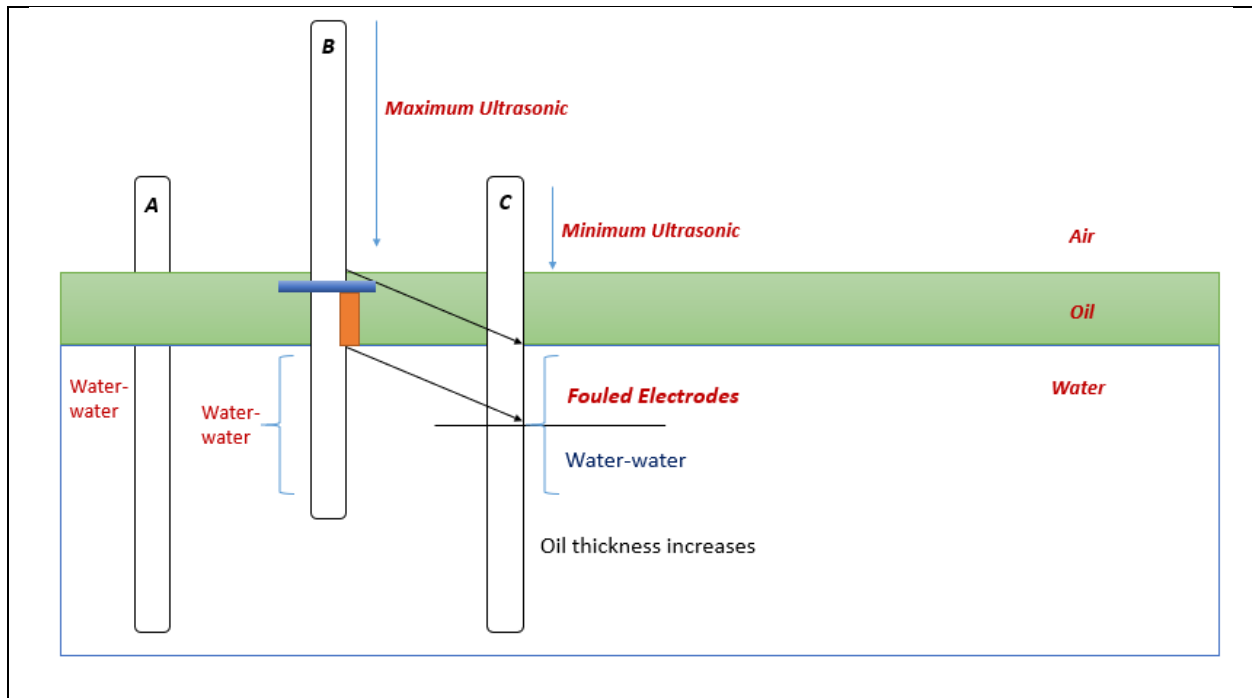


**Figure 3.20: Schematic showing the reduced set of dynamical states**

In the first state **(A)**, the sensor is in a static medium and the voltage signals do not change. In this case, the water-immersed section could be estimated by detecting the electrodes labeled as water-water (i.e., the electrodes that were immersed in water and stayed in water during the sensor motion). These electrodes are characterized by a high relative change and low temporal change (stable). As described previously, this region could be estimated using an SVM model.

The oil thickness is accurate in this case since the water-water electrodes represent the actual water section.

In the second state **(B)**, the sensor moves upwards, and part of the water-water electrodes moves into the oil phase (we label them as water-oil). The voltage signals of the water-oil electrodes change due to contact with oil. Our experiments showed that this change depends on the type of oil and on the time spent in water and oil phases. For example, when dealing with crude and thick oil types, the rate of change is relatively fast. However, when dealing with light oil types, the voltage signals showed a low rate of increase. To deal with all cases without depending on the exact types and properties of the oil, we suggested focusing on detecting the water-water electrodes by relying only on a one-class classifier. Accordingly, the classifier detects the water-water electrodes and labels the water-oil electrodes as outliers despite their actual values or amount of amplitude change. Calculating the water-immersed section using the water-water electrodes is expected to lead to accurate oil thickness.

To demonstrate the importance of using a one-class classifier, we plotted a set of intensity signals obtained from the liquid-immersed electrodes during one of the experiments in which the sensor is moving in vertical direction. The distances measured by the ultrasonic sensor reflecting the motion profile are shown in Figure 3.21. The signals obtained from the liquid-immersed electrodes are shown in Figure 3.22. In this experiment, a light engine oil sample was used. By observing the behavior of the signals, we note that the signals labeled 37, 38, and 39 showed a dynamic behavior due to their contact with oil. On the other hand, the signals labeled 40 – 48 showed consistent and stable behavior since they did not change their phase (water-water). The signals showed a clear difference between the two categories in terms of behavior. This fact further motivated the use of a one-class classifier to detect the water-water electrodes while dealing with the other signals as outliers.
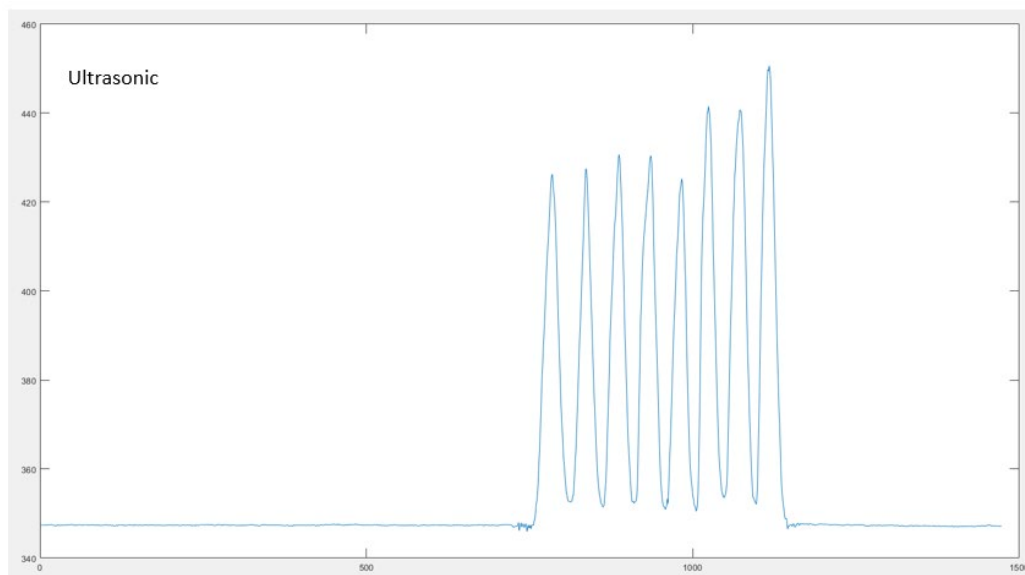


**Figure 3.21: Ultrasonic measurements recorded during the experiment**
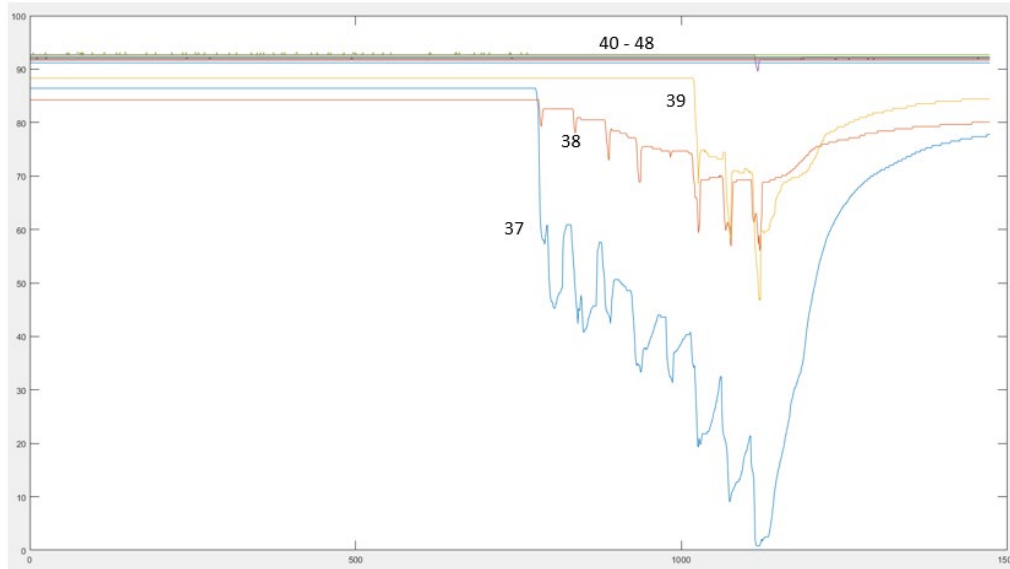
**Figure 3.22: Liquid-immersed intensity signals (relative change)**

In the third dynamic state **(C)**, the sensor moves downwards, and the electrodes immersed in water are of two types: the first one is the water-water electrodes that did not enter the oil region, whereas the second type is the fouled electrodes which we will name as the oil-water electrodes. In this case, the water-water electrodes represent a part of the actual water section. Thus, calculating the water section using the number of water-water electrodes only will result in an overestimation in the oil thickness. To handle this issue, we suggest relying on the ultrasound sensor above to limit our updates to instants where the capacitive sensor is known to give the correct thickness. Completing this analysis was essential to drive the implementation of the filtering strategy.

### 3.4.2  Discretization of Motion

As we mentioned before, in the data acquisition phase, we are storing a set of sequential values for each electrode. Thus, each electrode is represented by a discrete signal or a short time-series containing the set of intensities measured at a constant sampling rate during the temporal window. To investigate the local characteristics of the signals, we used a short window size of 10 samples within a duration of 1 second. Even if the sensor movement is non-linear, we can assume that the values taken during this short window were recorded during a linear portion of the motion profile. The motion of the sensor during this small window is categorized into one of three cases: increasing (sensor moving up), decreasing (sensor moving down), or stable. These cases could be inferred using the distances measured by the ultrasonic sensor as shown in the illustration in Figure 3.23.
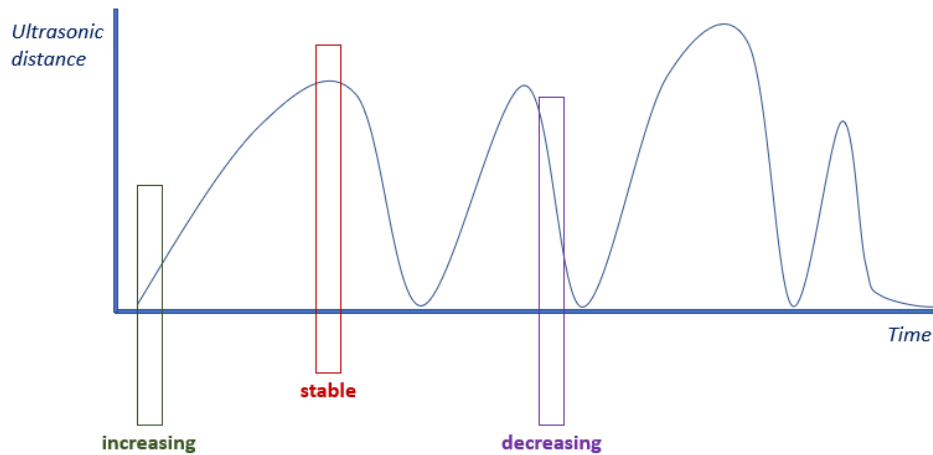
**Figure 3.23: Illustration of using temporal windows to detect linear motion.**

### 3.4.3   State Detection

First, we tried to detect the motion based on ultrasonic measures. This means that the variation in the sensor position relative to the liquid would cause one or more electrodes to change from one phase to another if it exceeds the width of one sensing unit gap. For example, for one of the handheld sensors, this width is 3 mm. Thus, we could use the width as a threshold to detect if the sensor moved or not. After recording five measurements (width of the temporal window in this test case) we calculate the slope of the ultrasonic measurements by subtracting the first distance from the last distance.

The sensor is assumed to be moving upwards if the slope is greater or equal to 3 mm, downwards if the slope is less than or equal to -3 mm, or stable if it is between -3 mm and 3 mm. For instance, in one test, we configured the linear actuator to move vertically while stopping 5 seconds at the top and bottom positions. The ultrasonic distances were recorded with the output of the algorithm which was configured to produce 1 for the upward state, -1 for the downward state, and 0 for a stable state. The results are plotted in Figure 3.24. The results of decreasing the stop duration to 1 second are shown in Figure 3.25.
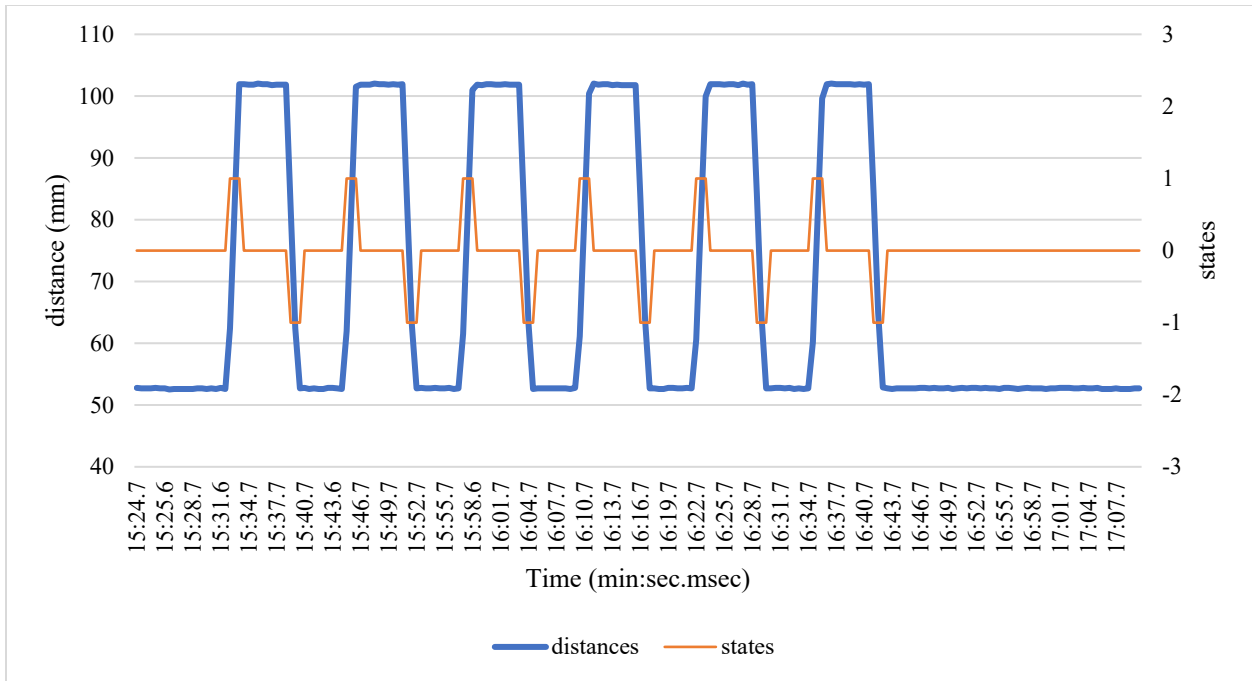
**Figure 3.24: Result of testing state detection algorithm (stop duration: 5 seconds)**
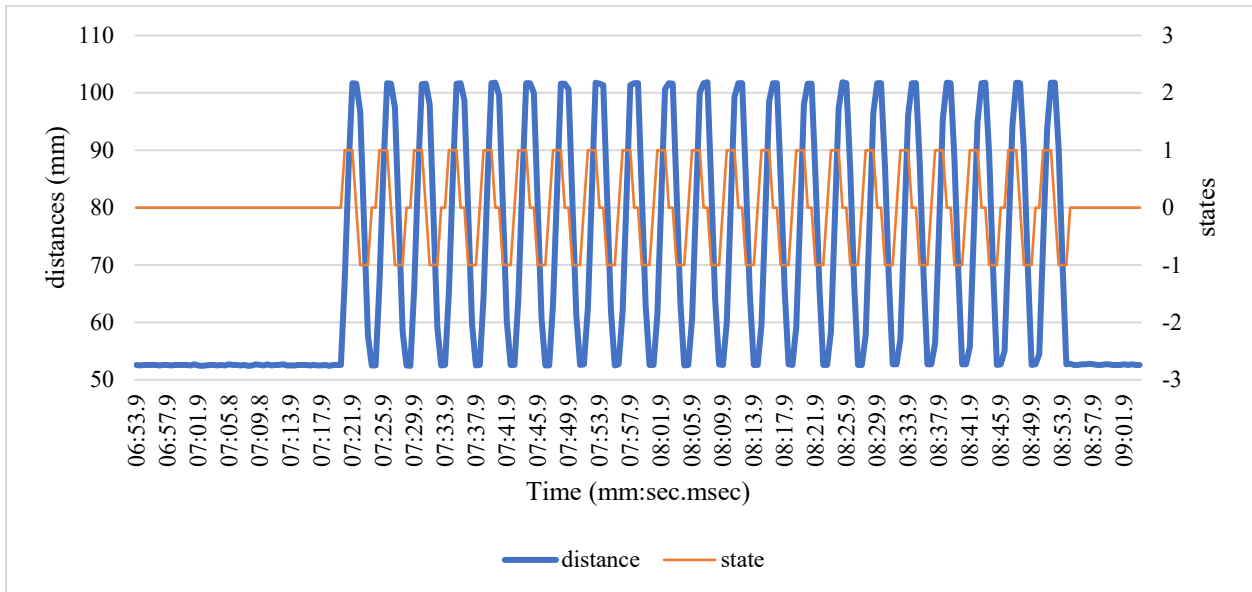


**Figure 3.25: Result of testing state detection algorithm (stop duration: 1 second)**

As shown, the state detection algorithm was able to detect the dynamic state of the sensor accurately in the two cases. Note that by counting the number of rising and falling edges during a certain amount of time, an indicator for the frequency of the motion could be obtained. This algorithm showed that it may be used to give information on the dynamic state of the sensor and the frequency of the motion.

113

### 3.4.4 Signal Types

As described previously, the main aim of the capacitive sensor is to detect the water-immersed cells. After detecting the water cells, we calculate the water-partition of the sensor then the oil thickness is inferred. The major problem with the detection of the water-immersed cells is that they need some time to converge to a large intensity value. To demonstrate this fact, we plot the intensities of one sensing cell while moving between oil and water phases. For this purpose, the sensor was mounted on a linear actuator that moves vertically up and down and stops in each state for a certain amount of time. In this case, the actuator was programmed to stop for 1 minute when the sensing cell 17 is in oil or water. The intensities were calculated by the microcontroller and reported to a laptop using serial communication. The intensities are plotted in Figure 3.26 and Figure 3.27.
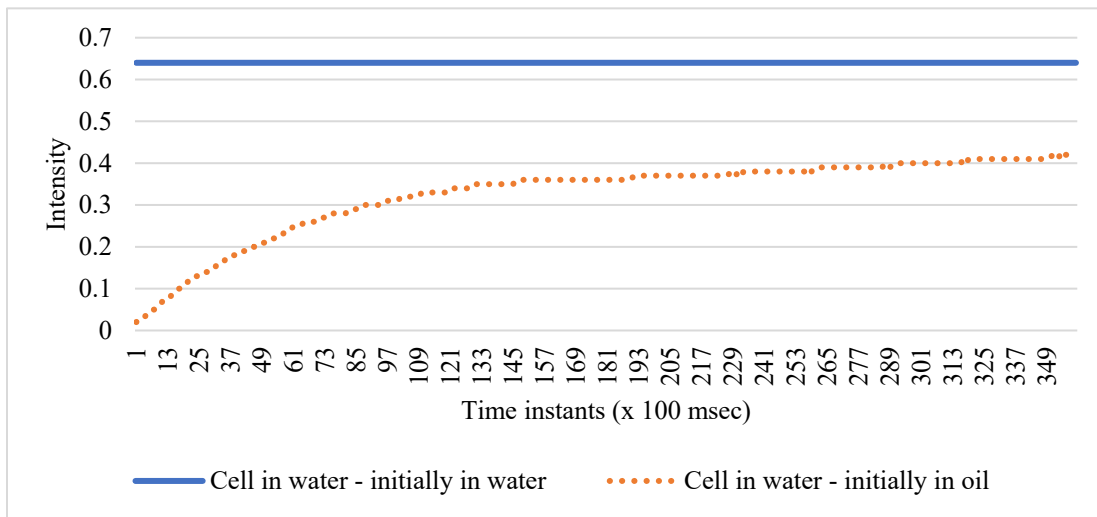


**Figure 3.26: Intensity of a cell immersed in water (initially in water and oil)**
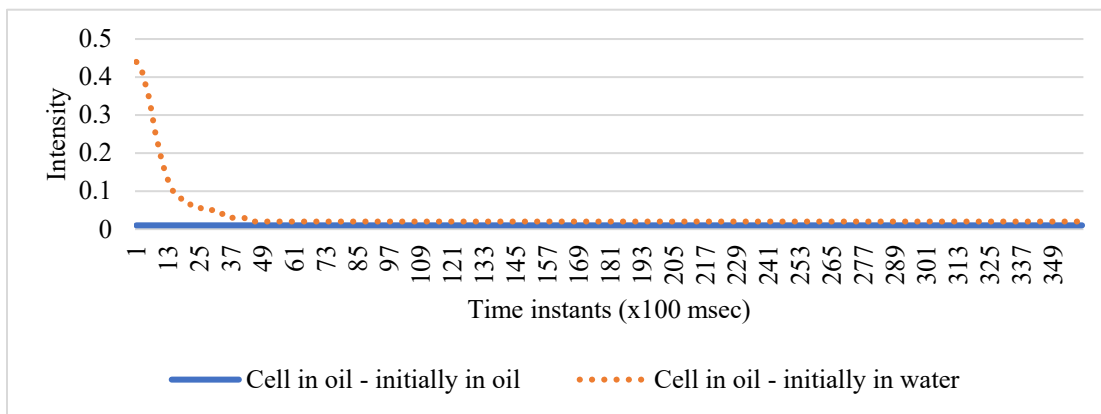


**Figure 3.27: Intensity of a cell immersed in oil (initially in water and oil)**

Based on the intensities plotted, we can say that the intensity signal of a sensing cell could be classified into four classes: water-water, oil-oil, water-oil, or oil-water depending on the shape of the signal. These cases are illustrated in Figure 3.28.
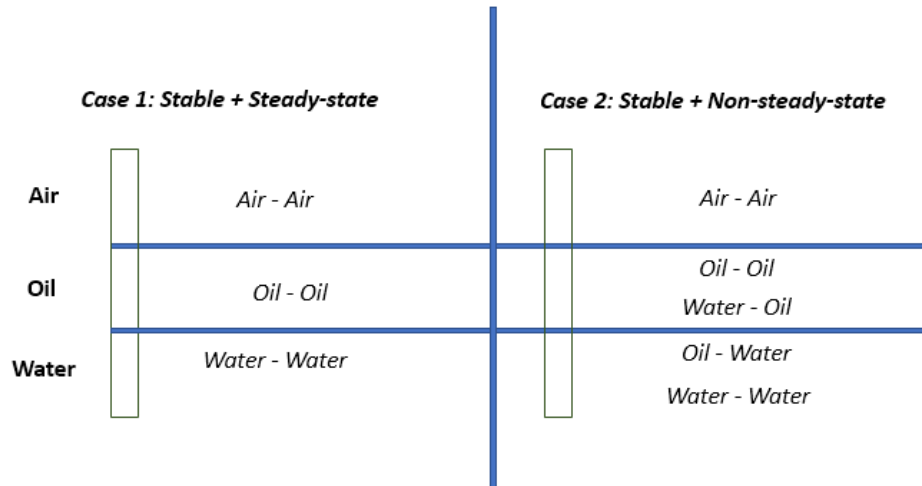
**Figure 3.28: Illustration of different types of signals depending on the state of the sensor.**

The four signal types could be described as:

1- **Water-water:** The electrode was in water under steady-state conditions before the movement and stayed in water during the temporal window.

2- **Oil-oil:** The electrode was in oil under steady-state conditions before the movement and stayed in oil during the temporal window.

3- **Water-oil:** The electrode was in the water before the window and moved to the oil phase. The intensity values decrease in a fast manner until it reaches the minimum value.

4- **Oil-water:** The electrode was in oil and moved to the water phase. The intensity signal continuously increases when the cell moves from oil to the water phase. The signal takes different slopes as time passes. Initially, the slope is high and decreases with time.

### 3.4.5 Classification of Water-Immersed Cells

Based on the analysis provided above, using an indicator for the shape of the signal in our classifier is very important to ensure a fast response rate of the sensing system while attaining high accuracy under dynamic conditions. The slope feature that was used in the SVM classifier developed before aimed to capture this concept. However, additional experiments showed that the slope feature was affected when using short temporal windows. To solve this problem, we introduced a new feature that can capture the shape of the signal more efficiently called "trend". The trend feature is calculated by subtracting two simple counters. The first counter "increment counter" is an integer variable that counts how many times the intensity signal increased. The second counter is the "decrement counter" which counts how many times the signal decreased. The trend is calculated as:

$$Trend = increment\ counter - decrement\ counter$$

After implementing the new feature calculation method into the microcontroller code, a dataset was gathered using the experimental setup. An image showing the dataset with the class labels is shown in Figure 3.29.
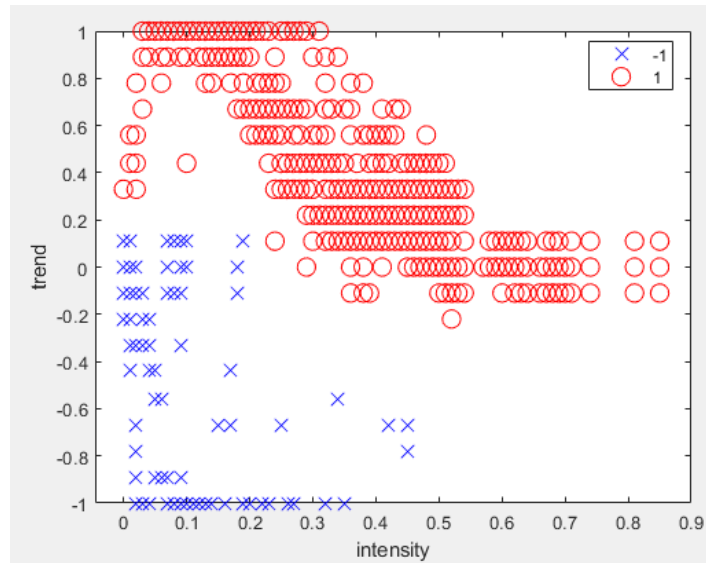
**Figure 3.29: Sample from the dataset in two-dimensional vector space.**

As shown in the figure, the trend feature plays a major role in differentiating between decreasing and increasing signals referring to oil and water samples respectively.

### 3.4.6 SVM Development and Kernel Selection

To select the best kernel for the SVM classifier, we tested several options and selected the solution that best fits the data. We started by the simplest hypothesis assuming that the two classes are linearly separable. Using the dataset collected, we used the python "sickit-learn" library to train a linear SVM model and the coefficients obtained were: Weights = [7.3850897 4.64482392], Bias = [-2.32931612]. The linear classifier is illustrated in Figure 3.30.
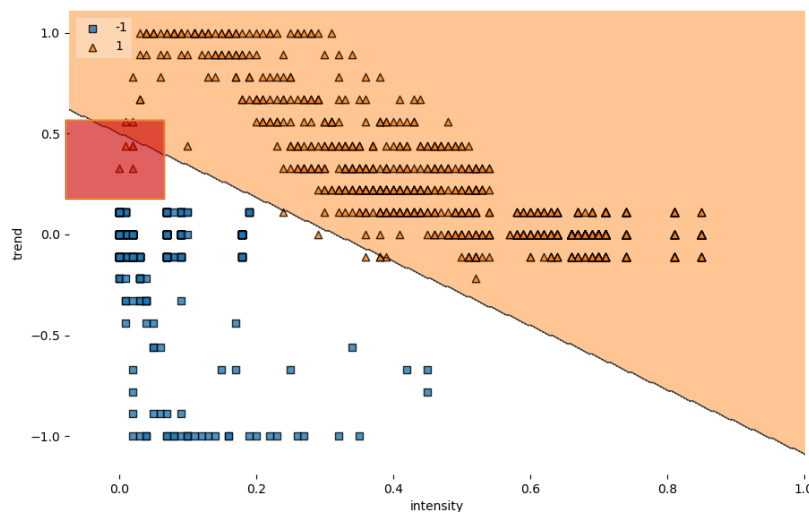


**Figure 3.30: Result of fitting a linear SVM to the training set.**

This test showed that not all samples could be classified by the linear boundary. Misclassification is most probable in the region where the intensity is small and the trend is

116

positive but less than 0.5 (indicated by the red square in the figure). This region represents the water-immersed electrodes that moved from the oil phase to the water phase (oil-water). Based on this observation, the linear model is expected to show the largest error at small time intervals after the sensor moves downwards (cells moving from the oil phase to the water phase).

Another popular kernel used in the context of non-linearly separable datasets is the Gaussian RBF kernel. This kernel transforms the input samples into a higher dimensional space where they can be linearly separated. Then, the obtained decision boundary is projected into the original space to perform classification. The result of training an RBF kernel SVM is illustrated in Figure 3.31.
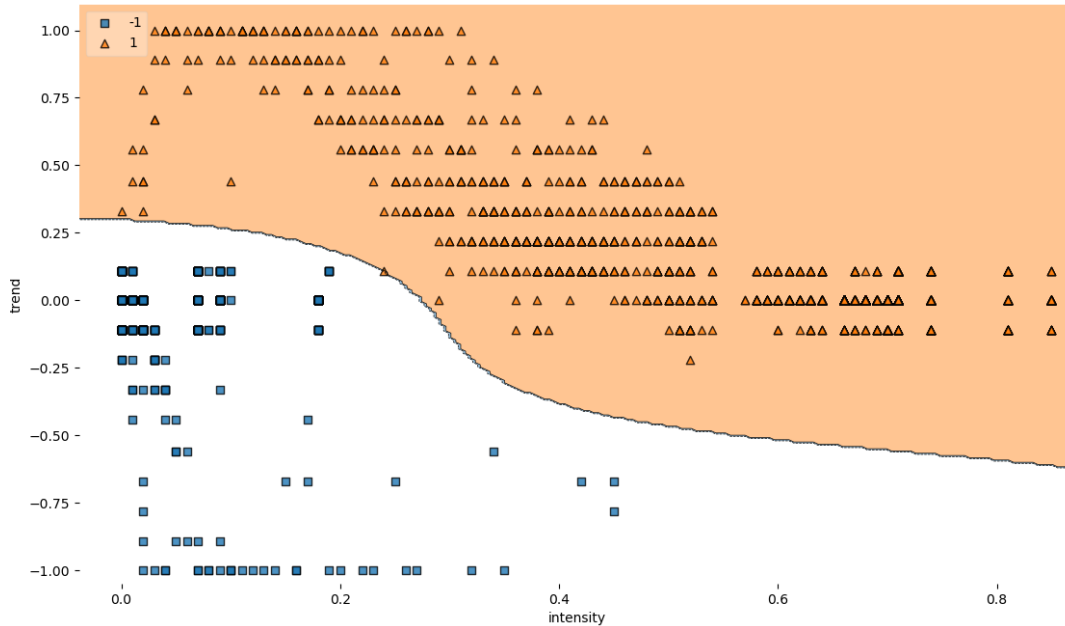


**Figure 3.31: Result of fitting an RBF kernel SVM to the training set.**

As shown in the figure, the RBF kernel SVM produced a non-linear decision boundary that can adapt to the distribution of the dataset and resulted in 100% accuracy on the testing set. Based on the obtained results, we deduced that the RBF kernel SVM is preferred over the linear kernel SVM since it produced 100% accuracy and created a non-linear decision boundary. However, in our analysis, we should take into consideration the disadvantages of using RBF kernels. First, unlike the linear kernel, the RBF kernel SVM is not parametric and its complexity grows with the size of the training set. This means that the RBF kernel SVM is more expensive to train than the linear SVM. Besides, the projection of the two-dimensional input samples into the higher-dimensional space is computationally expensive during prediction. Furthermore, we have additional hyperparameters to tune, so the model selection is more expensive as well. It is important to note that we have also tested SVMs with sigmoid and polynomial kernels starting from a degree of 2 to a degree of 8, however, they did not show any promising results.

### 3.4.7  Online Filtering Strategy

The online filtering algorithm builds on the information related to the sensor motion. We have two layers of filtering. In the first layer, we aimed to avoid the measurements calculated when the sensor is experiencing a fast motion within the short temporal window (1 second). To do this,

we created a function that takes the trend of the ultrasonic measurements as an input and outputs a membership value that controls how much this measure should be used to alter the overall filtered thickness. This function is a triangular function centered around zero and limited by +0.5 and -0.5. The function is illustrated in Figure 3.32.
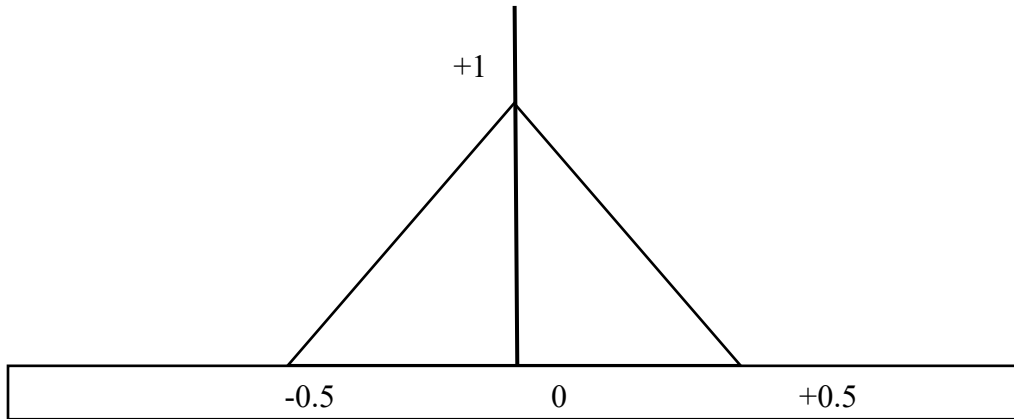


**Figure 3.32: Triangular membership function for the stable fuzzy region.**

As we described earlier, the trend feature ranges between -1 and +1. The x-axis represents the value of the input (ultrasonic trend), and the y-axis represents the output value which ranges between 0 and 1. The sensor is considered stable in the zone between -0.5 and +0.5. However, it is most stable when the trend is zero. In other words, this function takes that trend value and outputs a value between 0 and 1 representing how much the sensor is stable; 1 is most stable. This type of function is known as a triangular fuzzy membership function and is widely used in fuzzy logic applications.

The second layer of filtering is a traditional smoothing filter where the instantaneous measure is added to the overall measures by a small weight to avoid jumps in the overall measurements. This filter is applied as:

$$Filtered\_thickness = 0.8 * filtered\_thickness + 0.2 * instantaneous\_thickness$$

The filtering strategy is simple and is applied without the need for any additional libraries or complexities. The triangular function is expressed by a set of if-else conditions and the smoothing filter is applied in a single equation. To test the performance of the filtering strategy, we performed several tests as described next.

### 3.4.8 Online Testing

To test the performance of the filtering strategy, the sensor was mounted on the experimental setup and several motion profiles were used. Samples of the results obtained from each profile are discussed below.

**1- Actuator speed: 40 mm /sec – Span of motion: 5 mm - Stop duration: 5 seconds**



|  | Unfiltered | Filtered 1 | Filtered 2 |
|---|---|---|---|
| **Average measurement** | 33.70 | 33.74 | 33.75 |
| **Standard deviation** | 1.66 | 1.22 | 0.38 |
| **Average absolute error** | 1.70 | 1.74 | 1.75 |

As shown above, the two filtering methods provided good results with an absolute error of less than 2 mm. Note that the actual thickness is around 32 mm. However, the overall filtering provided the most stable result with a standard deviation of less than 0.5. Note that this test case represents small movements by the user hand in which the span of movement is around 5 mm.

**2- Actuator speed: 40 mm /sec – Span of motion: 10 mm - Stop duration: 5 seconds**
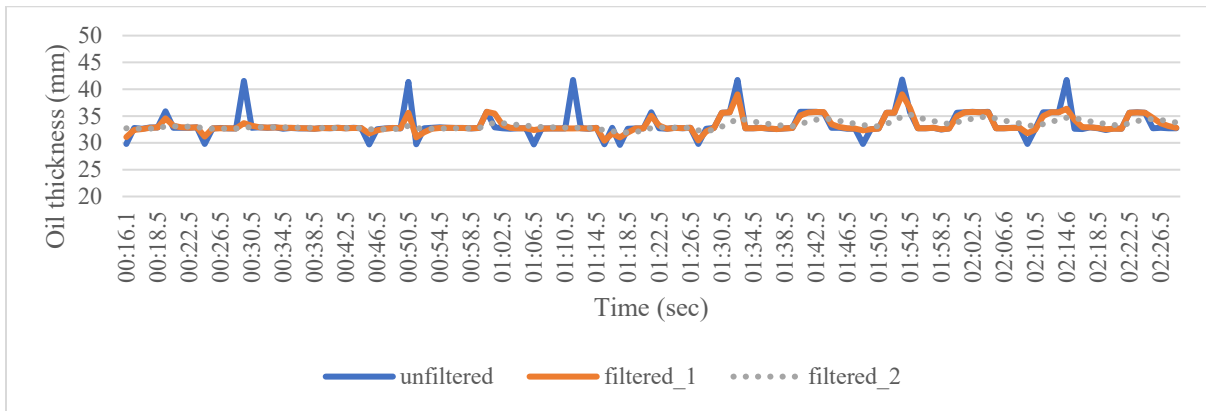


|  | Unfiltered | Filtered 1 | Filtered 2 |
|---|---|---|---|
| **Average measurement** | 33.41 | 33.31 | 33.29 |
| **Standard deviation** | 2.29 | 1.45 | 0.72 |
| **Average absolute error** | 1.41 | 1.31 | 1.29 |

With the increase of the span of motion, the spikes in the unfiltered measure increased, and the standard deviation also. However, the absolute error is still less than 2mm and the overall filtered result is stable and accurate (filtered_2).

### 3- Actuator speed: 40 mm /sec – Span of motion: 20 mm - Stop duration: 5 seconds
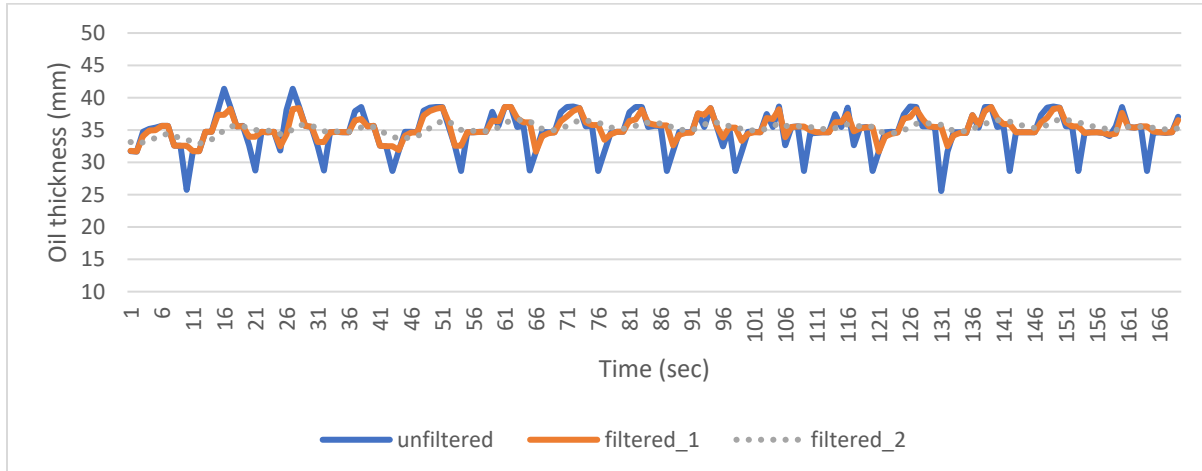


|  | Unfiltered | Filtered 1 | Filtered 2 |
|---|---|---|---|
| **Average measurement** | 34.83 | 35.3 | 35.2 |
| **Standard deviation** | 2.86 | 1.67 | 0.80 |
| **Average absolute error** | 2.83 | 3.30 | 3.26 |

Despite that the span of the motion was increased to 20 mm, the absolute error increased only to around 3 mm. However, as shown in the figure, the real-time measures smoothing is necessary to obtain a smooth instantaneous result.

### 4- Actuator speed: 40 mm /sec – Span of motion: 40 mm - Stop duration: 5 seconds
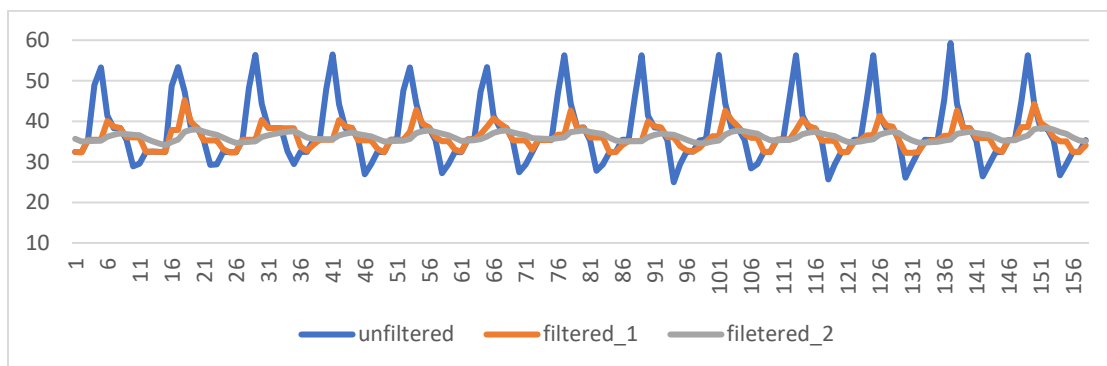


|  | Unfiltered | Filtered 1 | Filtered 2 |
|---|---|---|---|
| **Average measurement** | 37.49 | 36.1 | 36.19 |
| **Standard deviation** | 7.58 | 2.67 | 0.98 |
| **Average absolute error** | 5.49 | 4.16 | 4.19 |

120

In this test, the span of the continuous motion is increased to 40 mm, which is around half the sensing range. The error and variability of the unfiltered results increased. However, the overall filtered result still shows good accuracy with an error of 4 mm and high stability with a standard deviation of less than 1 mm. Also, the filtered result is smooth in real-time and doesn't show any large jumps.

## 3.5 Fourth Iteration Enhancements of the Measurement Algorithm (State Detection)

As mentioned previously, the ultrasound sensor, which is continuously measuring the distance to the liquid surface is used to detect the state of the system. The ultrasonic signal is divided into sub-sequences and analyzed sequentially to detect the state of the system. The oil-thickness estimation algorithm works best when the handheld device is stable relative to the liquid surface. Thus, to allow the user to carry and move the device during measurements, the system must be able to detect invalid cases, which include: (1) when the device is out of the liquid, and (2) when the user performs a fast movement such as moving upwards or downwards. In the valid cases, the liquid beneath the sensor may be steady or wavy depending on the environmental conditions. The wavy state of the liquid should not be confused with the dynamic state of the sensor caused by immediate user movements. The main phases of data acquisition are illustrated in Figure 3.33.
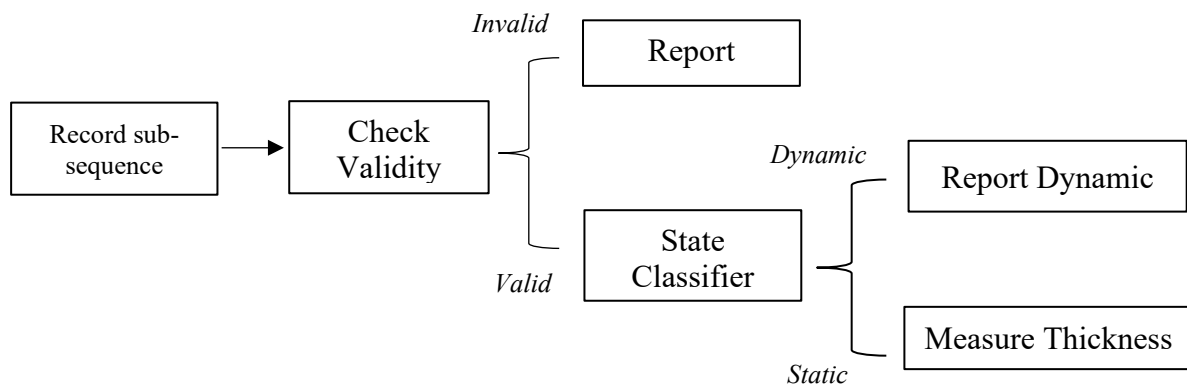


**Figure 3.33: Flowchart of the data-acquisition routine**

The data acquisition routine returns one of three states for each sub-sequence:
1- **Out of range:** if the distances recorded are greater than the maximum allowed distance.
2- **Dynamic:** if the distance signal shows a clear trend; either increasing or decreasing.
3- **Static:** if the distance signal shows a stable behavior; no dominant trend is detected.

Identifying the first case is simple because it relies on detecting several measurements that exceed the maximum valid range. To differentiate between the second and the third case, a classification criterion is required, which can assess from collected distance measurements if the state is static or dynamic.

### 3.5.1  Signal Analysis

To handle the problem of state detection, classification should be performed to differentiate between the static and dynamic cases. Previously, we used a simple threshold-based decision to achieve this goal; we calculated the difference between the largest (maximum) and smallest (minimum) distances in the sub-sequence and compared it to a certain threshold. Although this simple method worked accurately under laboratory conditions, when the sensor was mounted on a linear actuator and the water was in a steady state, it reported several false alarms under realistic testing. By realistic testing, we mean that the sensor is held by the user, and the liquid surface is wavy. Based on the new experimental results, we decided to extract and analyze the ultrasonic signal recorded under different conditions.

We started by acquiring a dataset that contains samples of distance signals under different conditions: 1) stable sensor/stable water surface, 2) stable sensor/wavy water surface, and 3) moving sensor/stable water surface. We programmed the microcontroller to read 10 consecutive distance measurements and send them to the computer in a continuous manner. Each message contains ten distances recorded sequential, at a sampling rate of approximately 100 milliseconds (*i.e.*, one message received per second). To acquire data samples related to the three test cases, three experiments were performed. In the first one, the sensor was held by the user in a static mode and the water surface was kept steady. In the second experiment, the sensor was held static, but slosh waves were introduced to the liquid by shaking the water container. In the third experiment, the water was steady, but the sensor was moved up and down in a continuous and fast manner. Samples of the different signals obtained from these experiments are shown in Figure 3.34.
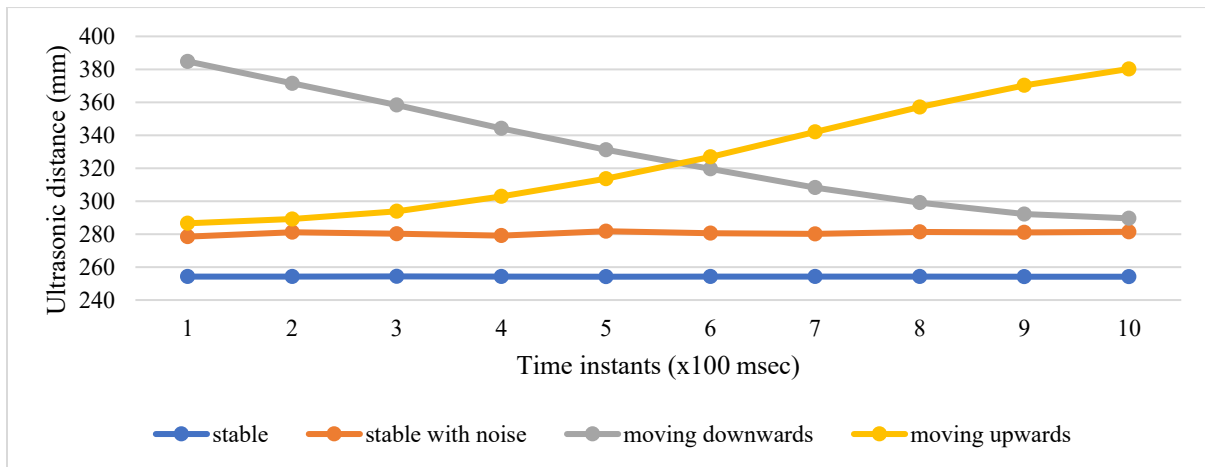


**Figure 3.34: Samples of raw ultrasonic signals obtained from state detection experiments.**

To remove the bias caused by the position of the sensor, we normalized the signals by subtracting the mean of each signal. The normalized signal samples are plotted in Figure 3.35.
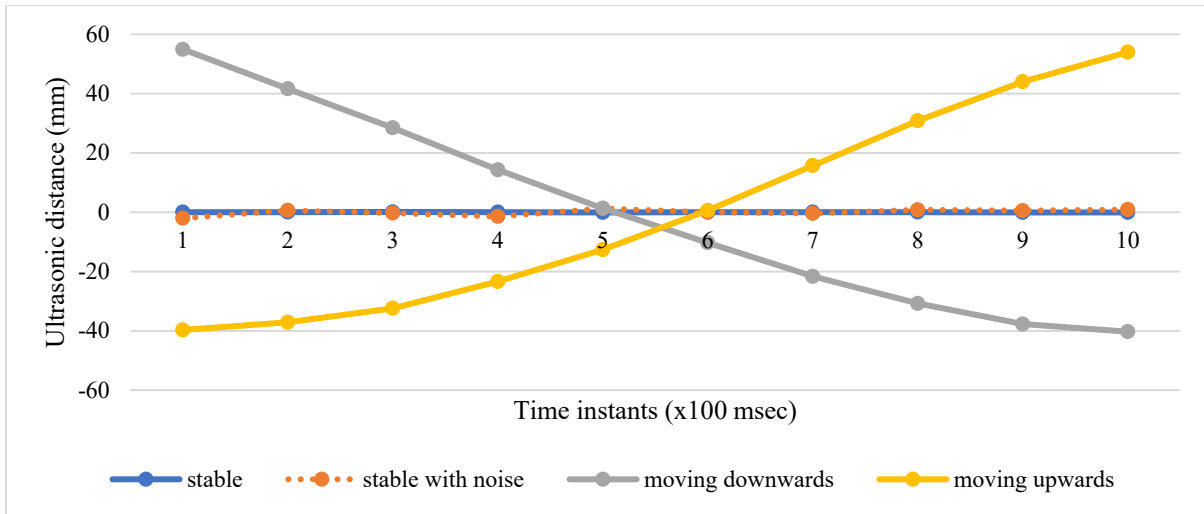
**Figure 3.35: Samples of normalized ultrasonic signals obtained from state detection experiments.**

As shown in the figures, the signals obtained from different test cases showed a clear difference in their shape. For instance, the signal recorded under static mode showed no trend. The signal taken during slosh waves showed some additional random noise but not a clear trend as in the dynamic cases, moving upwards or downwards. These results showed that the slope of the signal could be used as a major feature for state detection. However, the signal recorded under slosh waves did not show a major difference from the stable signal. This does not explain the false alarms recorded during realistic testing; for this purpose, we repeated the experiments while adding additional slosh waves and recording ultrasonic measurements for a much longer period. Samples from the recorded signals are shown in Figure 3.36 and Figure 3.37.
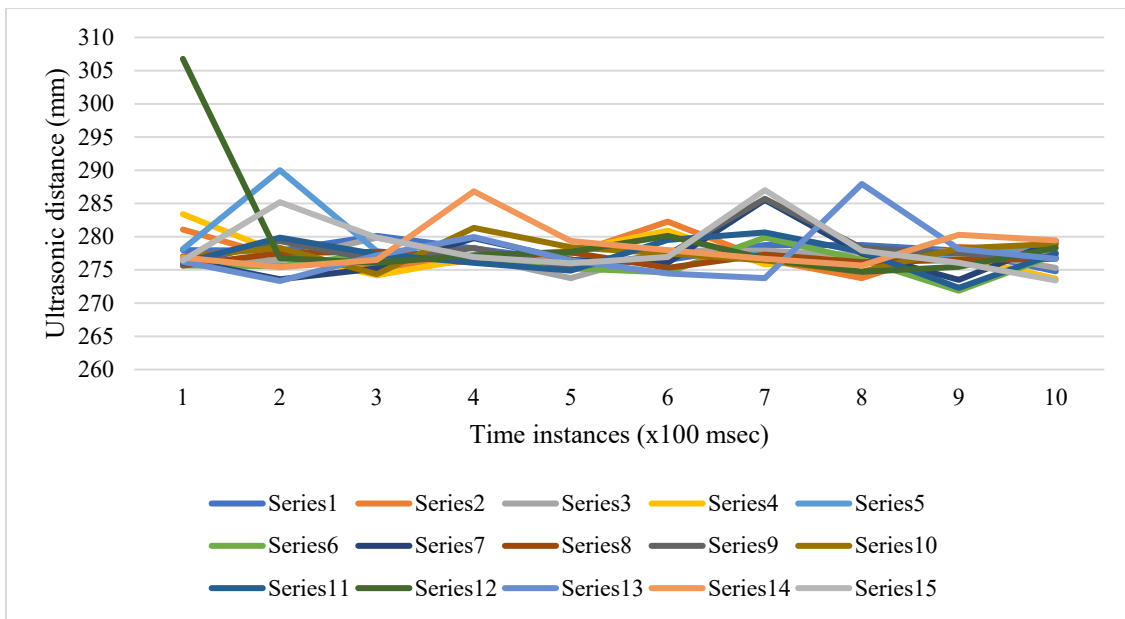


**Figure 3.36: Ultrasonic signals (time-series) recorded during extended slosh waves experiment.**
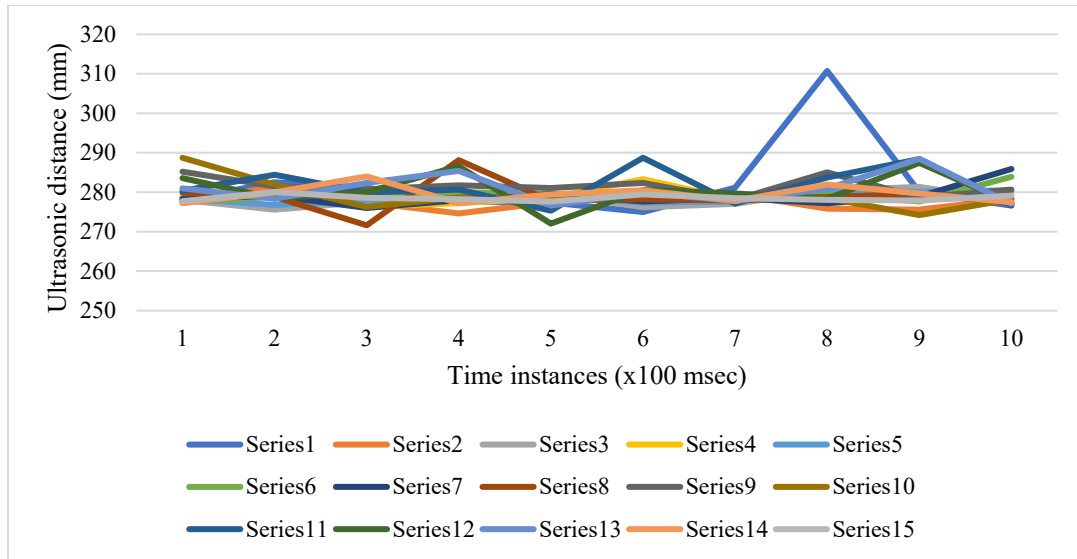
**Figure 3.37: Ultrasonic signals (time-series) recorded during extended slosh waves experiment.**

In each of the figures shown, we plotted 15 time-series selected randomly from the recorded dataset. The y-axis shows the distance measured in mm and the x-axis shows the time instants per 100 msec. Most of the signals are stable with small random noise added to them due to slosh waves; however, in some of the samples, we observed outliers showing a large increase from the average measured distance. Despite these outliers, the general trend of the noisy signals was not affected, and an observer could easily deduce that no major step-change occurred. On the other hand, these outliers could have significantly affected the threshold-based classification technique because it relies on calculating the difference between the maximum value and minimum value.

The results of these experiments were important to understand that slosh waves add high-frequency noise and should be removed from ultrasonic signals before further investigation. As a result, outliers would no longer affect the classification of the state of the sensor as static or dynamic, and more accurate ultrasonic distance measures could be estimated for the sake of calculating oil thicknesses.

### 3.5.2   Signal Filtering and State Detection

To remove high-frequency noise from signals, several methods of low-pass filtering are available in the literature. However, these methods include the analysis of the signals in the frequency domain and the application of specific transforms and algorithms. Since our sensor is microcontroller-based with limited technical capabilities and is required to act in real-time, we preferred to use time-domain analysis techniques for filtering purposes. These methods include basic statistical measures such as max, min, mean, median ...etc. Mainly, we developed three functions to calculate the maximum, mean, and median of each signal and compared the resulting signals plotted in Figure 3.38. The Max signal, plotted in blue, is obtained from the maximum distance from each sample. Note the large increases that occurred in the Max signal due to slosh waves relative to the average, which is around 280 mm. The outliers increased to 310 mm showing a large deviation of around 30 mm. The Mean signal, plotted in orange, showed a more stable behavior than the Max signal but still affected by the outliers. This is because the mean of a set of measurements is easily biased by one large outlier. The Median

124

signal showed the best result where the measurements were stable and not affected by the outliers.

Based on this result, we decided to apply a moving median filter on the ultrasonic signal before deciding on its state as static or dynamic. Also, the median value of each sub-sequence will be used to represent the ultrasonic measurement and calculate the air/liquid interface.
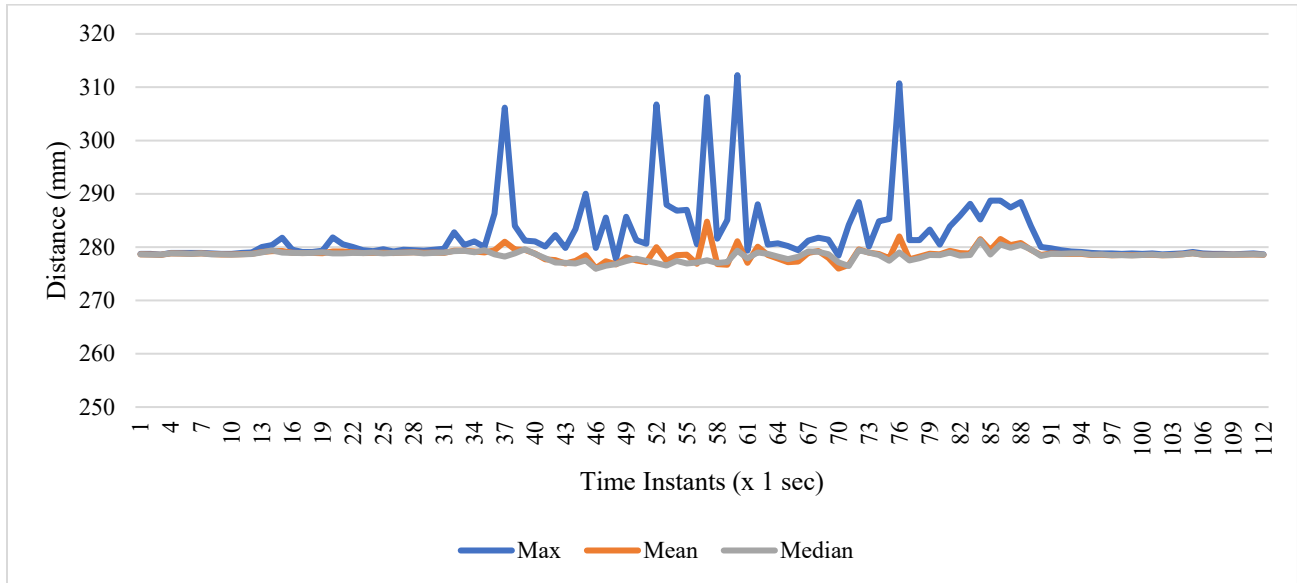


**Figure 3.38: Ultrasonic signals resulting from max, mean, and median filters.**

## 3.6 Final Enhancements of the Measurement Algorithm (Dynamic Measurements)

The proposed measurement algorithm showed very good results in static measurements for both sensors (handheld and skimmer), however it showed mixed results during significant dynamic tests. To mitigate this limitation, enhancements were introduced.

### 3.6.1 Handheld Algorithm Enhancement

For the handheld sensor, we updated the software by adding a condition to detect excessive motion. When excessive motion is detected during the measurement phase a "Dynamic" message is printed on the screen. The threshold for this detection is 10 mm, which can be relaxed or tightened according to the sensitivity requirements of the application.

### 3.6.2 Skimmer Algorithm Enhancement

For the skimmer sensor, the sensor had to support measurements in significant dynamic conditions and cannot just exclude them as done with the handheld sensor. Accordingly, we updated the filtering algorithm to take motion and sudden measurement changes into consideration.

In the main algorithm for skimmer, we calculated the filtered thickness (thickness to be displayed) as a weighted sum between the new calculated thickness and the previous one:

$$filtered\ thickness = w_1 \times old\ thickness + w_2 \times measured\ thickness$$

where $w_1$=1-$w_2$ and $w_2$ = 0.5 f, f being a factor calculated using a triangular membership function shown in Figure 3.39. This function takes the difference between the last two ultra-measurements as an input and gives a value between 0 and 1 as an output. Its maximum output (= 1) is obtained when the input is 0, *i.e.*, the sensor was at rest and no motion was detected. The "0.5" factor is used to limit the influence of new measurement on the sensor's updates; therefore, the maximum value that $w_2$ can have is 0.5. This way, we ensure that the sensor retains some memory to prevent volatility during motion. However, after testing the sensor during a quick up and down movement or a relatively quick down movement, the sensor failed to retain the correct measurement as shown in Figure 3.40 and Figure 3.41.
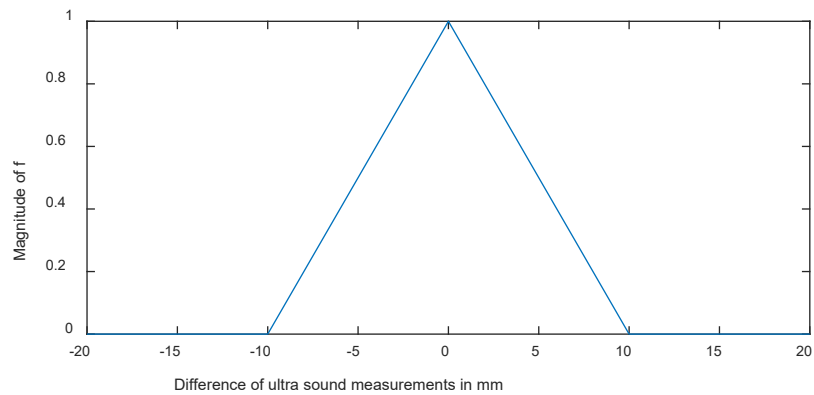


**Figure 3.39: Membership fucniton for factor f.**
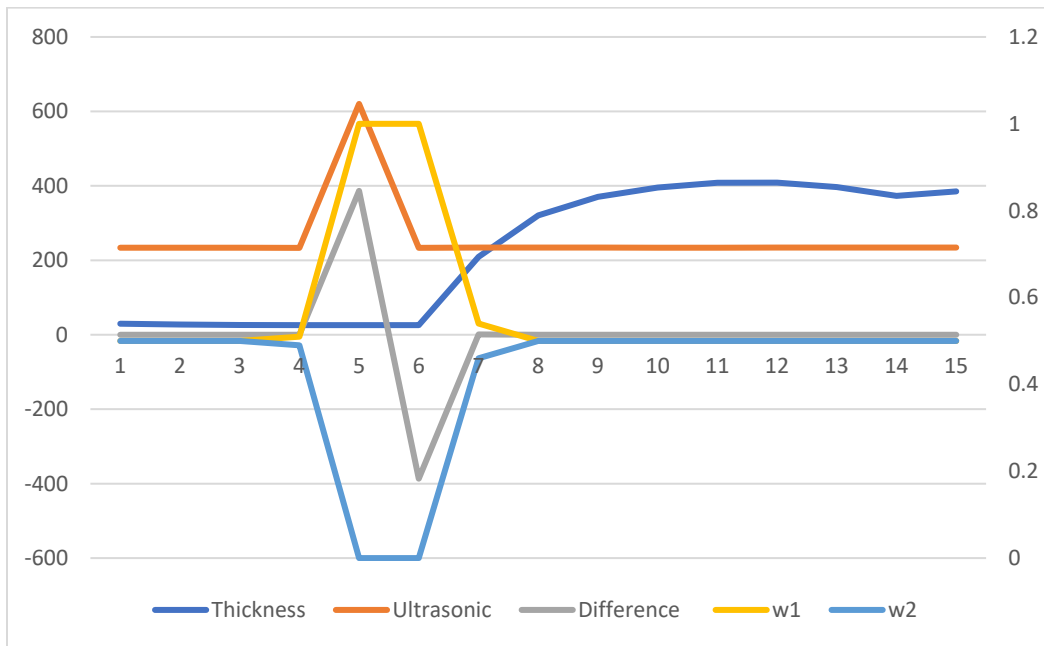


**Figure 3.40: Algorithm parameters and measurement during a quick "Up and Down" motion.**
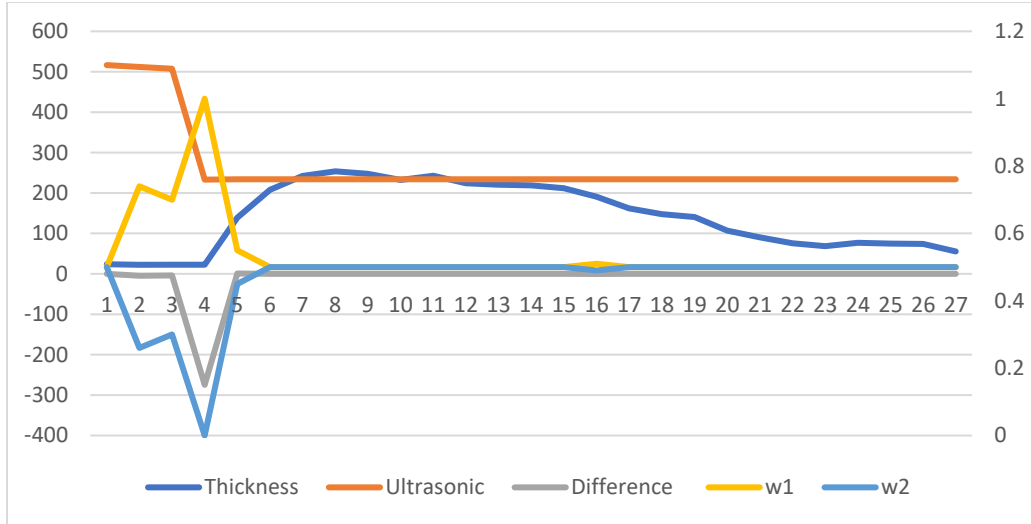
**Figure 3.41: Algorithm parameters and measurement during a down motion.**

Analyzing these results, we observed that when the sensor moved up and down quickly, $w_2$ dropped to zero and $w_1$ increased to 1, thus entering the sensor in a memorizing state for the thickness value. When the sensor returned to its position (Iteration 6), the ultrasonic was at rest, and the values of $w_1$ and $w_2$ were equal again, which implies new measures start getting weighted in again. After Iteration 6, the value of the thickness started increasing drastically. It reached 408mm although the true thickness was 29 mm. This increase was due to oil fouling since the sensor's up and down motion allowed the oil to slide on the board and through the pins. This caused misclassification of the nature of those pins and an undesirable error in calculating thickness. So, although the sensor was at rest, it came after a sudden drop and resulted in significant fouling. The sensor took significant time (approx. 50 sec) to yield a correct estimation of the actual thickness (after the oil fouling ceased.)

From these observations, we conclude two points:
1. instantaneous memory in dynamic measurement is not sufficient since oil fouling effect remains for some time after the motion is completed. Therefore, we should add another factor that factors the recent motion of the ultrasound to compensate for oil fouling effect,
2. thickness values cannot change instantaneously in nature, so, we need another factor to ensure that sudden jumps in measurements are filtered out.

With the addition of these factor, we obtained:

$$w_2 = \alpha \times \beta \times f$$

where Alpha($\alpha$) is a factor that depends on the history of motion (ultrasonic sensor) and Beta (ß) is a factor that depends on the thickness difference between previous and current measurement.

Alpha is calculated also using a triangular membership function, that takes as input the average of the last 5 absolute differences in ultrasound measurements and gives an output between 0.1 and 0.5 as shown in Figure 3.42.
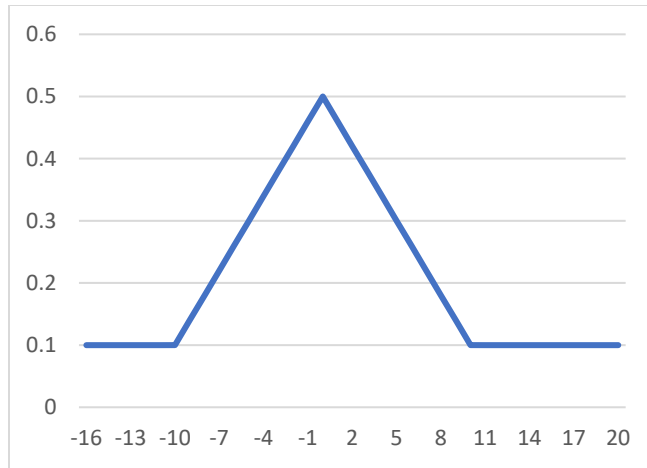
**Figure 3.42: Double sided alpha membership function.**

Like alpha and *f,* beta is an output of membership function that takes as input the difference between the last filtered thickness and new calculated thickness as showing in Figure 3.43. Since fouling leads the sensor to overestimate, the beta membership function was chosen to be one-sided. When the sensor measure drops (which could be expected for example when skimming is being conducted) beta saturates at 1.
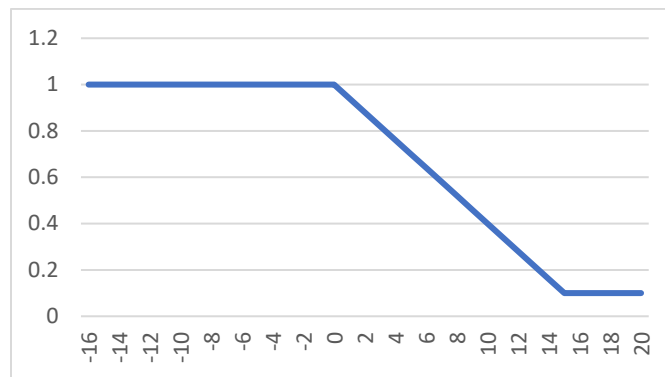


**Figure 3.43: One-sided beta membership function.**

After updating the filtering, we repeated the quick "up and down" test. The results (Figure 3.44) showed noticeable improvement in the estimation and dealing with both oil fouling and movement, where the measurement overshoot was much lower and the return to accurate measurement was much faster.
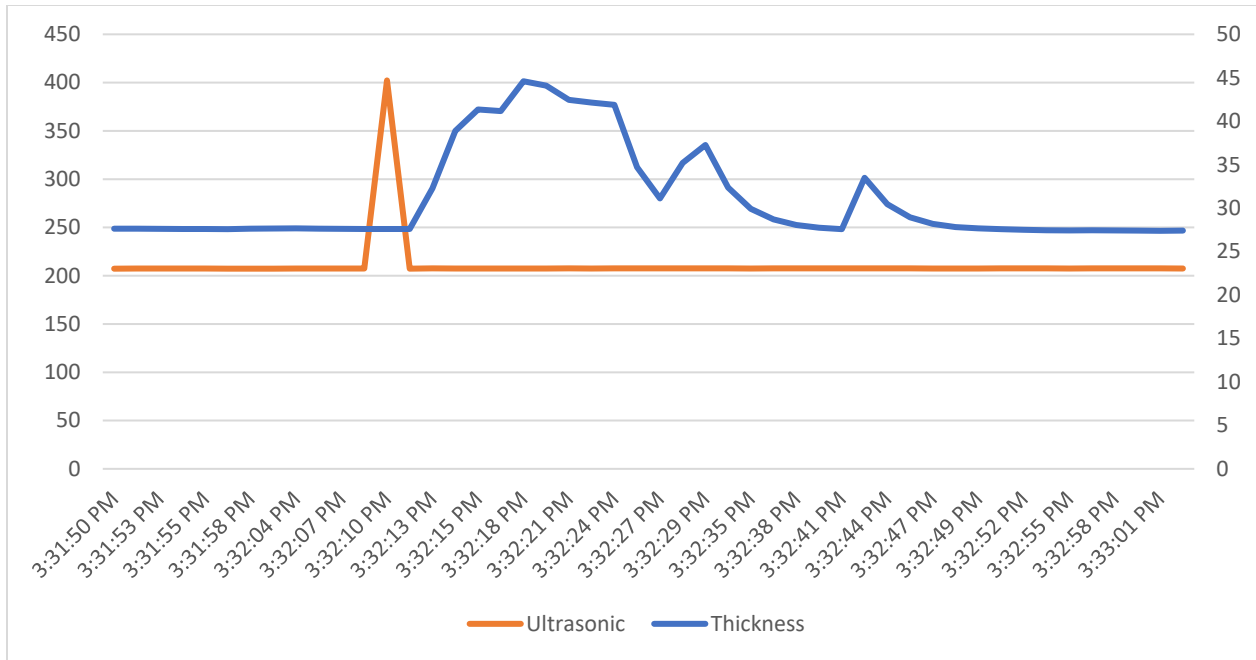
**Figure 3.44: Algorithm measurement during and after a quick "Up and Down" motion after filtering update.**

## 3.7 Development of Desktop Application for Skimmer Sensor

The software application used to receive and store the oil-thickness measurements sent by the skimmer-mount device was developed using the Microsoft C# Windows Forms platform. The user laptop is equipped with a wireless module (Figure 3.45) to receive the measurements and display the results through a user-friendly Graphical User Interface (GUI). The thickness received is plotted in real-time in a window on the left-hand side. Numerical measurements are displayed in a list box next to the chart (Data Messages). Another list box was used to display the communication messages (Received Messages). The oil-thickness measurements received by the application are automatically saved to a text file selected by the user. An image showing the basic GUI of the application is shown in Figure 3.46. A standard deviation list box, battery level label, and temperature label were added to the final version of the application.

The software application was enhanced by adding several buttons allowing the user to start and stop the communication with the COM port. Several functions were added to perform advanced software tasks such as handling the port setup and closure during operation, updating the GUI without blocking the working threads, and parsing of received messages with sub-messages. GUI-based software testing was performed by inputting different commands while the application is running. As a result, error handling strategies were enhanced by adding validation conditions and try-catch functions.

**Figure 3.45: Wireless Module supporting USB connection on Laptop.**
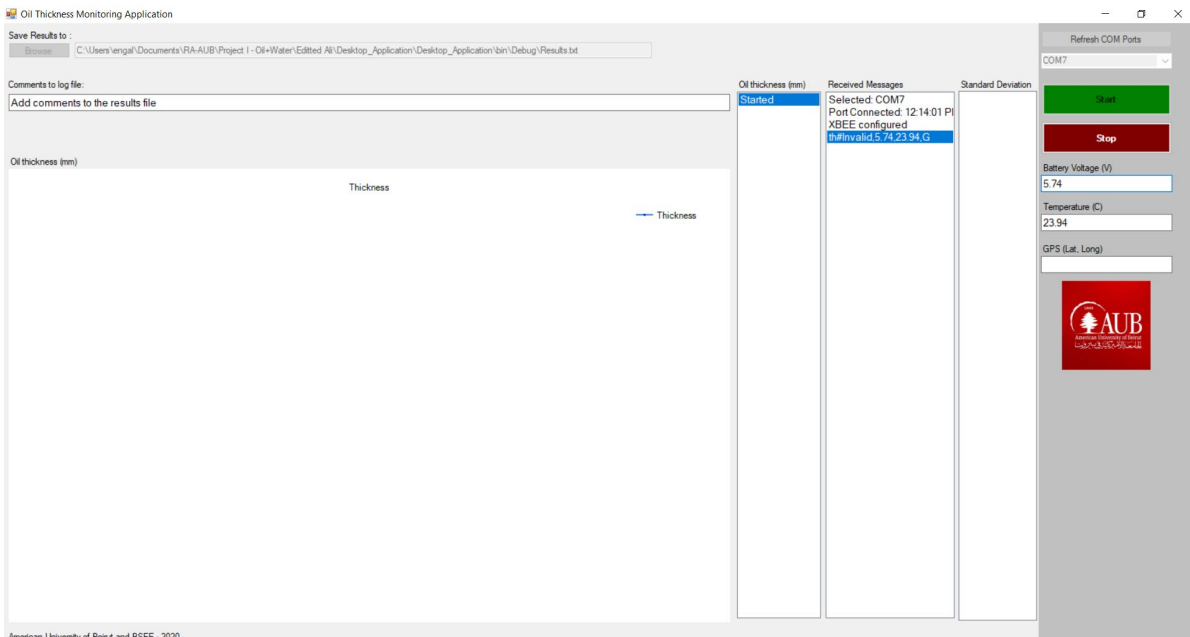


**Figure 3.46: Desktop application for skimmer sensor.**

## 3.8 Modes of Operation of Handheld Sensor

After the implementation and integration of all device components, the software for the menus was developed. The handheld control unit is equipped with four buttons. The roles of the buttons are: Back, Down, Up, and Enter. These buttons allow the user to navigate through the different options found in this sensor. When the device is powered on, three options are displayed in the main menu: Measure, Functions, and Other. The functionalities of the menu and sub-menu are described in the Table 3-7. To reduce accidental power loss, the handheld sensor was also equipped with an auto shutdown feature. The sensor powers off after 60 seconds from being in idle state (no button is pressed).

**Figure 3.47: Main menu on handheld screen**

**Table 3-7: Hanheld menu and sub-menu facultionalties.**

| | | |
|---|---|---|
| Measure Menu | Single Oil | Performs one thickness measurement and displays it. |
| | Continuous Oil | Keeps continuously measuring thickness and displays it. |
| | History | Displays the last 10 oil measurements. |
| Functions | Capacitive | Sends the voltages measured by the 48 electrodes to computer through serial communication. We also added a diagnostic feature for the MPRs, that displays the status of the four MPRs. |
| | Ultrasonic | Displays the distance measured by the ultrasonic. |
| | Power off | Powers off the sensor. |
| Other | GPS | Displays sensor's GPS position. |
| | Temperature | Displays ambient temperature. |
| | Battery voltage | Displays battery voltage level. |

# 4 Experimental Setup and Procedure

The developed sensors were tested at Cold Regions Research and Engineering Laboratory (CRREL) over 10 days during the period of 18 October to 29 October 2021.

The testing included:

- Testing different topologies for both sensors
- Using different types of oils
- Multiple thicknesses
- Static and Dynamic environments

## 4.1 Configurations of Sensors

The skimmer and handheld sensors used in the tests had different configurations (modes of mounting and resolution) (Table 4-1). For each mode, a given number was given to facilitate the data logging and labeling. In total, 4 sensors were used during all the experiments.

| Configuration Number # | Type of sensor | Resolution [mm] | Mounting |
|:---:|:---:|:---:|:---:|
| #1 | Handheld | 2 | No pole |
| #3 | Handheld | 3 | No Pole |
| #4 | Handheld | 3 | Pole |
| #5 | Skimmer | 7 | Handheld & Floater Skimmer |
| #6 | Skimmer | 12 | Handled & Fixed Skimmer |
| #7 | Handheld | 3 | Floater |

**Table 4-1: Configuration matrix for sensors.**

## 4.2 Testbeds

Two main test beds were used:

1- Two glass fish tanks were used for static testing of all sensors (Figure 4.1). The tank was placed on a table for manual measures, and on the floor for measures using the pole.
2- A wave tank was used for dynamic tests (Figure 4.2). An area of almost oval shape (about 184x93inches) was cordoned off using a boom tied to the sides of the wave tank (Figure 4.3). The two skimmer sensors were mounted on a Desmi Termite skimmer, which was then hoisted and lowered into the tank (Figure 4.4).

**Figure 4.1: Glass fish tank used for static tests.**




**Figure 4.2: Wave tank used for dynamic tests.**
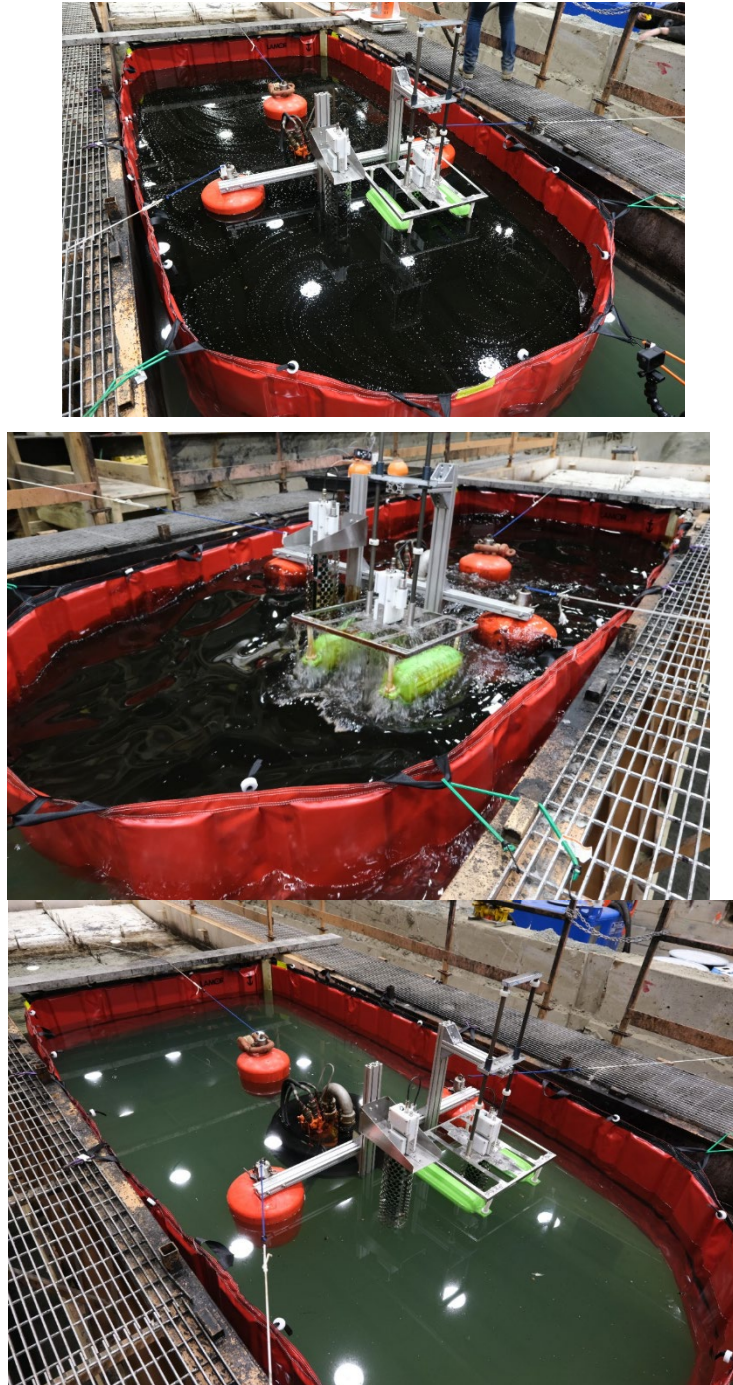
**Figure 4.3: Boom area used for dynamic tests.**
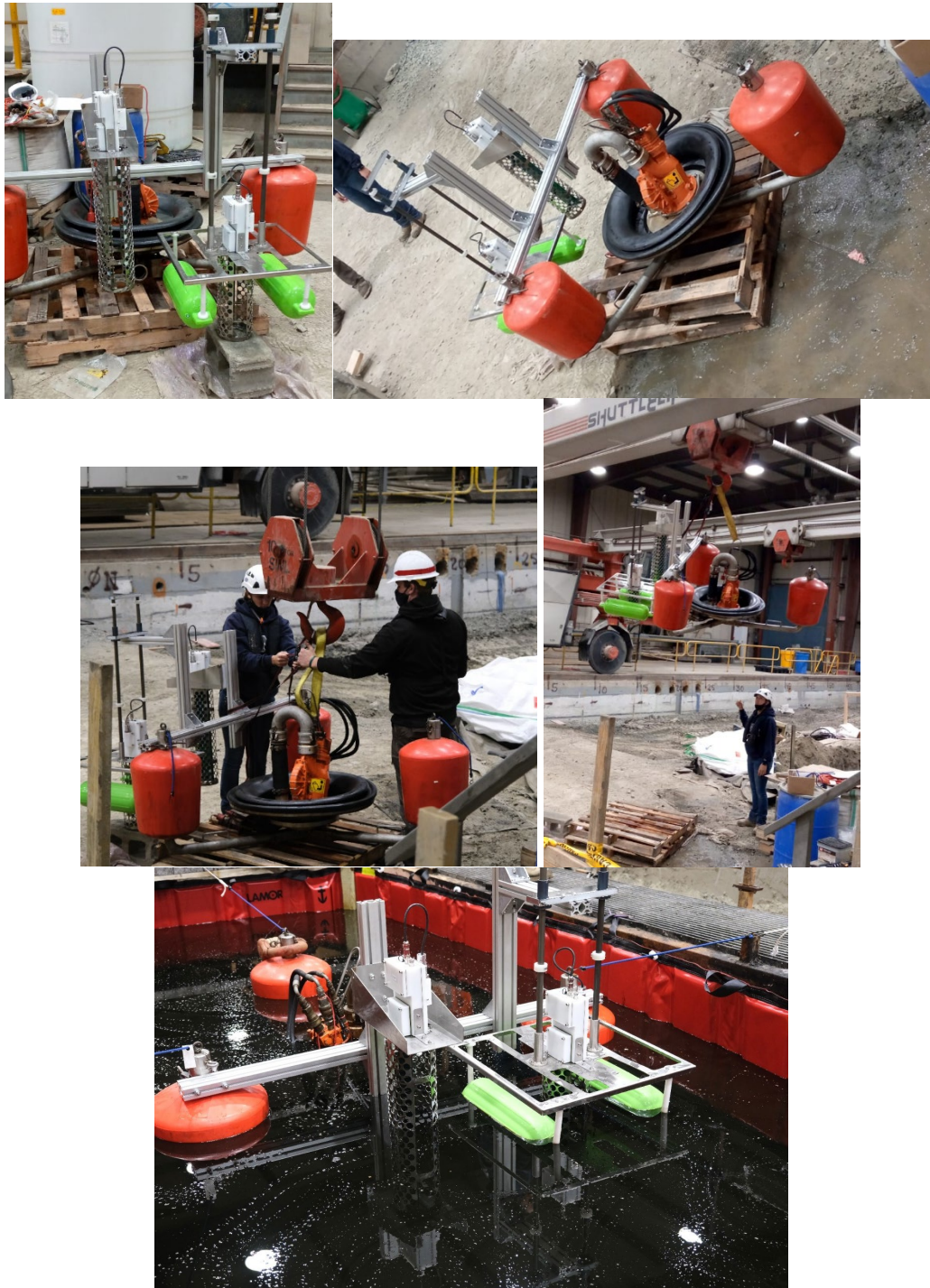
**Figure 4.4: Skimmer and sensors mounting and placement into the tank.**

## 4.3   Data Logging and Experimental Procedure

Tests were conducted by four subjects and data recorded by two subjects. Handheld data was read by the sensor operator and another person logged the measurement. Skimmer data was automatically saved to a local file on the PC communicating with the sensor.

For static measures (handheld and skimmer) the glass tank was placed on a table and the operator dipped the sensors in the tank (Figure 4.5). The handheld sensors were held off the bottom of the tank while the skimmer sensors were touching the bottom of the tank in most measures due to their length. When the sensors were dipped, the operator was allowed to slide the sensor or raise the sensor again before taking a measure. For each measure, the operator was required to remove the sensor from the tank and re-dip it for the next measure. During all these tests the operator was instructed to maintain the sensor as leveled as possible.
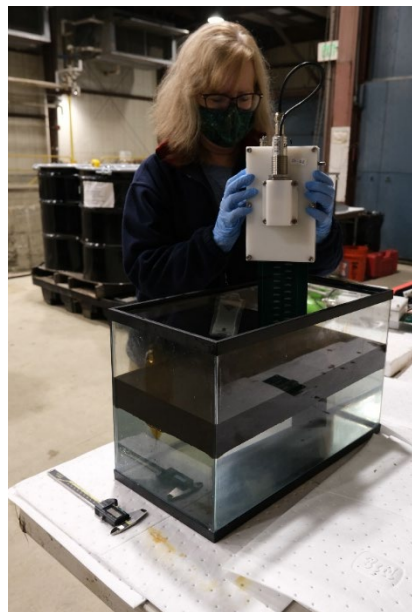


**Figure 4.5: Static testing in the glass fish tank.**

For measurement with the pole, the tank was placed on the floor and the operator was required to dip the sensor in it. The operators removed the sensor from the tank between measures and tried to keep the sensor leveled during measures. Two configurations were used, short and long (extended) pole (Figure 4.6).

For the wave tank measures, the skimmer with the sensors on it was allowed to free flow within the enclosed area while tied from three places to limit drift (Figure 4.7). For the handheld buoy measurements in the wave tank, the operator held the HMI in their hand and loosely held the rope tethered to the buoy (Figure 4.8).

Four wave configurations were used for testing ranging from moderate to significant as shown in Table 4-2. Logging of data started once the wave started. Water and oil were allowed to settle between different waves.

| Wave Number | Height (cm) | Duration (sec) |
|:-----------:|:-----------:|:--------------:|
| 0 | Static ||
| 1 | 6 | 2.5 |
| 2 | 12 | 3 |
| 3 | 6 | 2 |
| 4 | 6 | 1.5 |

**Table 4-2: Amplitude and duration of the produced waves.**
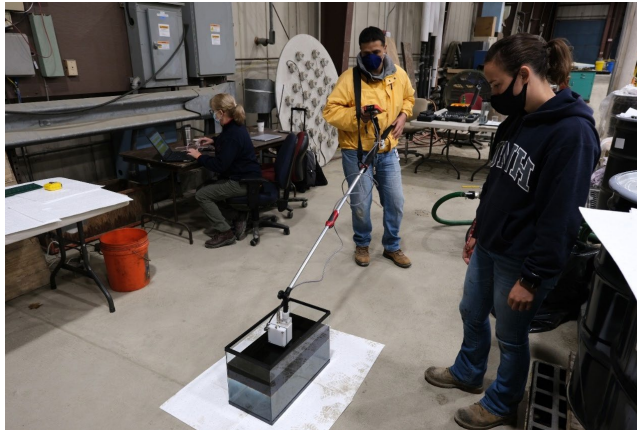


**Figure 4.6: Pole configuration of handheld.**



**Figure 4.7: Skimmer with sensors in the enclosed area.**

**Figure 4.8: Handhled sensor on bouy in wave tank.**

## 4.4  Oil Types

Five types of oils were used in the tests with different characteristics (Table 4-3). The reason behind this variety of oil samples is to test the generalizability of the sensor for different oils without the need to re-calibrate. Viscosity was measured on site using a rotational viscometer and temperature was measured using a handheld IR sensor.

| Oil Type | Oil Symbol | Viscosity |
|---|---|---|
| Diesel | (D) | 6.1 cP  at 17.5 $^{O}$C |
| Hydrocal 300 | (H) | 210 cP at 17.6 $^{O}$C |
| Calsol 8240 | (C) | 2789 cP at 17.1 $^{O}$C |
| Weathered HOOPs | (W) | 65.8 cP at 17.2 $^{O}$C |
| Emulsion | (E) | Not measured |

**Table 4-3: Oils used in testing.**

After giving a symbol for different configurations and oils, the tests nomenclature used was:
**[oil type][thickness in mm]# [sensor config]-[msmt type]**

This nomenclature is used throughout the entire testing, for example:
**D3-5-S2 Test**: is **diesel**, **3mm** thickness, sensor cfg **#5**, static measurement **#2**

The emulsion was created using 70% oil (HOOPS) and 30% water. The mixture was made in a bucket by using a handheld mixer and slowly adding the oil to the mixture until the required consistency is achieved (Figure 4.9).

**Figure 4.9: Emulsion mixing process.**

## 4.5   Oil Thickness Ground Truth

The oil thicknesses used in testing the different configurations included 3mm, 6mm, 13mm, 25mm, 51mm, 76mm, and random thicknesses. The water thickness/depth used for all tests was randomly set and not recorded. For the static tests conducted in the fish tanks, the thickness was obtained by first calculating the volume of oil needed given the inner surface area of the container and then using a graduated cylinder to measure and pour the oil in the tank (Figure 4.10). Then the thickness was validated using a caliper on the outside of the tank (Figure 4.11).



**Figure 4.10: Oil being measured and poured in the container.**

This process gave reasonable accuracies for most cases. Two challenges were faced: (1) with very thick oil like Calsol and thin slicks, it was challenging to have an even spread of the oil on

the surface of the water (Figure 4.12); (2) due to fouling and capillary effects in some cases it was challenging to validate the thickness from the outside of the tank using the calipar.
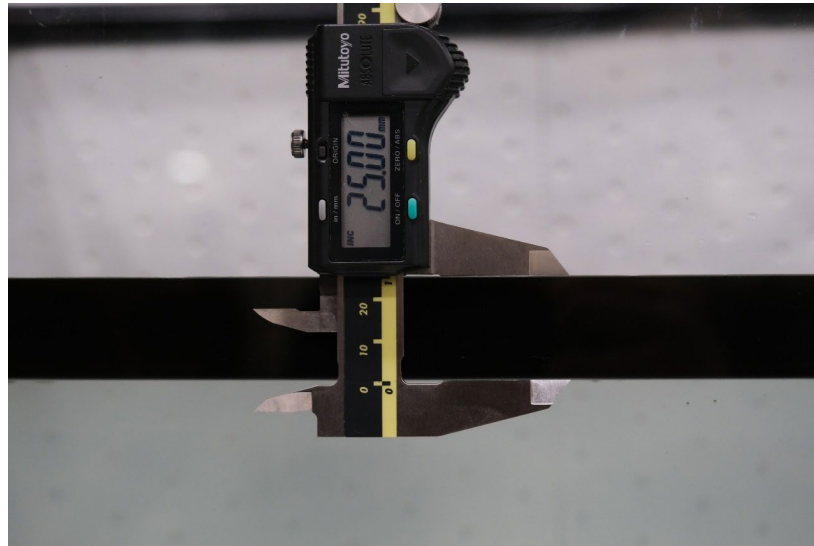


**Figure 4.11: Measuring the thickness of oil in the container from the outside.**
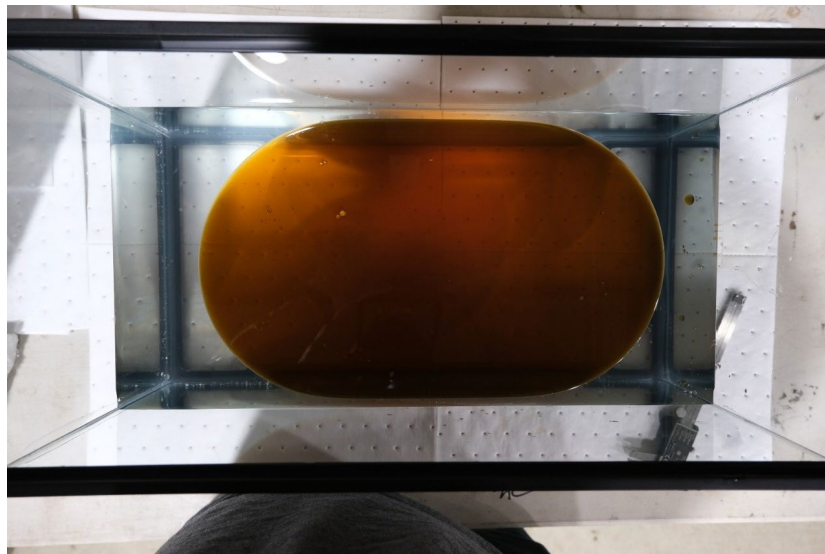


**Figure 4.12: Top view of Calsol oil sample not evenly spread in the container.**

For the tests conducted in the wave tank, the oil thickness needed was obtained by calculating the weight of oil (assuming 0.91g/ml density for Hydrocal) needed given the surface area of the enclosure. Then the oil was pumped into a bucket placed on a scale and then emptied into the area (Figure 4.13). Two challenges were faced, (1) the surface area calculation had to be estimated due to the non-uniformity of the shape and due to estimating the surface area that the skimmer takes, (2) the thickness changes during the measurement process due to skimmer and sensors being in the area and due to the waves themselves.

**Figure 4.13: Wave tank oil filling.**

## 4.6  Test Matrix

The static test matrix conducted is shown in Table 4-4. The wave tank test matrix (Static and Waves) is shown in Table 4-5.

| Type of Oil | Thickness Used (mm) | Sensor Configuration |
|---|---|---|
| Diesel (D) | 3, 6, 13, 25, 51, 76, random (50.4mm) | 1, 3, 5, 6 |
| Hydrocal 300 (H) | 3, 6, 13, 25, 51, 76, random (39mm) | 1, 3, 4*, 5, 6 |
| Calsol (C) | 3, 6, 13, 25, 51, 76 | 1, 3, 5, 6 |
| Weathered HOOPs (W) | 3, 6, 13, 25, 51, 76, random (60mm) | 1, 3, 4**, 5, 6 |
| Emulsion (E) | 13, 25, 51, 82 | 1***, 3, 5, 6 |
| * was not tested for 3mm and random | | |
| ** was not tested for random | | |
| *** was not tested for 82mm | | |

**Table 4-4: Static test matrix.**

| Type of Oil | Thickness Used (mm) | Waves | Sensor Configuration |
|---|---|---|---|
| Hydrocal 300 (H) | 13, 25, 71 | 0, 1, 2, 3, 4 | 5, 6 |
| Hydrocal 300 (H) | 13, 25, 71<br>71 | 0<br>1 | 7 |

**Table 4-5: Wave tank test matrix.**

## 4.7 Data Analysis

In the data analysis, for the handheld sensor, the first 5 valid measures were used in the calculations even if more measures were logged and for the skimmer sensor, the first 5 measures were skipped (to allow for waves to start in the dynamic case) and the next 10 measures were used in the calculations even though more measure were logged in all cases. Several criteria were used to assess the performance as described in Table 4-6.

| Column Label | Unit of Measurement | Description |
|---|---|---|
| Measurements $\bar{x}$ | mm | Average of the samples of measurement taken during testing. |
| STD | mm | Average of the standard deviation displayed by the handheld sensor during the measurements. |
| Error | mm | Average of the errors calculated for each of the samples where the error for each is calculated by: $\text{error}_i = \text{actual thickness} - \text{measured thickness}_i$ |
| Absolute Error | mm | Average of the absolute errors calculated for each of the samples where the error for each is calculated by: Absolute $\text{error}_i = \|\text{actual thickness} - \text{measured thickness}_i\|$ Note : Absolute error $\geq$ Error |
| % Error | Unit-less | Average of the relative % errors calculated for each of the samples where the relative % error for each is calculated by: $\% \text{ error}_i = \frac{100 \times \text{Absolute error}_i}{\text{actual thickness}}$ |
| % Repeatability | Unit-less | Average of the % repeatabilities calculated for each of the samples where the % repeatability for each is calculated by: $\% \text{ repeatability }_i = 100(1 - \frac{\|\bar{x} - \text{measurement}_i\|}{\bar{x}})$ |
| Inter-pin Error | Pins | Average of the inter-pin errors calculated for each of the samples where the inter-pin error for each is calculated by: $\text{Inter-pin error}_i = \frac{\text{absolute error}_i}{\text{inter-pin distance of the configuration}}$ |
| 95% Confidence Interval (I) | | $[\bar{x} - 1.96 * \frac{\text{standard deviation of 5 samples}}{\sqrt{5}} , \bar{x} + 1.96 * \frac{\text{standard deviation of 5 samples}}{\sqrt{5}}]$ |
| Amplitude of I | mm | It is the difference between the upper bound and lower bound of the 95% confidence interval |

**Table 4-6: Assessment criteria used to evaluate the sensors' performance.**

## 4.8 Data Organization and Visualization

To analyze the test results, we grouped them according to different criteria. First, handheld and skimmer sensor results were split. Then, static and dynamic tests were split. Within each section, the results were grouped and interpreted per configuration according to oil type and then according to thickness.

Most of the results are represented in similar tabular format. The tables formatting and color-coding interpretations for oil type tables are described in and for thickness tables are described in

| Label of the column | Color Code |
|---|---|
| **% Repeatability** | Green data bar from right to left to represent the goodness of the repeatability of the test. The larger the data bar is, the better the result is. |
| **Inter-pin Error** | Oil type based analysis: The best result within each category is highlighted in green. Thickness based analysis: Graded scale shading from Best (green) to worst (white) |
| **STD** | Graded 3 Color scale [0 2 5] with: Green for 0: Best Standard deviation Yellow for 2: Accepted Standard deviation Red for 5: Worst Standard deviation |
| **Absolute Error** | Oil type based analysis: Graded 3 Color scale with: Green for 0: Best Error Yellow for 1×actual Thickness: High Error Red for 2×actual Thickness: Worst Error Thickness based analysis: The best result within each category is highlighted in green. |
| **% Error (PE)** | Graded 3 Color scale applied over the whole column with: Green for 0: Best PE Yellow for 50% Percentile: Mid PE Red for the maximum error within the data: Worst PE |
| **Filled Cells  with solid** | No data for this test. |
| **Shaded Cells in red** | Suspected hardware failure |

**Table 4-7: Results tables' color coding.**

# 5 Handheld Sensor CRREL Test Results

In this chapter, we present the results of the tests that were conducted using the handheld sensors, which included static and (one) dynamic tests.

## 5.1 Handheld Sensor Static Tests

An example of this type of tests is shown in Figure 5.1.



**Figure 5.1: Handheld sensor static testing.**

### 5.1.1 Oil Type Analysis

When conducting the oil type analysis, we will compare the response of the sensor to different types of oils for the same configuration and thickness. The aim behind this interpretation is to evaluate the effect of oil type on the performance of the sensor, particularly as it relates to fouling impact.

**Configuration #1:**
The characteristics of the high-resolution handheld sensor are Gap: 0mm, Base Width: 2mm, Inter-pin Distance: 2mm. All the results of this case are shown in Table 5-1, Figure 5.2, and Table 5-2.

| Thickness | Oil Type | 1 | | | | | | | | | |
|---|---|---|---|---|---|---|---|---|---|---|---|
| | | Measurements | STD | Error | Absolute Error | % Error | % Repeatability | Inter-pin Error | 95% Confidence Interval I | | Width of I |
| 3 | Diesel | 5.72 | 0.60 | -2.72 | 2.72 | 90.53 | 83.79 | 1.36 | 4.55 | 6.88 | 2.33 |
| | Hydrocal 300 | 6.05 | 0.72 | -3.05 | 3.05 | 101.67 | 81.95 | 1.53 | 4.89 | 7.21 | 2.33 |
| | Calsol | 10.19 | 0.70 | -7.19 | 7.19 | 239.60 | 81.33 | 3.59 | 8.26 | 12.11 | 3.85 |
| | HOOPs | 5.15 | 0.87 | -2.15 | 2.15 | 71.53 | 89.37 | 1.07 | 4.42 | 5.87 | 1.45 |
| | Emulsion | | | | | | | | | | |
| 6 | Diesel | 6.29 | 0.82 | -0.29 | 0.60 | 9.97 | 92.10 | 0.30 | 5.68 | 6.90 | 1.22 |
| | Hydrocal 300 | 7.10 | 0.73 | -1.10 | 1.10 | 18.27 | 94.41 | 0.55 | 6.54 | 7.65 | 1.10 |
| | Calsol | 7.91 | 0.80 | -1.91 | 2.98 | 49.63 | 76.84 | 1.49 | 5.59 | 10.23 | 4.64 |
| | HOOPs | 7.19 | 0.75 | -1.19 | 1.41 | 23.43 | 80.92 | 0.70 | 5.62 | 8.77 | 3.15 |
| | Emulsion | | | | | | | | | | |
| 13 | Diesel | 13.35 | 0.72 | -0.35 | 0.42 | 3.25 | 97.24 | 0.21 | 12.93 | 13.77 | 0.84 |
| | Hydrocal 300 | 12.26 | 0.83 | 0.74 | 1.12 | 8.65 | 91.35 | 0.56 | 10.90 | 13.62 | 2.73 |
| | Calsol | 15.43 | 0.69 | -2.43 | 2.85 | 21.89 | 84.24 | 1.42 | 12.41 | 18.46 | 6.05 |
| | HOOPs | 15.07 | 0.73 | -2.07 | 2.40 | 18.43 | 89.26 | 1.20 | 13.29 | 16.85 | 3.56 |
| | Emulsion | 18.26 | 0.68 | -5.26 | 5.26 | 40.46 | 96.85 | 2.63 | 17.65 | 18.87 | 1.22 |
| 25 | Diesel | 24.36 | 1.11 | 0.64 | 1.07 | 4.29 | 97.04 | 0.54 | 23.44 | 25.29 | 1.85 |
| | Hydrocal 300 | 24.46 | 0.88 | 0.54 | 1.62 | 6.50 | 94.26 | 0.81 | 22.77 | 26.16 | 3.39 |
| | Calsol | 26.56 | 0.65 | -1.56 | 2.45 | 9.81 | 93.24 | 1.23 | 24.03 | 29.09 | 5.06 |
| | HOOPs | 24.22 | 0.88 | 0.78 | 1.98 | 7.93 | 92.46 | 0.99 | 22.29 | 26.14 | 3.85 |
| | Emulsion | 26.59 | 1.33 | -1.59 | 1.86 | 7.45 | 95.84 | 0.93 | 25.26 | 27.92 | 2.66 |
| 51 | Diesel | 48.67 | 0.88 | 2.33 | 2.33 | 4.57 | 98.37 | 1.17 | 47.87 | 49.47 | 1.59 |
| | Hydrocal 300 | 48.99 | 0.83 | 2.01 | 2.48 | 4.85 | 97.30 | 1.24 | 47.23 | 50.75 | 3.52 |
| | Calsol | 48.68 | 1.33 | 2.32 | 2.70 | 5.29 | 97.12 | 1.35 | 46.95 | 50.42 | 3.47 |
| | HOOPs | 48.26 | 0.74 | 2.74 | 2.74 | 5.38 | 98.27 | 1.37 | 46.99 | 49.53 | 2.54 |
| | Emulsion | 45.53 | 0.61 | 5.47 | 5.47 | 10.72 | 95.38 | 2.73 | 43.21 | 47.86 | 4.65 |
| 76 | Diesel | 72.01 | 1.14 | 3.99 | 4.76 | 6.27 | 94.51 | 2.38 | 67.79 | 76.22 | 8.43 |
| | Hydrocal 300 | 72.83 | 0.96 | 3.17 | 3.17 | 4.17 | 98.05 | 1.58 | 71.19 | 74.48 | 3.28 |
| | Calsol | 74.29 | 0.59 | 1.71 | 3.26 | 4.29 | 96.07 | 1.63 | 71.13 | 77.46 | 6.34 |
| | HOOPs | 71.66 | 0.83 | 4.34 | 4.34 | 5.71 | 99.03 | 2.17 | 70.77 | 72.55 | 1.78 |
| | Emulsion | | | | | | | | | | |

**Table 5-1: Test outcomes for configuration 1 (Color coding defined in Section 4.8)**
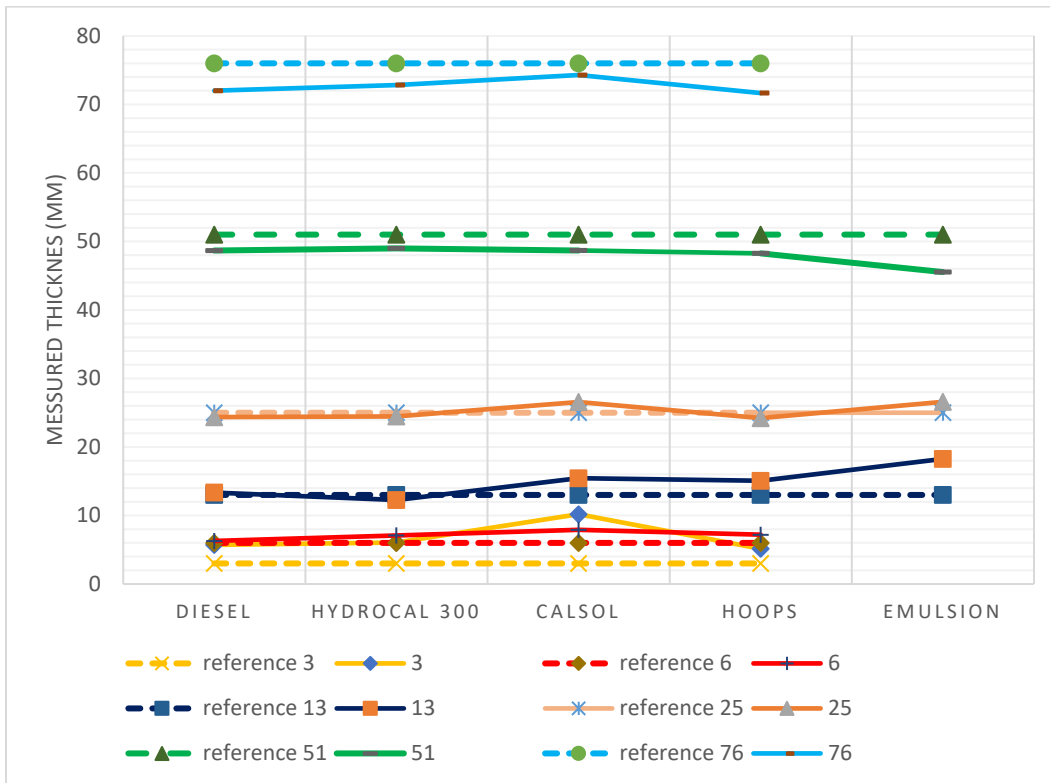


**Figure 5.2: Plot of the measured thickness vs. reference thickness Configuration 1**

145

**Table 5-2: Average, min and max performance across all thicknesses for all oils (Configuration 1).**

| Configuration | | Absolute Error (mm) | % Repeatability | Inter-pin Error |
|---|---|---|---|---|
| 1 | Average | 2.72 | 92.1 | 1.36 |
| | Min | 0.42 | 76.84 | 0.21 |
| | Max | 7.19 | 99.03 | 3.59 |

Observations based on the results:

- This configuration gave low errors in majority of cases. The overall average absolute error for all cases was 2.72mm. This translated to an average inter-pin error of 1.36, and showed that the sensor was able to perform well for the majority of oils, without the need for calibration for each oil.
- The sensor gave a high average overall percentage repeatability of 92.1%, which indicates that the measures were consistent across trials. This was also evident by the relatively narrow 95% confidence intervals which had an average width of 3.22mm. Another indication of the sensor consistency is the standard deviation of measures given by the sensor while measuring each trial. This standard deviation ranged between 0.59mm and 1.33mm.
- The oil causing the worst performance was Calsol, which turns out to be the case for all configurations as will be shown. This was clearly attributed to the very high viscosity of this oil. The over estimation, particularly for the 3 and 6mm cases, was visible to the observers as seen in Figure 5.3. The figure shows the submerged pins with a significant bulge of oil around them. It was observed that if the sensor is submerged in the oil quickly this fouling would increase significantly.
- The second most challenging oil for this configuration was the emulsion. This was also attributed to the fouling since it was observed that the tight arrangement of pins in this configuration did not allow oil to quickly disperse.

**Figure 5.3: Calsol fouling.**

## Configuration #3:

The characteristics of the low-resolution handheld sensor are Gap: 1mm, Base Width: 2mm, Inter-pin Distance: 3mm. All the results of this case are shown in Table 5-3, Figure 5.4, and Table 5-4. Observations based on the results:

- This configuration gave low errors in majority of cases. The overall average absolute error for all cases was 2.25mm, which was slightly better than Configuration 1 (2.72mm). This translated to an average inter-pin error of 0.87. This showed that the sensor was able to perform well for majority of oils without calibration for each oil.
- The sensor gave a high average overall percentage repeatability of 89.94% but lower than configuration 1 (92.1%), which indicates that the measures were consistent across trials. This was also evident by the relatively narrow 95% confidence intervals which had an average width of 3.19mm. Another indication of the sensor consistency is the standard deviation of measures given by the sensor while measuring each trial. This standard deviation ranged between 0.61mm and 1.67mm.
- As with Configuration 1, the oil causing the worst performance was Calsol; however, this configuration seemed to perform slightly better with Calsol than Configuration 1 particularly to low thicknesses.
- The second most challenging oil for this configuration was also the emulsion again with a slight advantage over Configuration 1. We observed that having the pins in this

configuration slightly further apart than configuration 1 allowed it to mitigate fouling slightly better.

**Table 5-3: Test outcomes for Configuration 3 (Color coding defined in Section 4.8)**

| Thickness | Oil Type | 3 | | | | | | | | | |
|---|---|---|---|---|---|---|---|---|---|---|---|
| | | Measurements | STD | Error | Absolute Error | % Error | % Repeatability | Inter-pin Error | 95% Confidence Interval I | | Width of I |
| 3 | Diesel | 3.08 | 0.85 | -0.08 | 0.86 | 28.80 | 71.42 | 0.43 | 1.88 | 4.27 | 2.38 |
| | Hydrocal 300 | 3.84 | 0.76 | -0.84 | 0.84 | 27.93 | 82.03 | 0.42 | 3.11 | 4.57 | 1.46 |
| | Calsol | 8.77 | 0.61 | -5.77 | 5.77 | 192.27 | 82.27 | 2.88 | 7.08 | 10.46 | 3.38 |
| | HOOPs | 3.67 | 0.95 | -0.67 | 0.74 | 24.80 | 71.92 | 0.37 | 2.40 | 4.94 | 2.54 |
| | Emulsion | | | | | | | | | | |
| 6 | Diesel | 5.83 | 1.28 | 0.17 | 0.64 | 10.60 | 89.39 | 0.32 | 5.11 | 6.55 | 1.44 |
| | Hydrocal 300 | 5.58 | 0.82 | 0.42 | 0.64 | 10.67 | 92.48 | 0.32 | 5.00 | 6.15 | 1.15 |
| | Calsol | 5.14 | 0.85 | 0.86 | 2.92 | 48.67 | 53.24 | 1.46 | 2.16 | 8.11 | 5.95 |
| | HOOPs | 5.77 | 0.82 | 0.23 | 1.50 | 25.03 | 74.77 | 0.75 | 4.07 | 7.47 | 3.41 |
| | Emulsion | | | | | | | | | | |
| 13 | Diesel | 14.49 | 1.18 | -1.49 | 2.17 | 16.72 | 87.71 | 1.09 | 12.52 | 16.45 | 3.93 |
| | Hydrocal 300 | 12.14 | 0.81 | 0.86 | 1.16 | 8.94 | 92.60 | 0.58 | 11.18 | 13.11 | 1.93 |
| | Calsol | 13.81 | 0.61 | -0.81 | 0.81 | 6.22 | 96.28 | 0.40 | 13.15 | 14.46 | 1.31 |
| | HOOPs | 11.18 | 0.81 | 1.82 | 1.82 | 14.03 | 94.02 | 0.91 | 10.46 | 11.89 | 1.43 |
| | Emulsion | 13.28 | 0.76 | -0.28 | 1.06 | 8.15 | 92.70 | 0.35 | 12.11 | 14.44 | 2.33 |
| 25 | Diesel | 23.90 | 0.99 | 1.10 | 1.24 | 4.98 | 95.67 | 0.41 | 22.76 | 25.04 | 2.28 |
| | Hydrocal 300 | 23.74 | 0.99 | 1.26 | 1.34 | 5.35 | 95.58 | 0.45 | 22.56 | 24.91 | 2.35 |
| | Calsol | 24.54 | 0.64 | 0.46 | 3.27 | 13.08 | 86.30 | 1.09 | 20.86 | 28.23 | 7.37 |
| | HOOPs | 22.77 | 0.90 | 2.23 | 2.23 | 8.92 | 93.90 | 0.74 | 21.26 | 24.28 | 3.02 |
| | Emulsion | 21.73 | 1.20 | 3.27 | 3.27 | 13.08 | 95.55 | 1.09 | 20.72 | 22.74 | 2.01 |
| 51 | Diesel | 49.04 | 1.06 | 1.96 | 1.96 | 3.84 | 98.29 | 0.65 | 48.00 | 50.09 | 2.09 |
| | Hydrocal 300 | 50.09 | 0.89 | 0.91 | 1.02 | 2.00 | 98.36 | 0.34 | 49.22 | 50.97 | 1.75 |
| | Calsol | 54.08 | 1.00 | -3.08 | 3.44 | 6.75 | 95.09 | 1.15 | 51.13 | 57.02 | 5.89 |
| | HOOPs | 50.55 | 1.67 | 0.45 | 2.09 | 4.11 | 96.03 | 0.70 | 48.35 | 52.76 | 4.41 |
| | Emulsion | 45.51 | 1.20 | 5.49 | 5.49 | 10.77 | 94.18 | 1.83 | 42.72 | 48.29 | 5.57 |
| 76 | Diesel | 73.25 | 0.75 | 2.75 | 2.75 | 3.62 | 98.86 | 0.92 | 72.26 | 74.23 | 1.97 |
| | Hydrocal 300 | 77.11 | 0.79 | -1.11 | 1.11 | 1.46 | 99.00 | 0.37 | 76.33 | 77.90 | 1.57 |
| | Calsol | 82.36 | 0.70 | -6.36 | 7.50 | 9.86 | 94.27 | 2.50 | 77.07 | 87.65 | 10.59 |
| | HOOPs | 74.07 | 1.07 | 1.93 | 1.93 | 2.54 | 98.85 | 0.64 | 73.15 | 74.99 | 1.84 |
| 82 | Emulsion | 78.63 | 0.98 | 3.37 | 3.37 | 4.10 | 97.59 | 1.12 | 76.66 | 80.61 | 3.94 |
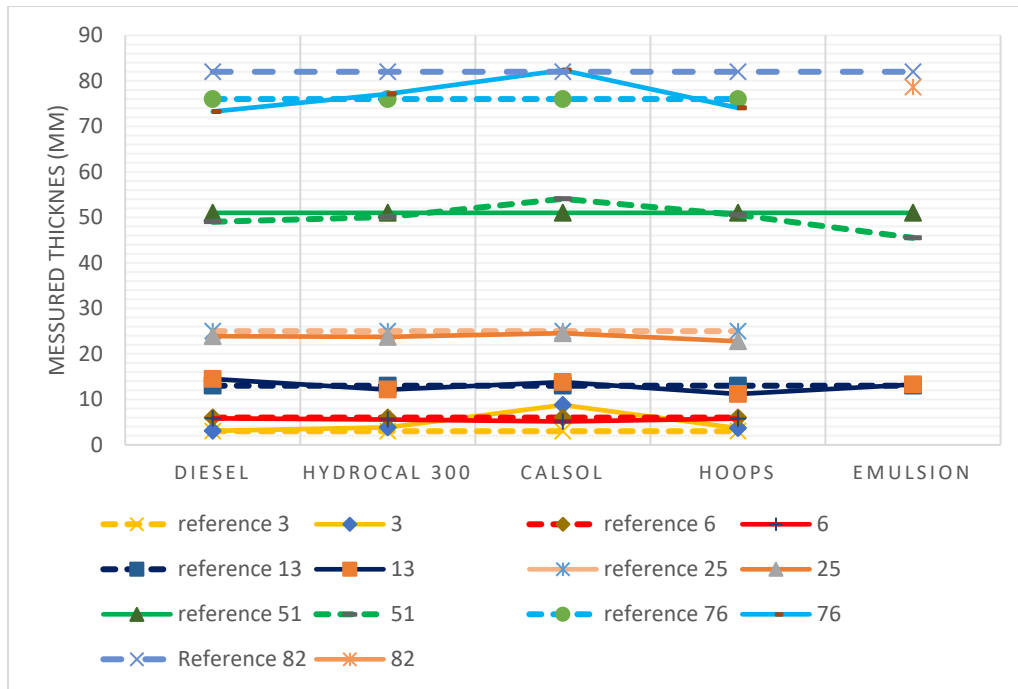


**Figure 5.4: Plot of the average measured thickness vs. reference thickness for Configuration 3**

**Table 5-4: Average, min and max performance across all thicknesses for all oils (Configuration 3)**

| Configuration | | Absolute Error (mm) | % Repeatability | Inter-pin Error |
|---|---|---|---|---|
| 3 | Average | 2.25 | 89.94 | 0.87 |
| | Min | 0.64 | 53.24 | 0.32 |
| | Max | 7.50 | 99.00 | 2.88 |

### 5.1.2 Thickness Analysis

Thickness based analysis focuses on the impact of oil thickness on the performance of the sensor.

**<u>Configuration #1:</u>**

The results of the tests organized to reveal thickness effect are shown in Table 5-5. The observations based on this table show that the lowest and highest thicknesses seemed to result in the worst measures in terms of accuracy ({Thickness, Error}: {3mm, 3.78mm}, {6mm, 1.52mm}, {13mm, 2.41mm}, {25mm, 1.80mm}, {51mm, 3.14mm}, {76mm, 3.88mm}). This can be attributed to two scenarios:

1- When the oil is thin and the sensor is dipped in it, many sets of pins would traverse the oil into the water. This results in have more set of pins being fouled.
2- When the oil is thick, it gets closer to the full range of measurement of the sensor. This was observed as a challenging scenario for used because to get some pins to reach the water the sensor had to be held very close to the surface of the oil.

In addition, for most oils the 3mm thickness resulted in the lowest repeatability and therefore consistency between trials.

**Table 5-5: Data arranged to reveal thickness effect on configuration 1**

| | | | | | | | | | 1 | | |
|---|---|---|---|---|---|---|---|---|---|---|---|
| Oil Type | Thickness | Measurements | STD | Error | Absolute Error | % Error | % Repeatability | Inter-pin Error | 95% Confidence Interval I | | Width of I |
| Diesel | 3 | 5.72 | 0.60 | -2.72 | 2.72 | 90.53 | 83.79 | 1.36 | 4.55 | 6.88 | 2.33 |
| | 6 | 6.29 | 0.82 | -0.29 | 0.60 | 9.97 | 92.10 | 0.30 | 5.68 | 6.90 | 1.22 |
| | 13 | 13.35 | 0.72 | -0.35 | 0.42 | 3.25 | 97.24 | 0.21 | 12.93 | 13.77 | 0.84 |
| | 25 | 24.36 | 1.11 | 0.64 | 1.07 | 4.29 | 97.04 | 0.54 | 23.44 | 25.29 | 1.85 |
| | 51 | 48.67 | 0.88 | 2.33 | 2.33 | 4.57 | 98.37 | 1.17 | 47.87 | 49.47 | 1.59 |
| | 76 | 72.01 | 1.14 | 3.99 | 4.76 | 6.27 | 94.51 | 2.38 | 67.79 | 76.22 | 8.43 |
| Hydrocal 300 | 3 | 6.05 | 0.72 | -3.05 | 3.05 | 101.67 | 81.95 | 1.53 | 4.89 | 7.21 | 2.33 |
| | 6 | 7.10 | 0.73 | -1.10 | 1.10 | 18.27 | 94.41 | 0.55 | 6.54 | 7.65 | 1.10 |
| | 13 | 12.26 | 0.83 | 0.74 | 1.12 | 8.65 | 91.35 | 0.56 | 10.90 | 13.62 | 2.73 |
| | 25 | 24.46 | 0.88 | 0.54 | 1.62 | 6.50 | 94.26 | 0.81 | 22.77 | 26.16 | 3.39 |
| | 51 | 48.99 | 0.83 | 2.01 | 2.48 | 4.85 | 97.30 | 1.24 | 47.23 | 50.75 | 3.52 |
| | 76 | 72.83 | 0.96 | 3.17 | 3.17 | 4.17 | 98.05 | 1.58 | 71.19 | 74.48 | 3.28 |
| Calsol | 3 | 10.19 | 0.70 | -7.19 | 7.19 | 239.60 | 81.33 | 3.59 | 8.26 | 12.11 | 3.85 |
| | 6 | 7.91 | 0.80 | -1.91 | 2.98 | 49.63 | 76.84 | 1.49 | 5.59 | 10.23 | 4.64 |
| | 13 | 15.43 | 0.69 | -2.43 | 2.85 | 21.89 | 84.24 | 1.42 | 12.41 | 18.46 | 6.05 |
| | 25 | 26.56 | 0.65 | -1.56 | 2.45 | 9.81 | 93.24 | 1.23 | 24.03 | 29.09 | 5.06 |
| | 51 | 48.68 | 1.33 | 2.32 | 2.70 | 5.29 | 97.12 | 1.35 | 46.95 | 50.42 | 3.47 |
| | 76 | 74.29 | 0.59 | 1.71 | 3.26 | 4.29 | 96.07 | 1.63 | 71.13 | 77.46 | 6.34 |
| HOOPs | 3 | 5.15 | 0.87 | -2.15 | 2.15 | 71.53 | 89.37 | 1.07 | 4.42 | 5.87 | 1.45 |
| | 6 | 7.19 | 0.75 | -1.19 | 1.41 | 23.43 | 80.92 | 0.70 | 5.62 | 8.77 | 3.15 |
| | 13 | 15.07 | 0.73 | -2.07 | 2.40 | 18.43 | 89.26 | 1.20 | 13.29 | 16.85 | 3.56 |
| | 25 | 24.22 | 0.88 | 0.78 | 1.98 | 7.93 | 92.46 | 0.99 | 22.29 | 26.14 | 3.85 |
| | 51 | 48.26 | 0.74 | 2.74 | 2.74 | 5.38 | 98.27 | 1.37 | 46.99 | 49.53 | 2.54 |
| | 76 | 71.66 | 0.83 | 4.34 | 4.34 | 5.71 | 99.03 | 2.17 | 70.77 | 72.55 | 1.78 |
| Emulsion | 13 | 18.26 | 0.68 | -5.26 | 5.26 | 40.46 | 96.85 | 2.63 | 17.65 | 18.87 | 1.22 |
| | 25 | 26.59 | 1.33 | -1.59 | 1.86 | 7.45 | 95.84 | 0.93 | 25.26 | 27.92 | 2.66 |
| | 51 | 45.53 | 0.61 | 5.47 | 5.47 | 10.72 | 95.38 | 2.73 | 43.21 | 47.86 | 4.65 |

## Configuration #3:

The results of the tests organized to reveal thickness effect are shown in Table 5-6. The observations based on this table show that the lowest and higher thicknesses seemed to result in the worst measures in terms of accuracy but not as evident as with Configuration 1: ({Thickness, Error}: {3mm, 2.05mm}, {6mm, 1.42mm}, {13mm, 1.41mm}, {25mm, 2.27mm}, {51mm, 2.8mm}, {76mm, 3.32mm}). As with Configuration 1, for most oils the 3mm thickness resulted in the lowest repeatability and therefore consistency between trials. This configuration had the advantage of measuring a longer range compared to Configuration 1 as was the case with emulsion (Configuration 1 was not used for the 82mm emulsion).

| | | | | | | | | | | |
|---|---|---|---|---|---|---|---|---|---|---|
| | | | | | | | 3 | | | |
| Oil Type | Thickness | Measurements | STD | Error | Absolute Error | % Error | % Repeatability | Inter-pin Error | 95% Confidence Interval I | | Width of I |
| Diesel | 3 | 3.08 | 0.85 | -0.08 | 0.86 | 28.80 | 71.42 | 0.43 | 1.88 | 4.27 | 2.38 |
| | 6 | 5.83 | 1.28 | 0.17 | 0.64 | 10.60 | 89.39 | 0.32 | 5.11 | 6.55 | 1.44 |
| | 13 | 14.49 | 1.18 | -1.49 | 2.17 | 16.72 | 87.71 | 1.09 | 12.52 | 16.45 | 3.93 |
| | 25 | 23.90 | 0.99 | 1.10 | 1.24 | 4.98 | 95.67 | 0.41 | 22.76 | 25.04 | 2.28 |
| | 51 | 49.04 | 1.06 | 1.96 | 1.96 | 3.84 | 98.29 | 0.65 | 48.00 | 50.09 | 2.09 |
| | 76 | 73.25 | 0.75 | 2.75 | 2.75 | 3.62 | 98.86 | 0.92 | 72.26 | 74.23 | 1.97 |
| Hydrocal 300 | 3 | 3.84 | 0.76 | -0.84 | 0.84 | 27.93 | 82.03 | 0.42 | 3.11 | 4.57 | 1.46 |
| | 6 | 5.58 | 0.82 | 0.42 | 0.64 | 10.67 | 92.48 | 0.32 | 5.00 | 6.15 | 1.15 |
| | 13 | 12.14 | 0.81 | 0.86 | 1.16 | 8.94 | 92.60 | 0.58 | 11.18 | 13.11 | 1.93 |
| | 25 | 23.74 | 0.99 | 1.26 | 1.34 | 5.35 | 95.58 | 0.45 | 22.56 | 24.91 | 2.35 |
| | 51 | 50.09 | 0.89 | 0.91 | 1.02 | 2.00 | 98.36 | 0.34 | 49.22 | 50.97 | 1.75 |
| | 76 | 77.11 | 0.79 | -1.11 | 1.11 | 1.46 | 99.00 | 0.37 | 76.33 | 77.90 | 1.57 |
| Calsol | 3 | 8.77 | 0.61 | -5.77 | 5.77 | 192.27 | 82.27 | 2.88 | 7.08 | 10.46 | 3.38 |
| | 6 | 5.14 | 0.85 | 0.86 | 2.92 | 48.67 | 53.24 | 1.46 | 2.16 | 8.11 | 5.95 |
| | 13 | 13.81 | 0.61 | -0.81 | 0.81 | 6.22 | 96.28 | 0.40 | 13.15 | 14.46 | 1.31 |
| | 25 | 24.54 | 0.64 | 0.46 | 3.27 | 13.08 | 86.30 | 1.09 | 20.86 | 28.23 | 7.37 |
| | 51 | 54.08 | 1.00 | -3.08 | 3.44 | 6.75 | 95.09 | 1.15 | 51.13 | 57.02 | 5.89 |
| | 76 | 82.36 | 0.70 | -6.36 | 7.50 | 9.86 | 94.27 | 2.50 | 77.07 | 87.65 | 10.59 |
| HOOPs | 3 | 3.67 | 0.95 | -0.67 | 0.74 | 24.80 | 71.92 | 0.37 | 2.40 | 4.94 | 2.54 |
| | 6 | 5.77 | 0.82 | 0.23 | 1.50 | 25.03 | 74.77 | 0.75 | 4.07 | 7.47 | 3.41 |
| | 13 | 11.18 | 0.81 | 1.82 | 1.82 | 14.03 | 94.02 | 0.91 | 10.46 | 11.89 | 1.43 |
| | 25 | 22.77 | 0.90 | 2.23 | 2.23 | 8.92 | 93.90 | 0.74 | 21.26 | 24.28 | 3.02 |
| | 51 | 50.55 | 1.67 | 0.45 | 2.09 | 4.11 | 96.03 | 0.70 | 48.35 | 52.76 | 4.41 |
| | 76 | 74.07 | 1.07 | 1.93 | 1.93 | 2.54 | 98.85 | 0.64 | 73.15 | 74.99 | 1.84 |
| Emulsion | 13 | 13.28 | 0.76 | -0.28 | 1.06 | 8.15 | 92.70 | 0.35 | 12.11 | 14.44 | 2.33 |
| | 25 | 21.73 | 1.20 | 3.27 | 3.27 | 13.08 | 95.55 | 1.09 | 20.72 | 22.74 | 2.01 |
| | 51 | 45.51 | 1.20 | 5.49 | 5.49 | 10.77 | 94.18 | 1.83 | 42.72 | 48.29 | 5.57 |
| | 82 | 78.63 | 0.98 | 3.37 | 3.37 | 4.10 | 97.59 | 1.12 | 76.66 | 80.61 | 3.94 |

**Table 5-6: Data arranged to reveal thickness effect on configuration 3.**

## Random Thickness:

We also tested the 1, 3, 5, and 6 configurations in cases where the thickness was randomly selected. The results of these tests are shown in Table 5-7 and Figure 5.5. Results show all configurations resulting in low inter-pin error except for two cases for configuration 5 and 6 in Diesel, which was caused by faulty MPRs which were replaced after those tests. All tests showed high repeatability. The results of these tests for all configurations were comparable to the other tests.

**Table 5-7: Random thickness tests for all configurations**

| | Configuration | Measurements | STD | Error | Absolute Error | % Error | % Repeatability | Inter-pin Error | 95% Confidence Interval I | | Width of I |
|---|---|---|---|---|---|---|---|---|---|---|---|
| Diesel -<br>50.4 mm | 1 | 46.39 | 0.80 | 4.01 | 4.01 | 7.95 | 96.51 | 2.00 | 44.41 | 48.38 | 3.97 |
| | 3 | 45.72 | 1.36 | 4.68 | 4.68 | 9.29 | 95.82 | 1.56 | 43.37 | 48.07 | 4.70 |
| | 5 | 15.26 | | 35.14 | 35.14 | 69.72 | 99.08 | 5.02 | 15.14 | 15.38 | 0.24 |
| | 6 | 14.43 | | 35.97 | 35.97 | 71.38 | 97.70 | 3.00 | 14.15 | 14.71 | 0.56 |
| Hydrocal -<br>39 mm | 1 | 37.37 | 0.62 | 1.63 | 1.63 | 4.18 | 98.93 | 0.82 | 36.87 | 37.86 | 0.99 |
| | 3 | 39.34 | 0.88 | -0.34 | 1.82 | 4.68 | 95.54 | 0.61 | 37.42 | 41.27 | 3.85 |
| | 5 | 29.43 | | 9.57 | 9.57 | 24.54 | 99.15 | 1.37 | 29.25 | 29.61 | 0.37 |
| | 6 | 45.13 | | -6.13 | 6.13 | 15.71 | 98.32 | 0.51 | 44.55 | 45.70 | 1.15 |
| HOOPs-<br>60 mm | 1 | 56.58 | 0.83 | 3.42 | 3.42 | 5.69 | 98.13 | 1.71 | 55.45 | 57.72 | 2.27 |
| | 3 | 59.77 | 1.55 | 0.23 | 0.85 | 1.41 | 98.66 | 0.28 | 58.85 | 60.69 | 1.84 |
| | 5 | 63.09 | | -3.09 | 3.09 | 5.14 | 99.56 | 0.44 | 62.88 | 63.29 | 0.42 |
| | 6 | 48.47 | | 11.53 | 11.53 | 19.22 | 96.71 | 0.96 | 47.19 | 49.75 | 2.57 |
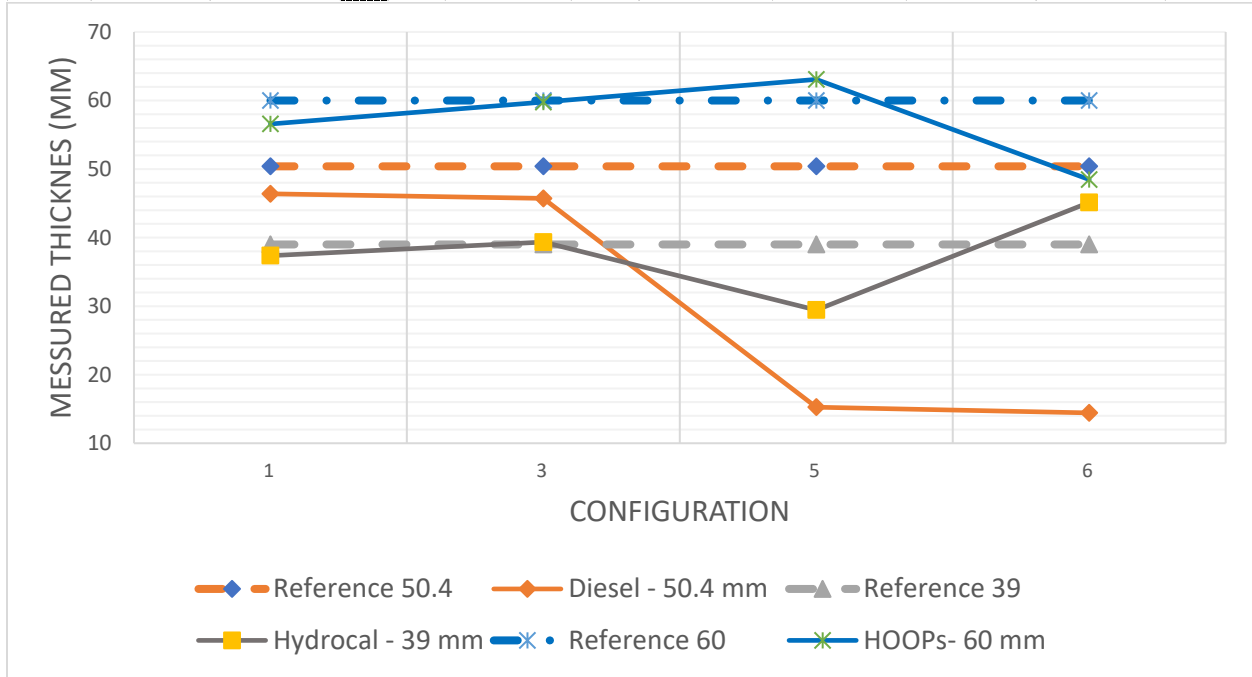


**Figure 5.5: Plot of the average measured thickness vs. reference thickness for random thickness tests**

## 5.2  Handheld Sensor Pole Tests

Configuration 4, shown in Figure 5.6, was used in half extended (39 inches) and fully extended (69 inches) scenarios. Results for the tests are shown in Table 5-8 and Table 5-9.



**Figure 5.6: Fully extended pole tests**

**Table 5-8: Results of testing handheld with pole (configuration 4) at retracted position (39 inches)**

| Oil Type | Thickness | Measurements | STD | Error | Absolute Error | % Error | % Repeatability | Inter-pin Error | 95% Confidence Interval I | | Width of I |
|---|---|---|---|---|---|---|---|---|---|---|---|
| | | | | | | **4 (39 Inches)** | | | | | |
| HOOPs | 6 | 5.51 | 1.42 | 0.49 | 2.46 | 41.00 | 57.14 | 0.82 | 2.03 | 9.00 | 6.97 |
| | 13 | 8.54 | 1.46 | 4.46 | 5.14 | 39.55 | 71.12 | 1.71 | 5.18 | 11.90 | 6.73 |
| | 25 | 21.38 | 2.29 | 3.62 | 3.62 | 14.47 | 92.27 | 1.21 | 19.58 | 23.19 | 3.61 |
| | 51 | 45.86 | 1.87 | -5.14 | 5.14 | 10.08 | 96.67 | 1.71 | 44.21 | 47.50 | 3.29 |
| | 76 | 71.47 | 1.75 | 4.53 | 4.53 | 5.96 | 98.03 | 1.51 | 69.86 | 73.08 | 3.21 |
| Hydrocal 300 | 3 | 8.13 | 0.95 | -5.13 | 5.13 | 171.00 | 69.00 | 1.71 | 4.99 | 11.27 | 6.29 |
| | 6 | 10.73 | 1.04 | -4.73 | 4.73 | 78.87 | 73.48 | 1.58 | 8.51 | 12.96 | 4.45 |
| | 13 | 16.16 | 1.45 | -3.16 | 3.16 | 24.31 | 92.13 | 1.05 | 14.59 | 17.73 | 3.15 |
| | 25 | 24.23 | 1.08 | 0.77 | 1.89 | 7.56 | 91.57 | 0.63 | 21.89 | 26.57 | 4.68 |
| | 51 | 49.83 | 0.89 | -1.17 | 2.84 | 5.58 | 94.76 | 0.95 | 47.00 | 52.66 | 5.66 |
| | 76 | 75.87 | 1.07 | 0.13 | 2.55 | 3.36 | 96.67 | 0.85 | 73.07 | 78.66 | 5.60 |

**Table 5-9: Results of testing handheld with pole (configuration 4) at extended position (69 inches).**

| | | | | | 4 (69 Inches) | | | | 95% Confidence Interval I | | |
|---|---|---|---|---|---|---|---|---|---|---|---|
| Oil Type | Thickness | Measurements | STD | Error | Absolute Error | % Error | % Repeatability | Inter-pin Error | | | Width of I |
| HOOPs | 6 | 4.47 | 0.90 | 1.53 | 3.67 | 61.23 | 24.65 | 1.22 | 0.99 | 7.95 | 6.97 |
| | 13 | 9.15 | 1.27 | 3.85 | 3.85 | 29.62 | 69.05 | 1.28 | 6.20 | 12.10 | 5.89 |
| | 25 | 20.04 | 2.38 | 4.96 | 5.04 | 20.16 | 86.29 | 1.68 | 16.88 | 23.20 | 6.33 |
| | 51 | 46.55 | 1.30 | -4.45 | 4.45 | 8.73 | 97.16 | 1.48 | 45.04 | 48.06 | 3.02 |
| | 76 | 68.90 | 1.41 | 7.10 | 7.10 | 9.34 | 99.12 | 2.37 | 68.19 | 69.61 | 1.42 |
| Hydrocal 300 | 3 | 7.33 | 1.74 | -4.33 | 4.33 | 144.27 | 84.37 | 1.44 | 6.07 | 8.58 | 2.51 |
| | 6 | 5.10 | 1.49 | 0.90 | 2.29 | 38.20 | 58.61 | 0.76 | 2.88 | 7.33 | 4.45 |
| | 13 | 16.81 | 0.99 | -3.81 | 3.81 | 29.31 | 82.53 | 1.27 | 13.73 | 19.89 | 6.15 |
| | 25 | 27.02 | 0.94 | -2.02 | 2.02 | 8.08 | 95.57 | 0.67 | 25.49 | 28.55 | 3.07 |
| | 51 | 52.67 | 1.16 | 1.67 | 2.03 | 3.97 | 97.88 | 0.68 | 51.07 | 54.26 | 3.20 |
| | 76 | 76.89 | 1.62 | -0.89 | 2.27 | 2.99 | 96.95 | 0.76 | 74.21 | 79.57 | 5.36 |

Based on the tables we can observe the following:

- Both configurations had similar average absolute errors (3.75mm and average inter-pin error of 1.25 retracted, 3.71mm and average inter-pin error of 1.24 extended) and both significantly higher than without the pole (2.25mm, average inter-pin error of 0.87). This difference is very significant considering this configuration was not tested with Calsol and emulsion.
- Percentage repeatability of the retracted pole (84.80%) was higher than the extended pole (81.11%) but significantly lower than no pole (89.94%). This is also reflected in the high width of the confidence interval of more than 4mm for both. This was clearly observed during testing by the frequent dynamic status prompted by the device.
- HOOPS caused more errors (4.5mm) than Hydrocal (3.09mm) for these tests and had lower percentage repeatability (79.15% versus 86.13%).
- Oil thickness in these tests did not seem to play a significant role in the performance.

## 5.3 Handheld Sensor Float Static and Dynamic Tests

In this configuration the handheld sensor with Gap 1mm, Base width 2mm, and inter-pin distance of 3mm, was mounted on the floater. In these tests, Hydrocal was used with the three thicknesses: 13, 25 and 71 for the static case and the 71 mm with wave 1 for the dynamic case.
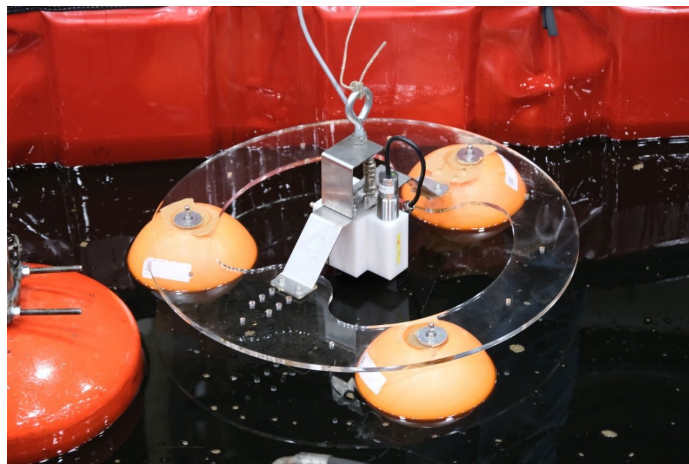


**Figure 5.7: Handheld in configuration 7 during test.**

Results are shown in Table 5-10 and Figure 5.8. In the static case, this configuration gave highly accurate measures with average absolute errors less than 1mm. In addition, the repeatability was high for all cases (higher than 96.57%) and the 95% confidence interval width was very narrow (less than 2mm). It is also worth noting that the sensor was giving very low standard deviation for each measure (less than 1.03). Even in wave conditions, the float provided good stability and leveling for the sensor which gave an error less than 2 inter-pin and repeatability of 98.81%.

**Table 5-10: Static and one dynamic test results.**

| Thickness | Conditions | Measurements | STD | Error | Absolute Error | % Error | % Repeatability | Inter-pin Error | 95% Confidence Interval I | | Width of I |
|---|---|---|---|---|---|---|---|---|---|---|---|
| 13 | Static | 13.33 | 0.09 | -0.33 | 0.54 | 4.15 | 97.42 | 0.18 | 12.90 | 13.75 | 0.85 |
| 25 | Static | 25.60 | 0.62 | -0.60 | 0.83 | 3.31 | 96.57 | 0.28 | 24.68 | 26.51 | 1.82 |
| 71 | Static | 70.76 | 1.03 | 0.24 | 0.79 | 1.11 | 98.84 | 0.26 | 69.76 | 71.76 | 2.00 |
| 71 | Wave 1 | 76.56 | 2.95 | -5.56 | 5.56 | 7.83 | 98.81 | 1.85 | 75.40 | 77.73 | 2.33 |
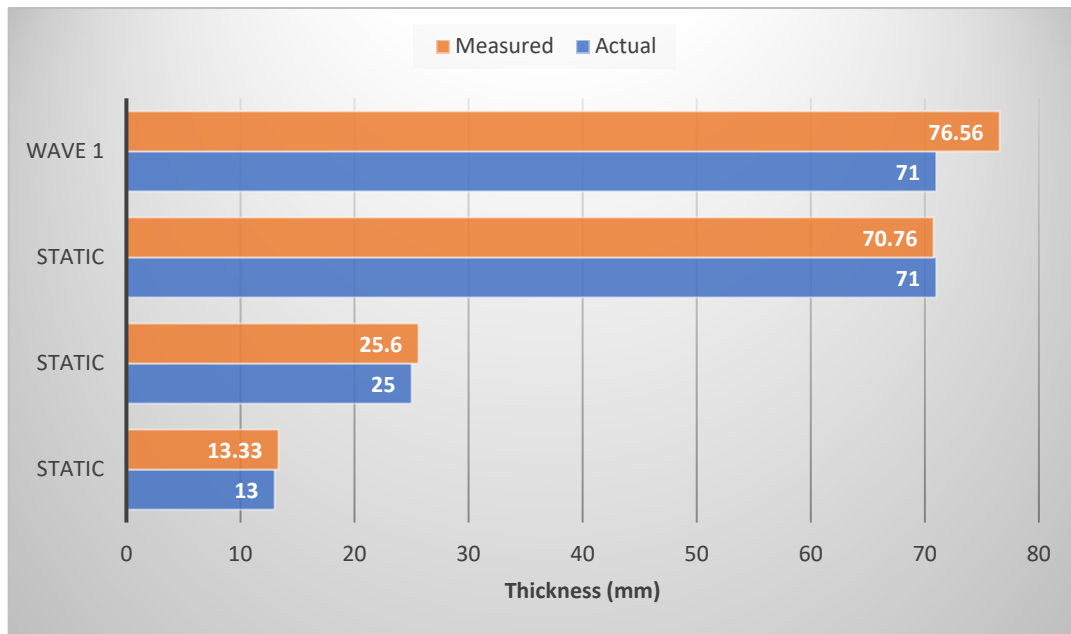


**Figure 5.8: Measured thickness vs. actual thickness.**

# 6 Skimmer Sensor CRREL Test Results

In this chapter, we present the results of the tests that were conducted using the skimmer sensors, which included static and dynamic tests.

## 6.1 Skimmer Sensor Static Tests

An example of this type of tests is shown in Figure 4.5.

### 6.1.1 Oil Type Analysis

When conducting the oil type analysis, we will compare the response of the sensor to different types of oils for the same configuration and thickness. The aim behind this interpretation is to evaluate the effect of oil type on the performance of the sensor, particularly as it relates to fouling impact.

**Configurations #5:**
The characteristics of the high-resolution handheld sensor are Gap: 5mm, Base Width: 2mm, Inter-pin Distance: 7mm. All the results of this case are shown in Table 6-1, Figure 6.1, and Table 6-2.

**Table 6-1: Test outcomes for configuration 5 (Color coding defined in Section 4.8)**

| Thickness | Oil Type | 5 | | | | | | | | |
|---|---|---|---|---|---|---|---|---|---|---|
| | | Measurements | Error | Absolute Error | % Error | % Repeatability | Inter-pin Error | 95% Confidence Interval I | | Width of I |
| 3 | Diesel | 3.31 | -0.31 | 1.64 | 54.57 | 52.01 | 0.23 | 2.14 | 4.47 | 2.33 |
| | Hydrocal 300 | 1.56 | 1.44 | 1.44 | 47.97 | 80.31 | 0.21 | 1.29 | 1.83 | 0.54 |
| | Calsol | 9.28 | -6.28 | 6.28 | 209.47 | 93.80 | 0.90 | 8.85 | 9.72 | 0.87 |
| | HOOPs | 3.94 | -0.94 | 0.94 | 31.43 | 99.08 | 0.13 | 3.92 | 3.97 | 0.06 |
| | Emulsion | | | | | | | | | |
| 6 | Diesel | 2.89 | 3.11 | 3.11 | 51.83 | 92.11 | 0.44 | 2.69 | 3.09 | 0.40 |
| | Hydrocal 300 | 4.55 | 1.45 | 1.45 | 24.22 | 99.05 | 0.21 | 4.51 | 4.58 | 0.07 |
| | Calsol | 13.68 | -7.68 | 7.68 | 127.92 | 90.57 | 1.10 | 12.68 | 14.67 | 2.00 |
| | HOOPs | 4.50 | 1.50 | 1.50 | 24.98 | 93.61 | 0.21 | 4.24 | 4.76 | 0.52 |
| | Emulsion | | | | | | | | | |
| 13 | Diesel | 11.54 | 1.46 | 1.67 | 12.82 | 92.29 | 0.24 | 10.85 | 12.24 | 1.39 |
| | Hydrocal 300 | 15.25 | -2.25 | 2.95 | 22.65 | 87.32 | 0.42 | 13.79 | 16.70 | 2.90 |
| | Calsol | 22.18 | -9.18 | 9.18 | 70.62 | 90.48 | 1.31 | 20.74 | 23.62 | 2.88 |
| | HOOPs | 10.40 | 2.60 | 2.60 | 20.01 | 94.05 | 0.37 | 9.90 | 10.90 | 1.00 |
| | Emulsion | 15.13 | -2.13 | 2.13 | 16.38 | 98.97 | 0.30 | 15.01 | 15.25 | 0.24 |
| 25 | Diesel | 25.15 | -0.15 | 1.06 | 4.22 | 95.69 | 0.15 | 24.36 | 25.94 | 1.57 |
| | Hydrocal 300 | 22.39 | 2.61 | 2.96 | 11.84 | 89.71 | 0.42 | 20.57 | 24.20 | 3.63 |
| | Calsol | 30.62 | -5.62 | 5.62 | 22.49 | 99.28 | 0.80 | 30.46 | 30.79 | 0.33 |
| | HOOPs | 19.16 | 5.84 | 5.84 | 23.36 | 99.15 | 0.83 | 19.04 | 19.28 | 0.24 |
| | Emulsion | 24.91 | 0.09 | 0.61 | 2.43 | 97.70 | 0.09 | 24.47 | 25.35 | 0.88 |
| 51 | Diesel | 50.34 | 0.67 | 0.67 | 1.30 | 97.04 | 0.10 | 50.21 | 50.46 | 0.25 |
| | Hydrocal 300 | 45.63 | 5.37 | 5.37 | 10.54 | 88.94 | 0.77 | 45.08 | 46.17 | 1.09 |
| | Calsol | 59.54 | -8.54 | 8.54 | 16.74 | 91.21 | 1.22 | 58.84 | 60.23 | 1.39 |
| | HOOPs | 46.79 | 4.21 | 4.21 | 8.26 | 90.41 | 0.60 | 46.36 | 47.21 | 0.86 |
| | Emulsion | 52.24 | -1.24 | 1.24 | 2.43 | 99.77 | 0.18 | 52.15 | 52.33 | 0.18 |
| 76 | Diesel | 79.45 | 1.55 | 1.55 | 1.92 | 99.82 | 0.22 | 79.34 | 79.55 | 0.21 |
| | Hydrocal 300 | 69.15 | 11.85 | 11.85 | 14.63 | 98.95 | 1.69 | 68.57 | 69.74 | 1.17 |
| | Calsol | 82.65 | -1.65 | 1.65 | 2.04 | 99.06 | 0.24 | 82.08 | 83.23 | 1.14 |
| | HOOPs | 71.62 | 9.38 | 9.38 | 11.58 | 99.33 | 1.34 | 71.28 | 71.95 | 0.67 |
| 82 | Emulsion | 79.75 | 1.25 | 1.25 | 1.54 | 99.90 | 0.18 | 79.69 | 79.81 | 0.12 |
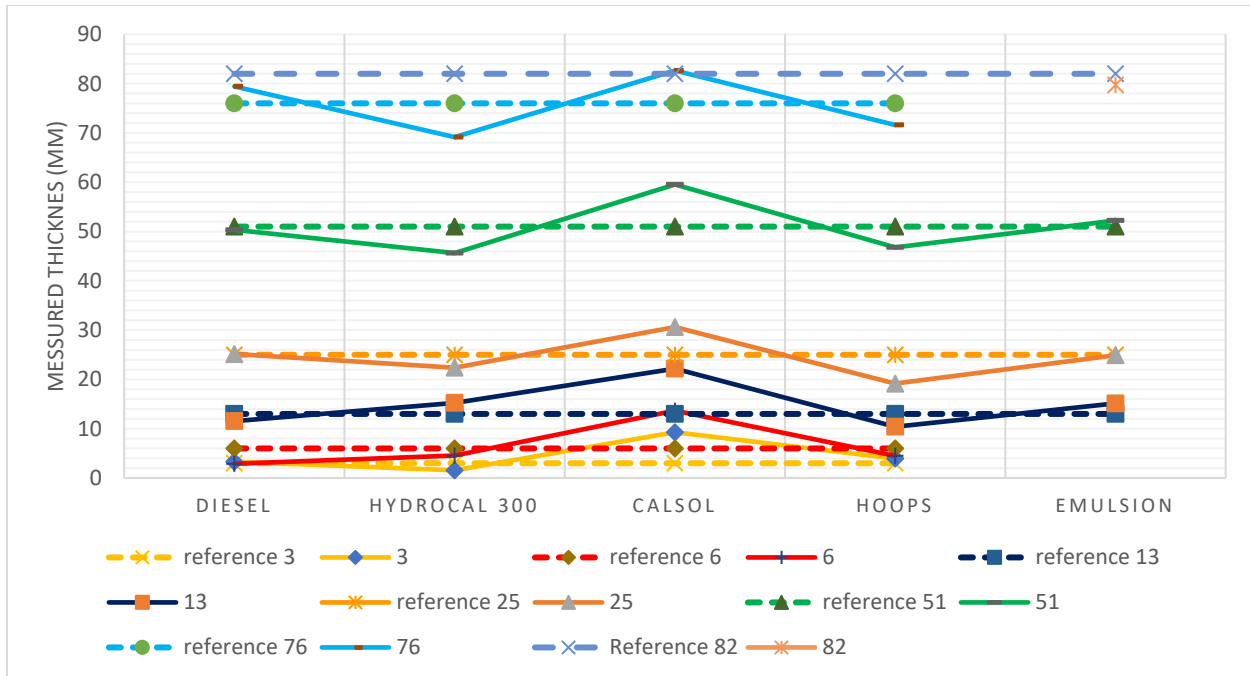
**Figure 6.1: Plot of the average measured thickness vs. reference thickness for Configuration 5**

Observations based on the results:

- Although the skimmer overall absolute error (3.73mm) was higher than the handheld (2.72mm), this is still impressive given that the inter-pin distance in this configuration is 7mm. Actually, the inter-pin error was 0.53 compared to 1.36 in handheld; this indicates that this sensor is able to mitigate fouling of pins more because the pins are less dense on the board.

- The sensor gave a high average overall percentage repeatability of 93.2% which was slightly higher than the 92.1% of configuration 1. This indicates that the measures were consistent across trials. This was also evident by the relatively narrow 95% confidence intervals which had an average width of 1.03mm, which was better than the 3.22mm for configuration 1.

- The oil causing the worst performance, as with handheld configurations, was Calsol. This was clearly attributed to the very high viscosity of this oil. Over estimation was particularly high for the 3 and 6mm cases.

- This sensor had very good performance with emulsion with an average absolute error of 1.31mm compared to 4.20mm in configuration 1.

- An important observation about the analysis for configuration 5 is that the first 5 measures were skipped (to allow for waves to start in the dynamic case) and the next 10 measures were used in the calculations. If instead we took the last 5 measures logged for each case, we can see the performance comparison for the two calculation methods in Table 6-2. On most criteria, particularly average absolute error, average repeatability, and average inter-pin error, the results were comparable with slight improvement in measures taken towards the end of the log file. This is attributed to the fact that the sensor had more time to converge to the correct value and demonstrates the consistency in the sensor performance.

**Table 6-2: Average, min and max performance across all thicknesses for all oils (Configuration 5)**

| Configuration | | Absolute Error (mm) | % Repeatability | Inter-pin Error |
|---|---|---|---|---|
| 5 (Initial Measures) | Average | 3.73 | 93.20 | 0.53 |
| | Min | 0.61 | 52.01 | 0.09 |
| | Max | 11.85 | 99.90 | 1.69 |
| 5 (Final Measures) | Average | 3.62 | 95.37 | 0.52 |
| | Min | 0.64 | 83.04 | 0.09 |
| | Max | 15.06 | 99.96 | 2.15 |

## Configurations #6:

The characteristics of the high-resolution handheld sensor are Gap: 10mm, Base Width: 2mm, Inter-pin Distance: 12mm. All the results of this case are shown in Table 6-3, Figure 6.2, and Table 6-4.

**Table 6-3: Test outcomes for configuration 6 (Color coding defined in Section 4.8)**

| Thickness | Oil Type | 6 | | | | | | | | |
|---|---|---|---|---|---|---|---|---|---|---|
| | | Measurements | Error | Absolute Error | % Error | % Repeatability | Inter-pin Error | 95% Confidence Interval I | | Width of I |
| 3 | Diesel | 17.05 | -14.05 | 14.05 | 468.23 | 97.68 | 1.17 | 16.75 | 17.35 | 0.60 |
| | Hydrocal 300 | 13.06 | -10.06 | 10.06 | 335.23 | 97.86 | 0.84 | 12.80 | 13.32 | 0.52 |
| | Calsol | 19.95 | -16.95 | 16.95 | 565.10 | 83.89 | 1.41 | 17.58 | 22.33 | 4.75 |
| | HOOPs | 19.53 | -16.53 | 16.53 | 550.93 | 98.97 | 1.38 | 19.36 | 19.69 | 0.33 |
| | Emulsion | | | | | | | | | |
| 6 | Diesel | 16.31 | -10.31 | 10.31 | 171.77 | 84.52 | 0.86 | 14.42 | 18.19 | 3.77 |
| | Hydrocal 300 | 21.64 | -15.64 | 15.64 | 260.70 | 98.37 | 1.30 | 21.37 | 21.92 | 0.55 |
| | Calsol | 26.16 | -20.16 | 20.16 | 336.07 | 95.81 | 1.68 | 25.37 | 26.96 | 1.60 |
| | HOOPs | 17.82 | -11.82 | 11.82 | 197.00 | 93.21 | 0.99 | 16.73 | 18.91 | 2.18 |
| | Emulsion | | | | | | | | | |
| 13 | Diesel | 13.92 | -0.92 | 0.92 | 7.06 | 98.75 | 0.08 | 13.76 | 14.07 | 0.31 |
| | Hydrocal 300 | 25.49 | -12.49 | 12.49 | 96.05 | 99.75 | 1.04 | 25.44 | 25.53 | 0.10 |
| | Calsol | 35.60 | -22.60 | 22.60 | 173.87 | 98.20 | 1.88 | 35.07 | 36.14 | 1.07 |
| | HOOPs | 18.75 | -5.75 | 5.75 | 44.21 | 97.81 | 0.48 | 18.45 | 19.04 | 0.59 |
| | Emulsion | 14.52 | -1.52 | 1.52 | 11.72 | 98.52 | 0.13 | 14.37 | 14.68 | 0.31 |
| 25 | Diesel | 27.36 | -2.36 | 2.36 | 9.42 | 99.32 | 0.20 | 27.22 | 27.49 | 0.28 |
| | Hydrocal 300 | 30.63 | -5.63 | 5.63 | 22.50 | 97.93 | 0.47 | 30.10 | 31.15 | 1.05 |
| | Calsol | 35.72 | -10.72 | 10.72 | 42.88 | 98.45 | 0.89 | 35.22 | 36.21 | 0.99 |
| | HOOPs | 21.56 | 3.44 | 3.85 | 15.40 | 89.94 | 0.32 | 19.79 | 23.33 | 3.54 |
| | Emulsion | 22.82 | 2.18 | 2.18 | 8.72 | 98.95 | 0.18 | 22.64 | 23.00 | 0.37 |
| 51 | Diesel | 51.37 | -0.37 | 0.44 | 0.86 | 99.44 | 0.04 | 51.15 | 51.59 | 0.44 |
| | Hydrocal 300 | 58.64 | -7.64 | 7.64 | 14.98 | 99.06 | 0.64 | 58.24 | 59.04 | 0.81 |
| | Calsol | 70.21 | -19.21 | 19.21 | 37.66 | 98.85 | 1.60 | 69.46 | 70.95 | 1.49 |
| | HOOPs | 45.87 | 5.13 | 5.13 | 10.06 | 94.46 | 0.43 | 43.88 | 47.86 | 3.98 |
| | Emulsion | 49.52 | 1.48 | 1.48 | 2.90 | 99.74 | 0.12 | 49.42 | 49.63 | 0.21 |
| 76 | Diesel | 83.01 | -2.01 | 2.01 | 2.49 | 99.88 | 0.17 | 82.94 | 83.09 | 0.15 |
| | Hydrocal 300 | 82.50 | -1.50 | 1.64 | 2.02 | 98.77 | 0.14 | 81.73 | 83.27 | 1.54 |
| | Calsol | 97.26 | -16.26 | 16.26 | 20.08 | 98.64 | 1.36 | 96.10 | 98.43 | 2.33 |
| | HOOPs | 68.49 | 12.51 | 12.51 | 15.45 | 98.94 | 1.04 | 67.97 | 69.00 | 1.03 |
| 82 | Emulsion | 78.65 | 2.35 | 2.35 | 2.90 | 99.37 | 0.20 | 78.23 | 79.07 | 0.84 |
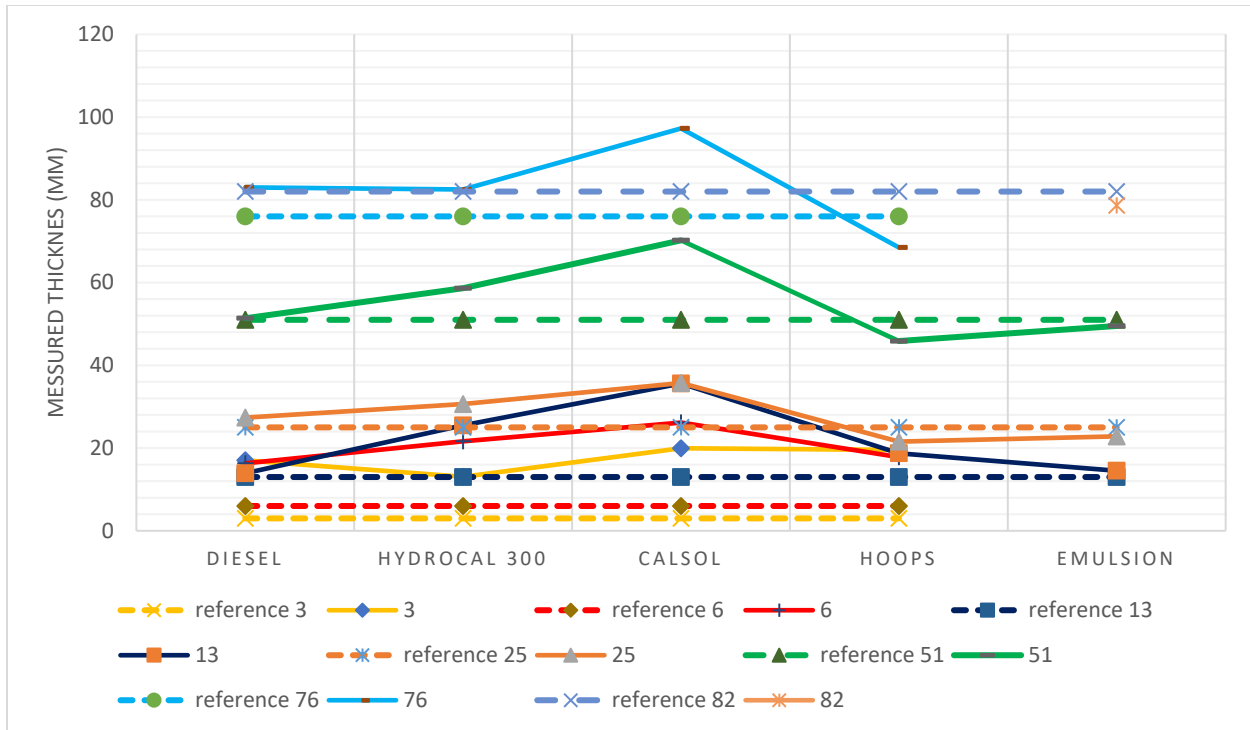
**Figure 6.2: Plot of the average measured thickness vs. reference thickness for configuration 6**

**Table 6-4: Average, min and max performance across all thicknesses for all oils (Configuration 6)**

| Configuration | | Absolute Error (mm) | % Repeatability | Inter-pin Error |
|---|---|---|---|---|
| 6 (Initial Measures) | Average | 9.01 | 96.97 | 0.75 |
| | Min | 0.44 | 83.89 | 0.04 |
| | Max | 22.6 | 99.88 | 1.88 |
| 6 (Final Measures) | Average | 7.41 | 97.93 | 0.62 |
| | Min | 0.28 | 88.69 | 0.02 |
| | Max | 18.3 | 99.92 | 1.53 |

Observations based on the results:

- This configuration gave higher average absolute error (9.01mm) compared to configuration 5 (3.73mm). This was particularly caused by Calsol, as with other configurations, and by small thicknesses (3mm and 6mm). These two thicknesses are so small compared to inter-pin distance of 12mm that we recommend this configuration not be used in those cases.
- The sensor gave a high average overall percentage repeatability of 96.97% which was higher than configuration 5 (93.20%) indicating consistent performance. This was also evident by the relatively narrow 95% confidence intervals which had an average width of 1.28mm.
- This sensor had very good performance with emulsion with an average absolute error of 1.88mm compared to 1.31mm in configuration 5.

- Similar to configuration 5, the first 5 measures were skipped (to allow for waves to start in the dynamic case) and the next 10 measures were used in the calculations. If instead we took the last 5 measures logged for each case, we can see the performance comparison for the two calculation methods in Table 6-4. Similar to configuration 5, on most criteria, particularly average absolute error, average repeatability, and average inter-pin error, the results were comparable with slight improvement in measures taken towards the end of the log file. Again, this is attributed to the fact that the sensor had more time to converge to the correct value and demonstrates the consistency in the sensor performance.

## 6.1.2  Thickness Analysis

Thickness based analysis focuses on the impact of oil thickness on the performance of the sensor.

**Configuration #5:**

The results of the tests organized to reveal thickness effect are shown in Table 6-5.

**Table 6-5: Data arranged to reveal thickness effect on configuration 5**

| Oil Type | Thickness | Measurements | Error | Absolute Error | % Error | % Repeatability | Inter-pin Error | 95% Confidence Interval I | | Width of I |
|---|---|---|---|---|---|---|---|---|---|---|
| Diesel | 3 | 3.31 | -0.31 | 1.64 | 54.57 | 52.01 | 0.23 | 2.14 | 4.47 | 2.33 |
| | 6 | 2.89 | 3.11 | 3.11 | 51.83 | 92.11 | 0.44 | 2.69 | 3.09 | 0.40 |
| | 13 | 11.54 | 1.46 | 1.67 | 12.82 | 92.29 | 0.24 | 10.85 | 12.24 | 1.39 |
| | 25 | 25.15 | -0.15 | 1.06 | 4.22 | 95.69 | 0.15 | 24.36 | 25.94 | 1.57 |
| | 51 | 50.34 | 0.67 | 0.67 | 1.30 | 97.04 | 0.10 | 50.21 | 50.46 | 0.25 |
| | 76 | 79.45 | 1.55 | 1.55 | 1.92 | 99.82 | 0.22 | 79.34 | 79.55 | 0.21 |
| Hydrocal 300 | 3 | 1.56 | 1.44 | 1.44 | 47.97 | 80.31 | 0.21 | 1.29 | 1.83 | 0.54 |
| | 6 | 4.55 | 1.45 | 1.45 | 24.22 | 99.05 | 0.21 | 4.51 | 4.58 | 0.07 |
| | 13 | 15.25 | -2.25 | 2.95 | 22.65 | 87.32 | 0.42 | 13.79 | 16.70 | 2.90 |
| | 25 | 22.39 | 2.61 | 2.96 | 11.84 | 89.71 | 0.42 | 20.57 | 24.20 | 3.63 |
| | 51 | 45.63 | 5.37 | 5.37 | 10.54 | 88.94 | 0.77 | 45.08 | 46.17 | 1.09 |
| | 76 | 69.15 | 11.85 | 11.85 | 14.63 | 98.95 | 1.69 | 68.57 | 69.74 | 1.17 |
| Calsol | 3 | 9.28 | -6.28 | 6.28 | 209.47 | 93.80 | 0.90 | 8.85 | 9.72 | 0.87 |
| | 6 | 13.68 | -7.68 | 7.68 | 127.92 | 90.57 | 1.10 | 12.68 | 14.67 | 2.00 |
| | 13 | 22.18 | -9.18 | 9.18 | 70.62 | 90.48 | 1.31 | 20.74 | 23.62 | 2.88 |
| | 25 | 30.62 | -5.62 | 5.62 | 22.49 | 99.28 | 0.80 | 30.46 | 30.79 | 0.33 |
| | 51 | 59.54 | -8.54 | 8.54 | 16.74 | 91.21 | 1.22 | 58.84 | 60.23 | 1.39 |
| | 76 | 82.65 | -1.65 | 1.65 | 2.04 | 99.06 | 0.24 | 82.08 | 83.23 | 1.14 |
| HOOPs | 3 | 3.94 | -0.94 | 0.94 | 31.43 | 99.08 | 0.13 | 3.92 | 3.97 | 0.06 |
| | 6 | 4.50 | 1.50 | 1.50 | 24.98 | 93.61 | 0.21 | 4.24 | 4.76 | 0.52 |
| | 13 | 10.40 | 2.60 | 2.60 | 20.01 | 94.05 | 0.37 | 9.90 | 10.90 | 1.00 |
| | 25 | 19.16 | 5.84 | 5.84 | 23.36 | 99.15 | 0.83 | 19.04 | 19.28 | 0.24 |
| | 51 | 46.79 | 4.21 | 4.21 | 8.26 | 90.41 | 0.60 | 46.36 | 47.21 | 0.86 |
| | 76 | 71.62 | 9.38 | 9.38 | 11.58 | 99.33 | 1.34 | 71.28 | 71.95 | 0.67 |
| Emulsion | 13 | 15.13 | -2.13 | 2.13 | 16.38 | 98.97 | 0.30 | 15.01 | 15.25 | 0.24 |
| | 25 | 24.91 | 0.09 | 0.61 | 2.43 | 97.70 | 0.09 | 24.47 | 25.35 | 0.88 |
| | 51 | 52.24 | -1.24 | 1.24 | 2.43 | 99.77 | 0.18 | 52.15 | 52.33 | 0.18 |
| | 82 | 79.75 | 1.25 | 1.25 | 1.54 | 99.90 | 0.18 | 79.69 | 79.81 | 0.12 |

The observations based on the table show that the average absolute error increased with thickness: ({Thickness, Error}: {3mm, 2.58mm}, {6mm, 3.43mm}, {13mm, 3.7mm}, {25mm, 3.22mm}, {51mm, 4.01mm}, {76mm, 6.11mm}). However, when all these errors are put in the context of inter-pin distance (7mm) the results is overall less than one pin error (0.53 average inter pin error).

## Configuration #6:

The results of the tests organized to reveal thickness effect are shown in Table 6-6.

**Table 6-6: Data arranged to reveal thickness effect on configuration 6**

| Oil Type | Thickness | Measurements | Error | Absolute Error | % Error | % Repeatability | Inter-pin Error | 95% Confidence Interval I | | Width of I |
|---|---|---|---|---|---|---|---|---|---|---|
| | | | | | | | | | | 6 |
| Diesel | 3 | 17.05 | -14.05 | 14.05 | 468.23 | 97.68 | 1.17 | 16.75 | 17.35 | 0.60 |
| | 6 | 16.31 | -10.31 | 10.31 | 171.77 | 84.52 | 0.86 | 14.42 | 18.19 | 3.77 |
| | 13 | 13.92 | -0.92 | 0.92 | 7.06 | 98.75 | 0.08 | 13.76 | 14.07 | 0.31 |
| | 25 | 27.36 | -2.36 | 2.36 | 9.42 | 99.32 | 0.20 | 27.22 | 27.49 | 0.28 |
| | 51 | 51.37 | -0.37 | 0.44 | 0.86 | 99.44 | 0.04 | 51.15 | 51.59 | 0.44 |
| | 76 | 83.01 | -2.01 | 2.01 | 2.49 | 99.88 | 0.17 | 82.94 | 83.09 | 0.15 |
| Hydrocal 300 | 3 | 13.06 | -10.06 | 10.06 | 335.23 | 97.86 | 0.84 | 12.80 | 13.32 | 0.52 |
| | 6 | 21.64 | -15.64 | 15.64 | 260.70 | 98.37 | 1.30 | 21.37 | 21.92 | 0.55 |
| | 13 | 25.49 | -12.49 | 12.49 | 96.05 | 99.75 | 1.04 | 25.44 | 25.53 | 0.10 |
| | 25 | 30.63 | -5.63 | 5.63 | 22.50 | 97.93 | 0.47 | 30.10 | 31.15 | 1.05 |
| | 51 | 58.64 | -7.64 | 7.64 | 14.98 | 99.06 | 0.64 | 58.24 | 59.04 | 0.81 |
| | 76 | 82.50 | -1.50 | 1.64 | 2.02 | 98.77 | 0.14 | 81.73 | 83.27 | 1.54 |
| Calsol | 3 | 19.95 | -16.95 | 16.95 | 565.10 | 83.89 | 1.41 | 17.58 | 22.33 | 4.75 |
| | 6 | 26.16 | -20.16 | 20.16 | 336.07 | 95.81 | 1.68 | 25.37 | 26.96 | 1.60 |
| | 13 | 35.60 | -22.60 | 22.60 | 173.87 | 98.20 | 1.88 | 35.07 | 36.14 | 1.07 |
| | 25 | 35.72 | -10.72 | 10.72 | 42.88 | 98.45 | 0.89 | 35.22 | 36.21 | 0.99 |
| | 51 | 70.21 | -19.21 | 19.21 | 37.66 | 98.85 | 1.60 | 69.46 | 70.95 | 1.49 |
| | 76 | 97.26 | -16.26 | 16.26 | 20.08 | 98.64 | 1.36 | 96.10 | 98.43 | 2.33 |
| HOOPs | 3 | 19.53 | -16.53 | 16.53 | 550.93 | 98.97 | 1.38 | 19.36 | 19.69 | 0.33 |
| | 6 | 17.82 | -11.82 | 11.82 | 197.00 | 93.21 | 0.99 | 16.73 | 18.91 | 2.18 |
| | 13 | 18.75 | -5.75 | 5.75 | 44.21 | 97.81 | 0.48 | 18.45 | 19.04 | 0.59 |
| | 25 | 21.56 | 3.44 | 3.85 | 15.40 | 89.94 | 0.32 | 19.79 | 23.33 | 3.54 |
| | 51 | 45.87 | 5.13 | 5.13 | 10.06 | 94.46 | 0.43 | 43.88 | 47.86 | 3.98 |
| | 76 | 68.49 | 12.51 | 12.51 | 15.45 | 98.94 | 1.04 | 67.97 | 69.00 | 1.03 |
| Emulsion | 13 | 14.52 | -1.52 | 1.52 | 11.72 | 98.52 | 0.13 | 14.37 | 14.68 | 0.31 |
| | 25 | 22.82 | 2.18 | 2.18 | 8.72 | 98.95 | 0.18 | 22.64 | 23.00 | 0.37 |
| | 51 | 49.52 | 1.48 | 1.48 | 2.90 | 99.74 | 0.12 | 49.42 | 49.63 | 0.21 |
| | 82 | 78.65 | 2.35 | 2.35 | 2.90 | 99.37 | 0.20 | 78.23 | 79.07 | 0.84 |

From the table the performance of this sensor with respect to thickness was closer to configuration 1 and 2, where the best performance was for the middle thicknesses and the worst by far was for the lowest thicknesses: ({Thickness, Error}: {3mm, 14.40mm}, {6mm, 14.48mm}, {13mm, 8.66mm}, {25mm, 4.95mm}, {51mm, 6.78mm}, {76mm, 8.11mm}). When those errors are put in the context of inter-pin distance (12mm) the results is overall less than one pin error (0.75 average inter pin error).

## 6.2  Skimmer Sensor Dynamic Tests

The setup with sample waves are shown in Figure 6.3. The response of the sensor was logged in static conditions before applying the waves. This was carried out this step to ensure that the sensor is measuring correctly before the applying the waves. This will also allow us to compare the results between static and dynamic cases.
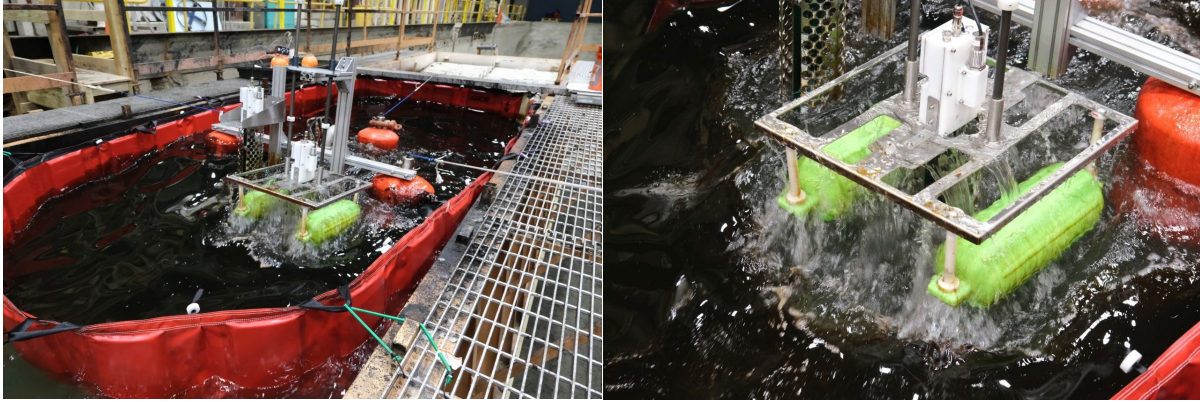
**Figure 6.3: Skimmer sensor during dynamic testing.**

## Configuration #5:

The results for this configuration are shown in Table 6-7 and Figure 6.4.

**Table 6-7: Test results in dynamic environment for configuration 5**

| Thickness | Wave Number | Measurements | Error | Absolute Error | % Error | % Repeatability | Inter-pin Error | 95% Confidence Interval I | | Width of I |
|---|---|---|---|---|---|---|---|---|---|---|
| | Static | 13.04 | -0.04 | 0.07 | 0.53 | 99.57 | 0.01 | 13.00 | 13.09 | 0.09 |
| | 1 | 7.68 | 5.32 | 5.32 | 40.89 | 88.41 | 0.76 | 7.03 | 8.34 | 1.31 |
| 13 | 2 | 6.91 | 6.09 | 6.09 | 46.83 | 77.39 | 0.87 | 5.52 | 8.31 | 2.79 |
| | 3 | 6.58 | 6.42 | 6.42 | 49.37 | 89.98 | 0.92 | 6.08 | 7.08 | 1.00 |
| | 4 | 9.58 | 3.42 | 3.42 | 26.34 | 99.43 | 0.49 | 9.53 | 9.62 | 0.09 |
| | Static | 12.20 | 12.80 | 12.80 | 51.20 | 93.09 | 1.83 | 11.48 | 12.92 | 1.43 |
| | 1 | 11.61 | 13.39 | 13.39 | 53.56 | 80.96 | 1.91 | 9.94 | 13.28 | 3.35 |
| 25 | 2 | 19.37 | 5.63 | 5.63 | 22.53 | 93.63 | 0.80 | 18.40 | 20.34 | 1.94 |
| | 3 | 18.39 | 6.61 | 6.61 | 26.44 | 95.37 | 0.94 | 17.69 | 19.09 | 1.41 |
| | 4 | 22.66 | 2.34 | 2.34 | 9.35 | 95.80 | 0.33 | 21.93 | 23.40 | 1.47 |
| | Static | 66.60 | 4.40 | 4.40 | 6.20 | 98.64 | 0.63 | 65.84 | 67.36 | 1.53 |
| | 1 | 66.55 | 4.45 | 4.45 | 6.27 | 99.17 | 0.64 | 66.09 | 67.01 | 0.93 |
| 71 | 2 | 67.27 | 3.73 | 3.73 | 5.26 | 99.96 | 0.53 | 67.25 | 67.29 | 0.04 |
| | 3 | 68.55 | 2.45 | 2.45 | 3.45 | 99.98 | 0.35 | 68.54 | 68.57 | 0.03 |
| | 4 | 63.16 | 7.84 | 7.84 | 11.04 | 99.54 | 1.12 | 62.84 | 63.47 | 0.63 |

Analyzing the results, we observe the following:

- The average absolute error for all wave cases (5.64mm) was comparable to the static case before waves were started (5.76mm). Even if we consider the last measures in the log the wave error is 5.09mm and the static error is 5.39mm, which is also comparable. This demonstrates that the sensor was able to mitigate most errors due to waves with an average inter-pin error of 0.81.
- The middle thickness seemed to have slightly higher error than the others: 13mm had an error of 5.31mm (3.68 end of log), 25mm had an error of 6.99mm (6.59mm end of log), and 71mm had an error of 4.62mm (5.01 end of log).
- Surprisingly, the wave configuration had minor effect on the performance:
  Wave 1: 7.72mm (6.33mm end of log)
  Wave 2: 5.15mm (4.05mm end of log)
  Wave 3: 5.16mm (3.45mm end of log)
  Wave 4: 4.53mm (6.54mm end of log)
- Overall the sensor had very good percentage repeatability of measures during waves of 93.30%.
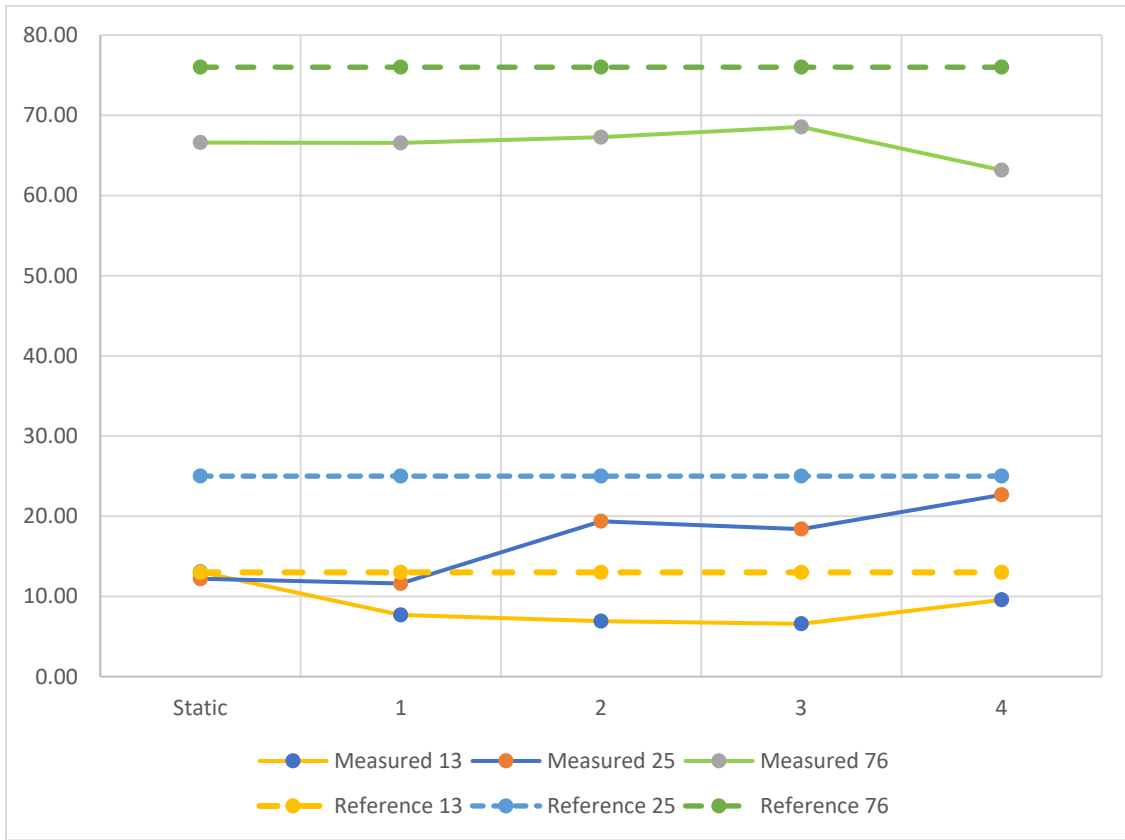
**Figure 6.4: Plot of measured thickness vs. actual one for configuration 5 in waves.**

## Configuration #6

The results for the final experiment are shown in Table 6-8 and Figure 6.5.

**Table 6-8: Test results in dynamic environment for configuration 6**

| Thickness | Wave Number | Measurements | Error | Absolute Error | % Error | % Repeatability | Inter-pin Error | 95% Confidence Interval I | | Width of I |
|---|---|---|---|---|---|---|---|---|---|---|
| 13 | Static | 15.43 | -2.43 | 2.43 | 18.68 | 99.80 | 0.20 | 15.40 | 15.46 | 0.06 |
| | 1 | 15.75 | -2.75 | 2.75 | 21.15 | 98.96 | 0.92 | 15.59 | 15.90 | 0.31 |
| | 2 | 14.86 | -1.86 | 1.86 | 14.30 | 99.87 | 0.62 | 14.85 | 14.87 | 0.03 |
| | 3 | 5.96 | 7.04 | 7.04 | 54.18 | 69.63 | 2.35 | 4.70 | 7.22 | 2.52 |
| | 4 | 13.15 | -0.15 | 1.63 | 12.57 | 88.24 | 0.54 | 11.88 | 14.42 | 2.54 |
| 25 | Static | 24.04 | 0.96 | 0.96 | 3.84 | 99.20 | 0.08 | 23.89 | 24.19 | 0.30 |
| | 1 | 33.35 | -8.35 | 8.35 | 33.38 | 99.94 | 0.70 | 33.33 | 33.36 | 0.03 |
| | 2 | 30.41 | -5.41 | 5.41 | 21.62 | 92.05 | 0.45 | 28.41 | 32.40 | 3.99 |
| | 3 | 35.47 | -10.47 | 10.47 | 41.86 | 98.63 | 0.87 | 35.07 | 35.87 | 0.80 |
| | 4 | 35.25 | -10.25 | 10.25 | 40.99 | 95.70 | 0.85 | 34.12 | 36.38 | 2.26 |
| 71 | Static | 69.38 | 1.62 | 1.62 | 2.28 | 99.97 | 0.13 | 69.37 | 69.40 | 0.03 |
| | 1 | 70.33 | 0.67 | 0.89 | 1.26 | 98.97 | 0.07 | 69.80 | 70.86 | 1.07 |
| | 2 | 79.65 | -8.65 | 8.65 | 12.18 | 99.97 | 0.72 | 79.63 | 79.67 | 0.04 |
| | 3 | 75.71 | -4.71 | 4.71 | 6.64 | 98.79 | 0.39 | 74.90 | 76.53 | 1.63 |
| | 4 | 76.50 | -5.50 | 5.50 | 7.75 | 97.13 | 0.46 | 74.95 | 78.05 | 3.09 |

Analyzing the results, we observe the following:
- The average absolute error for all wave cases (5.63mm) was higher than the static case before waves were started (1.67mm). Even if we consider the last measures in the log the wave error is 5.38mm and the static error is 1.71mm. This demonstrates that the sensor was able to mitigate most errors due to waves with an average inter-pin error of 0.75.
- The middle thickness had significantly higher error than the others: 13mm had an error of 3.32mm (2.10 end of log), 25mm had an error of 8.62mm (9.46mm end of log), and 71mm had an error of 4.94mm (4.58 end of log). This was similar to configuration 5.
- The wave configuration had minor effect on the performance:
  Wave 1: 4.00mm (3.27mm end of log)
  Wave 2: 5.30mm (6.76mm end of log)
  Wave 3: 7.41mm (4.30mm end of log)
  Wave 4: 5.63mm (7.19mm end of log)
  This effect was not consistent with configuration 5 and not consistent between start and end of log so cannot be generalized.
- Overall the sensor had very good percentage repeatability of measures during waves of 94.82%.
- Comparing the errors, configuration 5 in waves consistently under estimated while configuration 6 consistently over estimated. This could be due to how the sensors are situated relative to the water/oil interface.
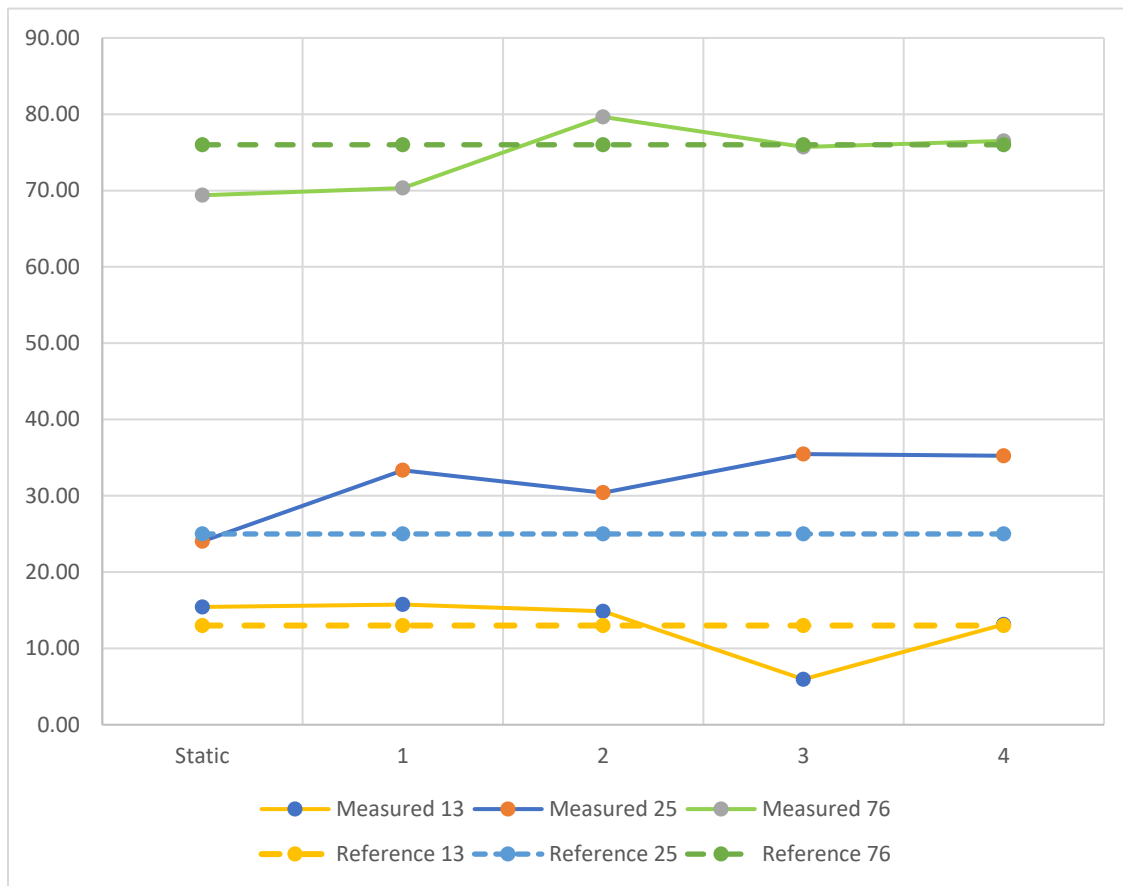


**Figure 6.5: Plot of measured thickness vs. actual thickness for configuration 6 in waves.**

## 6.3   Skimmer Sensor Static Test while Oil Being Skimmed from Tank

In this test, a skimmer was placed behind the Termite skimmer and was used to skim the oil in the tank as shown in Figure 6.6. No waves were generated during the test and the skimmer sensors were logging data continuously. It is not possible to know the group truth of the thickness during the skimming, but we know that the initial thickness was 71mm and at the end there was no oil left around the sensors.



**Figure 6.6: Skimmer placed behind the Termite to remove the oil**
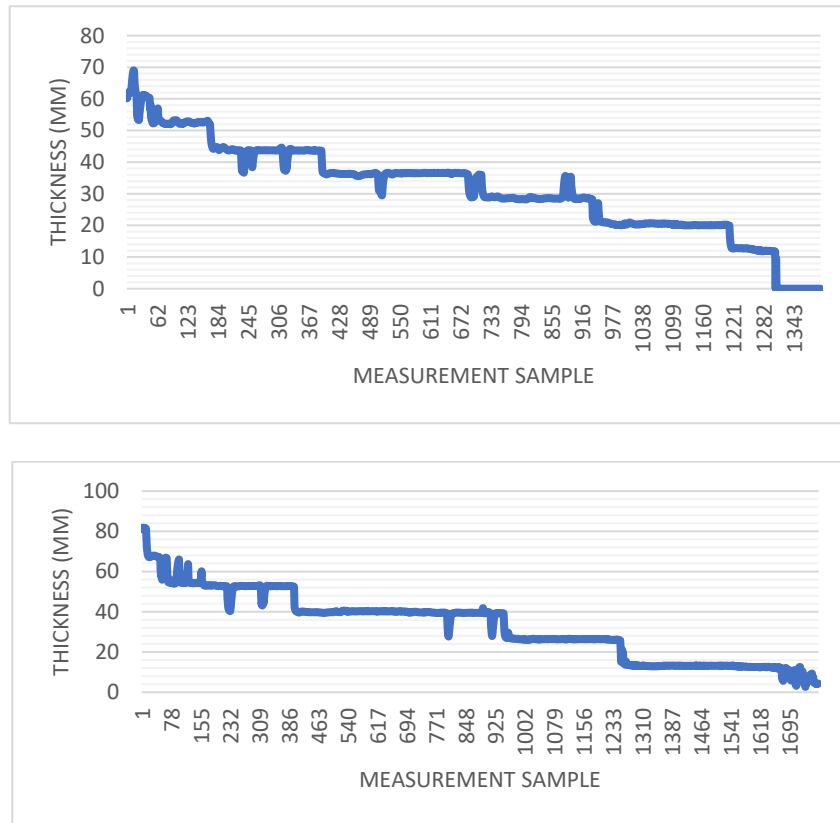
**Figure 6.7: Results of both skimmer sensors while the oil is being skimmed (Top: Configuration 5, Bottom: Configuration 6).**

Results are shown in Figure 6.7. Both sensors performed as expected showing the drop in oil thickness. In both cases, the spikes (up and down) are equivalent to one pin error. The staircase pattern is expected since as water rises to replace the oil there is a moment when a pin switches from oil to water, and this results in an inter-pin distance drop.

# 7 Conclusion, Observations and Recommendations

In conclusion, we summarize there the measurement performance of the different sensor configuration:

**Handheld 1** static testing gave an overall average absolute error of **2.72mm and 92.1%** average repeatability.

**Handheld 2** static testing gave an overall average absolute error of **2.25mm and 89.94%** average repeatability. On pole testing gave an overall average absolute error of **3.73mm and 82.96%** average repeatability. On float testing gave an overall average absolute error of **0.72mm for static and 5.56mm in waves and 97.61%** average repeatability for static and **98.81%** in waves.

Although Handheld 2 resolution was 3mm versus 2mm for Handheld 1, the performance was overall comparable and the sensing range was longer. This constituted an advantage of the 3mm resolution device.

**Skimmer mounted sensor 1** static testing gave an overall average absolute error of **3.73mm and 93.20%** average repeatability and in wave testing gave an overall average absolute error of **5.64mm and 93.30%** average repeatability.

**Skimmer mounted sensor 2** static testing gave an overall average absolute error of **9.01mm and 96.97%** average repeatability and in wave testing gave an overall average absolute error of **5.63mm and 94.82%** average repeatability.

Skimmer mounted sensor 1 (7mm resolution) had an advantage over sensor 2 (12mm resolution) in the static case although in the dynamic case the difference was not evident. However, the comparison in the dynamic case is not valid as the two sensors were mounted differently on the skimmer.

All sensor configurations resulted in an overall absolute error below their resolution except for the 2mm resolution handheld sensor which had an overall absolute error slightly over its resolution and the 3mm resolution handheld sensor which had a slightly higher absolute error when used with the pole and when subjected to waves.

During testing we had several observations and lessons learned which we will summarize next along with some improvements introduced post testing. We conclude this section with a list of additional future recommended improvements.

## 7.1 Automated MPR Testing

One of the most significant sources of large errors was the MPR chip damage. In several cases, it took some time to debug those defects and resulted in some tests logging high errors. The number of chips damaged was unreasonably high compared to what we had experienced along the years in the lab. This might be attributed to damage during shipping from temperature changes or vibrations.

On each sensor board, we use 4 MPR 121 Proximity Capacitive Touch Sensor Controllers. Every capacitive sensor supports 12 sensing channels connected to 12 electrodes. During our tests, some measurements failed and had unpredictable values. Figure 7.1 shows sample calibrated voltage values (Reference) compared to what the defective MPR was measuring and the replaced MPR was measuring.
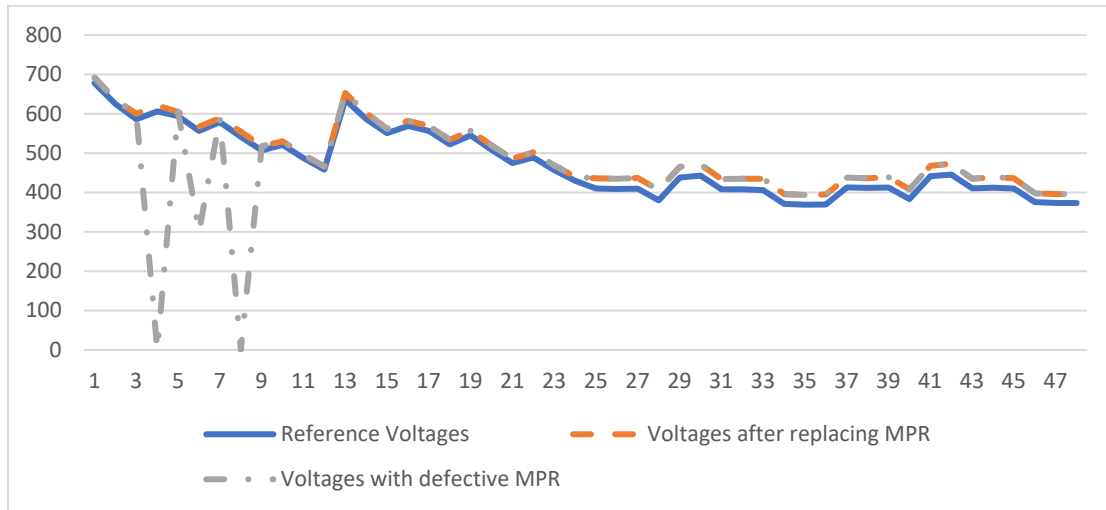


**Figure 7.1: Example of voltages measured by a defected MPR and values after it was replaced.**

The voltages measured at Electrodes 4, 6 and 8 dropped to values lower than the reference voltages. This caused misclassification of the nature of these electrodes (water or non-water), thus causing false thickness estimation by the sensor. Since the 3 faults are in the first 12 measurements, the defective MPR is the MPR 1. After replacing it with new MPR, the voltage curve retained its normal form (no zeros or outliers), the sensor estimation was corrected.

To detect MPR failure in future tests, we upgraded our software in both sensors Handheld and Skimmer so that before starting any test, a routine check is executed to monitor the health of the 4 MPRs, then an error message is displayed if a defective MPR is detected.

## 7.2 Skimmer Floating Platform

The second observation is related to the skimmer floating platform. Although the linear guides were aligned before moving the skimmer to the tank, this alignment was not maintained once the skimmer was lowered into the tank. This caused the floating platform not to respond as fast as expected during waves. This was not detrimental for most waves but for the highest wave, the platform was dipping into the oil/water and going out in a way that caused the oil to completely disperse from under the platform (see Figure 6.3). The platform did not mitigate well wave motion in multiple directions due to the single degree of freedom. Because of the significant motion, the sensor was ignoring most instantaneous measures (per the algorithm) to mitigate this effect. However, this resulted in the sensor not detecting the `no-oil' case for some time. To tackle this problem, we updated the software of the skimmer sensor to detect an extended period (10 consecutive iterations) during which instantaneous measures are not being accounted for. In

this case, the sensor sends a "no recent update is displayed" message to inform the operator that conditions are very difficult for measurement to be possible at that time.

On a related note, it was observed initially that the skimmer was tilting forward (due to bridge and sensors weight) and tilting sideways because the way sensors were placed initially did not distribute the weight evenly. The first issue was mitigated by placing a weight on the back float of the skimmer and the second issue was mitigated by moving the sensors closer to each other. The added weights on the skimmer caused it to sit too low in the water. If the skimmer was recovering oil in this case, it would be expected that it collects a large amount of water. Although in real field tests we would not have used both sensors at the same time, a lighter mounting alternative is still needed.

In addition, during one of highest wave action the frame and cage were slightly bent causing interference with the ultrasound signal. The cage had to be removed for subsequent tests.

## 7.3  Handheld Edge Cases and Cleaning

One edge case which was not being detected by the handheld sensor is when no pins are in water. In this case the sensor is submerged in the fluid, but all pins are in the oil (particularly in cases where the oil layer is very thick). We update the handheld sensor software to detect this case and prompt the user for adjustment. Now the sensor detects the following cases invalid measures, pins all in water, or pins all in oil.

Another observation is related to oil fouling. The next day after testing with Calsol we noticed that the oil had created a thick layer on the boards and pins causing the sensor to have wrong measures. This was resolved by dipping the boards in diesel oil, which was able to clean the boards easily. This is noted as a possible maintenance recommendation for the boards to be carried out especially after using it with very viscous oils.

## 7.4  Handheld Pole and Float Attachments Observations

For the handheld use cases, it was observed that switching from handheld to pole configuration took more time than expected (about 15min). In addition, the pole itself requires better harness design to facilitate its use. With the current design, holding the pole to keep the sensor leveled and without extensive motion proved to be challenging particularly after an extended period of use. This was especially the case for the fully extended configuration. On the other hand, the handheld float configuration proved to be very easy to use and resulted in excellent accuracies. This configuration can be deployed/retrieved using the pole or directly using the tether.

## 7.5  Other Observations

The wireless communication proven to be very reliable throughout the tests conducted. The waterproofing of the sensor packages performed as expected particularly for the skimmer sensor mounted on the floating platform because it got splashed significantly with no issues for the sensor. The batteries for both devices lasted a significant number of measures and were only replaced once or twice at most during the testing period. It would be helpful to have a low battery indicator along with showing the battery voltage.

## 7.6  Improvements

Although the sensors and most accessories performed as expected, there is always possibilities for improvements. Taking this device to the next TRL would require:

1. Reducing the weight of the overall packages for both sensors. This can be done by changing the material used and fabrication process.
2. Optimizing the attachment/detachment of different configurations to make it faster to switch between configurations (handheld -- float -- pole).
3. Skimmer mounting should be optimized by removing the bridge and reducing the weight. In addition, there is a need to make it easier to mount and adjust.
4. Given that the ultrasound requires the sensor to be kept relatively leveled, consumes significant power, and is expensive, there is a significant advantage in modifying the design and algorithm to be able to eliminate the need for the ultrasound. We will be considering machine learning algorithms for this purpose in our future research.

# Reference

[1] Mill-Max Mfg., "Press-fit PCB pins from Mill-Max are designed for plated through-holes", 2017. [Online]. Available: https://www.connectortips.com/press-fit-pcb-pins-from-mill-max-are-designed-for-plated-through-holes/

[2] M. Saleh, I. H. Elhajj, D. Asmar, "Capacitive Sensing for Measuring Oil Thickness Under Fouling Conditions," *2019 IEEE International Instrumentation and Measurement Technology Conference (I2MTC)*.

[3] Texas Instruments, "FDC1004". [Online]. Available: http://www.ti.com/product/FDC1004

[4] Smartec, "Universal Transducer Interface". [Online]. Available: https://smartec-sensors.com/cms/pages/products/uti-interface.php

[5] MaxBotix.com, "'MB7360 HRXL-MaxSonar-WR", 2017. [Online]. Available: https://www.maxbotix.com/Ultrasonic_Sensors/MB7360.htm/. [Accessed: 26 - April - 2019].

# Appendixes

# Appendix A: Technical Summary

REPORT TITLE: Development of an Oil Thickness Sensor Phase II

CONTRACT NUMBER(S): 140E0118C0003

FISCAL YEARS(S) OF PROJECT FUNDING: FY2018 to FY2022

CUMULATIVE PROJECT COST: $000,000

COMPLETION DATE OF REPORT: 07 February 2022

BSEE COR(S): Kristi McKinney

BSEE CO(S): Cielo Ibarra

PROJECT MANAGER(S): Imad Elhajj

AFFILIATION OF PROJECT MANAGER: American University of Beirut

ADDRESS: Bliss Street, Beirut, Lebanon

PRINCIPAL INVESTIGATOR(S)*: Imad Elhajj and Daniel Asmar

KEY WORDS: Floating oil thickness, in-situ, handheld, skimmer mount

* The affiliation of the Principal Investigators(s) may be different than that listed for Project Manager(s).

**Department of the Interior (DOI)**

The Department of the Interior protects and manages the Nation's natural resources and cultural heritage; provides scientific and other information about those resources; and honors the Nation's trust responsibilities or special commitments to American Indians, Alaska Natives, and affiliated island communities.

**Bureau of Safety and Environmental Enforcement (BSEE)**

The mission of the Bureau of Safety and Environmental Enforcement works to promote safety, protect the environment, and conserve resources offshore through vigorous regulatory oversight and enforcement.

**BSEE Oil Spill Preparedness Program**

BSEE administers a robust Oil Spill Preparedness Program through its Oil Spill Preparedness Division (OSPD) to ensure owners and operators of offshore facilities are ready to mitigate and respond to substantial threats of actual oil spills that may result from their activities. The Program draws its mandate and purpose from the Federal Water Pollution Control Act of October 18, 1972, as amended, and the Oil Pollution Act of 1990 (October 18, 1991). It is framed by the regulations in 30 CFR Part 254 – *Oil Spill Response Requirements for Facilities Located Seaward of the Coastline*, and 40 CFR Part 300 – *National Oil and Hazardous Substances Pollution Contingency Plan*. Acknowledging these authorities and their associated responsibilities, BSEE established the program with three primary and interdependent roles:

- Preparedness Verification,
- Oil Spill Response Research, and
- Management of Ohmsett - the National Oil Spill Response Research and Renewable Energy Test Facility.

The research conducted for this Program aims to improve oil spill response and preparedness by advancing the state of the science and the technologies needed for these emergencies. The research supports the Bureau's needs while ensuring the highest level of scientific integrity by adhering to BSEE's peer review protocols. The proposal, selection, research, review, collaboration, production, and dissemination of OSPD's technical reports and studies follows the appropriate requirements and guidance such as the Federal Acquisition Regulation and the Department of Interior's policies on scientific and scholarly conduct.